UNIVERSITY OF ALBERTA

Automated Fabrication and Surface Feature Classification for Atomic Silicon Devices

by

Jeremiah Croshaw

A thesis submitted in partial fulfillment for the degree of Doctor of Philosophy

in the

Faculty of Science
Department of Physics

©Jeremiah Croshaw December 2020

Abstract

The development of the modern transistor has sparked a technological revolution which has flourished for the past 70 years. Advancements in transistor design and fabrication have allowed for their continued shrinking in size and increase in operation speed. With the continued reduction in size of transistors to $\sim$ 10,000s of atoms, their expected increase in operation speed has reached a roadblock. In order to see any continued increase in operation speed, novel device designs made from few to single atoms or molecules must be explored. One such candidate is Binary Atomic Silicon Logic (BASiL) which relies on selectively patterning dangling bonds (DBs) on an otherwise hydrogen terminated silicon (H-Si) surface. These DBs act as quantum dots allowing for the controlled localization of charge within DB structures. While proof of concept studies have shown the utility in the application of BASiL devices to supplement and replace the transistor, further studies are needed to realize its full potential.

The automated fabrication of such devices is limited by the natural distribution of defects commonly found on the H-Si surface. By utilizing a combination of imaging modes of a scanning tunneling microscope (STM) and a non-contact atomic force microscope (nc-AFM), a catalogue of surface defects is created. This catalogue confirms the classification of previously reported and unreported defects providing experiential and theoretical evidence into their proposed assignments. The knowledge gained from this comprehensive study is used to create a neural network capable of segmenting and identifying defects of the H-Si(100)-2x1 surface. This network can distinguish between the defect free surface, charged defects, and uncharged defects through seven different classes. The locations of these defects are used for the automated fabrication of DB devices by patterning a DB structure in the most viable area of the surface as determined by the neural network. The accuracy and number of classes

of the neural network is improved by upgrading the quality of the training data used for the neural network enabling additional applications in surface quality assessment.

Utilizing one of the nc-AFM imaging modes refined in the creation of the defect catalogue, the AFM tip is turned into a charge sensor capable of distinguishing between the three charge states of the DB. This charge sensitivity is used to study DB wires fabricated on the H-Si(100)-2x1 surface revealing a previously unobserved ionic charge phase. Performing spectroscopic analysis, we identify higher energy configurations corresponding to an alternative lattice distortion as well as tip-induced charging effects. By varying the length and orientation of these DB structures, we further highlight key features in the formation of these ionic surface phases which provide the experimental insights needed for the incorporation of DB wires for BASiL device control. The combined efforts of developing a surface defect catalog, automated device fabrication scheme, and an understanding of the behaviour of DB wires work to further the development and application of BASiL devices enabling the replacement of current transistor technology by atom scale devices.

Preface

This thesis is an original work by Jeremiah Croshaw. It features three papers in which Jeremiah Croshaw is the first author as part of a collaborative effort with others. Author contributions to each of the three papers are indicated in Chapter 3, 4, and 5. The first two are referenced here [1, 2] with the third [3] in preparation for submission at the time of writing. The remaining work of this thesis is all original work done by Jeremiah Croshaw which either provides a necessary introduction to topics, or provides additional experimental findings that were not included in the three papers provided. Additional author contributions by Jeremiah Croshaw are referenced here [4–7]. Portions of relevant code used throughout the thesis are available here [8].

"All we need to decide is what to do with the time that is given us."

J.R.R. Tolkien

Acknowledgements

I would like to start by thanking my supervisor Robert Wolkow. I will be forever grateful for the opportunities you have given me and the positive impact you have had on my education. None of this would have been possible without you. I am very fortunate to have been part of such a wonderful lab group. From which, I would like to thank Martin Cloutier and Mark Salomons for sharing their technical expertise in vacuum systems, cryogenics, and lab maintenance. To Mohammad Rashidi and Thomas Dienel, I owe immersurable gratitude. Thank you both for your patience, guidance and friendship throughout my studies. It was a great honour to work with researchers who operate with such a passionate sense of wonder. To my fellow students Taleana Huff, Roshan Achal, Wyatt Vine, John Wood, Erika Lloyd, Stephanie Yong, Max Yuan, and Furkan Altincicek, thank you for sharing in the triumphs and failures of our work. I owe special thanks to Taleana Huff for her patience and mentorship. I would also like to thank lab members Jo Onoda, Jason Pitters, Radovan Urban, Bruno Martins, and Hedieh Hosseinzadeh for their guidance and support.

I would like to thank my family and friends for their support throughout my life. You have all had a positive impact on my life and I can confidently say I would not be where I am today without you. Lastly I would like to thank my partner Allison Owens. Your support, patience, and encouragement helped me get through my degree and I am forever grateful.

Contents

Abstract ii

Preface iv

Acknowledgements vi

List of Figures xi

List of Tables xv

Abbreviations xvi

1 Introduction 1
- 1.1 Computers . . . 1
  - 1.1.1 Binary Logic . . . 3
  - 1.1.2 Bipolar Junction and Field Effect Transistors . . . 5
  - 1.1.3 Short Channel Effects . . . 9
- 1.2 "Beyond CMOS" Devices . . . 10
- 1.3 Thesis Structure . . . 15

2 Experimental System and Techniques 17
- 2.1 Scanning Probe Microscopy . . . 17
  - 2.1.1 The Scanning Tunneling Microscope . . . 18
    - 2.1.1.1 Lock-In Detection . . . 22
  - 2.1.2 The Atomic Force Microscope . . . 23
    - 2.1.2.1 Kelvin Probe Force Microscopy . . . 29
    - 2.1.2.2 Noise . . . 31
- 2.2 The H-Si(100) Surface . . . 34
  - 2.2.1 Scanning Probe Imaging Modes . . . 35

2.2.1.1 Constant Current STM . . . 37
2.2.1.2 Constant Height STM . . . 38
2.2.1.3 Constant Height AFM . . . 40
2.2.2 Surface Dangling Bonds . . . 47
2.2.2.1 DB Devices . . . 52
2.2.2.2 DB Device fabrication . . . 53
2.3 Machine Learning and Neural Networks . . . 59
2.3.1 Applications to Scanning Probe Microscopy . . . 71
2.4 Summary . . . 74

3 Classification of Atomic Scale Defects of the H-Si(100) Surface using Multiple Imaging Modes 75
3.1 Introduction . . . 75
3.2 Atomic defect classification of the H-Si(100) surface through multi-mode scanning probe microscopy . . . 76
3.2.1 Abstract . . . 77
3.2.2 Introduction . . . 78
3.2.3 Results and Discussion . . . 80
3.2.4 Conclusion . . . 100
3.2.5 Methods . . . 101
3.2.6 Acknowledgements . . . 102
3.2.7 Funding . . . 103
3.2.8 Author Contributions . . . 103
3.2.9 Competing Interests . . . 103
3.2.10 Data Availability . . . 103
3.2.11 ORCID iDs . . . 103
3.2.12 Preprint . . . 104
3.2.13 References . . . 104
3.3 Atomic defect classification of the H-Si(100) surface through multi-mode scanning probe microscopy: Supporting Information . . . 104
3.3.1 Probe Particle Simulations . . . 107
3.3.2 Raised Silyl Groups . . . 117
3.4 Unpublished Supplemental Data Regarding Defects and Imaging Modes . . . 128
3.4.1 Apex Functionalization . . . 128
3.4.2 Defect Feature Fitting . . . 133
3.4.3 Additional Defect Information . . . 142
3.4.3.1 Dihydrides . . . 143
3.4.4 Missing Dimers . . . 147
3.4.5 Siloxane Dimer . . . 150
3.4.6 Neutral Point Defect . . . 152

4 Defect Identification and Segmentation Through Machine Learning 156
4.1 Deep Learning-Guided surface Characterization for Autonomous Hydrogen Lithography . . . 158
4.1.1 Abstract . . . 158
4.1.2 Introduction . . . 159
4.1.3 Methods . . . 162
4.1.4 Results and Discussion . . . 163
4.1.5 Conclusion . . . 168
4.1.6 Acknowledgements . . . 170
4.1.7 Author contributions . . . 170
4.1.8 Competing interests . . . 170
4.1.9 Data availability . . . 170
4.1.10 ORCID iDs . . . 170
4.1.11 References . . . 171
4.2 Deep Learning-Guided surface Characterization for Autonomous Hydrogen Lithography: Supporting Information . . . 171
4.2.1 Neural Network Architecture . . . 175
4.2.2 Scale Invariant Feature Transform Classification . . . 181
4.3 Unpublished Supplemental Data Regarding Defect Classification using Machine Learning . . . 187
4.3.1 Expanding Defect Classes . . . 187
4.3.2 Automated Quality Assurance and Defect Exploration . . . 191

5 Charge Distributions within Dangling Bond Structures 199
5.1 Charge Distributions in Silicon Atomic Wires . . . 205
5.1.1 Abstract . . . 206
5.1.2 Introduction . . . 206
5.1.3 The Single DB . . . 207
5.1.4 The Bare Dimer . . . 208
5.1.5 DB Wires . . . 212
5.1.6 Conclusion . . . 222
5.1.7 Methods . . . 222
5.1.8 Acknowledgements . . . 223
5.1.9 Author Contributions . . . 224
5.1.10 References . . . 224
5.2 Charge Distributions in Silicon Atomic Wires: Supporting Information . . . 225
5.3 Unpublished Supplemental Data Regarding DB structures . . . 233
5.3.1 The Hubbard Model . . . 235
5.3.2 The Bare Dimer . . . 238
5.3.3 Additional DB wire observations . . . 243

5.3.3.1 Si Tip Character and Charged Dangling Bonds 258
5.3.3.2 Capping DB Wires 265

6 Conclusion **269**

Bibliography **272**

List of Figures

1.1 The NOT, AND, and OR gate as fabricated with traditional field-effect CMOS transistors . . . 4
1.2 The Bipolar Junction Transistor (BJT) and Metal-Oxide-Semiconductor Field Effect Transistor (MOSFET) as indicated in the OFF and ON position . . . 8
1.3 Examples of atomic scale device architectures . . . 14

2.1 Energy diagrams of a metallic tip in contact with a semiconducting surface . 19
2.2 Density of States of W and Si . . . 21
2.3 Feature extraction using lock-in amplification. . . . 24
2.4 The Si and H-Si surfaces. . . . 36
2.5 Constant current STM of the H-Si(100)-2x1 surface . . . 37
2.6 Constant Current Imaging of surface features at differing tip biases and functionalizations. . . . 38
2.7 Constant Height STM images in different interaction regimes. . . . 41
2.8 Constant Height AFM images of the H-Si Surface. . . . 42
2.9 AFM spectroscopies with varying tip functionalizations. . . . 44
2.10 Limitations in AFM spectroscopy . . . 46
2.11 Spectroscopies over DBs. . . . 49
2.12 Varying spectroscopies of DBs on the surface. . . . 50
2.13 Automated DB fabrication. . . . 54
2.14 Tip shaping procedure . . . 56
2.15 STM feedback DB erasure. . . . 57
2.16 Make to erase repassivation . . . 58
2.17 Training a multi-layer perceptron. . . . 61
2.18 Machine learning techniques. . . . 63
2.19 Different image classification schemes . . . 66
2.20 Training of different models . . . 68
2.21 Unsupervised clustering . . . 70

3.1 Abstract image - Atomic defect classification of the H-Si(100) surface through multi-mode scanning probe microscopy . . . 78
3.2 Surface of H-terminated Si(100)-2x1 in different imaging modes. . . . 81

3.3 Common features of the H-Si(100)-2x1 surface imaged using the indicated STM and nc-AFM imaging modes. 85
3.4 Analysis of defects using dark-contrast AFM and profile extractions 93
3.5 Silicon vacancies at different lattice sites 97
3.6 Tip-induced removal of hydrogen atoms decorating neutral point defects . . . 99
3.7 Variation in dimer contrast in constant current STM topography of empty states imaging 104
3.8 Height series of constant height imaging 105
3.9 STHM images of the H-Si surface taken with different H-functionalized tips of differing flexibility 106
3.10 Relative height difference between a Si and H apex tip 107
3.11 Simulated STHM images in comparison with experiment 110
3.12 Simulated H-apex AFM images in comparison with experiment 113
3.13 Simulated Si-apex AFM images in comparison with experiment 116
3.14 Full and saturated colour scale images of the DB in STHM. 117
3.15 Common characteristics between Step Edges and Raised Si Clusters 119
3.16 Comparison between the bright and dark variation of the single dihydride-missing atom defect 120
3.17 Analysis of defects using Si-tip dark-contrast AFM and profile extractions with the probe particle model. 121
3.18 Line profiles across the Si vacancy “I” imaged with an H-functionalized AFM tip 122
3.19 A possible variation of the Si-vacancy. 123
3.20 Probe particle simulations of the Si vacancy 124
3.21 Adsorbed hydrogens 125
3.22 Another example of the H-removal of a point defect 126
3.23 Hydrogen removal from H-decorated point defects 127
3.24 Background subtraction of $\Delta f(z)$ spectroscopies 130
3.25 Multi contrast AFM functionalization 132
3.26 3x1 feature sizes 134
3.27 Single dihydride feature sizes 135
3.28 Dihydride pair feature sizes 136
3.29 Bright missing dimer feature sizes 137
3.30 Dark missing dimer feature sizes 138
3.31 Siloxane dimer feature sizes 139
3.32 Silicon Vacancy I feature sizes 140
3.33 Silicon Vacancy II feature sizes 141
3.34 Neutral point defect feature sizes 142
3.35 Dihydride Features of the Surface 144
3.36 dihydride pairs imaged with dark contrast 145

3.37 Erasing a dihydride pair 146
3.38 Dihydride pair shifting 148
3.39 Triple single dihydride 149
3.40 Bright and dark missing dimers 150
3.41 Missing dimer with a siloxane dimer 151
3.42 Oxygen contamination 152
3.43 The charged point defect. 154
3.44 Neutral point defect with a dihydride pair 155

4.1 Defect classes: empty state images of various defects found on a typical H-Si(100) surface labeled with their appropriate class. 162
4.2 A representation of the CNN architecture used in this study. 165
4.3 Traces of the predicted labels of the CNN and the original input images . . . 167
4.4 Automated pattern placement and fabrication 169
4.5 Normalized images of the defect classes 171
4.6 The effect of imaging bias on defect contrast 172
4.7 Surface scans and six of the labeled outputs from the neural network 173
4.8 Surface scans and one of the labeled outputs from the neural network 174
4.9 Heat maps from a random selection of the test data set 175
4.10 Architectures of each of the 10 models tested 177
4.11 Confusion matrices showing labelling accuracy of the test data set for each of the 10 models. 179
4.12 Decision tree summary followed in the lithography automation suite. 180
4.13 Scale invariant feature classification 182
4.14 An outline of the fabrication procedure. 183
4.15 An outline of the fabrication procedure. 184
4.16 Pattern patterning following defect classification 185
4.17 Pattern patterning following defect classification 186
4.18 Expanded defect classes for defect segmentation. 189
4.19 Confusion matrix of the updated neural network 191
4.20 A surface scan with defects as predicted by the updated model. 192
4.21 Autonomous surface quality assessment. 194
4.22 Mean shift clustering of unknown defects 195
4.23 Defect clusters of the Unknown class 197

5.1 Three Charge States of the Si DB 209
5.2 Charge Distributions of the Bare Dimer 210
5.3 Charge Distributions of the 5 DB wire 214
5.4 DB Wire Charge Distribututions 215
5.5 Charging of DB wires 218

5.6 Charging Voltage of DB Wires 219
5.7 DB Wires of Longer Length 221
5.8 Cluster of Surface DBs 225
5.9 STM measurements of the DB 226
5.10 Bare Dimer $I(V)$ Spectroscopy and STM Images 227
5.11 Band Diagrams for the Associated $\Delta f(V)$ Spectroscopy of a Bare Dimer. . . 228
5.12 Net Positive Configuration of a 5 DB wire as probed with an H terminated tip.229
5.13 Charge Distribution with Tip Height 230
5.14 KPFM Spectroscopy of DB Wires 231
5.15 Charge Distribution Among Longer Wires 232
5.16 The bare dimer anti-node 234
5.17 A perturbed bare dimer 239
5.18 A double bare dimer 241
5.19 The butterfly shape of the bare dimer 242
5.20 DB wire decoupling with bare dimer. 244
5.21 I(V) spectroscopy of DB wires 246
5.22 Constant height STM measurements of 3-7 DB wires at various bias values. . 247
5.23 Charge distribution with tip depth 250
5.24 Charging of DB wires with current signal 251
5.25 Charge distributions among longer wires with current signal 253
5.26 Filled and Empty States STM images of DB Wires 254
5.27 Polarization of a 4 DB chain. 257
5.28 Polarization states spectroscopies of 4 DB chain 259
5.29 Tip height dependence over a single DB 261
5.30 Tip height dependence over a 3 DB wire 262
5.31 Tip height dependence over a 4 DB wire 263
5.32 Tip height dependence over a 5 DB wire 264
5.33 Tip height dependence over a 6 DB wire 265
5.34 Tip height dependence over a bare dimer 266
5.35 H_2 passivation of DB clusters. 267

List of Tables

4.1 Parameters of each of the tested models highlighting key features of their architecture as well as classification performance. 178
4.2 Updated Defect Data Set Specifications. Defect count shows the unique labels in the 86 images used for the data set. 188

Abbreviations

AFM	**A**tomic **F**orce **M**icroscope
ALU	**A**rithmetic **L**ogic **U**nit
BASiL	**B**inary **A**tomic **Si**licon **L**ogic
BJT	**B**ipolar **J**unction **T**ransistor
CNN	**C**onvolutional **N**eural **N**etwork
CPD	**C**ontact **P**otential **D**ifference
CPU	**C**entral **P**rocessing **U**nit
DB	**D**angling **B**ond
DIBL	**D**rain **I**nduced **B**arrier **L**owering
DOS	**D**ensity **O**f **S**tates
ENIAC	**E**lectronic **N**umerical **I**ntegrator **A**nd **C**omputer
FIB	**F**ocused **I**on **B**eam
FIM	**F**ield **I**on **M**icroscope
FET	**F**ield **E**ffect **T**ransistor
H-Si	**H**ydrogen-terminated **Si**licon
IC	**I**ntegrated **C**ircuit
KPFM	**K**elvin **P**robe **F**orce **M**icroscopy
ML	**M**achine **L**earning
MOSFET	**M**etal **O**xide **S**emiconductor **F**ield **E**ffect **T**ransistor
nc-AFM	**N**on-**C**ontact **A**tomic **F**orce **M**icroscope
NDR	**N**egative **D**ifferential **R**esistance

PI	**P**roportional-**I**integral
PLL	**P**hase **L**ocked **L**oop
RAM	**R**andom **A**ccess **M**emory
RL	**R**einforcement **L**earning
SPL	**S**canning **P**robe **L**ithography
SPM	**S**canning **P**robe **M**icroscopy
SPS	**S**canning **P**robe **S**pectroscopy
STEM	**S**canning **T**ransmission **E**lectron **M**icroscope
STHM	**S**canning **T**unneling **H**ydrogen **M**icroscopy
STM	**S**canning **T**unneling **M**icroscopy
SIFT	**S**cale **I**nvariant **F**eature **T**ransform
TIBB	**T**ip **I**nduced **B**and **B**ending

Chapter 1

Introduction

1.1 Computers

The technological revolution seen with the development of the electronic computer has had dramatic effects on our society [9]. By automating simple yet time consuming processes, it has opened up a multitude of ways to streamline and optimize our daily lives. One of the earliest and most significant examples of this was in the calculation of the 1890 US census. By using the recently developed tabulating machine [10] and census data stored on punch cards, it allowed for a dramatic increase in the efficiency of processing the census data [11]. The tabulating machine consisted of a set of conducting pins which could be lowered to connect to a set of mechanical rotors. When a punch card is placed between the conducting pins and rotor contacts, it behaves as a switch only allowing an electrical connection to be formed where a hole has been punched from the card causing the rotor to turn. Operating like an electric abacus, the use of the punch card system to selectively turn corresponding rotors was one the first examples of using electrical signals for computation. Further sophistication and development of such tabulating machines lead to the founding of IBM [12].

The Harvard Mark 1 was one of the first general purpose electromagnetic computers. No longer requiring the use of punch cards to modulate the activation of rotors, the Harvard Mark 1 relied on a series of electromechanical relays. These relays featured two contacts with a movable wire between them. By using an electromagnetic coil, the wire could be moved into a position such that it allowed current to flow between the contacts, thus completing the circuit. By using programmable switches it was able to store numbers as well as add, subtract, multiply, and divide on the time scale of a few seconds each [13].

Further developments in computational switches lead to the invention of the triode vacuum tube replacing the somewhat fragile electromechanical relay with a fully electrical switch. A triode vacuum tube operates by using a heated metal cathode. When a nearby anode has a positive applied bias, electrons can flow freely across the junction via thermionic emission, completing the circuit. The addition of a grid allows the flow of electrons to be restricted when a negative bias is applied to the grid relative to the cathode. The Colossus Mark 1 was the first programmable all electronic computer which used these vacuum tubes with the more powerful ENIAC (Electronic Numerical Integrator and Computer) following shortly after [14]. Consisting of 18,000 vacuum tubes [15], the ENIAC was capable of computing roughly 357 multiplications per second and 35 divisions per second (a clock speed of 0.1 MHz) [16].

The development of the transistor, which served as a long term replacement for the vacuum tubes revolutionized the world of computing to this day. By connecting two ends of a semiconducting material (usually Si or Ge), current between the two ends could be turned on and off using a third gating connection to act as a switch, modulating the flow of electrons. First appearing in the IBM 608, this computer was capable of multiplying and dividing in milliseconds [17]. The semiconductor transistor has been the dominant workhorse of the computing industry ever since with a total revenue of $515 billion USD in 2019 [18] appearing in devices such as computers, cell phones, cars, microwaves, and TVs.

With the continued development of transistor technology, a scaling trend known as Moore's Law [19] was observed which noted that the number of transistor that could be placed on a chip doubled every 18 months leading to continued improvement in computers and similar technology. As the size of transistors continued to shrink, consistent device operation was not sustainable with the predicted behaviour of Moore's Law. Issues known as short channel effects [20] placed an upper limit on the clocking speed due to increased power consumption per unit area of the chips [21]. In order to continue developing smaller and faster switches, the search for a viable transistor replacement in the regime known as "beyond CMOS[1] devices" has been in the forefront of nanotechnology research since the predicted collapse of Moore's Law, leading to the development of numerous potential replacements. To better understand the need for these replacements, it is useful to provide a brief overview on the use of transistors in computers and how their decreasing size has lead to the breaking of Moore's Law.

1.1.1 Binary Logic

Modern computers use binary logic for computation, which represents data as either TRUE (1) or FALSE (0). In electrical computers, this corresponds to the presence (1) or absence (0) of an electrical current representing what's known as a bit. By combining 8 bits (also known as a byte), it is possible to represent numbers up to 256[2]. The ability to manipulate and compare binary information is realized through the development of logic gates. Consider the three most simply constructed gates shown in Figure 1.1. The NOT gate flips the input bit resulting in (1) going to (0), and a (0) going to (1). This is realized by connecting the input to the switch of the transistor and the output before the transistor (The transistor types drawn in Figure 1.1 represent a field effect transistor as described in the next section). If we supply current through the top wire down, it will only flow through to the output (1) if

[1] CMOS or Complimentary Metal-Oxide Semiconductors is a transistor architecture which will be explained in a short while

[2] These numbers are stored in base 2 so 11010110 is $128{\cdot}1 + 64{\cdot}1 + 32{\cdot}0 + 16{\cdot}1 + 8{\cdot}1 + 4{\cdot}0 + 2{\cdot}1 + 1{\cdot}1 = 219$

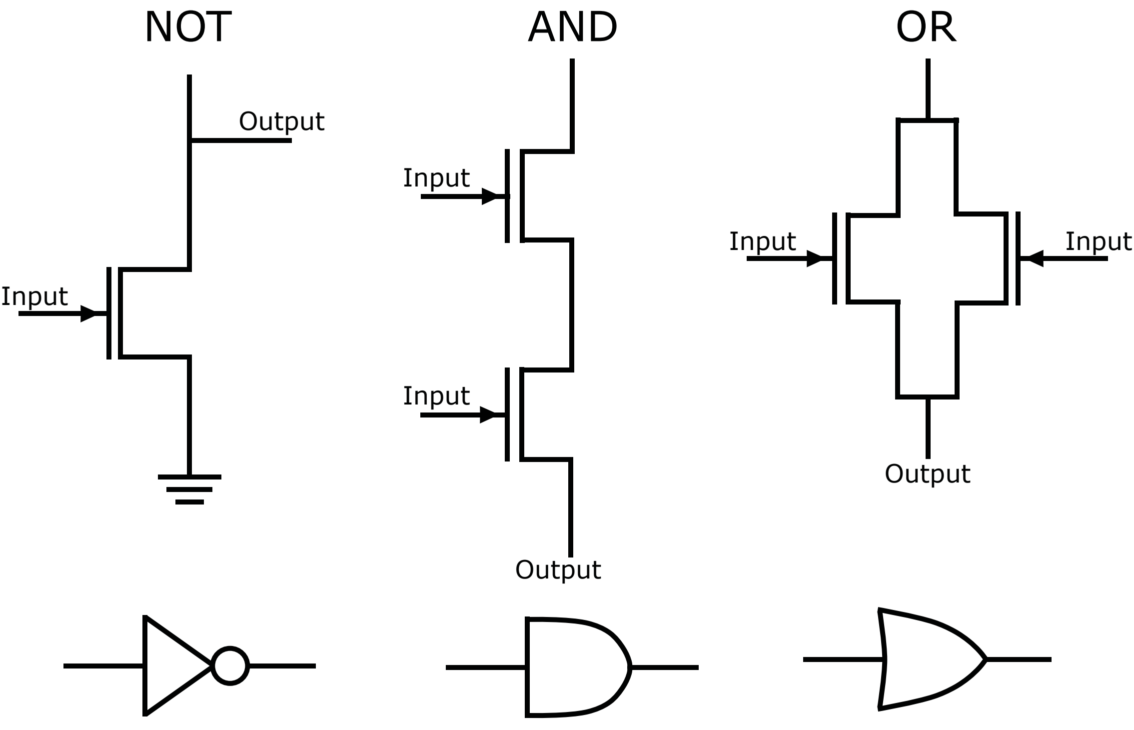

Figure 1.1: The NOT, AND, and OR gate as fabricated with traditional field-effect CMOS transistors. Inputs and outputs for each gate are indicated with the arrow direction on each input corresponding to an n-doped channel. The IEEE electronic symbol for each gate is drawn below. Adapted from [22].

the input is deactivated (0). If the switch is activated (1), current will instead flow to ground reducing the current measured at the output (0). The AND gate is capable of comparing two bits; the output is (1) if both inputs are also (1), and (0) if either or both inputs are (0). The AND gate circuit diagram in Figure 1.1 shows two transistors in series with each input connected to the switch of each transistor. Only if both inputs are activated (1) can current flow through the transistors to the output (1). If either switch is deactivated (0), no current is registered at the output (0). The OR gate compares two inputs giving a (0) at the output if both inputs are set to (0). If either or both inputs are (1), the output is also (1). To create this gate, two transistors are connected in parallel where current can flow to the output (1) through either or both transistors (Figure 1.1).

With these three building blocks, more complicated logic gates such as an XOR, NAND, and NOR can be created allowing for more complicated logic comparisons. Computers are built by combining more and more gates creating higher and higher levels of abstraction. By combining an XOR gate with an AND gate, one can create a half adder. Two half adders and an OR gate will create a full adder [22]. Combining more and more devices of these types can create arithmetic logic units (ALUs) which can execute a multitude of logic operations. When ALUs are combined to a random access memory system (RAM) they can be used to create a central processing unit (CPU) [23]. The CPU operates in cycles where it can fetch information, decode it, and execute algorithms allowing the computer to execute a number of different computations. The cycle rate determines how fast the CPU can switch between the fetch, decode, and execute procedures. This process is limited by how fast information (electrons) can physically propagate through the integrated circuits (IC) of a computer chip[3]. It is reasonable to assume that by shrinking the size of transistors on an IC, their clocking rate will also increase however, clocking rates have been held constant at 2-5 GHz since the mid 2000's despite the continued reduction in size resulting in the number of transistors on an IC increasing by nearly 100 times [21]. To understand why we need to better understand how transistors are used to modulate electric current.

1.1.2 Bipolar Junction and Field Effect Transistors

The bipolar junction transistor (BJT) and field effect transistor (FET) form the majority of transistors used in the semiconducting industry today, both of which are fabricated using a combination of p and n-type semiconductors. By adding dopant atoms to a semiconductor, it is possible to change the energy level of highest occupied electron states in the system (known as the Fermi level). The Fermi level of a silicon semiconductor can be raised (n-type) by adding electron rich group V atoms such as phosphorus and arsenic and lowered

[3]The speed of modern day chips is limited by the amount of heat produced per transistor switch. This will be of the form $P \propto CV^2 \cdot fn$ where C is the capacitance of a transistor, V is the voltage across a transistor, f is the switching frequency of the transistor, and n is the number of transistors on a chip

(p-type) by adding electron deficient group III atoms such as boron. If we fabricate these two doped semiconductors such that they are electrically connected, we create a p-n junction. As a result, the electrons from the n-type semiconductor move to the electron deficient p-type semiconductor in order to reduce the overall energy of the system. This creates an all important depletion region in the junction where the n-type depletion region has an overall positive charge (due to the (net) positively charged group V atom) and the p-type depletion region has an overall negative charge (due to the (net) negatively charged group III atom). If we connect the two ends of the semiconductor to a battery, we create a diode. By applying a forward bias, we reduce the size of the depletion region allowing for electrons to flow across the junction. Applying a reverse bias increases the depletion region making it more difficult for electrons to flow. This asymmetric current flow is what gives the diode its directional behaviour.

To make a BJT, a semiconductor is fabricated in an n^+pn (or p^+np) doping scheme where the + indicates a higher doping level as shown in Figure 1.2. These layers are referred to as the emitter, base, and collector. If we apply a bias between the emitter and collector, no electrons are able to flow between the two regions due to the depletion of electrons that's formed across the base. Now, if we apply a smaller bias between the emitter and the base, electrons begin to diffuse across the depletion region of the emitter-base junction. This results in electrons accumulating within the depletion region allowing for electrons to diffuse into the base. If the base width is small enough, electrons are able to travel into the collector allowing current to flow. This creates a binary switch, where the electron flow across the device is controlled by the current between the emitter and base.

A FET operates on a different principle. As the name suggests it relies on field-effects rather than current to drive the switching motion. Although many different designs exist, the most commonly used is a Metal-Oxide-Semiconductor FET (MOSFET). The n^+pn^+ (p^+np^+) doping scheme consists of a p-type substrate with two heavily doped n-regions known as the source and drain as shown in Figure 1.2 . On top of the silicon, an insulating layer is placed (SiO_2 was most commonly used) with a metal gate electrode patterned on top. If we apply

a bias between the source and drain, electron flow is stopped due to the depletion region between the source and substrate. To remedy this, a positive bias is applied to the gate which lowers the depletion region. With the continued attraction of negative charge, we are effectively changing the p-type substrate to behave as an n-type one allowing for current to flow across the junction in a continuous channel. A similar configuration can be achieved using a p^+np^+ doping scheme except a negative gate bias is needed to turn the transistor on. Many references exist which cover these and more transistor architectures in more detail [24–26].

One of the key differences between the BJT and FET is that a BJT wastes a small amount of current when in the ON position, while the FET does not[4]. This makes it difficult to scale the fabrication of the BJT as packing more transistors in a smaller area would mean more wasted current which translates directly to heat. Because FET operation does not produce as much heat as a byproduct, its fabrication is much more scalable making it the workhorse of the semiconductor industry for the past 60 years, accounting for 99.9% of all manufactured transistors [27]. The dominant source of wasted heat production for an FET is the continual charging and discharging of the gate capacitor. An approximation for the amount of power consumed (P) can be written as

$$P = \frac{1}{2}CV^2 \cdot f\alpha \tag{1.1}$$

where C is the gate capacitance, V is the applied voltage, f is the CPU clock frequency, and α is a functional scaling factor (not all transistors switch per clock cycle). If we assume the heat produced per unit area is around 100 W/area, and the total transistor density is around 10^9 1/area with a clock speed of 5 GHz, and an α of 1, the average energy used per

[4]The FET also wastes a small amount of current through leakage but this effect has only recently had an impact on device operation as will be described with "short channel effects".

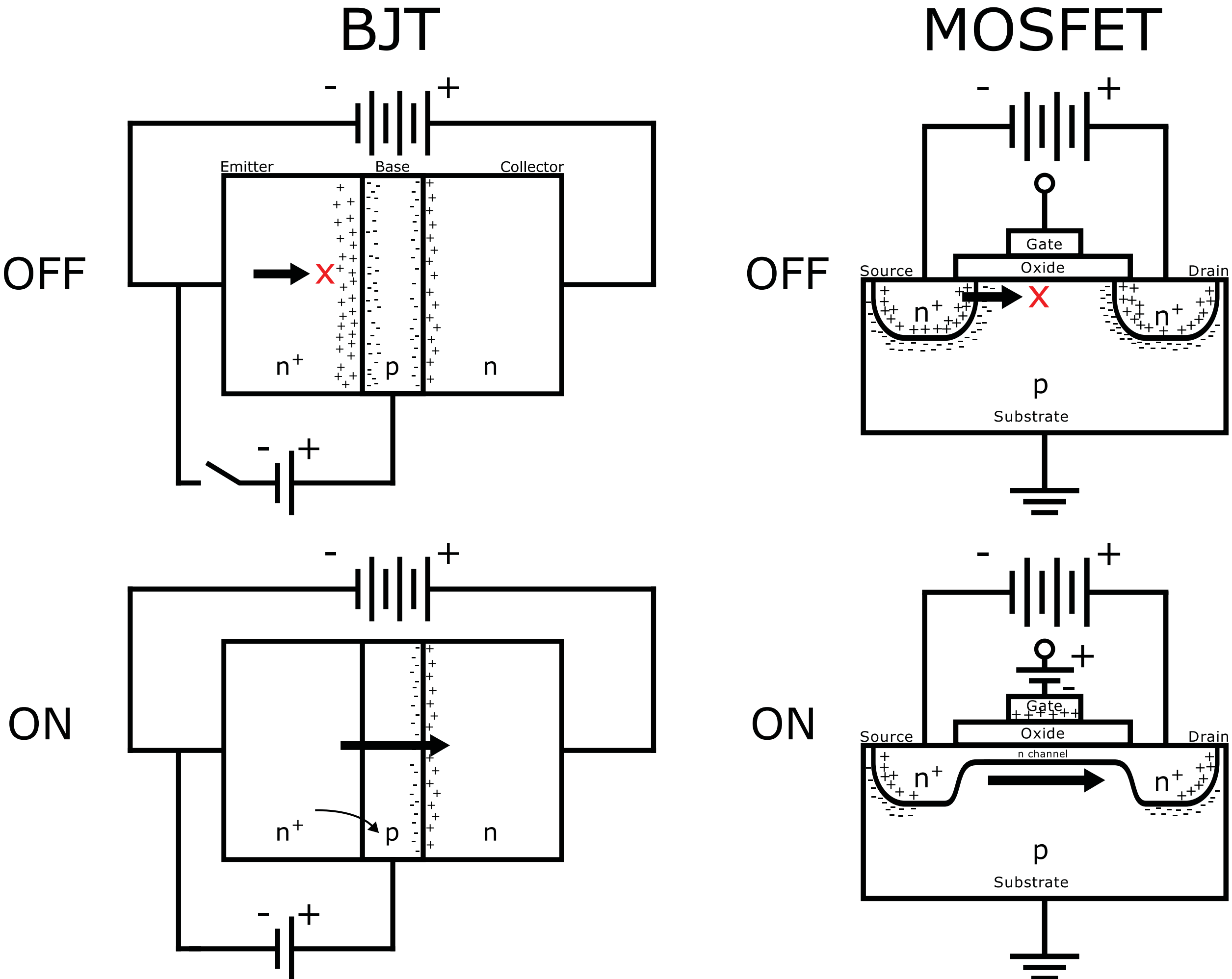

FIGURE 1.2: The Bipolar Junction Transistor (BJT) and Metal-Oxide-Semiconductor Field Effect Transistor (MOSFET) as indicated in the OFF and ON position. Positive and Negative charges within the semiconductor correspond to fixed charges from ionized atoms within the semiconductor. Adapted from [26]

.

transistor per cycle is around 125 eV[5] which gives an order of magnitude approximation for transistors within the 32 nm node regime [28]. As the design of FETs continued to advance and shrink in size, short channel effects began having an impact in the operational properties of FETs limiting how small they can be made [20].

[5]One key thing to note with this calculation is that in addition to increased power wasting through the transistor itself, the decreased size of the connecting wires adds some additional power consumption through a similar $1/2CV^2$ relation. As transistor devices become smaller and smaller, upwards of 50% of the power consumption is through interconnecting wires.

1.1.3 Short Channel Effects

Short channel effects are present when the channel length (distance between the source and drain) becomes so small that it can no longer act as a charge barrier. At larger length scales, this occurs through drain induced barrier lowering (DIBL) where the bias between the source and drain reduces the barrier height between them. This allows electrons to thermally hop over the barrier, negating the effect of the substrate depletion region resulting in an increased leakage current (heat) between the source and drain. This results in a reduction in the sub-threshold swing of the transistor meaning that a larger bias must be applied to get the same changes in current as longer channel transistors. If the channel becomes smaller still, electrons can simply tunnel through the barrier. This tunneling phenomenon can also be seen through the oxide layer between the metal gate and the substrate, contributing to unwanted leakage current between the gate and substrate. Despite still being operable with some leakage current, it results in the generation of additional heat which creates a trade off between the energy consumption and speed of the device [24].

Three short term solutions have been put forth to reduce this effect. By changing the dielectric constant (k) of the insulating layer, its thickness (t) can be increased without significantly altering the capacitance (C) of the system ($C \propto k/t$) thus reducing the amount of unwanted tunneling current [29]. This can be combined with building the semiconductor on an insulating layer which electrically isolates the transistor, reducing the leakage current from the gate allowing for greater control of the source-drain barrier [30]. Alternatively, novel channel designs are being used to increase the effective length of the channel. The finFET is one such device where the channel between the source and drain has been extended into 3 dimensions creating a fin [31]. This allows the gate to be patterned around three sides of the channel giving more control in current flow across the transistor [32].

As transistor sizes continue to shrink, these novel designs will eventually sucumb to the quantum effects limiting the ultimate size of transistors. Work is still being done to extend the

life of the modern day transistor through things like new advancements in lithography[6] [33] and transistor design such as the gate-all-around (GAAFET) [34] and tunnel FET (TFET) [35]. Although these techniques provided temporary solutions, the continued miniaturization of transistors still leaves them vulnerable to quantum tunneling and subsequent leakage current. This unavoidable effect will continue to affect the upper limit on both the transistor clock frequency and overall power consumption creating the necessity to look for alternative device designs. These new devices fall into the realm of "beyond CMOS" [36] which invoke novel architectures, fabrication schemes, and operational principles.

1.2 "Beyond CMOS" Devices

Since the ultimate size of computational devices will be limited by the size of their fundamental building block (the atom), significant research has been focused on developing logic devices that are made of molecules [37–41] or few to single atoms [42–49]. In order to provide a suitable replacement for CMOS transistors, these devices must be capable of demonstrating a similar ability to switch between two distinguishable states, an ON and OFF state. We will look at 4 different examples of such designs highlighting their viability in sustaining Moore's Law.

The work by Soe *et al.* [50] uses a combination of trinaphthylene molecules and gold atoms to reproduce NOR gate logic shown in Figure 1.3 (a). Using two ends of the triangle shaped molecule as inputs, they are able to modify a current signal measured at the remaining corner of the molecule. This output signal can be modified by adding gold atoms to one or both input corners of the molecule thus changing the output current of the molecule.

Similar work done by Khajetoorians *et al.* [42] demonstrated spin-based logic using Fe atoms and ferromagnetic Cobolt islands on a Cu surface shown in Figure 1.3 (b). By positioning

[6] In particular, this refers to the development of extreme ultraviolet lithography, which uses a smaller wavelength of light allowing for smaller transistor features to be fabricated.

Fe atoms in chains extending from cobalt islands and applying a magnetic field (0.2 T), the chains align in an antiferromagnetic fashion where the spin of the end Fe atom in the wire depends on the spin of the cobalt island. An odd length wire will flip the input spin while an even length wire will have the same spin as the Co island. These wires can be positioned in such a way that the spin of an additional Fe atom placed between two wires can flip corresponding to the input spins on the cobalt islands which propagate down the wires. By applying a magnetic field pulse, they are capable of switching the spin states of either cobalt island (by varying the magnitude and sign of the B field pulse they can select which island to address) reproducing both NOT and OR gate logic.

Despite the remarkable achievement shown by these two works in demonstrating atom scale logic, there are some limitations which would prevent a viable integration into full transistor logic. The ability to switch between states using the trinaphthylene molecule requires the movement of single gold atoms, limiting the switching rate of such a device. There is a potential to replace these gold atoms with extended atomic wires, however, a full demonstration has not yet been shown. The ability to switch between spin states of cobalt islands using magnetic fields allows the switching between states to operate at much faster rates, however a scalable design in which each cobalt island can be uniquely addressed has yet to be shown. In addition, the thermal stability of these structures is much lower than required. As these structures are only physisorbed to their respective surface, they are only structurally stable to temperatures of around 100 K making their use in modern electronics limited. It is true that certain applications which utilize cryogenic temperatures may be suitable, however, difficulties in storage and transportation require that atomic electronics that will eventually replace transistor technology be made from more stable structures.

Understanding the need for greater structural stability, there have been two related atomic scale devices which utilize a chemical incorporation. The work by Fueschle *et al.* [48] uses a single atom transistor made by the selective implantation of a single phosphorus atom within a Si substrate. Similar to a normal transistor, it consists of a source and drain, except the regulation of current is done by the single phosphorus atom positioned between them. This

phosphorus atom acts as an electron island, capable of localizing a single electron. By using a gate electrode, the current between the source and drain can be regulated via the phosphorus atom. Taking advantage of a process known as the Coulomb blockade, the transistor is in an OFF position when the phosphorus atom has no available states to allow the flow of electrons (similar to the OFF position of the MOSFET discussed above). By changing the gate bias, we can introduce an electron channel through the phosphorus atom moving the transistor to the ON position as shown in Figure 1.3 (c). One of the few potential limitations of this scheme is that a single transistor requires roughly 20 nm between the source and drain to properly couple to the single phosphorus atom placing a limit on the ultimate size density of these transistors. Additionally, such devices are still expected to have a non-zero subthreshold swing above cryogenic temperatures [51] meaning there will still be a slight leakage current when switching the device. Despite this, single-atom-transistors are still being investigated as potential replacements to CMOS technology [52, 53] and have additionally found applications in quantum computing and charge sensing [54].

Another system which uses a silicon based substrate for fabrication is binary atomic silicon logic (BASiL) developed by Huff *et al.* [46]. Similar to the work by Fueschle *et al.*, BASiL toggles between the ON and OFF state via the addition of single charges however, instead of phosphorus dopants, surface Si dangling bonds are used. A dangling bond is an unsatisfied bond of an atom which behaves as a quantum dot. This quantum dot behaviour means the DB can hold 0, 1, or 2 electrons putting it in a positive, neutral, or negative charge state respectively. By positioning two dangling bonds in close proximity, their electron occupation can be modified such that a single additional electron is shared between them (meaning one DB is neutral while the other is negative). The position of the extra electron can be toggled between the two dangling bonds representing (1) or (0) states. By patterning pairs of dangling bonds in various arrangements, logic gates such as an OR gate [46] as shown in Figure 1.3 (d) have been experimentally shown with theoretical modelling demonstrating AND, XOR, NAND, and XNOR gate functionality [55]. BASiL devices provide an additional advantage in that they're compact (the OR gate demonstrated only required a 3.9 x 3.9 nm^2

area), and they are physically stable at much higher temperatures [56, 57]. One disadvantage, much like the work of Soe *et al.*, is that toggling between states is still limited to the addition or removal of single atoms making the switching between states a slow process. To create a fully integrated circuit, it will become necessary to toggle between states using atomic wires much like the work of Fueschle *et al.*

Due to their size, the fabrication of such "beyond CMOS" devices is unobtainable by conventional CMOS fabrication techniques. As such, these devices are fabricated using scanning probe microscopes (a process known as scanning probe lithography (SPL)) [58]. In these instances, a sharp metal tip is used to manipulate atoms on the surface with sub nm resolution. In the cases of Soe, Kahjetooreans, and Huff, the scanning probe is also used to read the output of the logic devices. Despite the proven ability of scanning probe lithography to address atoms with sub-nanometer resolution, it requires intensive user input during the fabrication process requiring an operator to fabricate a single device at a time. Comparing this to CMOS lithography which is almost completely automated [59], it is clear that significant advancements in automating SPL are needed.

The reason current SPL methods are limited to single user fabrication is due to the fundamental size of these logic units. At such a size, surface variations and defects found on the patterning substrate have a more significant impact on the fabrication and operation of these devices compared to traditional transistor devices [6, 60, 61]. The difficulty in autonomously interpreting the types and locations of defects which would inhibit device fabrication thus presents itself as one of the largest challenges in automating SPL. Due in large to the complexity and variation of surfaces at the atomic scale, attempts to automate SPL using more traditional image analysis have fallen short [62–64]. As will be discussed in future chapters, by applying more complicated machine vision techniques using machine learning, it is possible to extract surface features necessary for the successful automation of SPM.

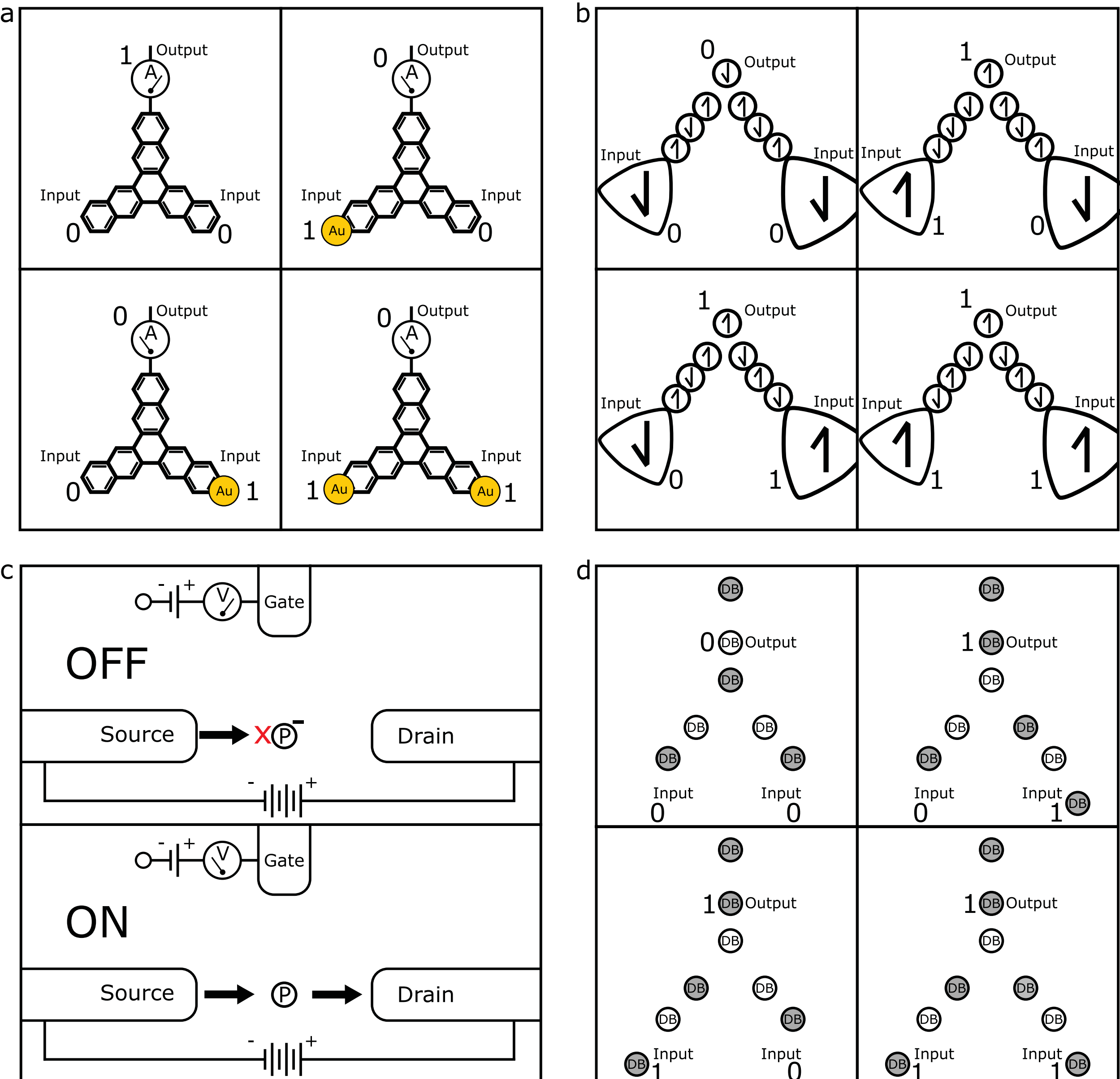

FIGURE 1.3: Examples of atomic scale device architectures. (a) The NOR gate functionality using the trinaphthylene molecule as shown in [50]. (b) The OR gate logic achieved using the spins of Co clusters and Fe atoms as shown in [42]. (c) The single atom transistor as shown in [48]. The OFF position shows an additional charge on the P atom indicating a coulomb blockage region. The ON position removes this blockade allowing current to flow. Additional Voltage configurations giving OFF/ON behaviour is achievable as well. (d) The OR gate logic using Silicon Dangling Bonds in [46]. Grey DBs indicate the localization of an additional electron.

1.3 Thesis Structure

The goal of this thesis is to provide further support in developing the understanding needed for the implementation of BASiL devices via Scanning Probe Lithography. Specifically, this thesis will be structured based on the findings of three separate papers outlined in Chapters 3, 4, and 5, along with supporting experimental techniques and theoretical details outlined in Chapter 2 and a concluding discussion in Chapter 6.

The theoretical details and experimental techniques outlined in Chapter 2 will aim to build an understanding of these concepts and how they have been implemented in the published works of the following chapters. Details of the hydrogen terminated silicon surface and its properties will be given along with a brief discussion of the fabrication and characterization of surface dangling bonds. Two variations of scanning probe microscopy are discussed, namely scanning tunneling microscopy and atomic force microscopy. Further alterations in the operating modes of these two techniques will also be discussed outlining their versatility in extracting both electronic and atomic surface features. In addition to this, an introduction to machine learning will be given. This introduction aims to provide a background in machine learning topics and explains how these techniques have been applied to scanning probe microscopy and lithography.

Chapter 3 will focus on the development of a surface defect catalogue of the H-Si(100)-2x1 surface. This work was done to build upon the use of machine learning for defect classification (presented in Chapter 4) and has aided in the development of a greater understanding of surface defects allowing for improvements to be made to the application of machine learning for defect classification. Using a total of 6 different imaging modes in scanning probe microscopy has allowed for a more comprehensive understanding of the surface. This understanding enabled the confirmation of assignments of previously reported defects and suggestions for new classifications to previously unreported and discrepant defects. The chapter concludes with supporting details outside the publication which further the understanding of several of the catalogued defects highlighting unique differences in their appearance and behaviour.

As mentioned, Chapter 4 will focus on the implementation of machine learning in surface classification and segmentation. Divided into two parts, the first half will showcase the published work which features a working neural network capable of distinguishing between 7 classes of surface features. This neural network was used to demonstrate the viability in autonomously fabricating BASiL devices using the feedback of the neural network to determine the most viable location for device placement. The remaining portion of this chapter focuses on the further development of the neutral network using information learned from the work in Chapter 3. Further insights into the variations of surface defects has allowed for a greater understanding of defect varieties leading to enhanced capabilities of the neural network.

Chapter 5 will shift the focus away from defects and look at dangling bond structures. With the ultimate goal of developing atomic wires used for device interconnects, this work looks at the behaviour of DB wires at various energies and lengths. By using a Si functionalized AFM probe (a process developed in Chapter 3), it is possible to more easily distinguish between all three charge states of surface DBs. This has allowed for a clear interpretation of charge distributions within DB structures giving insights into their expected viability as charge carriers.

Chapter 6 concludes with a brief summary of the results presented in the previous chapters and discusses their implications in the development and outlook of BASiL devices.

Chapter 2

Experimental System and Techniques

2.1 Scanning Probe Microscopy

The operation of a scanning probe microscope (SPM) in principle is very straightforward. A probe tip (usually metallic) is brought within interaction distance of a sample (in our case Si). This probe tip is then scanned across the surface using piezomotors allowing for sub-Å precision. By coupling these three components to control electronics, it allows for the measurement, control, and modulation of the tip-sample interaction. The nature of the interaction depends on the enabled mode of the microscope. If a bias is applied between the tip and sample and they are brought within tunneling distance (on the order of 1 nm), a tunneling current can be detected, amplified, and used as feedback as in a scanning tunneling microscope (STM). Alternatively, if the probe tip is mounted on an oscillating cantilever and scanned over the surface, deviations from the resonance frequency can be correlated to an interacting potential between the tip and sample creating an atomic force microscope (AFM). Numerous variations of the STM and AFM exist which can probe capacitance [65–67], spin and magnetism [68–70], contact potential difference [71, 72], and many others as discussed in [73]. In addition to microscopy, a scanning probe spectroscopy (SPS) variation

can be achieved by modulating a control parameter, (usually the tip-sample bias or tip-sample separation) and measuring the corresponding feedback channel (current, frequency shift (Δf), etc.). When combined, both the microscopy and spectroscopy variations of the STM and AFM allow for a deeper understanding of both the electronic and geometric nature of the sample under investigation.

2.1.1 The Scanning Tunneling Microscope

The STM, first invented by Binnig and Rohrer in 1981 [74] at IBM achieved a resolution of roughly 20 Å. Since then, significant advancements in piezo design, noise isolation, and cryogenic systems have improved the resolution down to the sub-Å level [75]. The theoretical understanding of how an STM works was first described by Tersof *et al.* [76] building off work done by Bardeen [77]. To better understand this work, consider a metal tip and semiconducting sample. If these two materials are electrically isolated, the vacuum level of these systems are aligned. The energy difference between the Fermi level in the metal tip and vacuum level is referred to as the work function (ϕ). Since the Fermi level in semiconductors can be modified by varying the doping levels, it is more common to refer to the electron affinity (χ) for semiconducting materials. This refers to the energy difference between the vacuum level and the bottom of the conduction band as depicted in Figure 2.1 (a). By electrically coupling the two materials, electrons are free to redistribute between them, lowering the energy of the system creating a contact potential difference between the two (Figure 2.1 (b))[1]. In the case of Tungsten ($\phi_W \approx 4.5$ eV) and Si ($\chi_{Si} \approx 4.05eV$)[2], the electric field can be nullified by applying a positive tip bias of ≈ 0.45 eV depending on the crystal face [78]. If we apply an additional positive or negative bias to the tip, we can lower or raise the tip electron energy levels relative to the sample such that electrons can tunnel

[1]The mechanism is identical to the creation of the depletion region in the p-n junction, however, the metallic behaviour of the tip screens any effects from metal ions so there is effectively no electric field created in the metal.

[2]The relevant quantity is actually the Fermi level of the silicon sample which can be approximated to χ_{Si} for degenerate (n-type) doping at low temperatures.

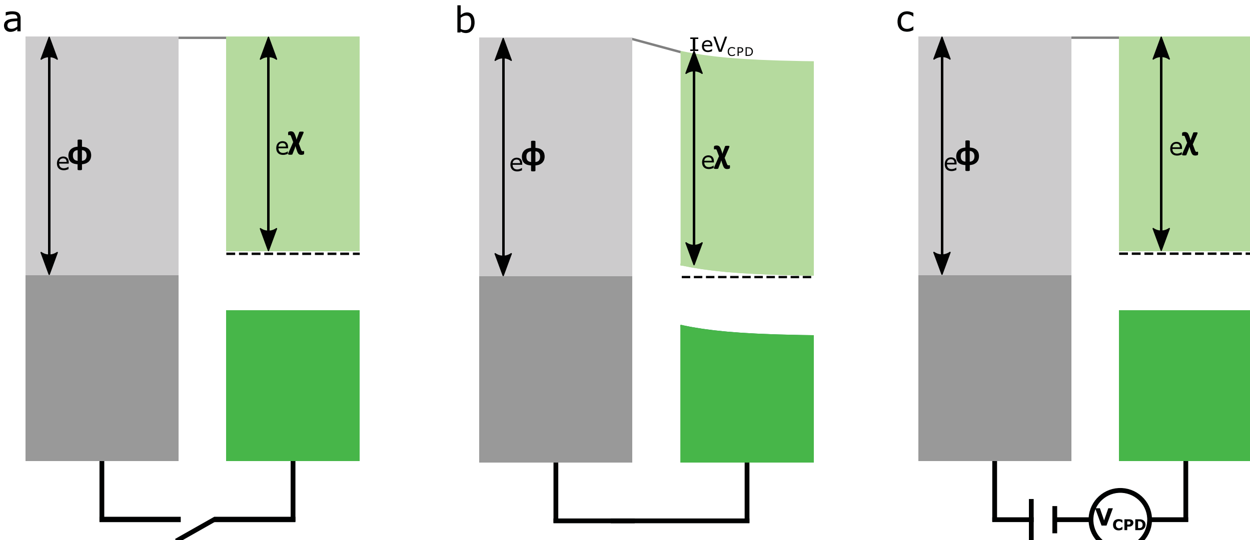

FIGURE 2.1: **Energy diagrams of a metallic tip in contact with a semiconducting surface.** (a) Materials that are electrically isolated will have electron energies given by their respective work functions (ϕ) and electron affinities (χ). (b) Once electrically connected, electrons will flow between materials to lower the overall energy of the system creating a contact potential difference between the two. (c) By applying a bias between the materials, the electric field can be nullified. The lighter colour of each material indicates the unoccupied states while the darker colour indicates the filled states. The vacuum level is the top of the unoccupied states. Here, the metal is W and the semiconductor is Si. The Fermi level of Si is shown for a heavily dopedd crystal.

from the valence band of the sample to the tip, or from the tip to the conduction band of the sample.

An expression for the tunneling current (I) between a tip and sample can be expressed using Bardeen's formalism, written as

$$I \propto \frac{2\pi e}{\hbar} \int_{E}^{E+eV} |M_{if}|^2 \rho_s\left(E\right) \rho_t\left(eV - E\right) dE \tag{2.1}$$

where ρ_s and ρ_t are the sample and tip electron density of states, respectively, and V is the applied bias between the two. M_{if} is the tunneling matrix element which is directly dependent on the probability of an electron tunneling from a filled electron state to an empty electron state. This can be approximated in one-dimension as

$$|M_{if}|^2 \propto e^{-2\beta d} \tag{2.2}$$

where $\beta = \sqrt{2m\left(\phi - E\right)/\hbar^2}$ and d is the distance between the tip and sample. Herein lies the source of the STM's functionality. The exponential dependence of the tunneling current means that an increase in gap distance by 1 Å results in a decrease in tunneling current by an order of magnitude [79]. allowing for a very localized source of tunneling current from the apex atoms of the tip giving the atomic resolution of the microscope.

Although usually depicted as a smooth surface in band diagrams (like in Figure 2.1), the density of states of a material is a complex mapping of electron energy due to the local interaction, bonding, and reordering of atoms within the crystal. Figure 2.2 shows the density of states of W (Figure 2.2 (a)) and Si (Figure 2.2 (b)). The band diagram for Si is shown for undoped Si with the energy level aligned for an n-doped crystal. In actuality, the presence of dopants creates a donor (n-type) or acceptor (p-type) band which contributes to the DOS of the crystal. In addition to a bulk density of states, surface atoms will also contribute depending on their reconstruction as shown in Figure 2.2 (c) and (d). These variations in the DOS across the surface allow for the extraction of unique surface features at varying tip-sample biases. The density of states in Figure 2.2 (c) shows the addition of surface features originating from a bare dimer (a common rearrangement of surface atoms of the Si surface as discussed in section 2.2) while Figure 2.2 (d) shows the same structure with the surface completely (labelled H-Si) or partially (labelled DB) quenched by atomic hydrogen thus changing the density of surface states. As shown in equation 2.1, the variation in the electronic density of states with changing energy can be probed by tuning the bias between the tip and sample.

There are two commonly used imaging modes of STM, namely constant current and constant height STM. As the name suggests, constant current imaging is done by maintaining a constant tunnelling current during the scan using a proportional-integral (PI) controlled feedback loop. As the tip scans over variations in the surface topography and conductivity,

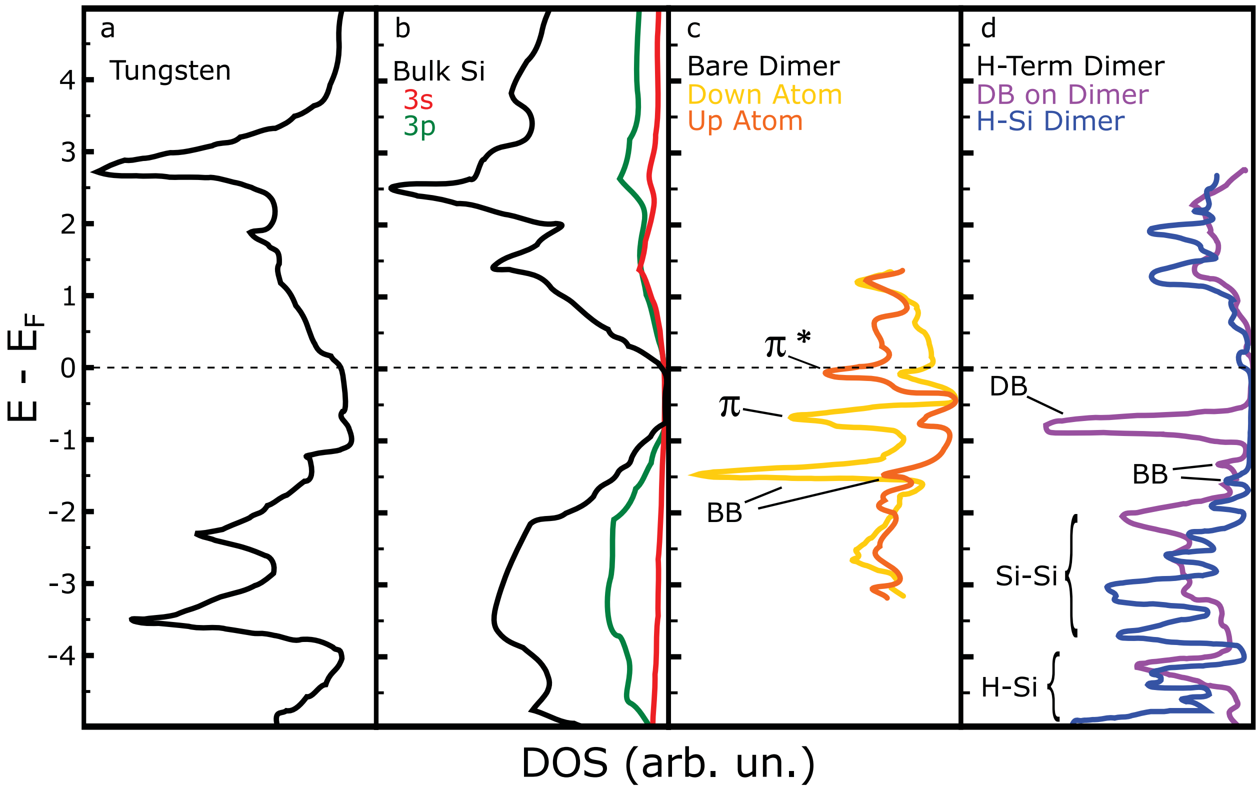

FIGURE 2.2: **Density of States of W and Si**. (a) Density of states of tungsten. (b) DOS of Si with contributions from the 3s and 3p level electrons highlighted in red and green respectively. (c) The DOS of surface atoms of the Si(100)-2x1 reconstruction. The energy levels of the π and π^* bonds as well as the back bonded atoms are shown and will be discussed with Chapter 5. The Down and Up atom refer to the contributions from the two different orientations of atoms on the surface (Chapter 5). (d) The DOS of the surface atoms of the H-Si(100)-2x1 reconstruction. The two variations show the completely hydrogen terminated surface in blue and a single dangling bond on an otherwise hydrogen terminated surface in purple. The DOS for each panel were taken from different sources so the magnitude of the DOS for each cannot be accurately compared. (a) adapted from [80], (b) adapted from [81, 82], (c) adapted from [83], and (d) adapted from [84].

the tip is moved closer to or further from the surface such that a constant tunneling current is maintained (All constant current images in this thesis are acquired using a constant tunneling current of 50 pA). The variation in the electronic density of states is thus recorded as changes in the tip height modulated by the PI controller. In constant height imaging, the feedback controller is turned off and the tip scans across the surface recording the changes in tunneling current directly. Constant current imaging is more commonly used as the feedback loop is capable of preventing unwanted tip-sample contact by varying the position of the tip over topographically varying features of the surface. The PI controller is also capable of

accommodating for any piezo creep or thermal drift making it a very stable scanning state. Constant height imaging is generally used for short periods of time as changes in tip-sample separation due to piezo creep, thermal drift, and variations in surface topography are usually large enough to crash[3] a tip during a scan. Constant height scans have an advantage in that they are capable of probing energy levels at the edge of or within the band gap of a material. If constant current mode was enabled with the probe bias within the band gap of a material, the PI controller would push the tip into the surface in an attempt to try and maintain a constant tunneling current since the sample has no conductive states available at gap voltages. By eliminating the need for a constant tunneling current it allows for the probing of localized electronic states that could exist within the band gap of the material.

2.1.1.1 Lock-In Detection

Going back to equation 2.1, the expression for the tunneling current is proportional to the integral of the density of states ρ. If we then take the derivative with respect to voltage (V) and assume the metallic tip's density of states is constant over the given voltage range, the sample density of states (ρ_s) is proportional to the differential conductance.

$$\frac{dI}{dV} \propto \rho_s (E + eV) \tag{2.3}$$

In practice, this signal can be acquired by taking the derivative of an acquired I(V) spectroscopy with respect to the voltage, however, this signal is usually quite noisy making it difficult to extract any useful details. Alternatively, this signal can be collected using a lock-in amplifier. By using a phase-locked-loop, a reference waveform is created given as $V_r sin(\omega_r t + \theta_r)$. This reference is passed through the experimental system returning a signal waveform $V_s sin(\omega_s t + \theta_s)$. By multiplying these signals together and passing the output

[3]crashing a tip is an eloquent way of saying the tip has moved close enough to the surface to cause an irreversible rearrangement of atoms on the tip or sample.

through a low pass filter, we can extract a frequency independent expression for the detected voltage given by

$$V_{det} = 1/2 V_r V_s cos(\theta_r - \theta_s) \tag{2.4}$$

When used in an STM, an AC bias signal is generated and applied to the tip. If the applied DC bias is slowly swept over the desired range while the AC oscillation is applied, a corresponding variation in current is recorded giving what is essentially a $\Delta I/\Delta V$ signal mapping of ρ_s. A more thorough discussion can be found in [85]. The utility of such a measurement can be seen in Figure 2.3. Figure 2.3 (a) shows a typical constant current image of the H-Si(100) surface, the details of which will be discussed in section 2.2. In addition to the constant imaging bias of -1.65 V, an oscillating voltage with an amplitude of 0.01 V was applied via a lock-in. As can be seen in Figure 2.3, the constant current image of the surface (Figure 2.3 (a)) doesn't show the additional electronic features seen in the lock-in signal in Figure 2.3 (b) which correspond to local variations in the density of states.

2.1.2 The Atomic Force Microscope

The need for a tunneling current between the tip and sample junction of an STM limits its applicability to conducting metals and semiconductors. Any information regarding states within the band gap of a semiconductor or properties of an insulating material are outside its abilities. The AFM does not require a tunneling current to study tip-sample interactions, and as a result, is capable of measuring surface properties on a much more diverse set of samples. Invented 5 years after the STM by Binnig, Quate, and Gerber [86], the AFM probes the force of interaction between the tip and sample, eliminating any need for a tunneling current. Finding applications in molecular and cellular biology [87–89] as well as condensed matter physics and chemistry [90–93], the AFM can be operated in multiple interacting modes using several signal detection schemes depending on the type of surface properties to

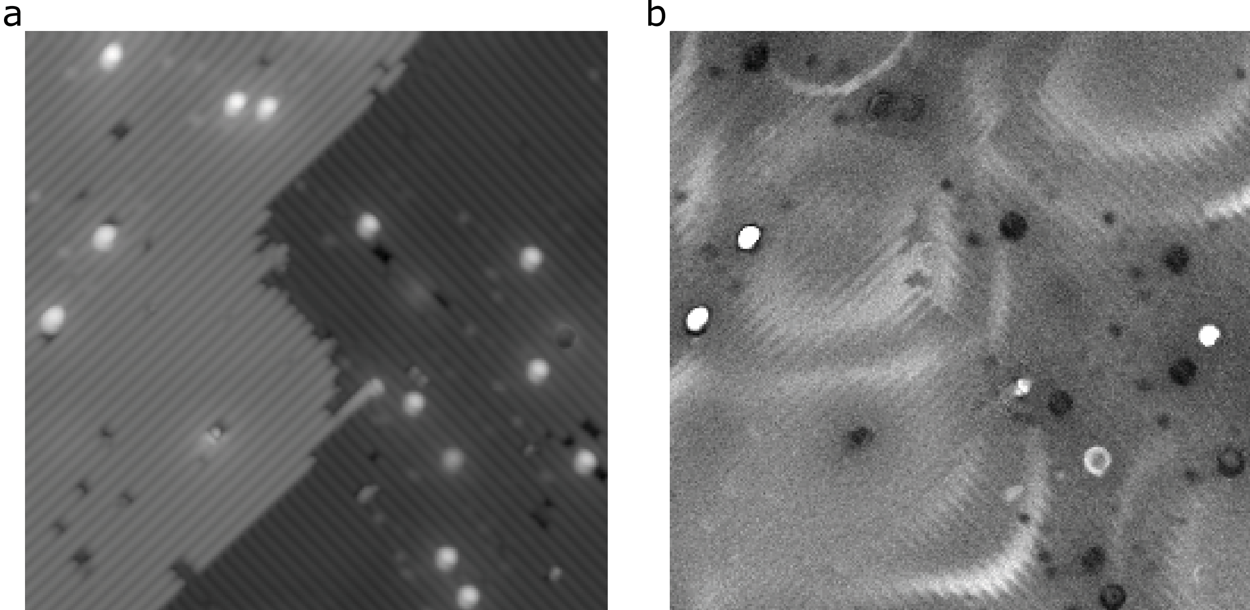

FIGURE 2.3: **Feature extraction using lock-in amplification.** (a) Constant current image of the H-Si(100)-2x1 surface. Details of surface features are discussed later. (b) The lock-in amplification channel corresponding to the dI/dV signal. V_S = -1.65 V, 40 x 40 nm^2. Lock in frequency = 800 Hz, amplitude = 0.01 V.

be studied [94, 95]. All experimental measurements herein rely on a commonly used non-contact interacting mode using a constant amplitude oscillation (All measurements herein use an oscillation amplitude of 50 pm) of a qPlus sensor, details of which can be found in [96]. In this configuration, two PI controllers are used. The first tracks the change in oscillation amplitude of the system with the second tracking the phase of oscillation (which is correlated to the Δf of the interaction). The Nanonis software employs a "Perfect-PLL" which assigns appropriate PI parameters for a given sensor quality factor (Q) and resonance frequency (f_o).

By oscillating the tip in non-contact mode, it behaves to first order as a damped, driven, harmonic oscillator. In an unperturbed system, the tip will oscillate at some resonant frequency f_0 as dictated by the mass (m) and spring constant (k_c) of the cantilever-tip system system. The addition of a tip-sample interaction results in a measured deviation (Δf) from f_0 via an effective linear addition to the spring constant (k_{t-s}) given as

$$\Delta f = f_0 - f_0'$$
$$\Delta f = \frac{1}{2\pi}\sqrt{\frac{k_c}{m}} - \frac{1}{2\pi}\sqrt{\frac{k_c + k_{t-s}}{m}} \tag{2.5}$$

If we take the binomial expansion of the square root (for $k_{t-s} \ll k_c$) and relate k_{t-s} to the force of interaction between the tip and sample (F_{t-s}) using Hooke's law, we can arrive at a very rough approximation relating Δf to F_{t-s} via

$$\Delta f = \frac{1}{2\pi}\frac{-f_0}{2k_c}\frac{\partial F_{t-s}}{\partial z} \tag{2.6}$$

In actuality, the experimentally observed frequency shift is also convoluted with the amplitude of the system. Numerical approximations such as the Sader-Jarvis approximation [97] are needed to properly correlate the frequency shift to the force of interaction between the tip and sample. The change in frequency Δf can be related to the force of interaction[98] via

$$\frac{\Delta f}{f_0} = -\frac{1}{\pi a k_c}\int_{-1}^{1} F_{t-s}(z + a(1+u))\frac{u}{\sqrt{1-u^2}}du \tag{2.7}$$

where a is the amplitude of oscillation and z is the distance of closest approach between the tip and sample as outlined in [97]. Following the work of Sader and Jarvis, the expression can be reciprocated giving an expression for $F_{t-s}(z)$ given as

$$F_{t-s}(z) = 2k_c\int_z^\infty \left(1 + \frac{a^{1/2}}{8\sqrt{\pi(t-z)}}\right)\Omega(t) - \frac{a^{3/2}}{\sqrt{2(t-z)}}\frac{d\Omega(t)}{dt}dt \tag{2.8}$$

and an expression for the interaction energy $U_{t-s}(z)$ as

$$U_{t-s}(z) = 2k_c\int_z^\infty \Omega(t)\left((t-z) + \frac{a^{1/2}}{4}\sqrt{\frac{t-z}{\pi}} + \frac{a^{3/2}}{\sqrt{2\,(t-z)}}\right)dt \tag{2.9}$$

where $\Omega(t) = \frac{\Delta f}{f_0}$

These integrals can be numerically calculated using methods like trapezoidal integration and will be used for curves presented in Figure 2.9 and 3.24. Coding for these calculations can be found here [8].

To understand what form these measurements will take, an understanding of the mechanism of the tip-sample interaction is needed. The interaction between a single atom on the tip apex and a single atom of the surface will be electromagnetic in nature. Since both atoms have positive and negative charges in the form of protons and electrons, the atoms of the tip and sample will experience both attractive and repulsive forces. The strength of these depends on both the tip-sample separation and the types of atoms interacting. For neutral atoms in which the electrons of the atoms are only minimally perturbed[4] , the interaction potential (and subsequently the force via $F = -\frac{\partial U}{\partial z}$) can be described using the Leonard-Jones potential

$$U_{LJ} = 4\epsilon \left[\left(\frac{z_m}{z} \right)^{12} - \left(\frac{z_m}{z} \right)^{6} \right] \tag{2.10}$$

where ϵ is a measure of the potential energy minimum at the equilibrium distance z_m. This expression holds both a repulsive term (12th power) and an attractive term (6th power). Due to the difference in powers between the two terms, the repulsive interaction only appears at very small tip-sample separations. The origin of the repulsive term is usually ascribed to a Pauli interaction. This will be explained in more detail in section 2.2.1.2 but for now it is enough to understand it as a repulsive force due to limits in electron occupation as set by the Pauli exclusion principle. The attractive term comes from Van der Waals forces involving permanent or induced dipoles. In the case of neutral atoms with no permanent dipole, only an induced dipole-induced dipole interaction can occur. Through random fluctuations in electron density, an atom can form a temporary dipole, which in turn induces a dipole in

[4]by minimally perturbed, it is meant that an ionic or covalent bond is not formed and that electrons will generally stay surrounding their host atom only

an adjacent atom. This interaction results in the London force. If one the probing atoms is part of a molecule with a permanent dipole, it can induce polarization in the second atom via the Debye force. If both interacting atoms are part of a permanent dipole structure, this interaction leads to the Keesom force. Conveniently, the r^{-6} dependency accounts for all of these forces grouping them together as the Van der Waals force [99].

In addition to probing the weakly attractive Van der Waals forces, it is also possible to observe more covalent and ionic behaviour. The nature of covalent bonding requires more complicated modelling schemes than that offered through a Leonard-Jones interaction as electrons are now shared between the interacting atoms. An intuition regarding the expected type of interaction to occur between two adjacent atoms can be achieved by looking to the groups in the periodic table. Group VIII atoms are completely full and as a result only participate in Van der Waals bonding as described above[5]. Combining group VII and group I atoms allows for an ionic bond where entire electrons can transfer between atoms. The interaction potential in an ionic crystal lattice U_{ion} can be described via

$$U_{ion} = -\frac{\alpha e^2}{z} + \frac{C}{z^m} \tag{2.11}$$

where α is the Madelung constant (which depends on the arrangement of atoms in a lattice, ≈ 1.7), e is the electron charge, and C and m are experimental parameters which best describe the repulsive interaction between atoms.

Covalent bonds are generally formed between group III and V atoms as well as between group IV atoms through the sharing of electron pairs such that the atoms retain a neutral charge. Much like the bonding potential of the Van der Waals interaction, covalent bonding also follows an anharmonic potential with a long range attractive and short range repulsive interaction. Understanding the attractive form is more complicated as electrons are shared between atoms without the creation of ion pairs. Instead, the strength of a covalent bond is

[5]This is why noble gases have such low evaporation temperatures compared to other elements

dictated by the overlap of valence electrons at corresponding atomic separations. The minimum (equilibrium) energy of the system corresponds to an atomic separation where sharing valence electrons between neighbouring atoms without incurring a dominant repulsive effect from proton-proton or electron-electron repulsion can occur.

By solving the wave equation for nuclear motion of a diatomic molecule, one can map an approximate interaction potential as derived by Morse [100] written as

$$U(r) = D_e \left(e^{-2a(r-r_e)} - 2e^{-a(r-r_e)} \right) \tag{2.12}$$

where r_e is the equilibrium bond distance, D_e is the potential well depth, and a is a parameter used to control the width of the well. Such a model has been used to model bonding potentials in group-IV semiconductors [101] as well as the strength of a covalent bond between molecules anchored to a substrate [102].

Despite the clean functional forms for such ionic, Van der Waals, and covalent bonding interactions, extracting such a behaviour through experimental Δf spectroscopy becomes difficult due to the combined effect of many sample atoms interacting with many tip atoms. Although the tip-sample interaction will be predominantly driven by the apex interaction, longer range electrostatic effects make it difficult to extract only the desired interaction between the tip apex atom and a single atom on the surface. For the sake of interpreting the AFM data presented in section 2.2, it is more useful to understand how the various bonding methods listed above compare in strength. In this way, the nature of the tip-sample interactions can be compared between different tip and sample atoms allowing for a better understanding of their interacting potential. Van der Waals interactions are the weakest with London dispersion interactions having an energy of roughly 0.01 eV. Dipole-dipole and ion-dipole have an interacting energy of around 0.05 eV and 0.2 eV respectively (with H-bonding around 0.2 eV as well). As mentioned before, the covalent and ionic interactions

are much stronger on the order of eV within the range of 1 eV to 5 eV (As a reference, Si-Si is 3.5 eV, H-H is 4.5 eV, and Si-H is 4.1 eV [103]).

2.1.2.1 Kelvin Probe Force Microscopy

In addition to the interaction dependence of the apex atom with a single surface atom, the measured frequency shift is also affected by macroscopic charging and potential differences between the tip and sample. Kelvin Probe Force Microscopy (KPFM) allows for these effects to be probed by measuring the change in frequency shift (Δf) by varying the applied bias values. As discussed earlier with Figure 2.1, when materials with differing Fermi levels are placed in electrical contact, electrons will flow between the materials to minimize the total energy. This new electron distribution results in a contact potential difference between the two materials as a result of the newly ionized atoms. This contact potential difference can be probed by measuring a capacitance between the tip and sample allowing for a relationship between the electrostatic force (F_e) and capacitance (C) given as

$$F_e = -\frac{\partial E_C}{\partial z} = -\frac{1}{2}\frac{\partial C}{\partial z}V^2 \tag{2.13}$$

where E_C is the energy stored in a capacitor, and V is the voltage. By applying an offset voltage (V_{DC}) (Figure 2.1 (c)), the voltage difference caused by the contact potential difference (V_{CPD}) can be extracted using the change in frequency shift of an AFM via

$$\Delta f(V_{DC}) \propto \frac{\partial F_e}{\partial z} = -\frac{1}{2}\frac{\partial^2 C}{\partial z^2}\left(V_{DC} - V_{CPD}\right)^2 + \Delta f(z) \tag{2.14}$$

This quadratic relationship between frequency shift and contact potential voltage allows for an approximation of the contact potential difference and subsequently the work function difference of the materials.

It is important to note that equation 2.14 only applies to conducting systems where free charges easily screen any penetrating field. In a semiconducting system however, these electric fields can penetrate the sample and influence the charge distribution within. The net surface charge per unit area σ_s is no longer a constant and must be treated as

$$\sigma_s = \int_{V_{CPD}}^{V} C(V')dV' \tag{2.15}$$

where C is the capacitance between the semiconducting surface and the probe tip which now holds some voltage dependence. This additional contribution can be better accounted for with the application of some oscillating voltage V_{ac} with frequency ω. F_e now becomes

$$F_e = -\frac{1}{2}\frac{\partial C}{\partial z}\left[(V_{DC} - V_{CPD}) + V_{ac}sin(\omega t)\right]^2 \tag{2.16}$$

This can be divided into three parts

$$F_{DC} = -\frac{\partial C(z)}{\partial z}\left[\frac{1}{2}\left(V_{DC} - V_{CPD}\right)^2\right] \tag{2.17}$$

$$F_{\omega} = \frac{\partial C(z)}{\partial z}\left(V_{DC} - V_{CPD}\right)V_{ac}sin\left(\omega t\right) \tag{2.18}$$

$$F_{2\omega} = \frac{\partial C(z)}{\partial z}\frac{1}{4}V_{ac}^2\left[cos(2\omega t) - 1\right] \tag{2.19}$$

where

$$F_{\omega} = -\frac{Q_s}{\epsilon_0}\frac{C_I C_D}{C_I + C_D}V_{ac}sin(\omega t) \tag{2.20}$$

which separates F_ω into contributions from the total charge near the semiconductor surface due to the surface potential of the material (Q_s), the capacitance associated with V_{ac} and the air gap between the tip and sample (C_I), and the capacitance associated with V_{ac} and the space charge layer of the semiconductor (C_D). With this in mind, it is still useful to associate the peak in Δf with the CPD, except this CPD is taken relative to the surface potential, which differs from the work function of the bulk crystal due to the space charge layer near the semiconducting surface [104–106].

In addition to measuring the relatively macroscopic property of the contact potential difference, KPFM has also proven useful to identify discrete charge transitions of surface atoms [46, 107–115]. Such a transition was observed by Gross *et al.* studying Au atoms physisorbed onto a NaCl salt layer on the metallic Cu surface [115]. In performing $\Delta f(V)$ spectroscopies, two discrete steps in Δf were observed corresponding to the transition of a neutral Au atom to the positive and negative charge states. By treating the total capacitance of the system as a sum of contributions from the tip-substrate, tip-Au atom, and Au atom-substrate capacitance, the $\Delta f(V)$ spectroscopy of such a system takes the form of

$$\Delta f(V) = a\,(b+V)^2 + cV^2 + \Delta f(z) \tag{2.21}$$

where a and b are dependent on the tip-Au atom and Au atom-substrate capacitance, respectively, while c depends on the tip-substrate capacitance. By fitting a measured $\Delta f(V)$ spectroscopy to a function similar to equation 2.21 it is possible to extract V_{CPD} via $\Delta f'(V) = 0$. By performing a grid spectroscopy measurement over the surface, it allows for a 2D mapping of V_{CPD} which can be correlated to surface and subsurface charges as done by Huff *et al.* [6].

2.1.2.2 Noise

When interpreting the measured Δf signal, it is useful to understand how noise contributes to the signal. The noise measured in Δf (written δf), is a combination of 4 separate sources

due to the noise in k_{ts}: the thermal ($\delta k_{ts\,thermal}$), sensor ($\delta k_{ts\,sensor}$), oscillator ($\delta k_{ts\,osc}$), and drift noise ($\delta k_{ts\,drift}$).

The thermal contribution is given by the square root of the ratio between the thermal energy ($k_B T/2$ per degree of freedom) and the total energy of the cantilever multiplied by the ratio of the bandwidth (B) with the resonant frequency (f_0) and quality factor (Q). Written as

$$\delta k_{ts\,thermal} = \sqrt{\frac{4 k k_B T B}{\pi A^2 f_0 Q}}, \tag{2.22}$$

the thermal noise is independent of the modulated frequency (white noise) and the dominant contribution for measurements without any additional tip-sample interaction.

The sensor noise originates from the error in the deflection measurement. Between some period of oscillation, there will be some uncertainty in detecting the position of the cantilever (q') which introduces some noise $\delta q' = 2 n_q \sqrt{B}$ over the oscillation amplitude (A). Here n_q is the spectral noise density, given in units $fm/\sqrt{Hz}$, it represents an increased uncertainty in the tip position q with increased measurement bandwidth ($\sqrt{B}$). If we assume that the bandwidth is much smaller than f_0, the precision is greatly enhanced with the added B/f_0 scaling to the noise. The deflection detector noise is then written as

$$\delta k_{ts\,sensor} = \sqrt{\frac{8}{3}} \frac{k n_q}{f_0} \frac{B^{3/2}}{A}. \tag{2.23}$$

This additional B dependence represents a linear correlation of the modulating frequency f_{mod} to the signal noise (blue noise). For larger frequencies (best discussed in [90]), the noise density n_q is dependent on the charge sensitivity (S_q) and the pre-amplifier noise density (n_{amp}) written as $n_q = n_{amp}/S_q$ highlighting that careful selection of the pre-amplifier system can also be used to reduce noise.

The oscillator noise originates from a finite Q factor of the oscillator. Small quality factors will have a larger oscillating frequency range surrounding the resonance peak. Lower Q

values will allow for more of the driving signal to be in phase with the response oscillation rather than at the expected $\pi/2$ phase shift. The error in $\delta k_{ts\,osc}$ is then written as

$$\delta k_{ts\,osc} = \sqrt{2}\frac{kn_q}{Q}\frac{B^{1/2}}{A}. \tag{2.24}$$

Much like the thermal noise, the $\sqrt{B}$ dependency results in a constant signal noise w.r.t. frequency (white noise).

The last source of error is due to drift in the resonant frequency of the cantilever over time. As long as the bandwidth is much greater than the inverse time it takes to acquire an image, the uncertainty due to drift can be written as

$$\delta k_{ts\,drift}(f_{mod}) \approx \frac{2krN}{f_0 \pi B} \tag{2.25}$$

where N is the number of pixels acquired and r is the drift rate. It is worth noting that this is the only noise source which varies with $1/B$ (resulting in a pink noise [$1/f$]) which enforces a balance between the noise reduction in the first three associated with a lower B and a reduction in the drift noise through larger B values.

These equations only serve to introduce the reader to the different noise contributions associated with AFM and the qPlus sensor. More details both in theoretical derivations, and experimental determinations should be read about here [90, 116].

With an understanding of the basic principles of both scanning tunneling, and atomic force microscopy, we will now look at the application of these techniques to the H-Si(100) surface and their relevance to subsequent chapters. As will be discussed, the measured interactions are often more complicated than the theoretical relationships previously presented, requiring more sophisticated and complex modelling. Such modelling is outside the scope of this thesis, however, the experimental results provide enough insight into the probed interactions that

accurate and distinct qualitative observations can be made and related to previous works, providing guidance for future experimental and theoretical works.

2.2 The H-Si(100) Surface

Silicon has proven to be a very useful material in the design of modern electronics. When bonded in crystal form, the atoms create an sp^3 hybridized system in a diamond lattice structure with a lattice constant of 5.43 Å (bond length of 2.35 Å). This results in an indirect electron energy band gap[6] of 1.14 eV at room temperature (approaching 1.17 eV at 0 K) [24]. At the surface, the Si crystal shows varying structural properties depending on which crystal face is exposed. Two of the most commonly studied are the (111) and (100) surfaces. Since the Si atoms at the surface-vacuum interface no longer have 4 bonding partners, they undergo significant structural reordering to lower the total energy of the surface. Si atoms of the (111) surface have a single dangling bond (unsatisfied bond) and undergo the complicated (7x7) reordering[7] where a surface unit cell consists of a trapezoidal 7 x 7 atom area of the unreconstructed surface giving the characteristic pattern observed in Figure 2.4 (a) [118, 119]. By reordering in this way, the surface energy is lowered as the number of surface dangling bonds is reduced from 49 to 19.

Surface atoms of the (100) surface have 2 dangling bonds extending into vacuum resulting in a paired reordering where 1 DB of each Si atom will bond with a DB of a neighbouring Si atom creating dimer structures along the surface. Each dimer consists of the two Si atoms which now only have one DB each, reducing the total number of surface DBs in half. This reordering into dimers creates the characteristic π and π^* surface electron bands creating a semiconducting distribution of electron surface states as mentioned in Figure 2.2 (c) [83].

[6] An indirect gap means that for an electron to transfer from the lowest energy state of the conduction band to the highest energy state of the valence band, it must also be accompanied with a momentum transfer usually mediated by a phonon interaction.

[7] A freshly cleaved (111) surface will go to a metastable 2x1 reconstruction first [117]. Only after thermal annealing does the surface reorder to the more stable 7x7 structure [118]

The energy of the (100) surface is further reduced through dimer buckling, raising one side of the dimer and lowering the other [120, 121]. The relative phase between neighbouring buckled dimers can further reduce the overall energy of the system forming the (c 4x2) or (p 2x2) phases [122, 123]. This lattice buckling corresponds to a charge redistribution as well, which is discussed in Chapter 5.

The subsequent hydrogen termination of the Si surface can be done to satisfy any remaining surface dangling bonds. H-termination of the (100) surface is most commonly done *in situ* (in the vacuum chamber) by resistively heating the crystal and exposing it to atomic hydrogen (Details are found in the methods section of Chapters 3-5). This removes the buckling of the surface giving symmetric dimers across the surface as shown in Figure 2.4 (g),(h). H-termination of the (111)-7x7 phase is much more difficult to achieve *in situ* as the reordered atoms of the 7x7 phase must be etched away exposing the clean 1x1 phase underneath [124]. This usually results in a defect ridden surface as shown in Figure 2.4 (e). Use of the Si(111) surface for BASiL device fabrication is attractive as the surface shows 6-fold symmetry providing a more uniform platform for DB fabrication. The (100) surface only features a 2-fold symmetry [125] and as such, device operation and fabrication is expected to be limited due to the directional dependence of the surface (See Chapter 5). Work is currently underway to routinely prepare a clean H-Si(111)-1x1 surface using chemical etching procedures [126–130], however difficulties in surface cleanliness are currently preventing its realization. All the work presented in this thesis use the (100) surface only due to the relative ease of preparing large, atomically flat, clean areas.

2.2.1 Scanning Probe Imaging Modes

As mentioned previously, insights into the electronic and structural characteristics of the H-Si(100)-2x1 surface can be achieved via scanning probe microscopy. STM allows for the interpretation of the electronic density of states of the surface and their correlation to the surface's atomic geometry, while AFM allows for the interpretation of the force of interaction

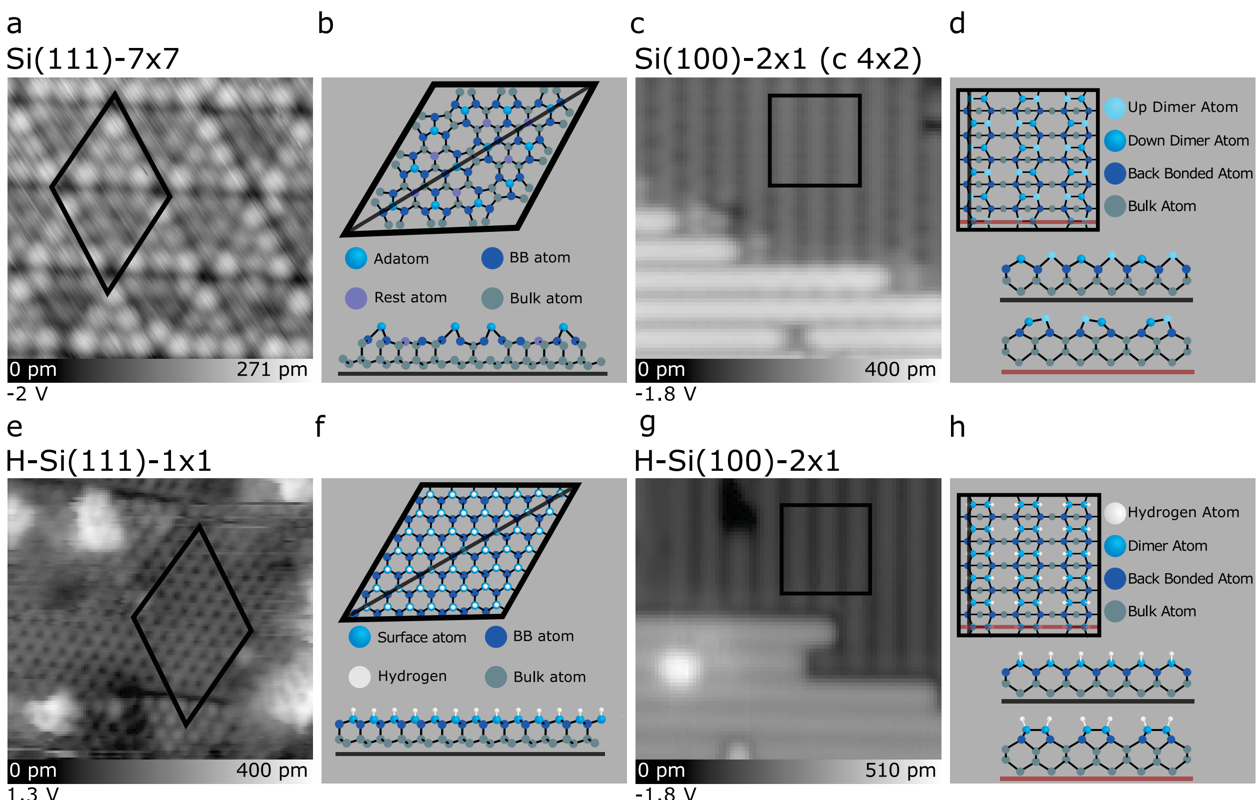

FIGURE 2.4: **The Si and H-Si surfaces.** (a) The Si(111)-7x7 reordering with the unit cell outlined. (b) The corresponding ball and stick of (a) and a cross sectional slice. (c) The Si(100)-2x1 (c 4x2) surface with a (6x6) cell highlighted. (d) The corresponding ball and stick of (c) with both directional cross sections. (e) The H-Si(111)-1x1 surface with a (7x7) unit cell outlined. As mentioned in the text, several large defects are seen across the surface. (f) The corresponding ball and stick outline of (e). (g) The H-Si(100)-2x1 surface with a (6x6) cell highlighted. (h) The corresponding ball and stick of (g). Each image was acquired with constant current STM (I = 50 pA), with the sample bias shown in the bottom left of each image. Each image is 8 x 8 nm^2

between the scanning probe and surface atoms. The differing yet complimentary information supplied via these two methods make it necessary for both to be used to give a more complete understanding of the surface. Further variations to the imaging modes of STM and AFM can also be used to better interpret the surface behaviour and structure. The work presented below and in subsequent chapters utilizes six different modes with variations in imaging bias and tip apex atoms offering a wide spectrum of characteristics to be extracted from the surface.

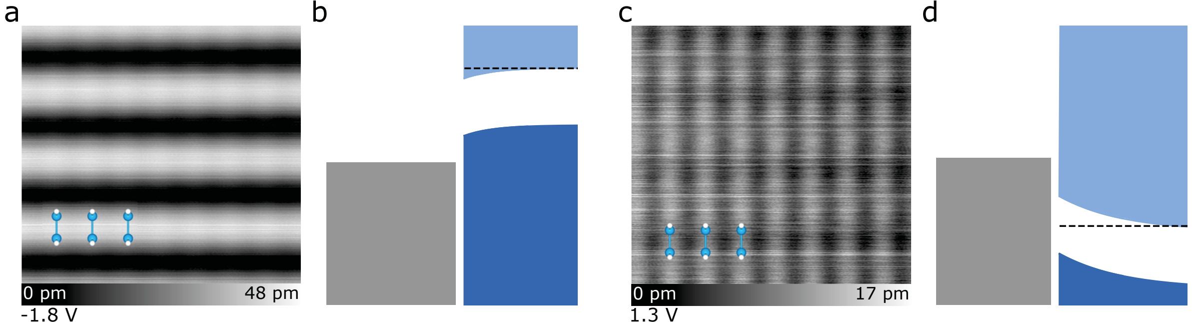

FIGURE 2.5: **Constant current STM of the H-Si(100)-2x1 surface.** (a) The filled states image of the surface with a ball and stick model highlighting its atomic structure. (b) The corresponding band diagram of (a). (c) The empty states image of the surface with a ball and stick model highlighting its atomic structure. (d) The corresponding band diagram of (c). The corresponding sample bias for each image is indicated in the lower left of each image. The image sizes are 3 x 3 nm ^{2}

2.2.1.1 Constant Current STM

The most commonly used method of imaging the Si surface is with constant current STM as it allows a variety of bias-dependent features to be observed while minimizing the risk of unwanted tip-sample contacts. By applying a sample bias of -1.8 V, the STM tip accepts electrons from the filled electron states of the valence band (Figure 2.5 a,b[8]). Alternatively, at a sample bias of 1.3 V, electrons tunnel from the tip to the empty electron states of the Si conduction band (Figure 2.5 (c),(d)). These two imaging biases are generally used for legacy reasons as they were found to be far enough from the band gap to enable good tip-sample conduction, but far enough from high biases which may cause unwanted changes to atoms of the tip or sample. The variation between these two imaging modes is immediately apparent when comparing Figures 2.5 (a) and (c), highlighting the difference in the density of states between the conduction and valence bands.

Although all images were acquired with a W tip, due to tip conditioning methods described in Chapters 3-5 it is understood that the tip is functionalized with a hydrogen-silicon cluster.

[8]The corresponding band structures have been calculated using SEMITIP [131–133], which solves the Poisson equation for a given dopant distribution and a hyperbolic shaped probe tip

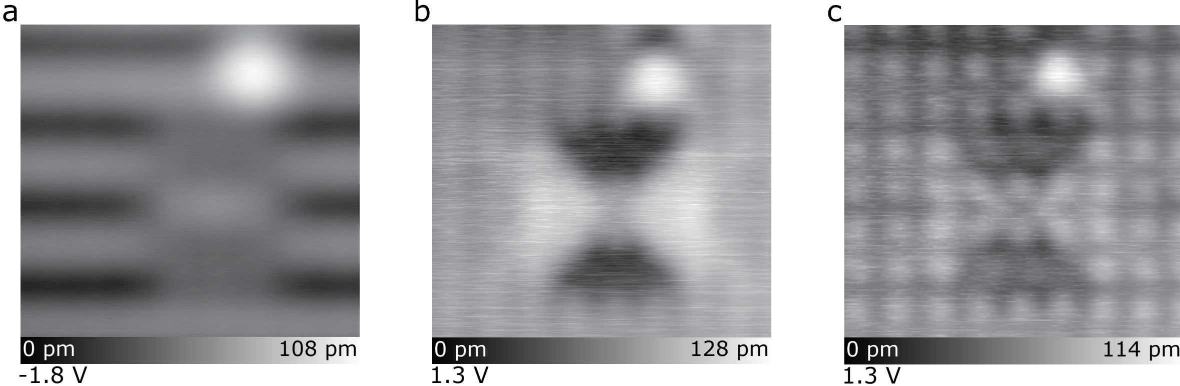

FIGURE 2.6: **Constant current imaging of surface features at differing tip biases and functionalizations.** (a) The filled states image of a 3x1 defect and a neutral point defect. (b) The empty states of the same area imaged with a Si tip. (c) The empty states image of (b) except with a hydrogen atom on the apex of the tip. Each image is 3.4 x 3.4 nm^2 which imaging biases indicated in the lower left.

As a result, the tip density of states is altered depending on the tip apex atom creating a preferential conductivity (via modifying the tip-sample orbital overlap) through different surface states of the silicon crystal [134]. Figure 2.6 shows three different images of the same area with differing biases and tip functionalizations. Figure 2.6 (a) shows a 3x1 defect, and a neutral point defect (as will be discussed in Chapter 3) with an imaging bias of -1.8 V. Figure 2.6 (b) and (c) show empty states images both acquired with the same sample bias of 1.3 V, but with two different tip functionalizations. As discussed in more detail in Chapter 3, (b) is thought to be imaged with a Si tip while (c) is imaged with a hydrogen terminated tip apex. Since (b) and (c) have the same imaging bias, the difference between the contrast in features originates from the different tip density of states due to the different functionalization as evident in equation 2.1.

2.2.1.2 Constant Height STM

The requirement that constant current imaging needs to probe a bias range where there are enough conducting states to maintain a constant imaging current results in the majority

of current originating from the bulk states of the crystal. By imaging in constant height, it is possible to image in bias regions that cannot provide a constant tunneling current needed to maintain constant current imaging. One such bias range that has proven useful is near the donor band and onset of conduction band at a bias of roughly 0.3 V. Due to the significant reduction in available empty states of the Si crystal, the tip-sample separation[9] must be reduced on the order of 300 pm so as to reduce the vacuum barrier width, increasing the tunneling current. The Si surface at this bias appears more like the expected ball and stick model due to the elimination of higher energy bulk states as shown in Figure 2.7 (a). Because this imaging bias also overlaps with the electron energy levels of added group V dopants in the Si crystal [24], it is also very useful for visualizing the location of dopants in the subsurface region [135]. Figure 2.7 (c) shows a typical empty states image in constant current mode. Figure 2.7 (d) shows the same area but imaged in constant height mode at a sample bias of 0.3 V with a relative tip height of -300 pm. The bright X shaped featured is understood to be a subsurface dopant which does not appear in the constant current image in (c).

Although the STM has no inherent force sensor, the reduced tip-sample separation necessary for constant height imaging at the onset of the conduction band increases the repulsive nature of the tip-sample interaction. By functionalizing a scanning probe tip with a flexibly bonded hydrogen atom, it is possible to achieve enhanced resolution through modifications in the tip-apex geometry and therefore conductance across the tunnel junction as the tip scans over regions of the surface with a greater repulsive interaction. As outlined in Chapter 3, similar enhancements in frequency shift in AFM measurements are routinely achieved via tip-apex functionalization. The first instance of enhanced resolution through apex functionalization using an STM relied on leaking H_2 into the vacuum chamber until a molecule became trapped in the tunnel junction, coining the term Scanning Tunneling Hydrogen Microscopy (STHM) [136–139]. As the tip scanned over the sample, areas of high electron density exhibit a

[9] For all data acquired in the thesis, a tip-sample separation of 0 pm corresponds to the distance between the tip and sample when a current of 50 pA is maintained using a sample bias of -1.8 V above a H-Si atom.

greater repulsive character than those with lower electron density allowing for the effective visualization of bonds in molecules. Similar contrast is achieved here by functionalizing the apex with a single covalently bonded H atom as shown in Figure 2.7. As the tip is scanned over the surface, the areas of greater repulsive interaction show sharp changes in the conductivity, creating a square pattern on the surface where each corner correlates to the position of an H-Si atom as shown in Figure 2.7 (e). The same effect has been shown using an AFM where images taken with an H-functionalized tip show the same square pattern of the surface [140].

As mentioned previously, the nature of the repulsive force between the tip and sample is due to Pauli repulsion [136]. Although correct in its assessment of the origin of the repulsive force, it is perhaps misleading to write it as such since the idea that there exists a "Pauli force" is incorrect. Due to the wavelike nature of an electron (or particle in general), this electron can be interpreted to exist over a set distance as defined by that particle's wave function. If a separate electron with identical quantum numbers (making the particles indistinguishable except for their coordinates) is brought within close proximity to the first electron, it is forbidden for these two electrons to exist within the same geometric space with the same quantum numbers. It is important to note that the act of being forbidden does not create an interacting force, but instead leads to a modification of the electron's wave function and subsequent alteration to the distribution of the charges within the atom. It is this wave function modification which raises the overall energy of the system resulting in a change in the electrostatic interactions between the particles. This electrostatic repulsion is conveniently mapped using the $1/r^{12}$ interaction term in the L-J potential shown in Figure 2.10. For those curious, a more thorough discussion is laid out in [141].

2.2.1.3 Constant Height AFM

As discussed earlier, the Δf signal as measured by the AFM is dependent on both the sample and tip properties. By changing the properties of the tip using different apex atoms, it is

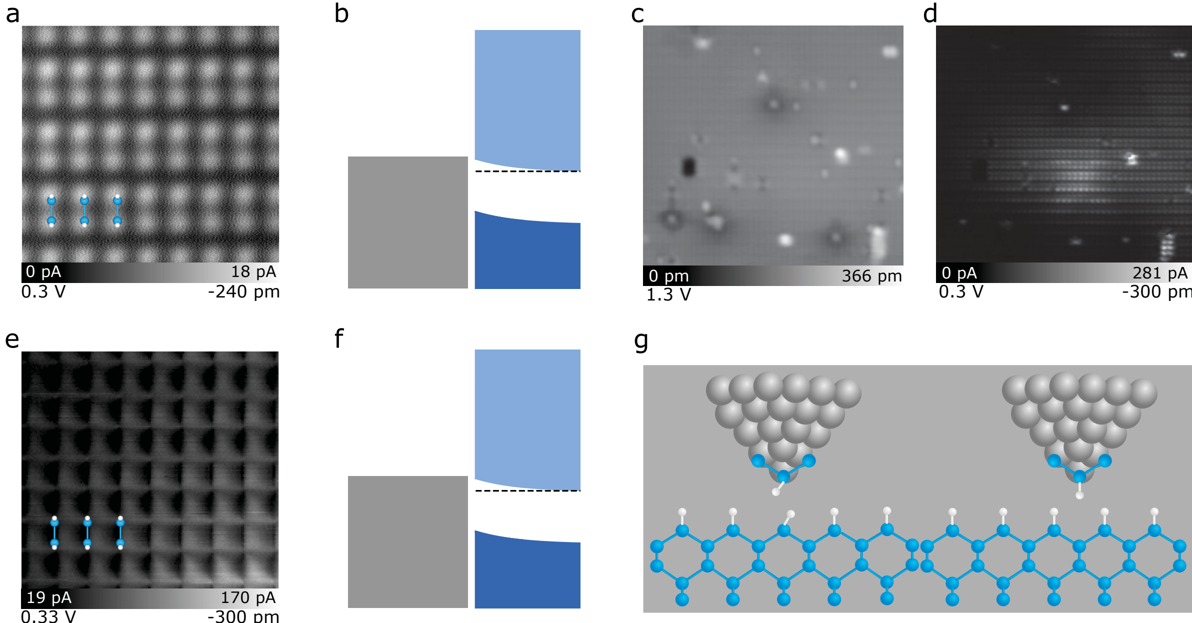

FIGURE 2.7: **Constant height STM images in different interaction regimes.** (a) A constant height STM image of the surface probing the onset of the conduction band and donor band as indicated in the band diagram of (b). (c) An area of the surface imaged in constant current mode. (d) shows the same area of the surface imaged in constant height mode revealing the electronic structure of any subsurface dopants. (e) The Scanning Tunneling Hydrogen microscopy image of the surface. The band diagram is shown in (f). (g) A model showing the imaging mechanism in STHM, where the degree of the repulsive interaction felt by the tip apex atom changes as different surface features are scanned. (a),(e) are 3 x 3 nm^2 while (c),(d) 20 x 20 nm^2.

possible to image the surface under different conditions. In general, tip conditioning done on the H-Si surface results in an apex atom that is either hydrogen or silicon. It is impossible to know the exact structure of the apex [142, 143] due to the perturbative nature of tip shaping and functionalization as discussed in the methods of Chapter 3 and elsewhere [139, 144–146], however two distinct trends are observed. When comparing the measured frequency shift of the tip over a dimer atom to the tip over a back bonded Si atom, two contrasts emerge depending on the tip functionalization. The dark contrast of Figure 2.8 (d), where surface H-Si atoms create a more negative Δf signal than back bonded atoms has been correlated to a Si tip apex (Figure 2.8 (f)) [140, 146–150]. The bright contrast tip of Figure 2.8 (a), which images H-Si atoms with a less negative Δf signal compared to the back bonded atoms of the surface corresponds to a hydrogen terminated Si tip (Figure 2.8 (c)) [140, 146, 147]. Since

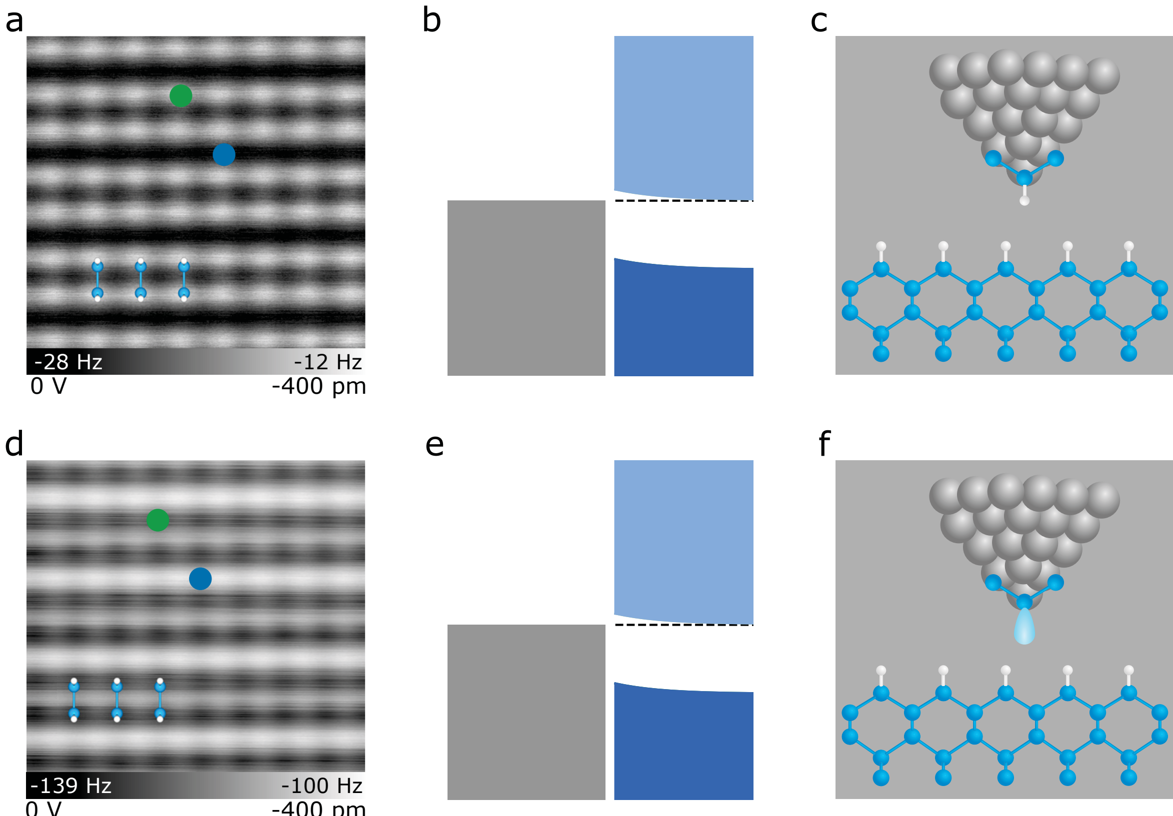

FIGURE 2.8: **Constant height AFM images of the H-Si surface.** (a) The H-Si surface images with an H-tip, (b) The corresponding band diagrams. (c) A model of the predicted tip functionalization. (d) The H-Si surface imaged with a Si apex tip. (e) The corresponding band diagram. (f) A model of the predicted tip functionalization.

the predominant tip-surface interactions usually occur at a tip-sample separation of $\sim$ - 300 pm, AFM images are usually acquired at such distances. Although it is possible to acquire a current signal during a constant height AFM scan, the reduction in tip height causes a dramatic increase in the tunneling current at biases similar to those used in constant current imaging. In addition, the cross talk between channels through the qPlus sensor often leads to false signals [151, 152] when high amounts of current are detected. As such, AFM images are generally taken at 0 or relatively low bias values as is done in this thesis.

The nature of these different contrasts results from different interaction potentials offered by each tip functionalization as highlighted in the Δf spectroscopies of Figure 2.9 [135]. The Si

functionalized tip features a neutral DB [139, 143] at the apex with the primary contribution coming from a covalent interaction between the tip and surface atoms [146, 149, 150]. A secondary charge induced dipole is also expected but only offers a significant contribution when imaging charged surface features [150]. The H-functionalized tip consists of a single H atom at the apex with the major contributions in signal coming from a less reactive Van der Waals interaction [140, 146, 147]. The curves of Figure 2.9 (a) show the $\Delta f(V)$ spectroscopies for an H-apex tip and a Si-apex tip above the two locations shown in Figures 2.8 (a),(d) highlighting their differing reactivities. The green spot over an H-Si atom has a less negative Δf signal than the back bonded atom (blue spot) for the H tip indicating that the tip-sample interaction between the H atom of the tip and the H atom of the surface is more repulsive than the tip and the back bonded atoms. At larger tip-sample separations, the probed interaction is more aligned to an attractive Van der Waals interaction which results in an apparent inversion in contrast (the back bonded atoms appear brighter than the H-Si atoms as shown in $\Delta f(V)$ spectroscopies of Figure 3.2 and in Figure 3.8). Images in this range are used less often as the long range interactions are less localized resulting in a reduction in atomic resolution. The Si-apex tip shows a more negative Δf signal over an H-Si atom of the surface than over a back bonded Si atom due to the strong covalent interaction between the Si DB of the tip and the surface H atom. Since the covalent interaction over the H-Si atom is stronger at all depths, the "dark" contrast remains consistent throughout the probed depth range. The same trend can be seen in the calculated force curves of Figure 2.9 (b), further supporting the nature of the interaction for each tip termination. At the smallest tip-sample separation, we can begin to see an effect from the repulsive forces acting on the H-functionalized tip correlating to the onset of repulsive Van der Waals interactions [92, 153, 154]. The Si-terminated apex does not show any repulsive interactions and continues its downward trend as the tip-sample separation is reduced increasing the strength of the covalent interaction with the surface.

Looking at the calculated potentials of Figure 2.9 (c), one can see how large the energy difference between the two tips are. The spectroscopies show a minimum observed potential

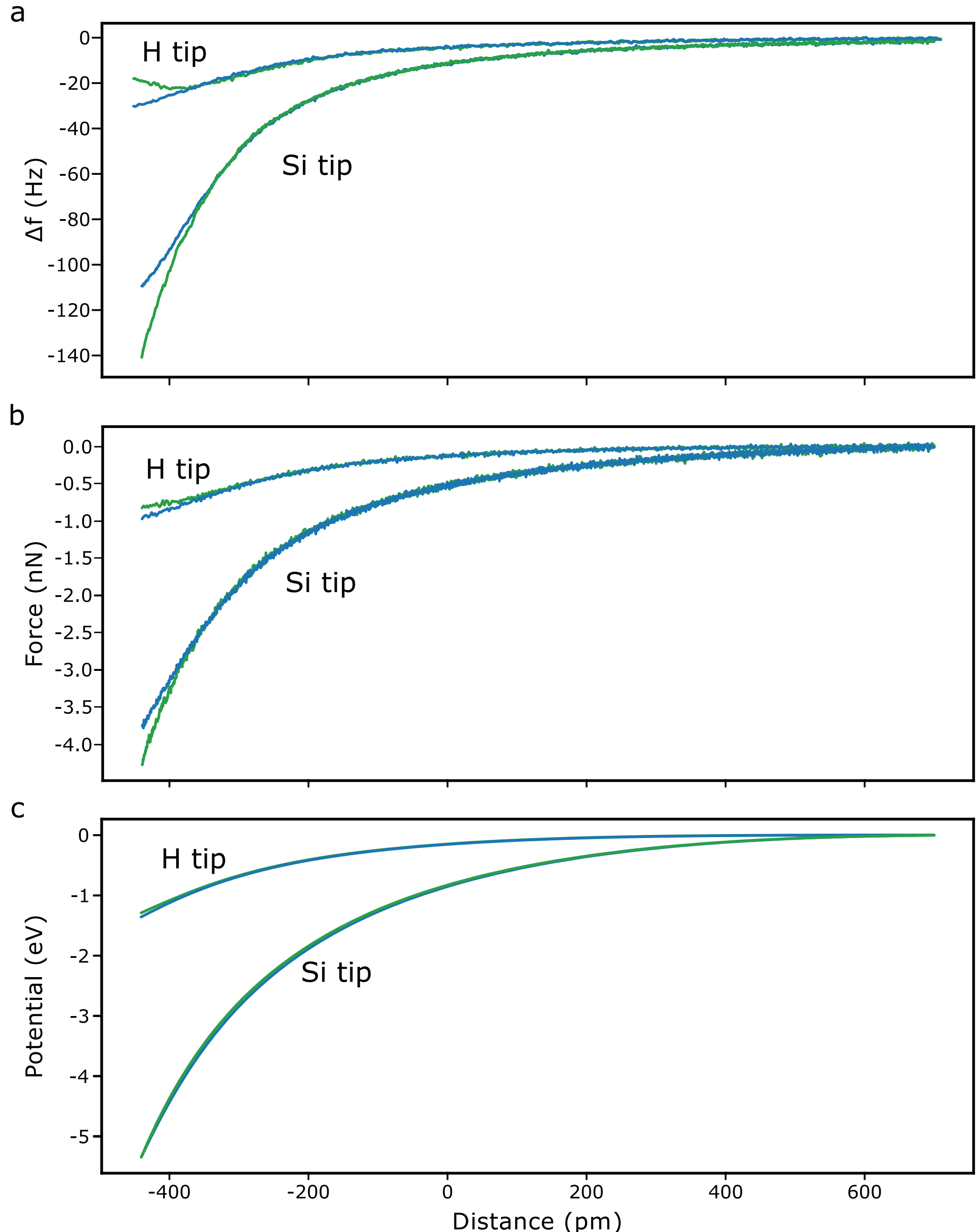

FIGURE 2.9: **AFM spectroscopies with varying tip functionalizations.** (a) The $\Delta f(z)$ spectroscopies above the locations indicated in Figure 2.8. (b) The calculated Force spectroscopies and (c) The calculated Potential interaction spectroscopies.

of around -1.3 eV for the H tip and a stronger -5.3 eV for the Si tip. It is important to mention that although the tip apex in each case is a single atom, long range interactions from off apex tip atoms, neighbouring surface atoms, and capacitive effects of the bulk contribute to the measured Δf signal and subsequently the calculated force and potential of the interaction. A more accurate study of the apex interaction can be done by subtracting a background spectroscopy taken over a more inert portion of the sample [155], as will by shown in Chapter 3.

Since both $\Delta f(z)$ spectroscopies shown in Figure 2.9 only appear to show the onset of the repulsive interaction, it appears obvious that more information regarding the nature of each interaction can be gained by further reducing the tip-sample separation. The experimental realization of such a measurement is more difficult as the increased repulsive nature often results in changes to the tip apex or surface atoms thus changing the nature of the interaction. As discussed with STHM, a H atom bonded to the apex of the tip can bend off apex due to the bond flexibility and increased repulsive tip-sample interactions. Looking at the $\Delta f(z)$ spectroscopy of Figure 2.10 (a), one can see the typical minimum in the potential at roughly -200 pm associated with an H-terminated tip. At decreased tip-sample distances, the increased repulsive interaction causes the H atom to bend off apex exposing the Si atom underneath, as marked by the sharp decrease in the Δf signal as seen with Si terminated tips. If the tip-sample separation is reduced even further, it is common for the H atom at the apex to be completely removed.

When using a Si tip with reduced tip-sample separation, it is very common for a surface hydrogen to transfer to the tip creating a surface DB and an H-functionalized tip. Such a transition can be seen when looking at Figure 2.10 (b). The forward curve in black measures a Si apex tip over an H-Si atom while the red curve measures the now H-functionalized Si tip over the newly created surface DB. Although the structural models in the inset show a single H atom transferring from the surface to the tip, it is possible for significant structural changes to the tip to also occur.

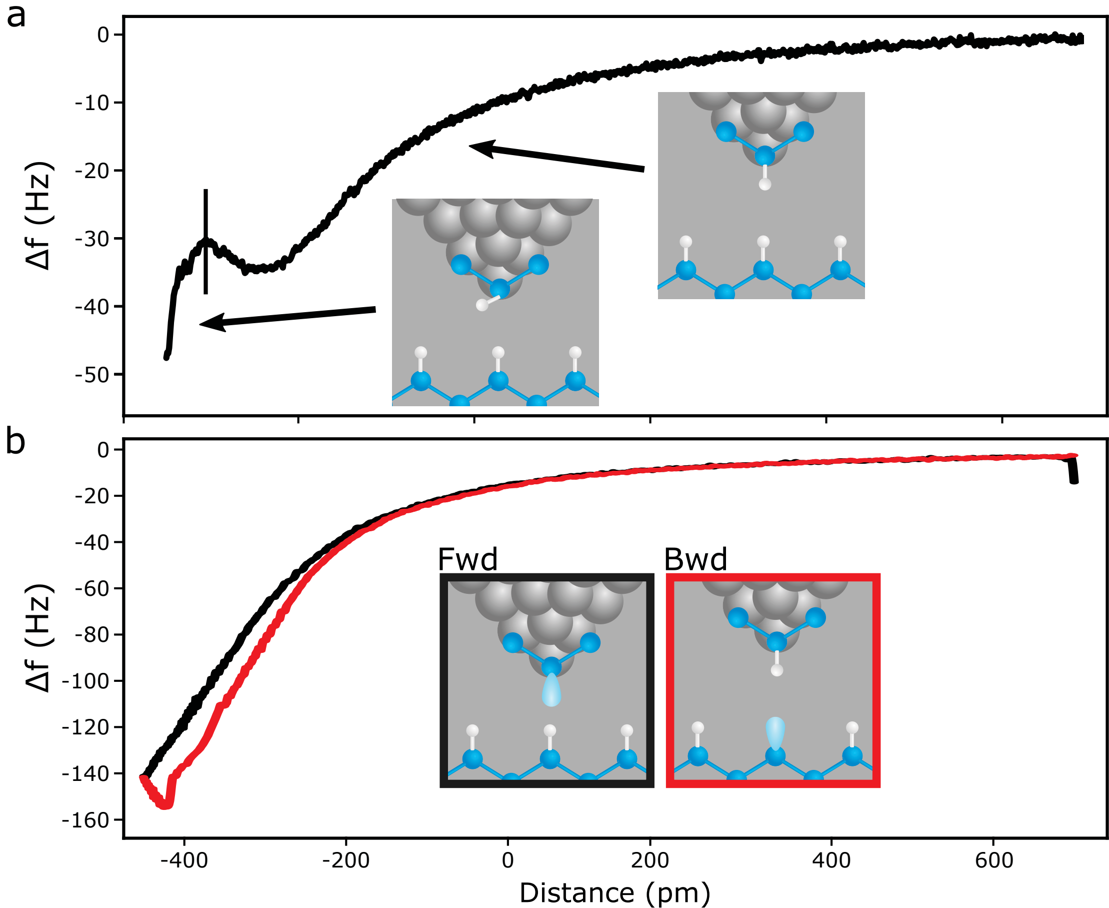

FIGURE 2.10: **Limitations in AFM spectroscopy**. (a) A $\Delta f(V)$ spectroscopy of a flexibly held hydrogen apex tip. The vertical line indicates the depth when the apex atom is bent off axis exposing a Si atom underneath, as indicated with the ball and stick diagrams. (b) A $\Delta f(V)$ spectroscopy of a Si terminated tip where a DB is created on the surface as shown in the insets.

Observing the difference in spectroscopies shown in Figure 2.10 between a H- and Si-terminated tip further show the nature of their interaction. The H-apex tip experiences an increased repulsive interaction consistent with a more weakly interacting Van der Waals potential [140, 142]. The Si-apex tip interacts via a stronger attractive covalent interaction [140, 147, 156–158] in which a covalent bond can form between a surface atom and the tip before the onset of a repulsive interaction is felt. Much like probing the empty and filled

electronic states of the crystal using an STM, probing the surface using multiple tip functionalizations using an AFM allows for a deeper understanding of the surface atoms under study. The combination of all six imaging modes allows for the measurement and interpretation of both the atomic and electronic properties of the crystal as will be applied in Chapter 3.

2.2.2 Surface Dangling Bonds

Following the preparation of a hydrogen terminated Si surface, individual surface DBs can be selectively re-added using the probe tip. By applying a bias pulse ($\sim$ 2.0 V) above a hydrogen atom, the H-Si bond can be broken leaving a single DB in its place [159–162]. This single Si DB can hold 0, 1, or 2 electrons rendering it in a positive, neutral, or negative charge state, giving rise to two distinct charge transitions, the positive to neutral(+/0) and the neutral to negative (0/-) [46, 163, 164] (and Chapter 5). These charge states exist within the band gap of Si allowing for the isolation[10] of DB electrons from the bulk charges in the conduction and valence band of the crystal [46, 166–168].

The presence of these gaps states can be revealed by performing either $\Delta f(V)$ spectroscopies with an AFM sensor or $I(V)$ spectroscopies using an STM. The $I(V)$ spectroscopies in Figure 2.11 are taken above an H-Si atom (blue), and two different DBs (red, and purple). The tip-sample distances for each spectroscopy is indicated relative to an initial height set point by maintaining a constant current of 50 pA above an H-Si atom at a sample bias of -1.8 V. The H-Si curve shows the characteristic band gap extending from roughly -1.1 V to 0.4 V (extracted from the log-scale inset). This gap will reduce to the expected 1.17 eV gap as the tip-sample separation is reduced further [169]. The red DB spectroscopy shows a narrowing of the gap to roughly -0.9 V to 0.25 V. This current in the band gap is due to the enhanced conductivity through the DB gap states, the magnitude of which is dependent on the emptying and filling rates of electrons passing from the tip, to the DB, and DB into

[10] Here, isolation means that electrons localized to a DB are unable to elastically scatter off electrons from the VB or CB. DB electrons may still interact with the VB and CB but inelastically via phonon mediated processes [165].

the bulk Si states or vice versa [170]. Since the DB and the bulk valence and conduction bands are misaligned in energy, the emptying and filling of DB electrons to and from the bulk states is facilitated via vibronic coupling [165]. The purple curve shows a narrowing of the band gap relative to H-Si (blue curve), but it is still wider than the previous DB (red). This is because the charge transitions of the DB are shifted relative to the Fermi level due to local electrostatic perturbations [6] (and Chapter 5), which changes the emptying and filling rates [7, 167] and subsequently the conductivity of the DB. This effect can also be seen when comparing the empty and filled states images of each DB in Figure 3.3 (red curve) and Figure 5.9 (purple curve).

The general shape of the $I(V)$ spectroscopies of DBs, specifically near the onset of the valence band, is found to vary significantly due to subsurface dopants and their varying conduction channels. Figure 2.12 shows an example of 5 DBs patterned within 15 nm of each other. Although they all show a similar current onset at roughly -0.5 V, the general shape and conductivity of each DB varies significantly. One of the most unique spectroscopies can be seen in red. At -0.75 V, the magnitude of current decreases until -1.1 V giving a negative differential resistance (NDR) pattern. As studied by Rashidi *et al.* [7, 167], this corresponds to the competing emptying and filling rates of the (0/-) and the (+/0) DB transition levels. The initial increase in current (-0.5 V to -0.75 V) is due to the tip overlapping with the (0/-) transition level. Electrons from the DB are emptied moving the DB from negative to neutral. The neutral DB is subsequently charged again by filling from the conduction and donor band of the crystal. The decrease in current (-0.75 V to -1.1 V) corresponds to the tip overlapping with (+/0) transition level. When electrons are emptied from the neutral charge state, the subsequent positive DB is filled with electrons from the conduction and donor band at a much slower rate due to the highly inelastic overlap of the conduction band with the (+/0) charge transition[11]. The current then increases again at -1.1 V as the (+/0) transition level becomes resonant with the valence band of the bulk crystal. Similar shapes

[11] Using pump-probe techniques the filling rate of a neutral DB from the conduction band is found to be roughly 0.3 ns while the positive DB is roughly 20 ns [167]

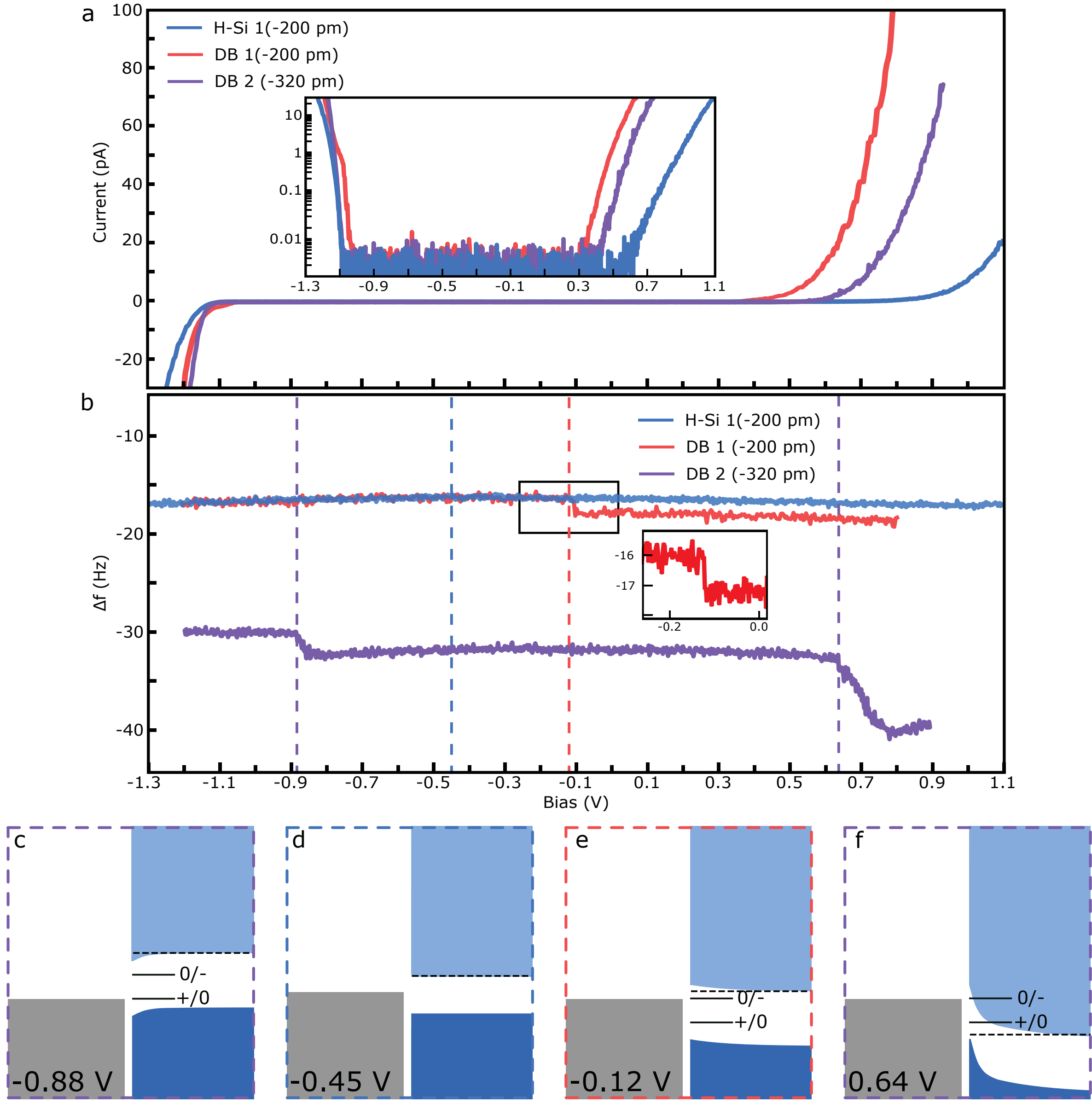

FIGURE 2.11: **Spectroscopies over DBs.** (a) The I(V) spectroscopies above an H-Si atom and two different DBs with the relative height indicated. (b) The Δ f(V) spectroscopies of H-Si and two different DBs with the relative height indicated. The inset shows the charge transition as indicated. The vertical lines correspond to the calculated band diagrams in (c)-(f).

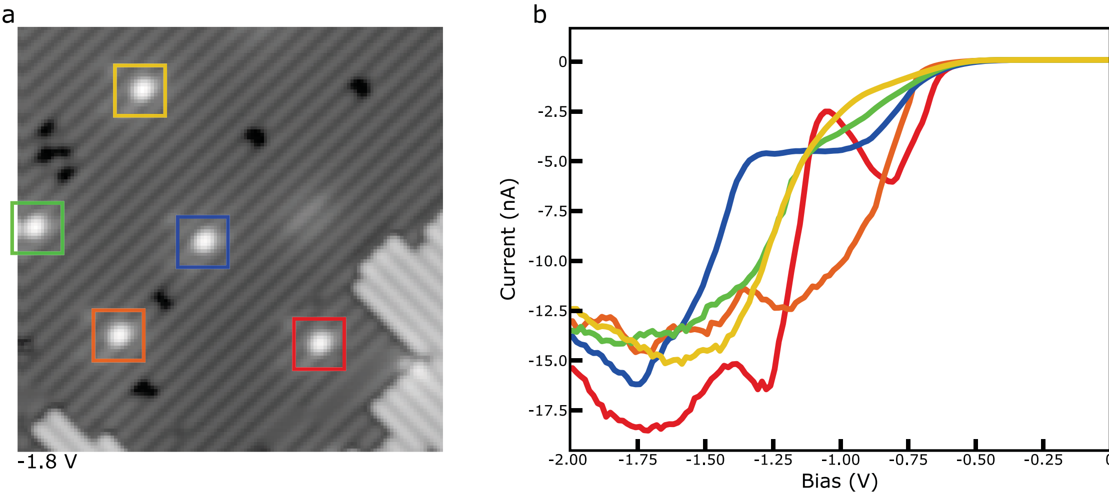

FIGURE 2.12: **Varying spectroscopies of DBs on the surface.** (a) Filled states images of 5 unique DBs on the H-Si(100) surface. Colours of bounding squares match the spectroscopies shown in (b) highlighting their variability in I(V) characteristics.

in spectroscopies can be seen in the other DBs as well with the source of the difference originating from correspondingly different emptying and filling rates of the DBs due to different alignments of the charge transition levels with the valence and conduction band, as well as from charge perturbation from neighbouring DBs and subsurface dopants [6, 7].

By measuring $\Delta f(V)$, it allows for a more direct way to probe the charge transitions levels as KPFM is more susceptible to the capacitance (and subsequently the charge) of the surface than I(V) spectroscopies [107, 115] allowing for transitions within the band gap of the material to be measured. The spectroscopy above the H-Si atom in Figure 2.11 (b) (blue curve) shows the expected parabolic shape associated with the CPD of the surface as expected from equation 2.21 [6]. At roughly -0.45 V, the parabola reaches its maximum value corresponding to the point where the field between the tip and sample is minimized indicating the difference in work functions of the Si sample and W tip (4.05 eV - 4.5 eV = - 0.45 eV) as shown in the band diagram of Figure 2.11 (d). The exact value of the CPD changes depending on the tip functionalization as well as the subsurface and surface charge distribution of the crystal, as

studied by Huff *et al.* [6]. The slight deviation from the parabolic shape at roughly 1.0 V is likely due to unwanted capacitive coupling between the frequency shift and current carrying lines of the AFM sensor.

When looking at DBs, the $\Delta f(V)$ spectroscopies reveal discrete changes in the signal corresponding to a charge state transition. The spectroscopy in red shows the charge transition of the (0/-) level at -0.12 V, as indicted by the step in Δf (corresponding band diagram is seen in Figure 2.11 (e)). The corresponding difference in Δf between the two charge states is a combination of varying electrostatic and covalent interactions as well as a slight change in the tip-sample separation due to a lattice distortion of the DB structure [165, 171] (as will be discussed further in Chapter 5). The measured bias of this charge transition is found to vary between roughly -0.4 eV and 0 eV [6, 46] depending on the tip functionalization, as well as the distribution of subsurface and surface charges. It is usually quite difficult to measure the position of the (+/0) charge transition as it often overlaps with the onset of current from the valence band [7, 167]. Only in exceptional cases where the energy levels of the DB charge transitions are raised significantly above what is usually seen, can this charge transition be observed. The purple curve of Figure 2.11 b shows the spectroscopy of such a DB. Due to a large number of DBs patterned around this DB, the energy level of the (0/-) transition was raised by roughly 0.85 eV. As a result, the (+/0) transition can now be seen at -0.88 V. The corresponding band diagrams are shown in Figures 2.11 (c) and (f). Comparing the two $\Delta f(V)$ spectroscopies of the DBs, two differences can be observed in their shape. The difference in Δf between the neutral and negative charge state of the red curve (see inset) is much less pronounced compared to the same transition in the purple curve. This difference can be attributed to the different tip-DB separations highlighting the difference in $\Delta f(z)$ as a function of DB charge [6, 155]. In addition to the step depth, the angle of the charge step is also observed to differ between the two measurements. The inset of Figure 2.11 b shows the charge transition step is much more sudden for the red curve, similar to measurements done on molecules and metals with an insulating salt layer [107, 115]. The charge transitions in the purple curve show a much more sloped curve, suggesting the measured charge state of

the DB is actually an averaged value due to the competing emptying and filling rates of the DB. When the positions of these steps are compared to the I(V) spectroscopies, the relative position of the charge step with the onset of current from the conduction and valence bands supports the claim that the sloped nature of the DB charge step is a result of an averaging of the net charge of the DB.

2.2.2.1 DB Devices

The ability to control the energy level of the (0/-) charge state transition relative to the Fermi level of the crystal is the basis for Binary Atomic Silicon Logic devices [46]. If this charge transition occurs above (below) the Si Fermi level, it will exist in a natively[12] neutral (negative) charge state. If two DBs are patterned within close proximity to each other, they form a DB pair where the added electrostatic perturbation raises the charge transition of the DBs making one neutral and one negative [163]. The localization of a negative charge within a DB results in a lattice distortion, lowering the energy of the system (on the order of 100 meV) and raising the host atom by approximately 30 pm [165, 171–174]. In an unperturbed system, the negative charge can localize between either DB with equal probability. By adding a perturbing DB to either side of the pair, the charges are localized such that the total energy of the 3 DB system is minimized (i.e. The negative charge of the DB pair is localized to the DB furthest away from the perturber).

This polarization of the DB pair is used to represent binary information with a left polarized pair representing a 1 and a right polarized pair representing a 0. Given that DBs can be patterned at any H-Si lattice site, a multitude of DB geometries can be patterned giving a tailored set of characteristics. The work done by Huff *et al.* [46] demonstrates a binary wire where a series of DB pairs have been patterned, allowing for information to propagate 10s of nm's across the surface. In addition to this, a logical OR gate was patterned by placing 3 DB pairs in a Y pattern. The patterned DB geometry allowed for each of the

[12] Here natively means without any perturbation from the probe tip.

DB pairs to hold a single charge. By adding perturbing DBs, the corresponding charge rearrangement of the DB structures was able to mimic OR gate logic (shown in Figure 1.3 (d)). A recent theoretical work has outlined potential DB geometries to create AND, XOR, NAND, and XNOR logical gates which is a current area of experimental research [55]. Current experimental limitations in realizing a wider range of logical devices is due to a lack of understanding and quantification in the behaviour of the (0/-) charge transition with varying subsurface dopant distributions, as well as the addition of neighbouring DB charges. Theoretical work supports that by adding subsurface electrodes [55], these issues could be controlled, however, such a demonstration has yet to be realized [175].

2.2.2.2 DB Device fabrication

The fabrication of such DB devices is done by controlled bias pulses with the probe tip above the desired H-Si lattice site [145, 160, 161, 176]. By applying a positive sample bias pulse of $\approx$ 1.8 to 2.4 V with a pulse width of 10 ms to 30 ms, inelastic tunneling electrons excite and break the H-Si bond, leaving behind a Si DB. The hydrogen atom can either transfer to the tip resulting in a tip functionalization, or to the vacuum chamber [4, 177]. As will be shown in Chapter 4, the automating of such patterning can be achieved by providing tip coordinates for DB sites allowing the automated DB fabrication software to move to each coordinate and apply a bias pulse of increasing magnitude and/or width until a DB is created. The creation of the DB is confirmed by measuring an increase in tunneling current associated with the higher conductivity of the DB compared to an H-Si atom. A DB pattern fabricated in this was is shown in Figure 2.13 (a), with the corresponding lattice positions marked in Figure 2.13 (c).

Errors can occur in fabrication if the scanning probe tip is unstable or not atomically sharp. Figure 2.13 (b),(d) shows an example of two such errors. The absence of the DB in the bottom left of the pattern means that the patterning software measured a false positive, most likely due to a change in tunneling current caused by a change in the distribution of

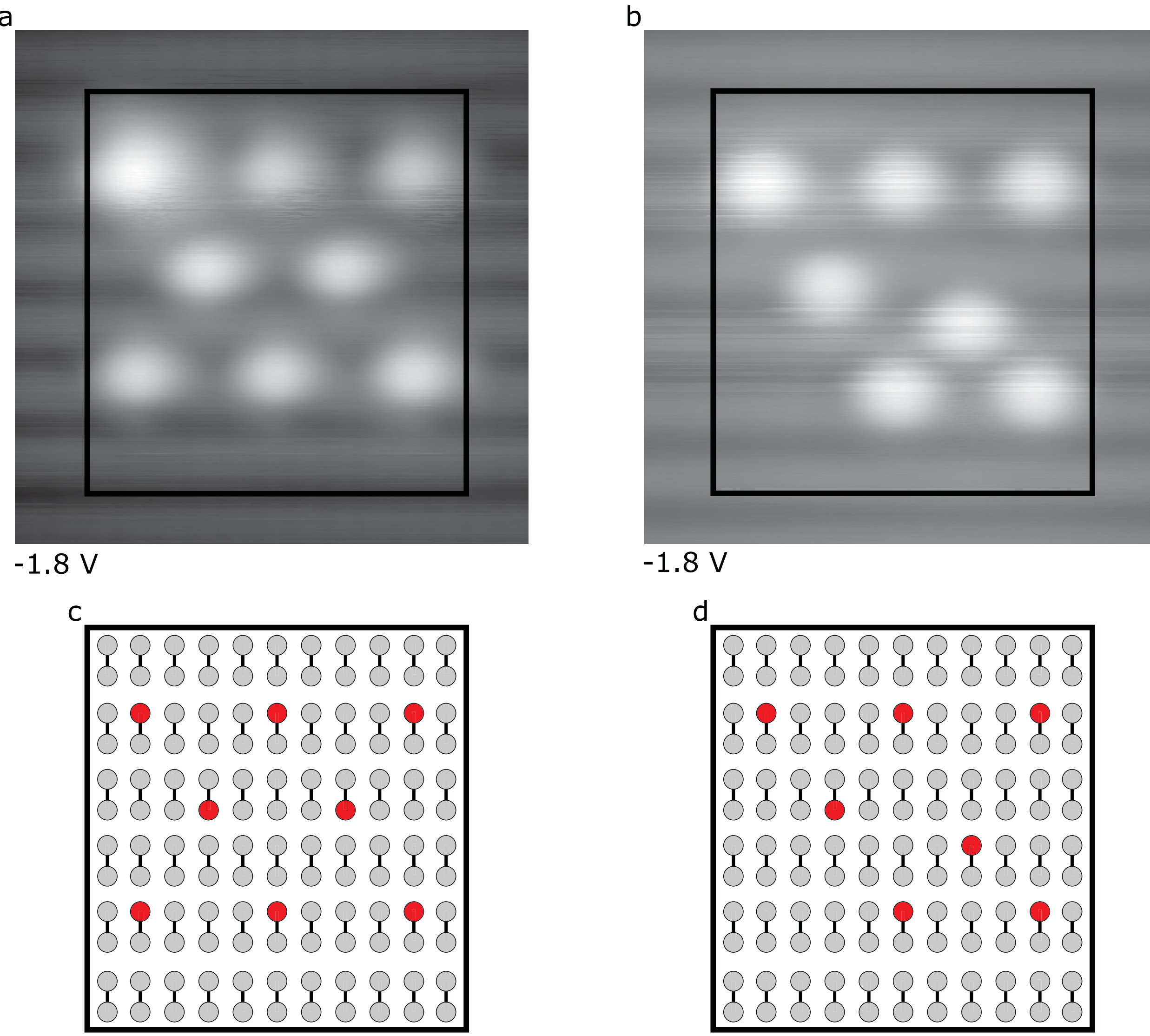

FIGURE 2.13: **Automated DB fabrication.** (a) A DB pattern that was done using an automated patterning software. (b) The same pattern done with 2 mistakes. (c) The pattern of (a) and (d) The pattern of (b). The intended pattern in (b) was supposed to match (a). (a) and (b) are 6.5 x 6.5 nm^2 with the bounding box 5 x 5 nm^2

tip apex atoms. The DB on the right side of the middle row was patterned in an incorrect spot, most likely due to piezo creep or a "dull" tip apex structure. Quite often, the scanning probe tip can be functionalized with multiple apex atoms giving the surface a blurry look as it is scanned by a larger tip structure as shown in Figure 2.14 (a) and (d). When bias pulses intended to create DBs are applied with a double tip, the tunneling current is distributed throughout each of these apex atoms resulting in the potential for DBs to be created at multiple lattice sites. In order to remove these multiple apex atoms, controlled tip contacts are performed on either clean Si or H-Si depending on the desired tip functionality. The controlled contacts are done by decreasing the tip-sample separation between 600 - 1400 pm with a negative sample bias of -1.8 V as shown in Figure 2.14 (b) and (e). Eventually, the apex of the tip will change so that all DBs imaged appear as a single bright protrusion on the surface as shown in 2.14 (c) and (f). The slight spherical asymmetry of the DB in (f) is from the DB being slightly tilted due to the dimer geometry and not an asymmetry in the tip apex atom. Maintaining tip quality is the time limiting procedure in device fabrication, with tip shaping taking anywhere between 5 minutes and 4 hours. If a tip depth of 1400 pm is reached and no atomically sharp tip is achieved, it is often more time efficient to resharpen the tip by field evaporation and N_2 etching in a field ion microscope (FIM) [178]. Once the tip is removed from the microscope chamber and into the FIM chamber, any progress made by patterning is effectively lost as it is nearly impossible to reapproach a tip to the same spot once it has been removed from the scanning chamber.

One of the key advantages that DB devices offer over other atomic fabrication schemes is that they can be erased almost as easily as they can be created. By adding hydrogen back to the surface creating an H-Si bond where the DB used to be, the former DB site becomes indistinguishable from the rest of the H-Si surface. This H-repassivation has been successfully demonstrated in 2 ways. First, by functionalizing the probe tip with hydrogen and bringing it towards the surface dangling bond, the hydrogen atom can transfer from the tip to the surface [4, 147, 177]. In AFM, this is usually done with a constant height

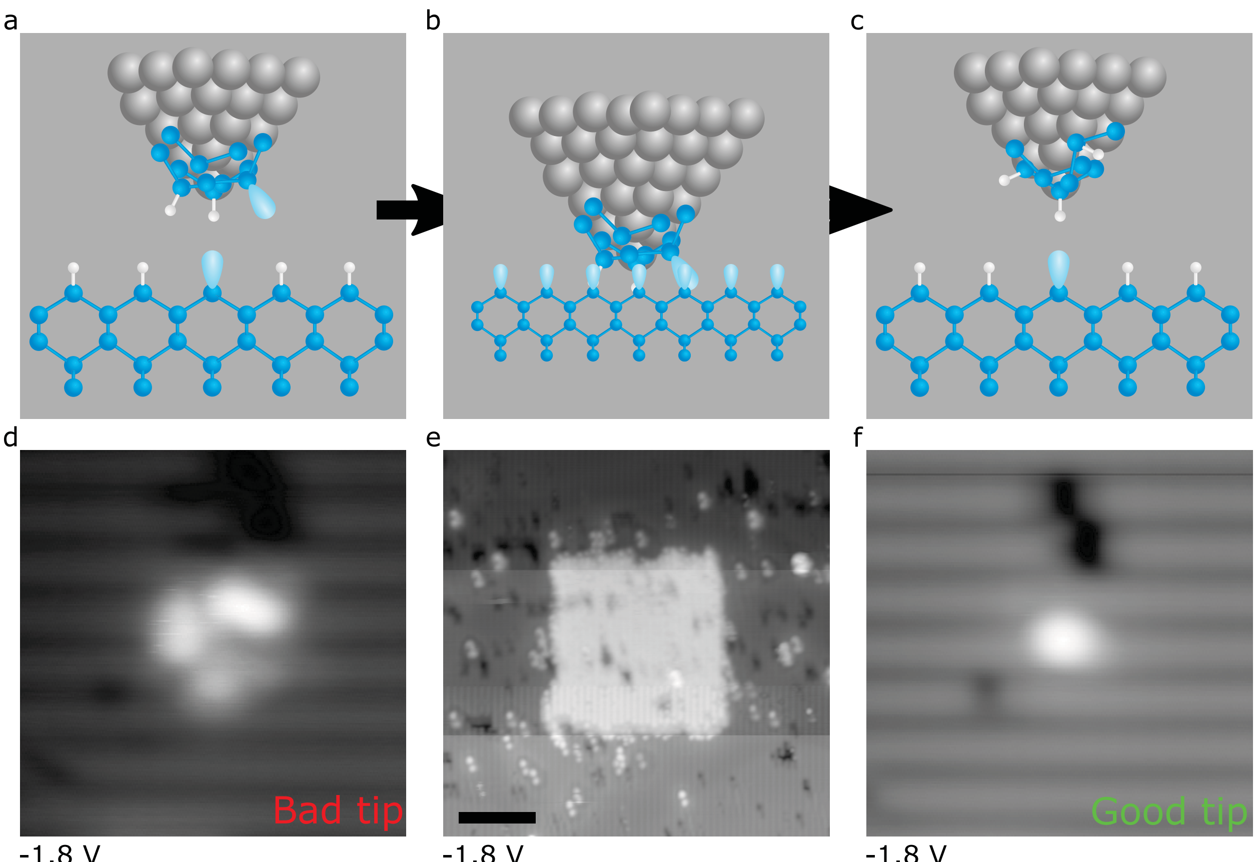

FIGURE 2.14: **Tip shaping procedure.** (a) A model of the tip with multiple imaging apex atoms. (b) The mechanism of the controlled tip contact in a patch of bare silicon. (c) The newly formed tip apex with a single imaging atom. (d) A DB imaged with a multi atom tip apex. (e) A hydrogen desorbed patch on the surface with horizontal changes in contrast resulting from tip surface contacts. (f) The same DB as (d) imaged with a single atom tip apex. (d) and (f) are 6 x 6 nm^2 and the scale bar in (e) 10 nm long.

scan where the hydrogen transfer is often marked with a change in contrast from an H-terminated tip to a Si-terminated tip (Shown in Figure 3.10). A slightly more perturbative method has also been shown in STM in which an H-functionalized tip is brought closer to the surface via a $I(z)$ spectroscopy measurement. By applying a small positive bias, the transfer of H to the surface is observed by a sharp step in conductivity. Two different trends in I(z) spectroscopy are observed as shown in Figure 2.15. A decrease in conductivity is associated with the termination of the surface DB via an off-apex H atom(2.15 (a)), while an increase in conductivity is associated with the termination of the surface DB via an H atom on the apex of the tip. The ability to terminate DBs with off-apex H atoms allows the

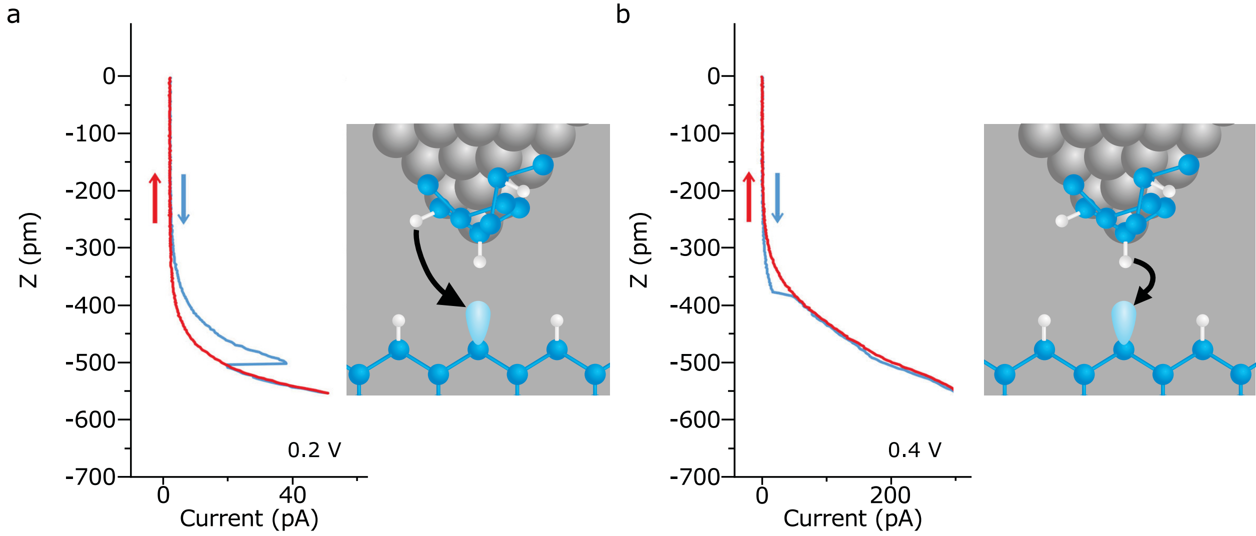

FIGURE 2.15: **STM feedback DB erasure.** (a) The characteristic I(z) tracing of a DB passivization via an off-apex H atom. (b) The I(z) spectroscopy of the DB passivation via an apex H-atom. The data for the spectroscopies have been published in [4].

tip to be "loaded" with hydrogen so that multiple DB erasures can be executed without the need to re-terminate the tip with hydrogen. These two differing trends can be intuited by understanding that the majority of tunneling current is mediated via the tip apex atom. In the off-apex case, the conductivity through the apex atom remains unchanged and any drop in current is dominated by the removal of the highly conductive DB surface state. In the on-apex case, the conductivity through the apex changes due to the change in atomic structure, as well as a change in tip-sample separation. The reduction in conductivity through the loss of the DB is overshadowed by the increase in conductivity via the change in the tip apex resulting in an increase in current (the measurements in Figure 3.10 confirm that a Si apex tip is more conductive than an H apex tip). Although this H-repassivation method is useful for addressing single DBs, it is very time consuming and necessitates the tip being refunctionalized often.

The unique geometry of the H-Si(100)-2x1 surface also allows for an alternative "make to erase" repassivation scheme [5]. When two DBs are patterned along a dimer row, they are able to react with molecular hydrogen inside the vacuum chamber and re-terminate the surface [179]. This reactivity is site selective as single DBs and bare dimers do not react

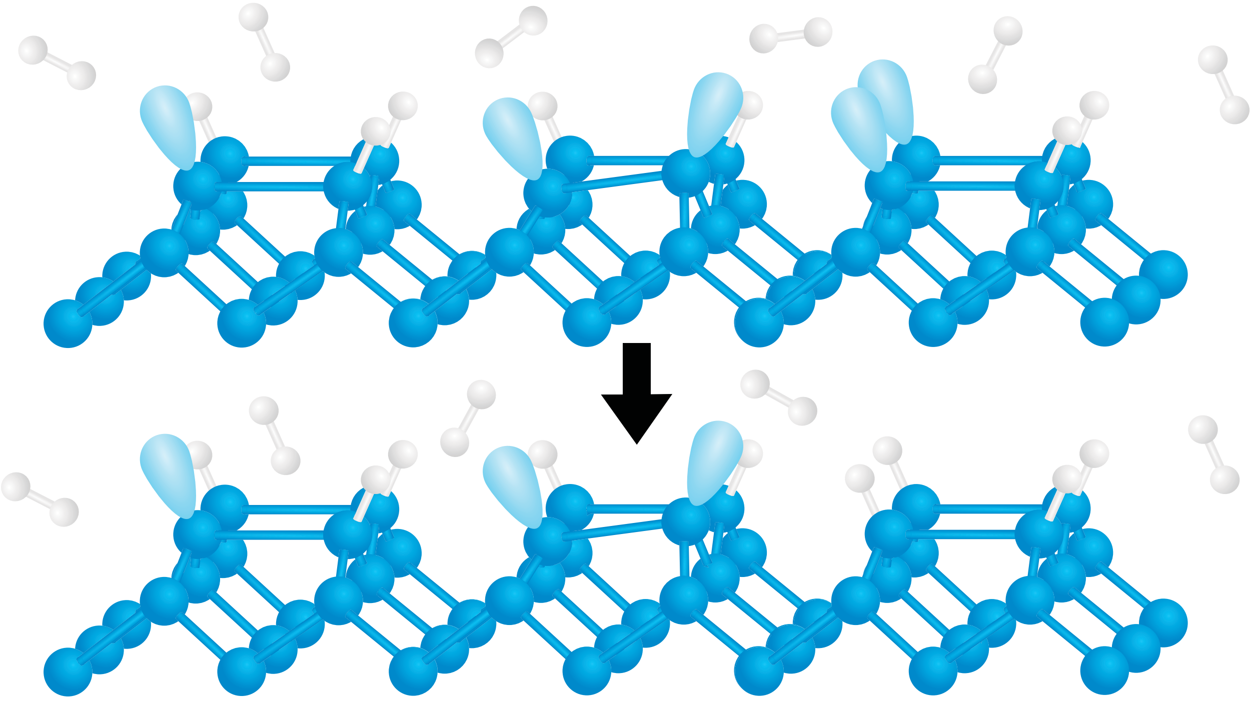

FIGURE 2.16: **Make to erase repassivation.** The ball and stick model shows three unique configurations of DB patterns. The left shows a single DB, the middle shows a bare dimer, and the right shows 2 DBs along the same side of a dimer row. After exposing the system to molecular hydrogen, only the 2 DBs along the same side of a dimer row are erased.

with molecular hydrogen in this way as drawn in Figure 2.16 and shown in Figure 5.35. Any incorrectly patterned DBs can then be erased by fabricating an additional DB along the same side of the dimer row with a background pressure of molecular hydrogen ($\sim 1 \times 10^{-8}$ Torr). The only downside is that the molecular repassivation scheme is rendered useless to any DBs that are part of a bare dimer. As a result, a combination of tip functionalization and molecular hydrogen repassivation is often used in practice.

As will be addressed in Chapter 4, the successful automation of DB fabrication is dependent on 3 limiting factors: the maintenance of an atomically sharp tip capable of pattering DBs, the ability to identify and locate surface and subsurface defects which would prevent DB fabrication, and the ability to recognize and correct any fabrication mistakes. The successful implementation of the first two factors was realized by coupling scanning probe microscopy to machine learning algorithms to allow for automated analysis of images taken by the scanning

probe system. By examining the state of surface DBs, the tip quality can be assessed as either a single or multi-apex tip as shown in Figure 2.14. Automated tip conditioning is used to form the tip back to a single atom apex [180].

The quality of a prepared surface can be assessed by using a machine learning algorithm capable of identifying and locating specific defects on the surface. These defects limit the patternability and viability of DB devices, so by knowing their location, it is possible to pattern DBs in an optimal surface position. The former will be discussed in section 2.3 while the latter will be described in more detail in Chapter 4. The work of automated error correction is currently being developed and is thus outside the scope of this thesis. All necessary concepts to better facilitate the understanding of these machine learning techniques will now be addressed providing the foundations for machine learning and its applications into scanning probe microscopy.

2.3 Machine Learning and Neural Networks

A subset of artificial intelligence, machine learning (ML) very broadly applies to the improvement of program or code via experience. Much like human learning, machine learning is done by exposing the algorithm (or brain) to some training data, say pictures of giraffes. If we expose the ML algorithm to enough pictures of giraffes, we should be able to give it a never before seen picture of a giraffe and have it correctly identified as such. The overarching ability of our neural network depends entirely on how we present the training data. If we want the algorithm to identify which pictures have giraffes and which do not, then we need to include pictures of things that aren't giraffes in our training data. A human knows that a rhino is not a giraffe because we have seen both rhinos and giraffes previously. A ML algorithm that has never seen a rhino before might look at it and extract that it has two eyes, four legs, horns, and a tail and classify it as a giraffe. Only after we expose it to images of rhinos and giraffes is it able to distinguish between the two animals. From this

it is very clear to see that the quality of a neural network depends on a well designed and labelled training data set. A properly trained ML algorithm is only capable of performing a classification or action on some data set if that data set shares enough similarities with data used to initially train the neural network.

Without delving into the details of the history of Machine Learning, it has been around since the 1940s [181]. Only with recent developments in computer hardware, algorithms, and accessibility to large amounts of useful data has the most recent surge been possible. Recent machine learning applications include their use in self-driving cars [182–185], medical image analysis [186–188], the game go [189], speech recognition [190], material science [191], fraud detection [192], and scanning probe microscopy [193–196]. To understand the fundamental principles of the many variations of machine learning algorithms, it would take an entire textbook [197–199] so instead we will focus on those algorithms which have proven useful to scanning probe microscopy.

There are three main types of learning approaches used when training an algorithm: supervised, unsupervised, and reinforcement learning. As the name suggests, supervised learning is done with human supervision of the training process. Training data given to the algorithm has been labelled so the network may be assessed for its accuracy in correctly predicting the input data. By assessing the accuracy of the prediction, the algorithm undergoes a back propagation step in which the "degree of wrongness" is used to correct the algorithm so its prediction may better match the data label. The application of supervised machine learning for image classification has been best realized by using deep learning and convolutional neural networks. The concept of deep learning builds off the concept of a multilayer perceptron (Figure 2.17) in which information is propagated through layers of "neurons" allowing for feature extraction from the data. This neural network is designed in such a way that data (an image of a giraffe or rhino) is passed to the input layer (blue), then passed through a series of hidden layers[13] (purple) until they reach an output layer (green). The output layer

[13] They are referred to as hidden because in general, a user does not care what values they have been assigned as long as the neural network works correctly

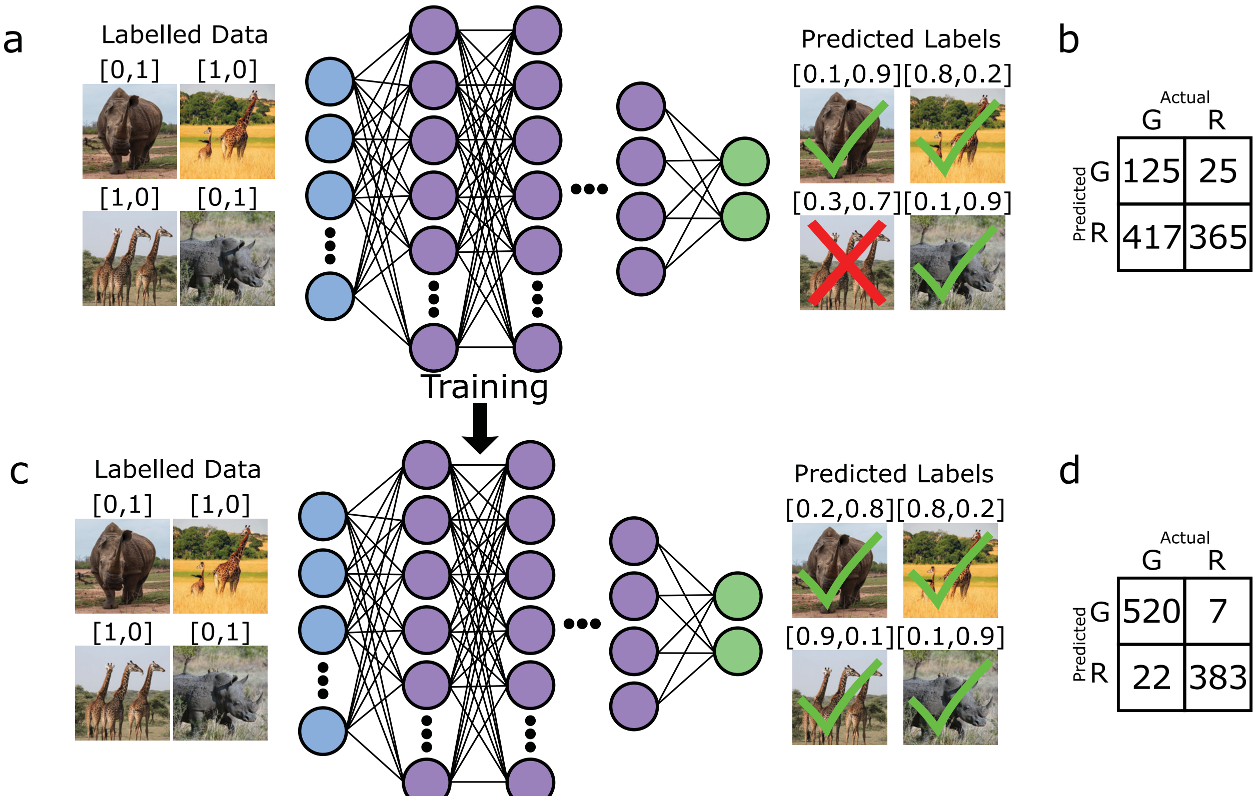

FIGURE 2.17: **Training a multi-layer perceptron.** (a) The configuration of such a network that poorly identifies giraffes. This accuracy is represented in the confusion matrix of (b). After training the network shown in (c) the accuracy has been greatly improved, as shown in (d). The blue nodes represent the input layer, the purple nodes represent the hidden layers, and the green nodes represent the output layers.

is designed so that each output value corresponds to one of the desired classes the NN is supposed to identify. In our case, we have two outputs, one corresponding to a giraffe [1,0], and the other corresponding to a rhino [0,1]. The accuracy of the network is best represented using a confusion matrix shown in Figure 2.17 (b), and (d). The confusion matrix of the poorly trained model in Figure 2.17 (a) shows that a large number of giraffes are being interpreted as rhinos. After further training of the network, the updated truth table of Figure 2.17 (d) now shows that both classes are correctly predicted with high accuracy.

In a multi layer perceptron, information is passed through to nodes of each layer via connecting weights and bias values. The value of the ith node in the jth hidden layer is expressed as

$$h_{j,i} = \phi\left(\sum_{k=0}^{n_{j-1}} w_{ik} h_{j-1,k} + b_i\right) \tag{2.26}$$

where n_{j-1} is the number of nodes in the $j-1^{th}$ layer, $h_{j-1,k}$ is the value of the kth node in the $j-1^{th}$ layer, w_{ik} is the weight connecting the $j-1, k^{th}$ node to the j, i^{th} node, and b_i is an applied bias. The activation function ϕ is applied to each node value to normalize the parameters to minimize the risk of runaway computations[14]. Figure 2.18 (b) shows three such examples of normalizing functions. Earlier networks utilized such functions as the tanh or sigmoid, however, this often resulted in a vanishing gradient problem where values above a certain threshold would all be approximated to 1 thus losing any information on the gradient. These were replaced with variations of the rectified linear unit (ReLU) which retained the relevance of larger node values. The entire parameter space of the neural network is commonly written as $\theta(w, b)$ which encompasses all trainable parameters (weights, biases, etc.) of the network. By defining some loss function, the accuracy of the network can be assessed as a function of $\theta(w, b)$. By minimizing the loss function for a given set of training data, $\theta(w, b)$ can be optimized to maximize the accuracy of the network. There are several variations of loss functions depending on the data used. The cross entropy loss function is used in Chapter 4 as it best applies to single classification data (the image is either of a giraffe, or rhino, but not both), where each piece of input data corresponds to a single output classification (1 if true, 0 if not true) given as

$$L(y, \hat{y}) = -\sum_{j=0}^{m} (y_j \cdot log(\hat{y}_j)) \tag{2.27}$$

Where y is the labelled data value, and $\hat{y}$ is the predicted value, and m is the total number of classes. For example, consider a labelled piece of data $y = [1, 0]$ and three different predictions $y_1 = [0.9, 0.1]$, $y_2 = [0.5, 0.5]$, and $y_3 = [0.1, 0.9]$ corresponding to three different configurations of the network θ_1, θ_2, and θ_3. The loss for each configuration corresponds to

[14] bias values were able to approach very large positive and negative numbers very quickly when training

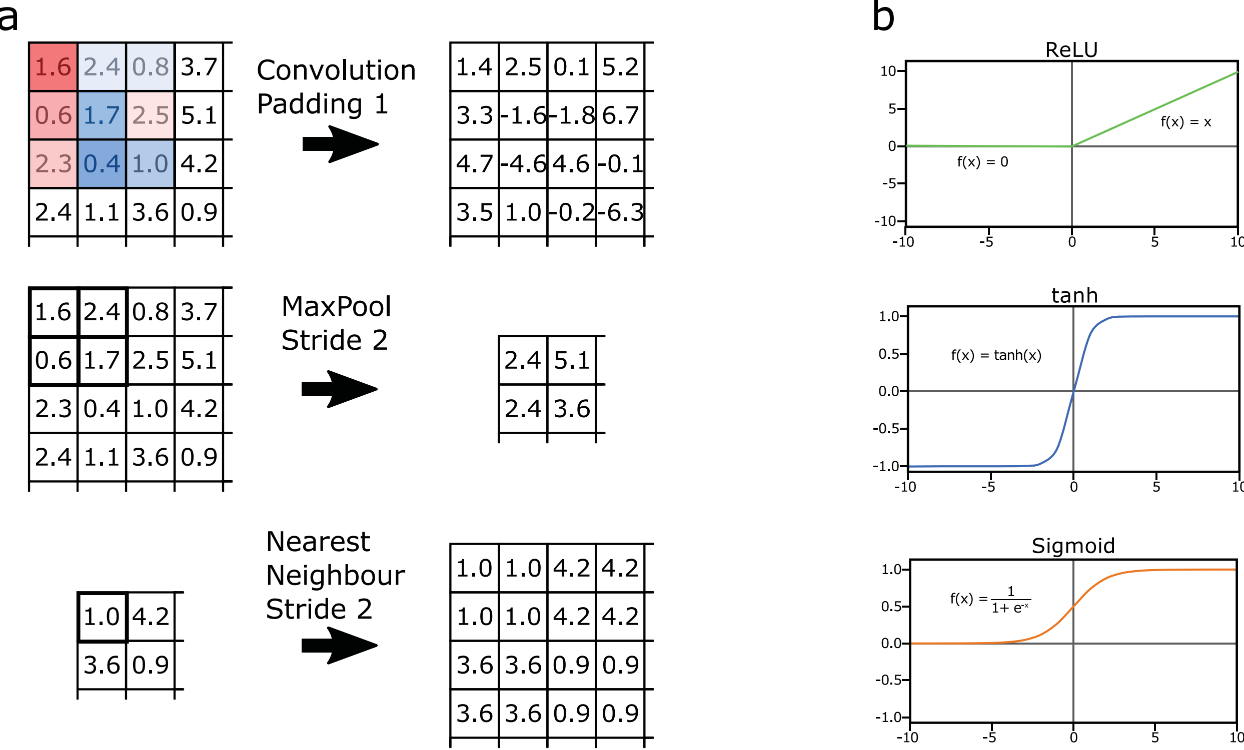

FIGURE 2.18: **Machine learning techniques.** (a) Three methods of data filtering commonly used in convolutional neural networks. (b) Three different activation functions commonly used.

$L_1 = 0.046$, $L_2 = 0.30$, and $L_3 = 1$. Since the goal is to minimize the loss function, θ_1 appears to be the most well performing compared to θ_2 and θ_3. In order to increase the performance of θ_2 or θ_3, network training must occur via back propagation in which the inaccuracy of the network is propagated from the output layer to the input layer. By adjusting the values of weights and biases which contribute to an inaccurate prediction for each image, the loss function is minimized as a function of the entire training data set. This process is often expressed as

$$\theta = \theta - \eta \cdot \nabla L(\theta) \tag{2.28}$$

where η is the learning rate applied to the loss function and $\nabla L(\theta)$ represents the gradient of the loss function. Once the parameters in θ have been adjusted so the gradient is zero, the training process is complete. The training process is best applied using mini-batch training where the data set is broken into much smaller sizes. The loss function is then calculated

for each batch and the network parameters in θ are adjusted so that a shift in parameter space (the size of the shift is given by η) results in the largest reduction in $L(\theta)$. As training is done over multiple iterations of the entire data set (known as an epoch), it is useful to begin with a large value of η so the training does not become stuck in a local minimum in L. As training continues, the learning rate is reduced so the global minimum is more exactly converged upon.

The speed at which the neural network finds the minimum of $L(\theta)$ greatly depends on the method of optimization used. One of the most commonly used is the Adam optimizer [200]. The success of Adam comes from the calculation of an exponential moving average of the gradient and the squared gradient tuned to parameters β_1 and β_2 which control the learning rate for each calculation of the gradient. The moving averages of the tth iteration are given by

$$\begin{aligned} m_t &= \beta_1 m_{t-1} + (1 - \beta_1)\, g_t \\ v_t &= \beta_2 v_{t-1} + (1 - \beta_2)\, g_t^2 \end{aligned} \tag{2.29}$$

where g_t is the gradient calculated over the mini-batch. In the first iterations, the averages m_{t-1} and v_{t-1} are initialized to zero. This introduces a bias in the estimation of the average and as such, they must be correct via

$$\begin{aligned} \hat{m}_t &= \frac{m_t}{1 - \beta_1^t} \\ \hat{v}_t &= \frac{v_t}{1 - \beta_1^t} \end{aligned} \tag{2.30}$$

Initial values of $\beta_1 = 0.9$ and $\beta_2 = 0.999$ are often used so these corrected values only have a significant effect at low values of t. The model weights are then updated via

$$w_t = w_{t-1} - \eta \frac{\hat{m}_t}{\sqrt{\hat{v}_t} + \epsilon} \tag{2.31}$$

where ϵ is usually set to 1×10^{-8} to prevent divergence at small values of $\sqrt{\hat{v}_t}$.

The field of image classification using neural networks is still an active area of research with newly developed methods commonly tested against image databases such as MNIST [201] and CIFAR-10 [202]. A network architecture which has been shown with greater accuracy than the multilayer perceptron utilizes convolutional filters to extract higher order features from the data set. The use of convolutional filters allows the network to extract information on how each pixel in the image correlates to neighbouring pixels rather than just looking at each pixel individually. The size of the filter is defined when initiating the network architecture. Instead of learning a single weight for each node connection, the values of the filters are learned to extract higher order features. Each filter is rastered through the data to be classified at a specific layer in the network (for each layer, this results in n representations of the data where n is the number of filters applied in that layer) shown in Figure 2.18 (a). Similar methods are used for edge detection in traditional image analysis, but by allowing the network to learn the best filter configuration, optimal values can be determined for the given data set. For many data sets the dimensionality must also be reduced to the desired output size (a 1028 x 1028 pixel image of a giraffe must be reduced to a 1-d vector [1,0]). The most common technique used to reduce the dimensionality is pooling where a filter is rastered through a layer with a stride value (raster step size) resulting in a reduced dimensionality. Common methods include max pooling where the maximum value in a 2x2 matrix is taken, or average pooling where the average of a 2x2 matrix is calculated (Figure 2.18 (a)).

For image segmentation applications, where a distinction must be made between each pixel in an image (maybe we want to know which pixels in the image belong to the giraffe and which are background) as shown in Figure 2.19, the input layer must have the same dimensionality as the output layer. In order to achieve this, typical network architectures use an encoder-decoder type structure where dimensionality is reduced to extract higher order features (encoding) and subsequently expanded via a process called up-sampling to allow for a direct comparison between the input and output layer (decoding). Each pixel of the output layer would correspond to a single array corresponding to the number of pixel classes (maybe

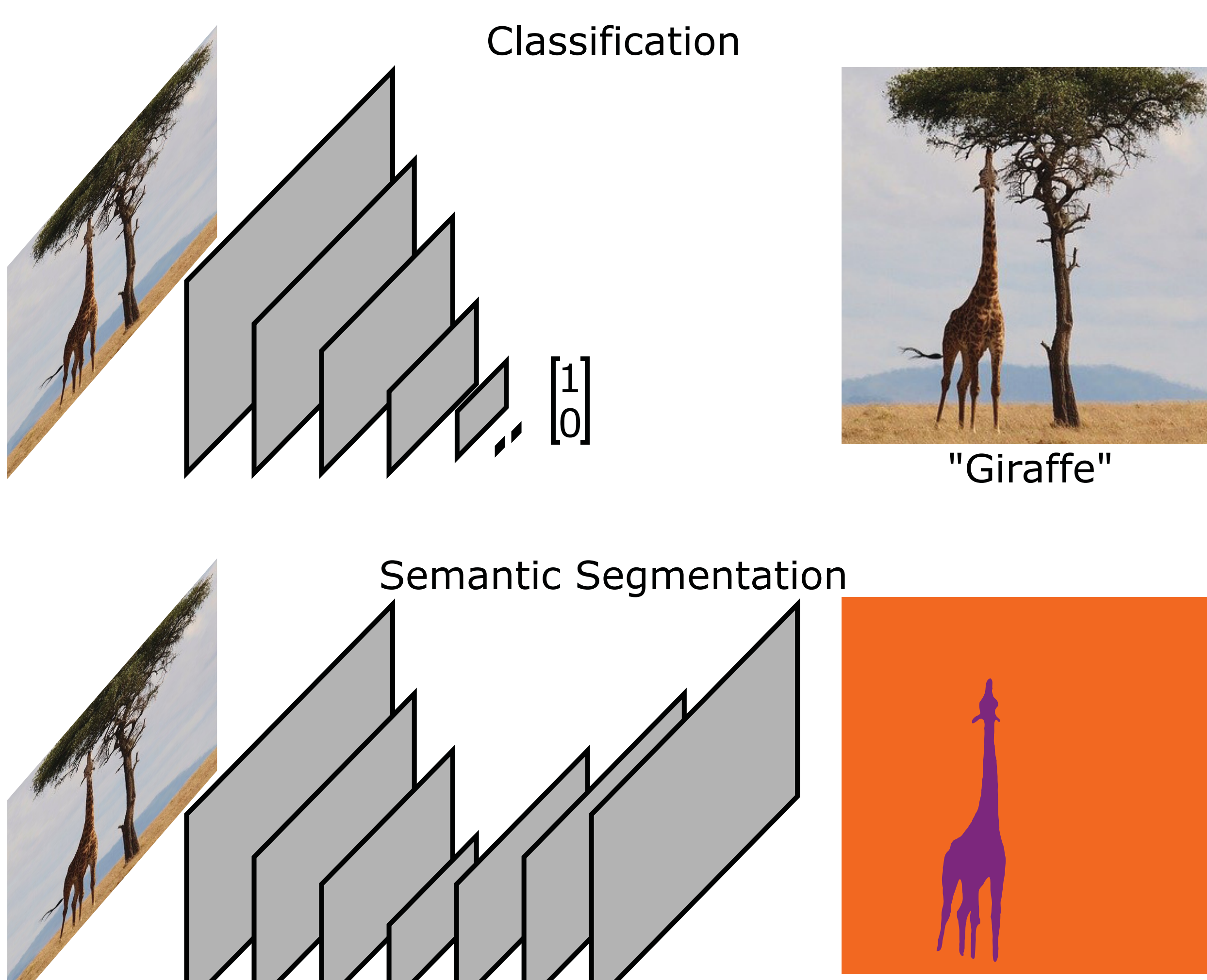

Figure 2.19: **Different image classification schemes.** (a) A typical neural network architecture for image classification where the output is used to determine if an object is present or absent. (b) A more advanced technique known as semantic segmentation where the pixels that make up the image are labelled (giraffe = purple, background = orange).

giraffe, rhino, and background). The process of up-sampling (Figure 2.18 (a)) can also be done in many ways including nearest neighbour sampling where the value in each element is applied to the entire 2x2 area of the next layer, or max unpooling where each value of the 2x2 array is applied to a single node of the next layer corresponding to the location of the maximum element during pooling.

The architecture of the network can be tuned by changing such values as the number of convolutional filters, the size of max pooling filters, the number of downsampled layers,

optimization parameters, etc. These are referred to as hyperparameters. When training a neural network with set hyperparameters it is common to divide the data set into three unique components, training, testing, and validation. The validation set is used to asses and tune the hyperparameters to maximize initial performance with the data set. Once an architecture is set, the network is trained using the training data set. This data set is usually at least 2/3 of the entire data set and used to refine the model parameters such as the filter and bias values. Figure 2.20 shows the training process for two different network configurations. For both models, the loss function for the training data is continually reduced as the network is trained over each epoch (Figure 2.20 (a),(c)). When looking at the testing data, we can see how the network predicts data that it hasn't seen before. The less complicated model 1 reaches a minimum loss function of around 0.23 at epoch 14 (Figure 2.20 (b))) while the more complicated model 2 reaches a minimum loss function of 0.24 at epoch 40. For both models, the loss function is continually improved for the training data emphasizing the importance of calculating the loss function for unseen data. Models which are trained passed the minimum values in the testing data are referred to as "over trained" as they have learned the features of the training set so well that they cannot be applied to data that hasn't been used in training, even if they have similar features. If the network does not perform well enough at the end of training, different architectures, hyperparameters, or data formatting could be explored to improve accuracy.

Unsupervised learning presents the algorithm with unlabelled data allowing it to develop its own classifications of the training data. This method can often run into issues though as the algorithm has no inclination of what features may be important for classification. Going back to our rhino and giraffe example, an unsupervised algorithm may end up classifying the data set based on if the picture was taken at night or during the day regardless of what animal is present. It is better suited for automated feature classification where data sets are either too large or too difficult to label. Just like supervised learning, there are many different ways to perform unsupervised learning but here emphasis will be given to the k-means [203] and mean shift clustering [204].

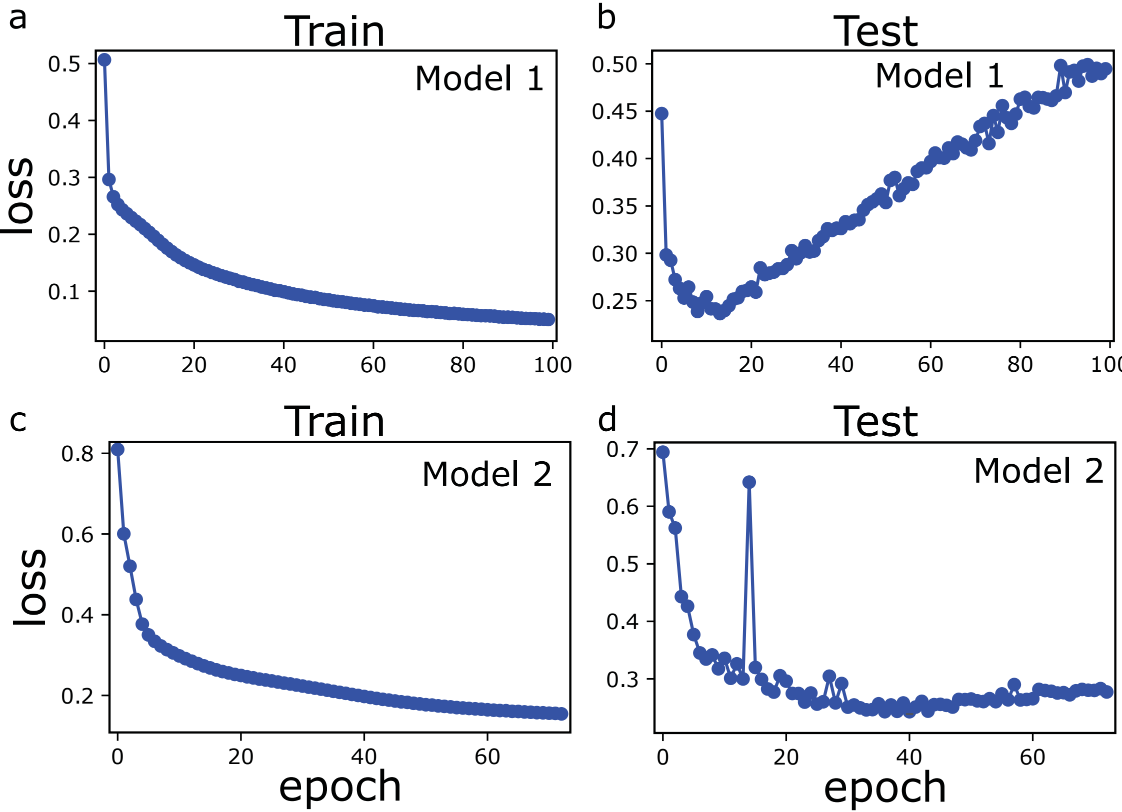

FIGURE 2.20: **Training of different models.** (a),(b) The loss function calculated for the training and testing data using a less complicated model. A minimum loss function of 0.23 was achieved at epoch 14 in (b). (c),(d) The loss function calculated using an over complicated model. A minimum loss function of 0.24 was achieved at epoch 40.

K-means clustering looks to divide a data set into k different groups based on the measured similarities of the data. The k-means clustering algorithm works in three steps; first it randomly assigns k mean values in the feature space. Second, it then assigns the remaining data points to one of the means based on their distance in feature space. Finally, it works to shift the mean value for each such that the cost function

$$Cost = \sum_{j=1}^{N} \left(argmin_i ||x_j - c_i||_2^2 \right) \tag{2.32}$$

is minimized, where x_j represents each point in feature space and c_i is the assigned mean value. This algorithm essentially tries to redistributed k means in a set of data points such that the euclidean distance between the means and their respective data points is reduced. This algorithm can be sped up by taking mini batches of the data set when computing the cost instead of going through the entire data set with minimal loss in performance. It is possible for a user to tune the discernibility between data sets by applying data filters such as convolutional filters, scale invariant feature transforms [205], or histograms of gradients [206].

Mean shift clustering [207] works similarly to the k-means except that k does not need to be defined. Instead, a number of means are initialized and the mean for each data point is determined, then a mean shift is calculated via

$$m(x_i) = \frac{\sum_{x_j \in N(x_i)} K(x_j - x_i) x_j}{\sum_{x_j \in N(x_i)} K(x_j - x_i)} \tag{2.33}$$

where $N(x_i)$ is the neighbourhood of samples within a distance around x_i and $K(x_j - x_i)$ is a distance estimate between the points x_j and the mean point x_i. By shifting each mean via $x_i = m(x_i) - x_i$, the locations of the mean values converge and are grouped together until a set number of discrete means remain. The difference between a k-means and mean shift clustering algorithm is shown in Figure 2.21.

Lastly, reinforcement learning is done by providing the algorithm with experience and either rewarding or punishing it based on the outcomes within that experience [208]. If we consider an STM, we can create an algorithm in which success is defined as "not crashing the tip while scanning", and allow it to control the piezo motors of the scanner and punish it every time the current increases above a threshold. It would take very little time for the algorithm to learn the best way to avoid tip crashing is to withdraw the tip fully removing any risk of ever crashing the tip while scanning. A better question would be to ask the algorithm to "maintain a constant tunneling current of 100 pA while scanning". By assigning a positive reward for scanning while within a certain range of 100 pA and a negative reward while

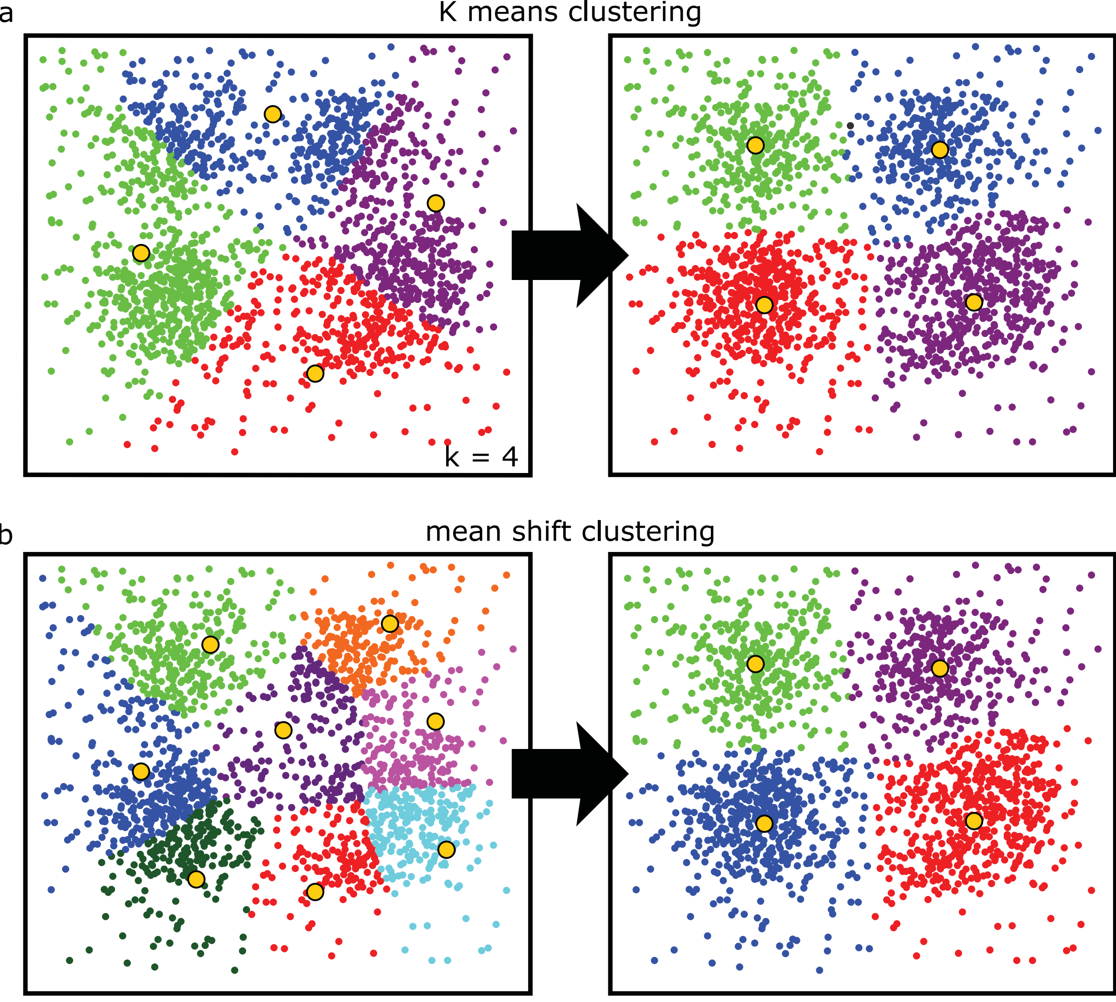

FIGURE 2.21: **Unsupervised clustering.** (a) An example of k-means clustering where a feature space is defined with 4 mean values. As the means are recalculated, data is more correctly assigned to each mean. (b) A simplification of mean shift clustering where the number of means converge until only 4 distinct means remain to group the data.

scanning outside that range, the algorithm would eventually learn to control the scanner in such a way that a constant tunneling current of 100 pA was maintained. This would essentially replace the already satisfactory PI controller, so it is unexpected that such an application would be useful. More useful applications of unsupervised, supervised, and reinforcement learning applied to SPM are discussed in the following section.

2.3.1 Applications to Scanning Probe Microscopy

The applicability of machine learning to scanning microscopy is mainly due to the relative ease in collecting a high volume of high quality images. Images acquired using scanning probe microscopy often include repeatable surface features in either the foreground or background of the image, making it relatively easy for a neural network to learn and extract image features. Additionally, the relative ease in collecting many images of similar quality make it easy to build large amounts of training images for image analysis. One of the first applications of ML to nanoscale images was through work done by Modaress *et al.* [209] where they developed a machine learning algorithm capable of classifying scanning electron microscope images into 10 different classes including nanowires, particles, and powders. Neural networks like these can be used for classification of image databases that come with shared user microscopes.

In addition to image classification, Ziatdinov *et al.* [210] have shown the use of CNNs combined with a Markov random field [211][15] model to classify the states of molecules adsorbed onto a metal surface. By automating the analysis of a sumanene molecule[16] in either an up or down orientation on the Au(111) surface, they are able to model a correlation between the self assembly of the molecules and their rotation and structural orientation on the surface. Such a demonstration shows the utility in coupling machine learning algorithms to enhance the capabilities of extracting image features for physical modelling.

[15] A markov random field is similar to a multilayer perceptron with connecting nodes passing information, except the values of such nodes are modelled through user input.

[16] $C_{21}H_{12}$. This looks like part of a buckyball and can either be in a cup or dome orientation

Additional work done by Ziatdinov *et al.* [212] uses "weakly" supervised machine learning to study the graphene surface imaged with a scanning transmission electron microscope (STEM). This weakly supervised method relies on training a neural network to distinguish between graphene, dopants, and vacancies. By extracting atomic coordinates using the neural network, they are able to distinguish between several distinct varieties of defects that were not present in the initial training set (hence "weakly supervised"). In addition, they were able to use the coordinate extraction to track the movement of dopants within the graphene lattice over time, enabling automated defect manipulation and tracking. Similar work by Maksov *et al.* under the same group has applied similar methods to beam-induced transformations in WS_2 using a STEM. By training a convolutional neural network, they were able to distinguish between ordered and disordered sections of a Mo-doped WS_2 material. They then used a Gaussian Mixing Model [213] [17] to split defects into subclasses based on features extracted using the CNN. By splitting the defects into smaller subclasses and correlating them to unique lattice positions, they are able to trace defects over time as they shift within the lattice from beam induced transformations.

Work done by Rashidi & Wolkow [155] allowed for the automated assessment and reconditioning of a scanning probe tip using Si DBs on the otherwise hydrogen terminated surface. As discussed previously, the ability to pattern DBs on the H-Si surface depends on the atomic sharpness of the tip used. By training a CNN to identify when the tip has a single atom apex vs. a multi-atom apex, the output of the CNN is used to initiate an automated tip shaping suite which increases the tip depth of controlled tip-sample contacts. The quality of the tip is continually assessed until an atomically sharp apex is restored. Similar methods to assessing the tip quality have been done in two works by Gordon *et al.* [193, 214]. The first work demonstrates the use of CNNs in the assessment of the H-Si(100), Au(111), and Cu(111) surfaces. Multiple CNN architectures showed different network efficiencies on each of the surfaces as a result of the varying features between each surface. Instead of just determining

[17] A type of unsupervised clustering similar to a mean-shift algorithm except the data is assumed to be in some gaussian distribution

if the tip was in a single or multi-atom state, this work was able to distinguish between surface contrasts resulting from differing tip states as mentioned in [145]. The second work made significant progress in mimicking a human operator by assessing the quality of a tip as the scan is completed. By using a Long Short term Memory layer [215][18] and assessing individual line scans as an image is acquired, any tip changes are easily detected before the full scan is complete potentially saving minutes for each tip assessment.

As the implementation of machine learning with scanning probe microscopy continues to progress, more advanced methodologies are being realized. Preliminary work by Leinin *et al.* [216] looks at using reinforcement learning (RL) to manipulate molecules on the surface using a SPM tip. PTCDA molecules[19] are selectively removed from the surface through the formation of a tip-molecule bond and a subsequent breaking of any surface-molecule bonds. By allowing the RL algorithm to explore different tip retraction pathways, it was able to learn a path such that the molecule was removed from the surface without incurring any damage to the tip apex. The ability of the RL algorithm to learn its own procedure allows for the exploration of any variations that might not be accounted for in a purely preprogrammed withdrawal procedure.

Finally, work by Krull *et al.* [194] has demonstrated the most successful implementation of a fully automated scanning probe system to date. Named DeepSPM, this system incorporates an algorithmic search for a good sample area, a CNN to assess the quality of images acquired, and a deep reinforcement learning agent to reliably condition the state of the probe. The workflow of the algorithm starts by approaching the tip and moving to an area to scan. Once an image is acquired, it is assessed as either a good image, bad tip, or bad sample. A good image is processed and stored and the tip is moved to the next spot. For a bad tip or sample, the tip is moved to a new spot for probe repair. The RL agent learns from a selection of actions, including a 4 V tip pulse, 1.8 nm tip dip, and a 5 nm tip dip, how

[18] LSTMs incorporate some memory of the previous output in the next input. This allows the algorithm to "remember" previous outputs incorporating some time dependence into data analysis.

[19] $C_{24}H_8O_6$. A dipolar flat molecule with negatively polarized oxygen ends and positively polarized hydrogen edges which usually self aligns perpendicular to adjacent PTCDA molecules on a metal surface

to best restore the tip quality. This process is completely self sufficient, capable of running multi-day acquisition experiments with no user intervention needed.

The work discussed in Chapter 4 relies on the use of a CNN to assess the quality of a hydrogen terminated surface. Defects commonly found on the surface which would prevent DB creation at a desired DB lattice site are avoided, allowing for an automated DB creation suite enabling autonomous DB fabrication.

2.4 Summary

The techniques in Chapter 2 were presented to provide a brief overview needed for the understanding and analysis of results presented in the following chapters. The six different imaging modes are used to develop a comprehensive defect catalogue presented in Chapter 3. The added benefit of combining multiple imaging modes allows for the most comprehensive analysis of defects of the H-Si surface to date, leading to the classification of several new defects. In Chapter 4, this understanding of defects is used to develop a CNN capable of distinguishing between such defects, allowing for fully automated algorithms to identify the most viable location on the surface to pattern a DB device. This CNN is coupled to the previously mentioned tip shaping and DB fabrication suite creating a fully autonomous DB fabrication program. The development of the CNN is further refined through the inclusion of several new defects learned through the creation of the defect catalogue. This enhanced network shows higher functionality as well as more advanced applications. The work done in Chapter 5 utilizes the charge sensing capability of KPFM measurements to observe charge reordering within DB structures. This work demonstrates the utility of using a Si-terminated probe in the detection of surface charges, giving insights into the behaviours of DB structures and subsequently, their viability as device components. The information presented in each of these chapters contributes to the understanding, development, and refinement of DB devices and their fabrication.

Chapter 3

Classification of Atomic Scale Defects of the H-Si(100) Surface using Multiple Imaging Modes

3.1 Introduction

The invention of the STM in 1981 allowed for unprecedented atomic resolution of the surface. Instead of ensemble averaged surface properties offered by diffraction experiments, STM allowed for atomically precise resolution of the surface. With this enhanced resolution, it became clear very quickly that the surface was not as uniform as expected. Jerry Tersoff of IBM, a theorist working with STM [76], noted “Surfaces were nothing like what we had thought. It was kind of scary to see how messy and complicated [they] were.” [217].

Indeed, shortly after the identification of the 7x7 reconstruction on Si(111) [218], the first STM images of the Si(100) surface reported a “relatively large number of defects” [219]. As will be discussed in the coming section, these defects were primarily due to missing or additional silicon atoms relative to a perfect Si(100)-2x1 surface.

The work presented in the following section builds upon the many previous works which aimed to classify various defect types commonly found on the H-Si(100)-2x1 surface. New insights are provided by combining multiple imaging modes of a SPM. As mentioned in Chapter 2, this allows for a combined interpretation of the electronic density of states at various energies, and the atomic positions of atoms within a lattice. In total, this work studies 14 commonly found defects using the 6 different imaging modes introduced in Chapter 2. This work confirms previously made assignments of some common defects, provides alternative classifications of unconfirmed defects, and also characterizes and offers classifications to previously unreported defects. In addition to defect classification, this work shows the first images of an H-Si surface as studied using STHM as well as provides an alternative, potentially more controllable method for contrast enhancement via STHM.

The Supporting Information also presents a theoretical study of the surface using the probe particle model. This model is able to simulate AFM images by calculating the force of interaction of a probe particle using a double Leonard-Jones potential accounting for the probe particle-tip, and probe particle-surface interactions. The inclusion of these simulations provide some confirmations to the defect classifications and also highlight potential deficiencies in both the model and proposed defect structures which will require further theoretical work using more robust models to confirm the defect classifications made [220].

3.2 Atomic defect classification of the H-Si(100) surface through multi-mode scanning probe microscopy

Reproduced in accordance with the Beilstein-Instut copyright and license agreement. [2]

Jeremiah Croshaw[1,2], Thomas Dienel[1,3], Taleana Huff[1,4], and Robert A. Wolkow*[1,2,4]

[1] Department of Physics, University of Alberta, Edmonton, Alberta, T6G 2J1, Canada

[2] Quantum Silicon Inc, Edmonton, Alberta, T6G 2M9, Canada

[3] Department of Material Science and Engineering, Cornell University, Ithica NY 14853, USA

[4] Nanotechnology Research Centre, National Research Council Canada, Edmonton, Alberta, T6G 2M9, Canada

* corresponding author.

Keywords: atomic force microscopy; hydrogen-terminated silicon; scanning tunneling microscopy; scanning tunneling microscopy; surface metrology

Supplementary material for this article is available in section 3.3

3.2.1 Abstract

The combination of scanning tunnelling microscopy (STM) and non-contact atomic force microscopy (nc-AFM) allows enhanced extraction and correlation of properties not readily available via a single imaging mode. We demonstrate this through the characterization and classification of several commonly found defects of the hydrogen-terminated silicon (100)-2x1 surface (H-Si(100)-2x1) by using six unique imaging modes. The H-Si surface was chosen as it provides a promising platform for the development of atom scale devices, with recent work showing their creation through precise desorption or placement of surface hydrogen atoms. While samples with relatively large areas of the H-Si surface are routinely created using an *in situ* methodology, surface defects are inevitably formed reducing the area available for patterning. By probing the surface using the different interactivity afforded by either hydrogen- or silicon-terminated tips, we are able to extract new insights regarding the atomic and electronic structure of these defects. This allows for the confirmation of literature assignments of several commonly found defects, as well as proposed classifications of previously unreported and unassigned defects. By combining insights from multiple imaging modes, better understanding of their successes and shortcomings in identifying defect structures and origins is achieved. With this, we take the first steps toward enabling the creation of superior H-Si

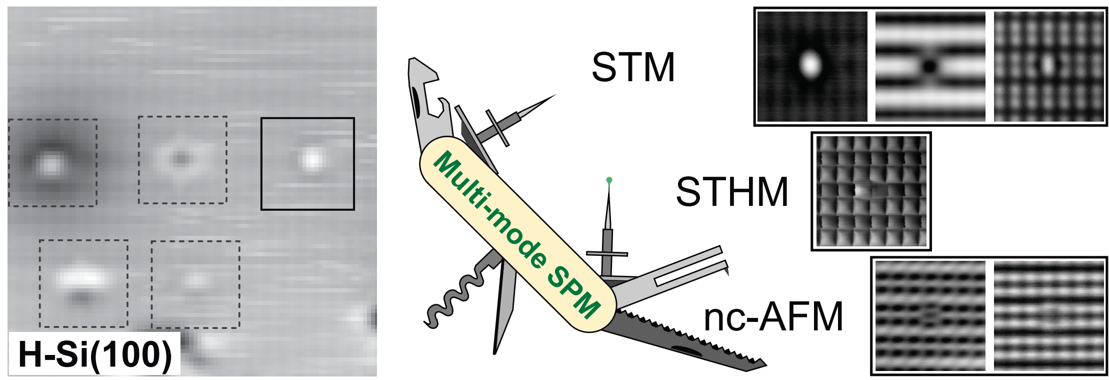

FIGURE 3.1: **Abstract image -** Atomic defect classification of the H-Si(100) surface through multi-mode scanning probe microscopy

surfaces through an improved understanding of surface defects, ultimately leading to more consistent and reliable fabrication of atom scale devices.

3.2.2 Introduction

Novel approaches to advance integrated circuitry beyond CMOS have focused on atom scale structures and their reliable fabrication [221]. Hydrogen-terminated silicon (H-Si) surfaces are one such versatile platform for the patterning and operation of atom scale devices including qubits [54, 222] and single electron transistors [48, 53] made from atomically precise implanted donor atoms near the H-Si surface, and logic structures using fabricated silicon dangling bonds [43, 45, 46]. In many cases the structures' functional elements are comprised of a few or even single atoms. At such dimensions, atomic scale defects of the surface and in the shallow subsurface region can have a significant impact on device patternability and operation [6]. In order to develop suitable means to accommodate defects, whether it be by optimizing sample preparation, quantifying how defects affect device operation [6], or by using convolutional neural networks to autonomously identify defects [1, 193, 223], a comprehensive understanding of the many varieties of defects is needed.

Native silicon atoms at the unreconstructed (unterminated) (100) surface would, by argument of the crystal geometry, extend two unsatisfied bonds into vacuum. To minimize the surface energy, each silicon atom bonds with a neighbouring Si atom to create a dimer, thus reducing the number of dangling bonds (DBs) by half [224]. Rows consisting of many of these dimers are formed, which run parallel along the surface. The study of Si(100) surface defects was one of the first applications of scanning probe microscopy [225]. The three observed species were identified as a missing silicon dimer, a pair of missing silicon dimers, and a missing pair of Si atoms on the same side of two neighbouring dimers. Subsequently, the latter had been reassigned as an H, OH pair originating from dissociative attachment of a residual water molecule in the vacuum system [226–228]. Further insights became available by non-contact atomic force microscopy (nc-AFM), separating the electronic and structural behaviour of the Si(100) surface [135].

The addition of hydrogen to surface silicon atoms saturates all available bonds [229] and three surface reconstructions are commonly observed. The 2x1 phase - frequently used in hydrogen lithography, and can be prepared in situ resulting in large,defect free areas [230] - has each surface Si atom in a dimer bonded to one hydrogen atom (Figure 3.2(a),(b)). The 1x1 phase is characterized by the absence of dimer bonds, with each surface Si atom instead saturated by 2 hydrogen atoms, forming silicon dihydrides (H_2-Si). The 3x1 phase is a combination of the previous two, consisting of alternating 2x1 dimers and 1x1 dihydrides [231, 232]. With continued study, it became apparent that the complexity of possible surface reconstructions and surface defects extended well beyond those initially observed. Here, we provide a comprehensive overview of the H-terminated Si(100)-2x1 surface, its structural features, and defects. Six different scanning probe imaging modes are performed using both STM and nc-AFM. By combining the accessible information with probe particle simulations [233, 234] (presented in Supporting Information) of the expected structural geometry (see Methods), we are able to confirm the atomic structure of several commonly reported defects, as well as to classify previously unknown defects. The latter includes a point defect that can be found decorated with a single H-atom, rendering the otherwise neutral structure

negatively charged. We demonstrate the tip-induced removal of the weakly bound H atom, leaving the site neutral. While we present an extensive experimental analysis supplemented with simple simulations of common surface defects on H-terminated silicon, we anticipate that the provided assignments will foster further investigation with more robust theoretical frameworks such as by density functional theory.

3.2.3 Results and Discussion

SPM imaging modes

The variability observed in differing scanning probe imaging modes originates from the applied feedback mode, different tunnelling parameters, or the functionalization of the probe tip. Figure 3.2 showcases the imaging modes employed in this work as applied to the defect-free H-Si(100)-2x1 surface (see Methods for details about the sample preparation). In the well known STM topographies probing empty and filled states in Figure 3.2 (c) and 3.2 (d), respectively, the dimer rows can readily be seen running horizontally across the image (constant current imaging [50 pA], sample bias as indicated in the lower left of each panel). Recent work has reported that tip functionalization affects the contrast sharpness and apparent atomic positions in STM images of the H-Si(100) surface [140, 145]. Additional examples of this effect are displayed in Figure 3.7.

Constant height STM images can provide further insights, as shown in Figure 1(e), probing the onset of the conduction band and donor band of our crystal (sample bias: +0.3 V) [6, 135, 235]. Individual atoms within each dimer are clearly visible, with minimal conductance occurring directly through the bulk states (requiring a reduction in tip-sample separation). This imaging mode is useful for cases where excessive bulk current could mask more subtle features. For all constant height modes, the reported approach of the tip is relative to a constant current tunnelling position above an H-Si atom with a sample bias of -1.8 V and a tunnelling current of 50 pA (as discussed in Methods). The heights for each mode are chosen

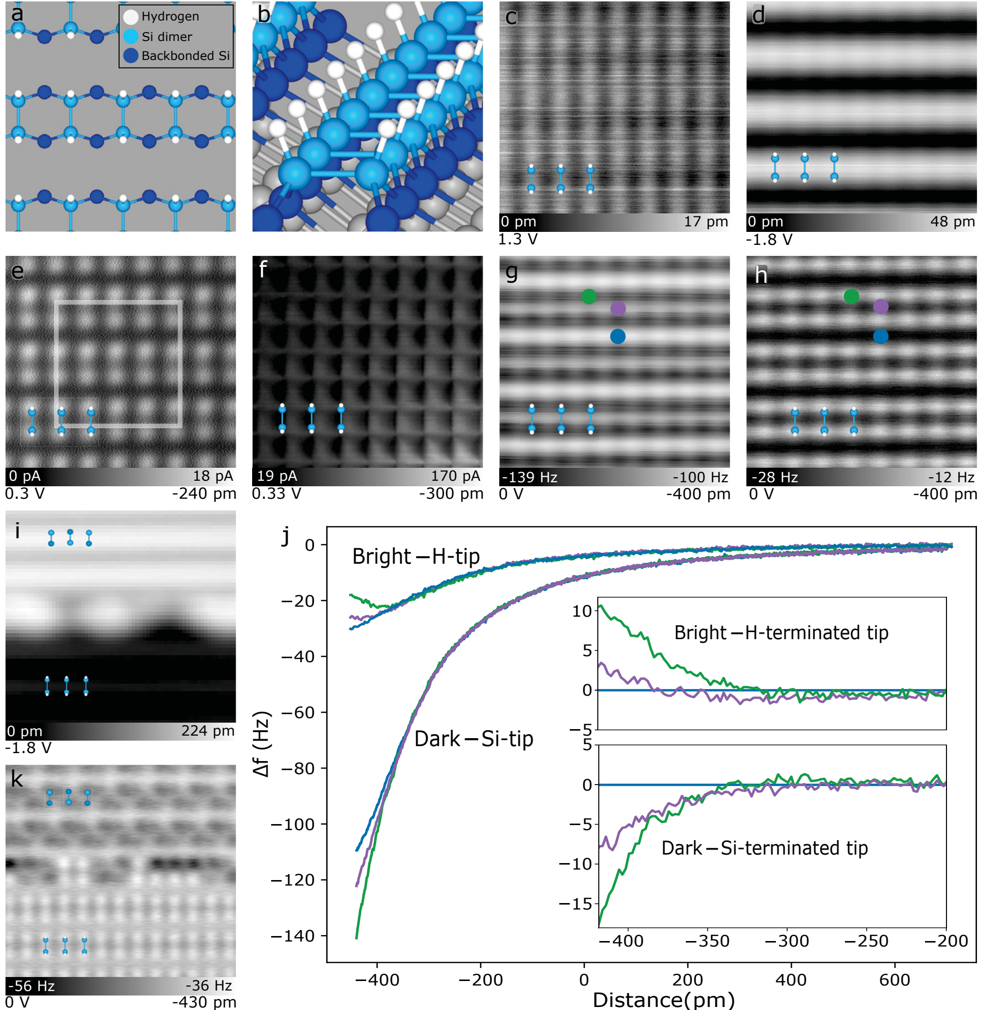

FIGURE 3.2: **Surface of H-terminated Si(100)-2x1 in different imaging modes.** (a,b) Top and isometric projection of a structural model of the H-terminated Si(100)-2x1 surface. The size of the area shown in (a) is outlined in (e). (c,d) Constant current (I = 50 pA) STM topography probing empty and filled states of the surface (bias voltages indicated in the lower left of each panel). (e) Constant height STM image with a fixed bias and height.(f) Scanning tunnelling hydrogen microscopy image of the surface. (g) nc-AFM frequency shift map using a Si-functionalized tip that displays the hydrogen atoms in "dark contrast". (h) nc-AFM frequency shift map measured with a H-functionalized tip showing hydrogen atoms in "bright contrast". Images (c-h) are all 3.2x3.2 nm^2, the indicated height offset (Δz at the bottom right of relevant panels) is initialized referencing a STM tunnelling setpoint of I = 50 pA and V = -1.8 V over a H-Si surface atom. (i) Constant current STM topography of a half hydrogen-terminated (bottom) half unterminated silicon (top) surface (5x5 nm^2, V = -1.8 V, I = 50 pA). (j) Position-dependent frequency shift spectroscopy $\Delta f(z)$ in bright and dark nc-AFM modes (positions indicated in (g) and (h)), highlighting the quantitative differences in tip reactivity for different apex terminations. The insets show the calculated difference spectra in reference to the spectra taken between the dimer rows (blue position marker). (k) AFM image of the same area shown in (i) using a H-functionalized, bright contrast tip. The bottom part shows the characteristic bright contrast features of H-Si, while the unterminated Si portion shows the inverted contrast (atoms appear dark) of alternatingly buckled, unterminated dimers with a slight double tip artifact

to optimize the desired surface contrast (as shown in Figure 3.8) while avoiding unwanted tip-sample contact.

Figure 3.2 (f) shows a variation of constant height STM where the tip apex is functionalized with a flexible hydrogen atom. The use of a flexible species at the apex of a metallic tip to provide enhanced contrast was first reported using CO-functionalized AFM tips to image the molecular structure of pentacene [236]. Other functionalizations of AFM tips have been explored including Cu-O tips [237, 238] and Xe tips [239, 240]. The use of H_2 [241, 242] and D_2 [136] provided the first successful demonstration of the enhanced imaging contrast by scanning tunnelling hydrogen microscopy (STHM) [136, 137]. Rather than direct tip functionalization as done in nc-AFM, STHM in these original studies was achieved by leaking in a background of molecular hydrogen ($\sim 1 \times 10^{-9}$ Torr) until an H_2 molecule became trapped in the tip-sample junction. Here, we achieve STHM-like resolution by directly functionalizing the tip apex with a single hydrogen atom, picked up from the H-Si surface through the application of a voltage pulse, as reported in prior works [4, 145, 177]. Our ability to achieve STHM resolution using an H-functionalized tip aligns with recent STHM theory suggesting that the H_2 molecule dissociates on the apex, resulting in a singly H-functionalized tip [138]. In Figure 3.2 (f), the use of STHM displays the surface as a series of squares with each of the square corners correlating to a H-Si atom. The image's slight asymmetry can be attributed to a corresponding asymmetry in either the shape of the tip apex, or the attachment location of the functionalizing H atom. To highlight how differing asymmetries can affect STHM image appearance, Figure 3.9 shows a variety of images of the H-Si(100)-2x1 surface acquired with different H-functionalized tips.

A true measurement of the force interaction between the tip and sample can be visualized with frequency-shift maps generated by non-contact AFM [157]. In our work, we observe two different imaging modes that we denote as dark (Figure 3.2 (g)) and bright contrast AFM (Figure 3.2 (h)), based on the apparent contrast of the hydrogen atoms with the surrounding surface. Previous studies have identified the two contrasts as resulting from differing chemical reactivity of different functionalizing apex atoms [157], where the dark contrast image

corresponds to a Si-terminated tip [146–148] and the bright contrast image corresponds to an H-terminated tip [146, 147]. The transition between the two modes through the loss of H-functionalization of the tip (by capping a surface dangling bond [147]) can be seen in Figure 3.10. This differing chemical reactivity is seen in Figure 3.2 (j), where the height-dependent frequency shift spectra ($\Delta f(z)$) taken above select positions on the surface (see Figure 3.2 (g),(h) for positions), shows significantly different character for each tip termination. To highlight the termination dependent reactivity, frequency shift difference spectra [243] were calculated for both terminations (shown in the insets in Figure 3.2j). The spectra taken above an H-Si atom (green marker) and above a dimer bond (purple marker) were referenced to the "between dimer" position (blue marker). As evidenced by the differing inflection between the functionalization types, a stronger repulsive component is observed for the more inert H-functionalized tip probing the H-atom (bright contrast), while the more reactive Si-terminated tip (dark contrast) leads to a stronger attractive interaction (more negative Δf) at the same site [140, 146–150]. Simulations of the STHM, H-apex AFM, and Si-apex AFM images of the defect free H-Si(100)-2x1 surface using the probe particle model [233, 234] can be found in Figures 3.11, 3.12, and 3.13, respectively.

Similar to how a change in tip functionalization can change the observed contrast (Figure 3.10), a fixed tip functionalization can exhibit inverting contrast if features of different chemical reactivity are scanned. Figure 3.2i,k shows the surface where the terminating hydrogen atoms were selectively desorbed from the upper half of the shown area. Examining the filled states STM image in Figure 3.2i, the bare silicon appears brighter when compared to its H-terminated counterpart [140]. Scanning the same area in AFM with an H-functionalized tip in Figure 3.2k reveals that the H-covered half (bottom) shows the rows as expected in bright contrast, but an inverted dark contrast for the unterminated portion (top). This demonstrates that the dark contrast is a result of the high reactivity between two different species - silicon and hydrogen - interacting with each other in the tip-sample junction, regardless of which species functionalizes the tip. The alternating asymmetry of the unterminated dimers

along the dimer row is resultant from the buckling known to occur for the reconstructed bare surface [121, 244–246], as well as a slight double tip artifact.

Defect catalogue

Combining all six imaging modes allows for an in-depth characterization of the most common surface features and their local environments, as shown in Figure 3.2, arranged by their overall appearances. While not an exhaustive list, it features defects routinely seen when the surface is prepared using the procedure outlined in the Methods section. To categorize the defects one could focus on functional aspects (charged vs neutral features) [6], or structural aspects (including missing or additional atoms). Here, we categorize the defects on structural commonalities, based on the number of affected atoms. First, we list features that involve only one side of a dimer. These include a dangling bond (DB) of a surface Si atom (Figure 3.3 (a)), a subsurface vacancy (Figure 3.3 (b)), a SiH_3 group (Figure 3.3 (i)), and an unidentified surface point defect (Figure 3.3 (k)). Second, defects affecting a whole dimer which include two missing H atoms creating a bare dimer (net neutral, shown in [84, 247]), two additional H atoms on a dimer to create a dihydride pair (Figure 3.3 (d)), a single additional H atom on one side of a dimer to form a single dihydride which, in turn, requires the neighbouring Si atom to be missing (Figure 3.3 (e)), the removal of the whole dimer (two missing Si atoms) accommodated by either H-termination (Figure 3.3 (f)) or dimer formation in the second layer (Figure 3.3 (g)). Alternatively, the dimer bond could be replaced by either a SiH_2 group (Figure 3.3 (j)) or an oxygen atom (siloxane bridge, Figure 3.3 (h)), presenting as row-centred features. Remaining surface features are often a combination of two or more smaller structures, with one example being the often seen 3x1 reconstruction which is a combination of dimer rows and dihydride atoms (Figure 3.3 (c)).

We start with a discussion of silicon DBs, which are well studied unterminated silicon atoms [159, 166, 173]. In STM, the centre of a DB is imaged as a bright protrusion due to its conductive orbital which extends into vacuum. DBs have been observed to act like quantum dots and have discretized charge states in the band gap of the material [46]. Due to the degenerate n-type doping of our substrate (see Methods) [46, 173], DBs are natively negatively

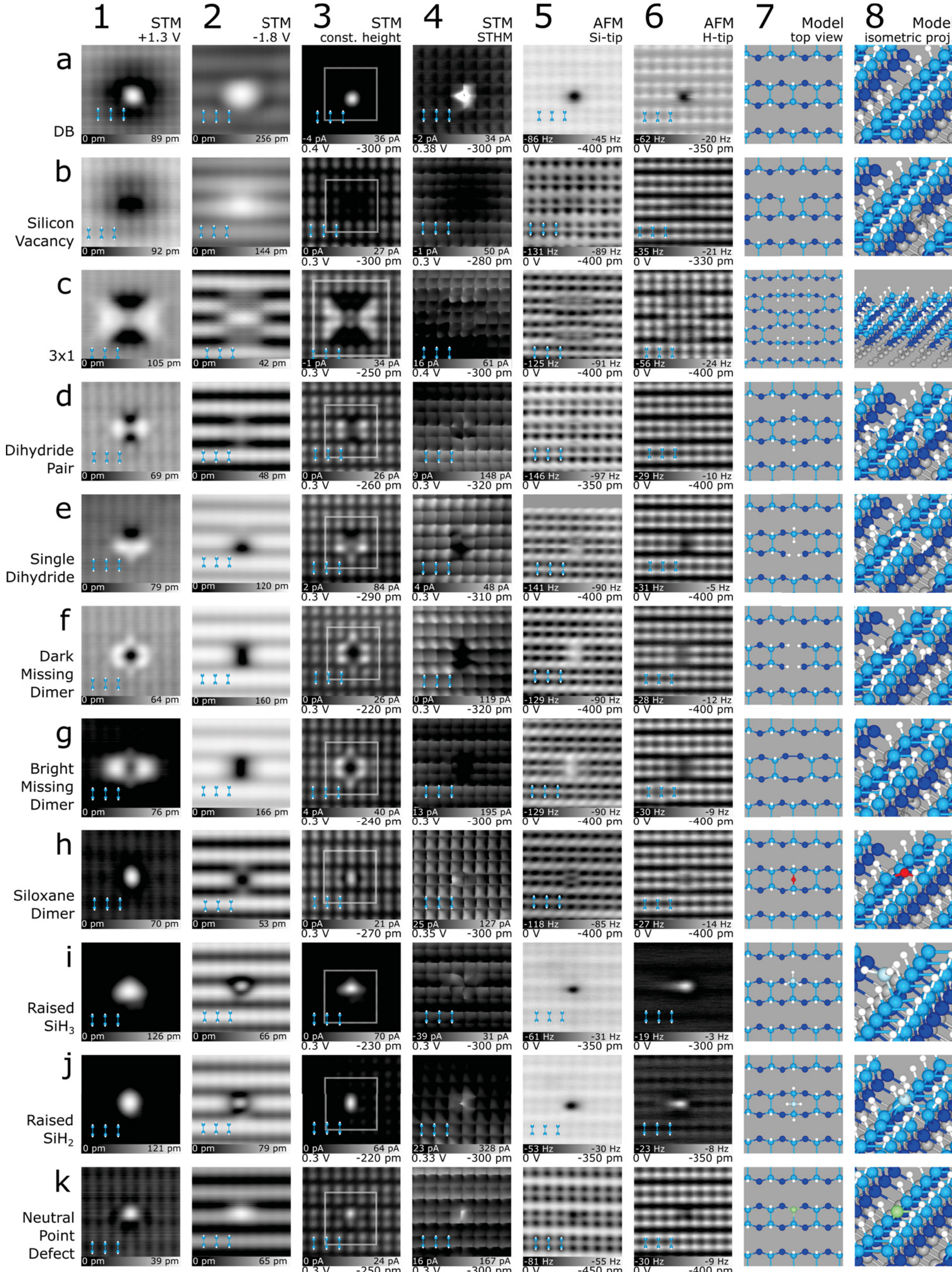

FIGURE 3.3: **Common features of the H-Si(100)-2x1 surface imaged using the indicated STM and nc-AFM imaging modes.** The identity of the features is listed on the left of the rows, with a ball and stick model of the dimer structure shown as an overlay in each scan (lower left corners, 0.77 nm width). The area of the structural models in column 7 is indicated by the grey box surrounding the defect in column 3. For the constant-height analysis types in columns 3-6, the applied constant bias value and relative tip-sample height are given in the lower left and lower right, respectively, of each frame. Colours in the ball and stick models are: H - white, Si dimers - royal blue, back-bonded Si - dark blue, O - red, raised Si - sky blue, and unknown species - green. Images are 3.2 nm x 3.2 nm.

charged when imaging the empty states of the surface. This localized negative charge leads to band bending around the DB location at these biases, giving the DB a dark "halo" around the bright orbital protrusion (Figure 3.3 (a)-1) [166, 173]. Filled states imaging (Figure 3.3 (a)-2) lacks the charge-induced band bending around the DB due to competing electron emptying and filling rates, rendering the DB neutral on average [166, 248]. The constant height STM and STHM images in Figure 3.3 (a)-3 and Figure 3.3 (a)-4 also reveal the central protrusion. The STHM image showed an extremely localized current signal over the DB and has been artificially saturated from a 2.4 nA range to better show the H-Si atoms of the surface relative to the DB. A full-scale image of the DB is shown in Figure 3.14.

Finally, AFM analysis in Figure 3.3 (a)-5 and Figure 3.3 (a)-6 presents the DB as a large negative frequency shift, with both tip terminations seeing a strong attractive interaction (further details of all Si-tip based images in column 5 are discussed below with Figure 3.4). Since the Si-functionalized tip is predicted to be neutral [139, 143], the dominant attractive contribution above the DB with both tip functionalizations is due to a covalent interaction between the surface DB and the H or Si atom of the tip [146, 149, 150]. Since the surface DB is negatively charged at 0 V, an additional attractive interaction due to the polarization of the tip is also expected to contribute to the strength of the attractive interaction [150]. To highlight the attractive contributions, Figure 3.2 (k) from earlier can be referenced; the unterminated portion consists of many neutral bare dimers displaying as lighter in contrast than their single DB counterparts demonstrating the Coulombic contributions (see the 4 dark DBs present at the edge between the bare and H-terminated surface) while both the bare dimer and single DB have an additional covalent interaction with the tip that is not seen above H-Si atoms. Complementary modelling of the DB defect and all subsequent defects of Figure 3.3 as imaged with STHM, H-apex AFM, and Si-apex AFM has been done using the probe particle model [233, 234] and is discussed in Section 3.3, with Figures 3.11, 3.12, and 3.13.

Figure 3.3 (b) shows a suspected silicon vacancy (discussed in more detail below in Figure 3.5), previously referred to as a type 2 (T2) defect in the literature [249]. Prior works

speculated a variety of origins for this defect, including a negatively charged As dopant [249] , Si-vacancy hydrogen complexes [6], and B dopants [250, 251]. Crystal vacancies have previously been identified in other materials using scanning probe microscopy including Ga vacancies in GaAs [252], As vacancies in GaAs [253], and P vacancies in InP(110) [254]. Due to the common nature of these defects in other semiconductors and the similarity in imaging character, we thus attribute this defect to most likely be a Si vacancy. Further discussion of our assignment and additional evidence is given later as part of Figure 3.5. Empty states STM in Figure 3.3 (b)-1 shows that the vacancy exists as a negatively charged species as evidenced by the reduction in brightness around the defect from charge-induced band bending. Unlike the DB, the vacancy's charge state is observed to remain fixed even at filled states STM probing, with the charge-induced band bending enhancing the conductivity locally around its location, as seen in Figure 3.3 (b)-2. In the constant-height STM frame in Figure 3.3 (b)-3 a reduction of current due to the charge-induced band bending is again observed, along with a distortion of the density of states of the surface H-Si atoms above the sub-surface vacancy. 3.3 (b)-5 and 3.3 (b)-6 show similar distortions in the AFM frequency shift signal around the two H-Si atoms closest to the vacancy, suggesting a modification in their position or electronic character.

Next we discuss the raised SiH_3 or silyl group (Figure 3.3 (i)) [255, 256]. This group exists where a silicon adatom replaces the H atom on one side of a dimer, achieving stability by saturation of the remaining free bonds with H. Larger groups of similar raised Si groups have been observed to bond and form islands [232, 257]. The triangular shape of the defect as seen in the STM images (Figure 3.3 (i)-1,2,3) highlights the preferred tetrahedral bonding orientation of the saturating hydrogens of the Si, with the fourth bond affixing it to the side of the dimer beneath. The characteristic dark border in Figure 3.3 (i)-1 and enhanced brightness in Figure 3.3 (i)-2 are features commonly observed in raised Si clusters of various sizes as discussed with Figure 3.15.

The raised nature of the silyl group has implications for all the performed constant-height analysis; in constant height STM (Figure 3.3 (i)-3) it dominates the current as it is closer

to the tip, in STHM (Figure 3.3 (i)-4) it leads to extended distortions due to the group's high flexibility (only one bond affixing it to the surface), and finally it gives rise to stronger frequency shifts in nc-AFM (Figure 3.3 (i)-5,6), again due to its closer proximity to the tip. The absence of the anticipated hydrogen splitting features of the SiH_3 group is likely due to the added flexibility of the defect itself. Unfortunately, such an effect cannot be reproduced with the rigid structure used in the probe particle model as discussed with Figures 3.11, 3.12, and 3.13 and requires further theoretical verification.

Figure 3.3 (k) shows a previously unreported neutral point defect. Experiments presented later as part of Figure 3.6, Figures 3.22, and 3.23 show that this defect initially exists in a negatively charged, H-decorated state. It transitions to the neutral variety presented here by removal of the decorating hydrogen with the probe tip as the defect is scanned. This tip-induced H liberation occurs easily, rendering it difficult to obtain a full set of images of the H-decorated species. The neutral variation exists very close to the surface both spatially and electronically, as indicated by the height scales in the constant current STM images in Figure 3.3 (k)-1,2. In the constant height STM image of Figure 3.3(k)-3, it shows only a slight increase in conductivity localized to a single atomic site, suggesting that the Si atom on one side of the dimer is perhaps replaced by this point defect. The AFM images of Figure 3.3 (k)-5,6 confirm this localized nature, with the defect appearing as a slightly darker circular feature of enhanced reactivity. In addition to the absence of any charge-induced band bending surrounding the neutral point defect in empty states imaging, the defect was also shown to have no effect on the contact potential difference of the surface as measured with KPFM (Figure 1 of [6]).

We now move to a discussion of defects that affect a whole dimer, starting with dihydride pairs (Figure 3.3 (d)) and single dihydrides (Figure 3.3 (e)). Instead of a silicon bonding with its neighbouring Si atom to create a dimer, it can be saturated with 2 H atoms to create a dihydride. This leaves the second Si atom of the dimer to also bond with 2 H atoms (resulting in a pair of dihydrides (Figure 3.3 (d))) [231, 258–260] or be absent (resulting in the single dihydride of Figure 3.3(e)). The concentration of dihydrides can be controlled by

lowering the annealing temperature during sample preparation [229, 261]. While the two varieties of dihydride look unique overall in STM empty states topography (Figure 3.3 (d)-1 and Figure 3.3 (e)-1), the side of the pair that the dihydride unit(s) appear on consistently presents as a dark depression. A reversed trend is seen in filled states imaging (Figure 3.3 (d)-2 and Figure 3.3 (e)-2), with the dihydride side(s) diffusely bright. In constant height STM imaging (Figure 3.3 (d)-3 and Figure 3.3 (e)-3), dihydride sites image as areas of reduced current, with neighbouring dimers showing an enhanced current [255]. The STHM image of Figure 3.3 (e)-4 provides an interesting example of STHM's utility, allowing for a direct comparison between the dihydride and a missing atom. At the dihydride site (top of row) we observe a significant deviation from the square pattern, suggesting that additional atoms are present. The missing atom portion of Figure 3.3 (e)-4 (bottom of row) conversely shows darkening and an absence of the expected right-angled intersections that make up the corners of the squares, suggesting a missing feature. Finally, dihydrides provide a good example of the benefit of different AFM imaging contrasts. Examining the dark contrast AFM images based on Si-terminated tips in Figure 3.3 (d)-5 and Figure 3.3 (e)-5, the dihydride(s) possess a dark splitting feature, corresponding to the presence of the two H atoms. The difference in contrast of the splitting feature between the two dihydride variations is believed to originate from a tilting of the hydrogen atoms in the dihydride pair relative to the surface plane and will be discussed in more detail with Figure 3.4. Contrarily, the splitting of the dihydride site is not readily apparent in the H-functionalized AFM images (Figure 3.3 (d)-6 and Figure 3.3 (e)-6), presumably due to the flexibility of the H-sensitized tip or its lower reactivity. The dihydride pair in Figure 3.3 (d)-6 becomes almost indistinguishable from the background and the missing silicon site as part of the single-dihydride in Figure 3.3 (e)-6, however, does show up as an area of reduced frequency shift.

Next, we discuss two variations of missing dimer defects denoted as dark missing dimer (Figure 3.3 (f)) and bright missing dimer (Figure 3.3 (g)) [225, 262, 263]. These missing dimer defects appear almost identical for most analyses done, except when comparing the STM empty state images in Figure 3.3 (f)-1 (dark) and Figure 3.3 (g)-1 (bright). To support

that these two defects are unique and not the consequence of a tip change, the data were taken sequentially while continuously monitoring for tip changes (except STHM), ensuring identical apex character. The two varieties originate from different reconstructions of the exposed next-layer silicon atoms, similar to what was found on the unterminated surface [264]. The formation of two dimer bonds - orthogonal compared to the top layer dimers (model in Figure 3.3 (g)-7,8) - corresponds to the bright variation (Figure 3.3(g)), and H-termination of all exposed sites in the second layer (model in Figure 3.3 (f)-7,8) leads to the dark variation (Figure 3.3 (f)). The latter has been reported to cause less lattice strain [265], matching our observation of less distortions in the STHM and nc-AFM images near the missing dimer (Figure 3.3 (f)-4,5,6 compared to Figure 3.3 (g)-4,5,6 and shown in Figure 3.4). The single dihydride defect of Figure 3.3(e) has also been observed to show bright and dark variations surrounding the missing Si atom shown in Figure 3.16. Figure 3.3 (c) explores the 3x1 reconstruction of H-Si [230, 266, 267]; a structure composed of a combination of H-terminated dimers and dihydrides. Instead of two parallel dimer rows as in the normal surface reconstruction, there exists only a central dimer row of variable length (here we show one that is 3 dimers wide), with the remaining unpaired silicon atoms fully saturated as dihydrides (model in Figure 3.3 (c)-7,8). STM imaging in Figure 3.3 (c)-1 and Figure 3.3 (c)-3 show an enhancement in conductivity at dimers neighbouring the reconstruction and a reduction above the H_2Si atoms. Figure 3.3 (c)-2 shows a dimer row that has been formed between two of the regular dimer rows, with Figure 3.3 (c)-3 also highlighting this realignment. The dihydrides in the 3x1 reconstruction show similar features to the single and paired dihydrides discussed earlier, including the distortions in the STHM image from the presence of H_2Si (Figure 3.3 (c)-4) and the split-appearance of the two hydrogens in the Si-tip AFM scan (Figure 3.3 (c)-5). A direct comparison of the differences observed in nc-AFM using a Si-tip (dark mode imaging), including the assignment of individual H atoms at the dihydride sites, is given later in Figure 3.4.

Defects that we observe to be centred within a dimer manifest themselves through the insertion of additional atoms between the dimer bond. We show a SiH_2 group (Figure 3.3

(j)) and an oxygen atom (Figure 3.3 (h)) in such a position. Starting with the SiH_2 group, it represents a silicon adatom in the bridge position between two top layer silicon atoms (model in Figure 3.3 (j)-7,8). It can be compared to the earlier discussed SiH_3 group, with both groups showing similar image contrast in STM topography (compare Figure 3.3 (i)-1,2,3 with Figure 3.3 (j)-1,2,3 and Figure 3.15). Their distinct location with respect to the dimer, however, is easily discerned throughout all analysis types in Figure 3.3 (i),(j). In Si-tip AFM images (Figure 3.3 (i)-5 and Figure 3.3 (j)-5), the chemically reactive silicon tip strongly interacts with both defects. Conversely, images with H-functionalized AFM in Figure 3.3(i)-6 and Figure 3.3(j)-6 shows a less reactive character, with the inert tip probing inert hydrogen-saturated groups. At close defect-tip separation they should mutually repel each other resulting in a less negative frequency shift over the group location, as shown. Again, AFM does not allow one to discern among individual hydrogen atoms due to the assumed flexible nature of the raised groups, creating a blurred appearance in AFM imaging as the group is pushed during the raster scan.

The siloxane dimer of Figure 3.3 (h), previously denoted in the literature as a split dimer [268, 269] and also incorrectly identified as a dihydride [222, 270], is thought to be an oxygen bonded between the two Si atoms of a dimer. STM imaging reveals a localized defect with only subtle impact on neighbouring dimers (Figure 3.3 (h)-1,2,3). STHM in Figure 3.3 (h)-4 shows slight variation from the regular box-like appearance of the 2x1 dimer, with the positions of the atoms in the oxygen-bridged dimer further apart and a central bright feature present. This agrees with the Si-tip AFM data in Figure 3.3 (h)-5, showing that the "dimer" indeed contains a third atom in the centre. In bright contrast AFM, the attractive interaction between the H-tip and the oxygen's non-bonding electron pair leads to a slight depression in the centre, with the dimer's H atoms "pushed out" (Figure 3.3 (h)-6). A defect of similar appearance was reported in a prior work exploring chlorine-terminated silicon [271] which was linked to water contamination in the vacuum chamber (observed as H and OH bonded to the unterminated surface [226–228]). A mild annealing followed by halogen-termination allowed the oxygen to enter into the dimer, creating an Si-O-Si bond [272]. The authors

commented that they expect this feature to also be present on hydrogen-terminated silicon, which we support here with our analysis.

This family of defects explored in Figure 3.3 underlines the importance of combining several modes of SPM imaging to differentiate among structures that might otherwise be assumed equivalent. Each imaging mode highlights different defect features so that when combined, a greater understanding of the defect is achieved. In general, however, we found AFM with Si-terminated tips to often be the most discriminating. It consistently demonstrates the highest spatial resolution, presumably due to the Si-terminated apex's greater chemical reactivity and reduced apex flexibility. Thus, we employ Si-tip based AFM imaging to further examine select defects.

Details of nc-AFM using silicon-terminated tips

In Figure 3.4, we compare AFM line profiles taken across the defect of interest (blue) and a corresponding defect-free region (grey) with a simple theoretical structure optimized by molecular dynamics calculations (see Methods for parameters). A preliminary comparison of Figure 3.4 with the simulated line profiles is shown in Figure 3.17. We start by comparing dihydride-based defects. Figure 3.4 (a) shows a Si tip AFM image of a 3x1 reconstructed region, with the locations of the two comparative line profiles marked. Figure 3.4 (b) plots the extracted cross-sections (averaged over the thickness of the lines), which are matched to the proposed structure at the bottom of the panel. This analysis highlights the dimer row that is out of phase with the surrounding dimers and the earlier discussed splitting feature observed over the two dihydride-hosting atoms. Similarly, a single dihydride adjacent to a missing atom is displayed in Figure 3.4 (c),(d), with the dihydride again showing a splitting feature. The slight depression at the location of the missing Si atom (blue curve displays less frequency shift compared to the defect-free grey curve) suggests that the tip cannot fully probe the vacancy's depth. Both of these dihydride variants can be compared to the final example of a dihydride pair in Figure 3.4 (e),(f). It interestingly appears remarkably similar to the normal dimer cross-section, with only slight variation at the position of the outermost H atoms. The lack of a hydrogen-related splitting feature, as seen with the other dihydride

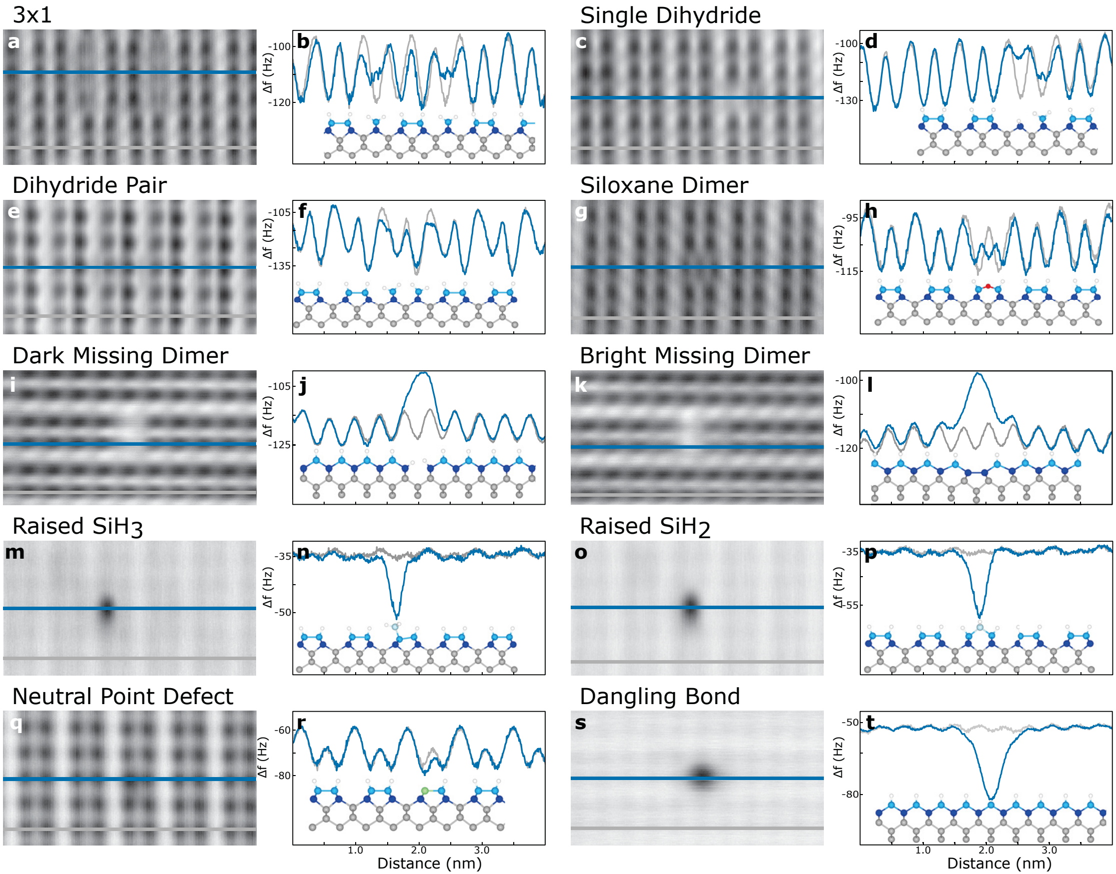

FIGURE 3.4: **Analysis of defects using dark-contrast AFM and profile extractions.** Line cuts of the AFM scans using Si-terminated tips were performed by averaging over 6 adjacent lines, with the thickness of the line profile indicating this averaging. The defect-including profiles are indicated in blue, while the defect-free profiles for each panel are in grey. The defect type is indicated above the relevant panels. See Figure 3.3 for the experimental image parameters.

species, can be explained by looking at the modelled geometry of the two closely-spaced dihydride species in the dimer in Figure 3.4 (f). Local repulsion between the two nearest hydrogen atoms on the inside of the pair results in the tilting of the dihydrides with respect to the surface. Thus, the position of the outer two hydrogens are now further away from each other and closer to the underlying bulk atoms, making the feature less visible to the AFM tip.

Examining the siloxane dimer in Figure 3.4 (g),(h), three distinct minima are in place of the dimer. As mentioned earlier, the outer two hydrogen atoms spatially shift to accommodate the oxygen atom, extending the dimer structure by approximately 30% compared to a regular dimer.

Particularly interesting is the comparison between the two variations of the missing dimer. Figure 3.4 (i),(j) probe the dark missing dimer in which the unsatisfied bonds of the back bonded Si atoms are terminated with hydrogen. As such, any lattice strain is reduced and the neighbouring dimers show minimal variation compared to the defect free profile. Conversely, the maxima of the bright missing dimer in Figure 3.4 (k),(l) is accompanied by two local minima "shoulders". These have a less negative frequency shift, with the minima pulled spatially towards the centre of the defect. We propose that this observation is a result of the second layer Si atoms forming dimer bonds at the defect location, introducing horizontal lattice strain. This pulls the neighbouring atoms inwards more than in the dark missing dimer case, accounting for the shoulders in 3.4 (l) which are absent in 3.4 (j). Importantly, these two defects were imaged in succession, ensuring any variations are a consequence of their differing nature, not a tip alteration. The slight asymmetry between the profiles on the left and right of the missing dimers in both cases is a result of a slight tip asymmetry.

The two raised Si species in Figure 3.4 (m),(n) (SiH_3) and Figure 3.4 (o),(p) (SiH_2) present an extra challenge to analyze, as they must be imaged with a larger tip-sample separation to prevent damaging tip contact. As a result, the magnitude of the frequency shift of the unperturbed surface is small compared to the strong defect signal. Despite this, examination of the cross-sections for the SiH_3 and SiH_2 respectively, resolves the position of the defect with respect to the lattice; the SiH_3 originates above one side of a dimer, while the SiH_2 is centred between the two atoms of a dimer.

The neutral point defect in Figure 3.4 (q),(r) displays as a slight decrease in the minima above the defect. The almost normal appearance of the defect cross section compared to the regular surface suggests a similarly coordinated substitutional species. A slightly more

negative frequency shift is observed suggesting the defect is chemically different from the surrounding H-Si atoms. As discussed with the simulations in Figures 3.11, 3.12, and 3.13, such a feature is not captured with the probe particle model suggesting that additional theoretical work is needed to identify its true nature.

Lastly, a lone DB shows up as a localized feature of enhanced reactivity when compared to the surrounding H-terminated surface (Figure 3.4 (s),(t)). This reactivity extends spatially away from the DB location, generating a broad minimum that eclipses the signal from neighbouring lattice sites. Due to the DB's highly reactive nature, AFM imaging of DBs must be done with significant tip-sample separation to prevent any alteration to the tip or surface.

The silicon vacancy

We now focus on an in-depth analysis of the silicon vacancy defect introduced in Figure 3.3 (b). While all of the other defects examined are observed with the same consistent appearance, there are several distinct species we attribute to the proposed Si vacancy. Figure 3.5 shows empty states, filled states, and constant current images of 3 different configurations of the defect, corresponding to different vacancy depths. Each of the configurations in Figure 3.5 (a)-(d), (e)-(h), and (i)-(l) are denoted in the provided ball and stick models. These are all predicted to exist as negative charge centres, owing to the presence of unsatisfied bonds of atoms neighbouring the vacancy, which localize charge due to the degenerate doping of the crystal (see Methods for sample details). Starting with Figure 3.5 (a) (labelled I), the defect is centred around a surface lattice site affecting one side of a dimer, with the negative charge bending the bands down locally as evidenced by the radial dark depression around the defect centre. The filled states STM image of 3.4 (b) shows an increase in measured height, correlating again to the fixed negative charge of the defect [249]. Looking at the constant height STM image in Figure 3.5 (c), it appears that no atom is present at the defect lattice site. This is supported through examination of the AFM line cuts of this defect in Figure 3.5 (m),(n) (and Figure 3.18), which show the expected missing atom as an area of less negative frequency shift (blue curve in Figure 3.5 (n)). Due to a missing first-layer silicon

atom, the AFM probe is actually measuring a signal from the back-bonded and bulk silicon atoms. This is verified by comparing the magnitude of this smaller frequency shift to an equivalent measurement of other back-bonded Si atoms, as would be measured in a cross section taken between dimers (burgundy line in Figure 3.5 (n)). Their similar magnitude supports there is no atom present, while also lending evidence to its correct classification as a Si vacancy [273, 274]. Additionally, a more negative frequency shift minimum is seen in Figure 3.5 (m),(n) above the remaining atom of the dimer, with a shift of the minimum toward the site of the vacancy as shown in the blue cross-section in Figure 3.5 (n). The localization of the subsurface vacancy's charge through the unsatisfied DBs is thought to prevent the otherwise required dihydride (Figure 3.3 (e)) at the site of the neighbouring atoms from forming although further theoretical exploration is required to support this. A potential variation of the vacancy where one of the back bonded DBs is terminated with an H is presented in Figure 3.19 and the probe particle modelling of the Si vacancy "I" variety shown in Figure 3.20.

Figure 3.5 (e)-(h) shows another variant of the silicon vacancy (labelled II). The broad features of the STM probing vacancy II in Figure 3.5 (e)-(g) are similar to vacancy I, however, it can be seen that the defect no longer appears to affect a single atomic site, but rather reduces the apparent height of two adjacent dimers as shown in Figure 3.5 (g). While the subsurface defect cannot be directly probed, the similarities it shares with Figure 3.5 (a) supports its assignment as a Si vacancy below the surface (see the ball and stick model in Figure 3.5 (h),(p)). This is further corroborated by line-cut analysis of vacancy II in Figure 3.5 (o),(p). The two atoms centred above the defect in 3.5 (t) show a reduced minimum, as well as a horizontal shift in position towards the defect centre due to a polaronic distortion induced by the vacancy's localized negative charge. Molecular dynamics relaxation was unable to capture this effect as part of the modelling, so the ball and stick models of Figure 3.5 (h),(p) have been manually edited to show this effect.

Figure 3.5(i)-(l) shows the third common type of Si vacancy (labelled III). This defect shares similar STM features when compared to the previous vacancy examples, but is spatially

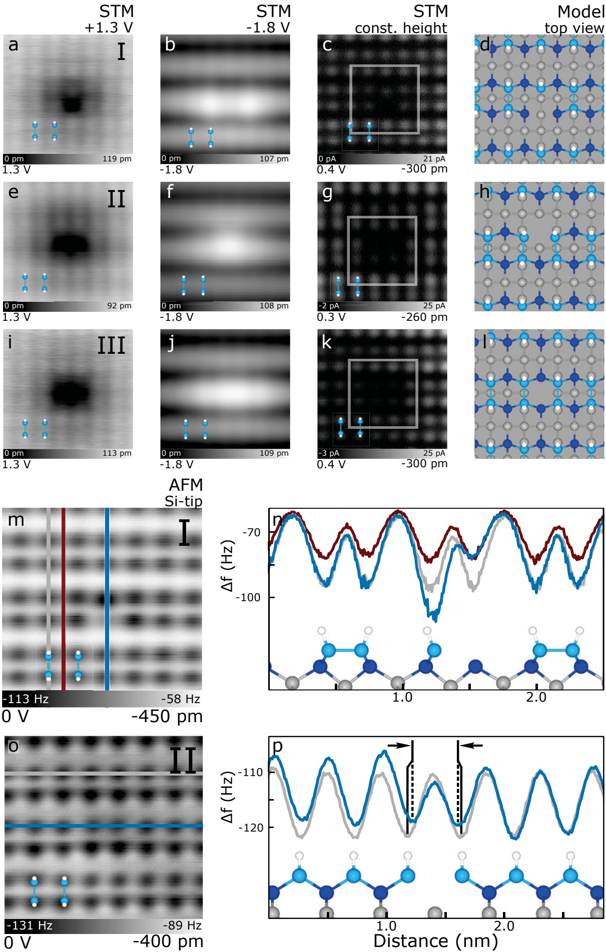

FIGURE 3.5: **Silicon vacancies at different lattice sites.** (ad), (eh), and (il) The changing STM appearance of silicon vacancies located at different depths and lattice sites, labelled I, II, and III, respectively. A ball and stick model of the dimer structure is shown as an overlay in each scan (lower left corner, 0.38 nm width). Each STM image is 3.4 nm x 3.4 nm. (m,n) The line cuts of vacancy I in (a) while (o,p) show the line cuts of vacancy II in (e) with the apparent change in atom separation highlighted (reduction of approximately 15%). Each AFM image is 2.8 nm x 2.8 nm. The defect-including profiles of n and p are indicated in blue, the defect-free profiles are in grey, and a background (between dimer pairs) profile is in burgundy. Colours in the ball and stick models are: H - white, Si dimers - royal blue, back-bonded Si - dark blue, and bulk Si - grey.

shifted with respect to the Si lattice. In detail, the dark depression in Figure 3.5 (i) is now symmetric in appearance and centred in the dimer row, the bright enhancement in Figure 3.5 (j) extends over many dimer pairs, and in the constant height STM in Figure 3.5 (k) the two dimers above the defect centre show a reduction in apparent height. Aligning the centre of this defect to a model of the underlying Si lattice (see Figure 3.5 (l)) and factoring in that the missing atom must preserve the observed experimental symmetry, it is likely the position of this vacancy is in the third atomic layer (missing grey atom in the centre of Figure 3.5 (l)). While our assignment of this defect as a Si vacancy is consistent with our experimental results, detailed modelling will be needed to investigate the various rebonded and H-capped alternatives and compare them to the STM and AFM images.

The neutral point defect

We now return to a discussion of the neutral point defect, which we noted initially exists in a negatively charged, H-decorated state. Figure 3.6 provides three examples of tip-induced transitions of a negative species to the neutral point structure. For each case, the leftmost panel shows a dark depression scanned at positive STM bias that is associated with a localized negative charge (similar to the dark halo around a DB in Figure 3.3 (a)-1 or the vacancies in Figure 3.5). At this point, one could be tempted to assign the dark feature to the same vacancy defect as in Figure 3.5 due to their similar likeness. However, this species is found to be unstable and irreversibly altered upon scanning at negative bias (in constant current mode) or zero bias (with reduced tip-sample separation in AFM mode) (Figure 3.6 (b),(e),(h)), with the consistent observation of a sharp discontinuity close to the site of the defect. The discontinuity is accompanied by a change in appearance of the defect which remains in the subsequent empty states images (compare Figure 3.6 (c),(f),(i) to the first scans in Figure 3.6 (a),(d),(g)). Importantly, we observe the complete absence of a charged species after the transformation and a replacement with the neutral point defect. The change in contrast of the AFM image of Figure 3.6 (h) further suggests that the tip apex transitioned from a Si-tip to a H-tip through the liberation of the H atom decorating the defect. Efforts to replace an H atom on such a site were unsuccessful.

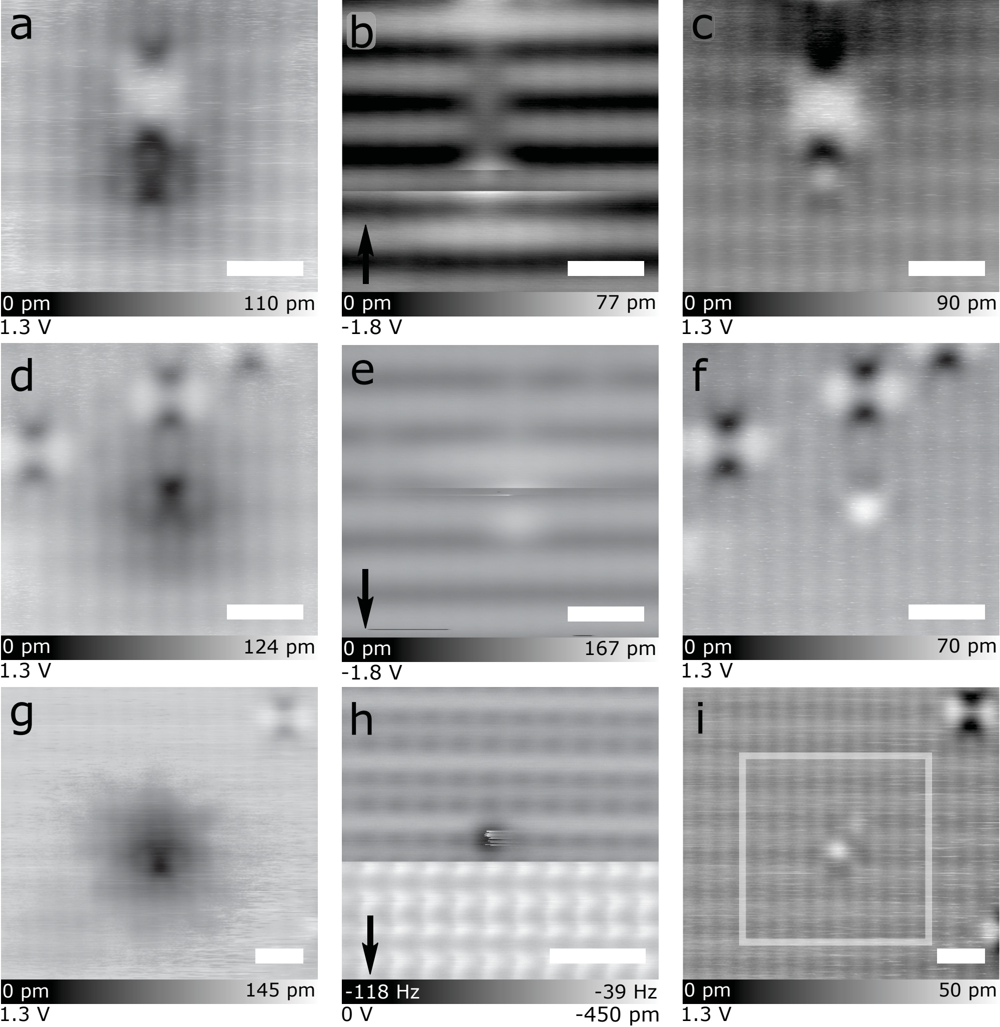

FIGURE 3.6: **Tip-induced removal of hydrogen atoms decorating neutral point defects.** (a-c), (d-f), and (g-i) Three instances of the apparent neutralization of a negatively charged defect. (a,d,g) Empty states images of the negatively charged H-decorated point defect before H liberation. (b,e) Show filled states STM removal events, while (h) An AFM removal event. The arrows in the lower left indicate the scan direction, with contrast changes in the scan indicating a removal event has occurred. (c,f,i) Empty states STM images of the same frames as (a,d,g), but after the H removal. The point defects no longer display charge-induced band bending around their location. The white box in (i) indicates the size of the scan frame in (h). Scale bars are 1 nm.

Furthermore, our assignment that the neutral point defect acts as a hydrogen trap during sample preparation is based on the similarity of the defect's negative state to physisorbed hydrogen atoms on the surface (see Figure 3.21 for STM images of physisorbed hydrogen atoms). Prior work reported that lone hydrogen atoms are negative on a H-terminated degenerately doped n-type sample, while another reported they could be picked up from the surface during filled states STM imaging [177]. Additional examples of the H removal along with STM I(V) and dI/dV spectroscopy of the neutral point defect can be seen in Figures 3.22 and 3.23. This evidence, together with the fact that our sample preparation methodology produces many hydrogen radicals that can penetrate the surface, supports the idea that the neutral point defect behaves as a hydrogen trap. As to its identity, it has been reported in the literature that boron, when added to silicon, can behave as a hydrogen trap [275–278]. Its trivalent nature would place the atom in a neutral charge configuration when substituted for a Si atom within a dimer. The addition of a hydrogen atom could then force a weakly held bond to form, allowing for the localization of an additional electron leaving the boron in a negative charge state. While this seems to support its assignment as boron, the areal concentration these neutral point defects are observed at (0.1-7.6 defects/10 nm^2) is higher than would be expected for contaminant boron from commercial wafer processing [249]. Further investigation into the origin of this defect will be required for a conclusive determination.

3.2.4 Conclusion

In this work we have created a comprehensive catalogue of commonly found defects on the H-Si(100)-2x1 surface analysed using a combination of several STM and nc-AFM imaging modes, with reproducibly formed tip terminations of different reactivity. Through this analysis we are able to identify unique electronic and structural signatures associated with the defects of each imaging mode. By combining these results with a simple probe particle simulation of the STHM and AFM images, we were able to confirm the underlying mechanism of

STHM, the classification of several surface defects, as well as more confidently identify the previously reported T2 defect as having character more consistent with a silicon vacancy. Finally, we examined the previously unreported neutral point defect, observing its transition from a negatively charged species by means of tip-induced liberation of an atomic hydrogen from the defect site. While our work presents a comprehensive understanding of the experimental nature of these defects, additional theoretical studies using more powerful techniques such as DFT is still needed to confirm the results presented here and provide a potential classification of the point defect. We also note that it is expected that other sample termination methods, Si wafers, and vacuum systems could potentially lead to additional defects not reported here. While this means this is not an exhaustive list, our analysis provides fresh insight into the nature of many commonly observed defects. Through this now enhanced understanding of the nature of the most common defects, we enable informed refinement of standard HSi wafer preparation methods, leading to a more reliable platform for the creation of these devices.

3.2.5 Methods

Experiments were performed using an Omicron LT STM and an Omicron qPlus LT AFM [90, 279] system operating at 4.5 K and ultrahigh vacuum (3×10^{-11} Torr). STM tips were electrochemically etched from polycrystalline tungsten wire, resistively heated, and field-evaporated to clean and sharpen the apex using a field ion microscope (FIM) [178]. AFM tips used the third-generation Giessibl tuning forks with a FIB mounted tungsten tip ($f_0 \approx 28$ kHz, Q-factor $\approx$ 16k-22k) [280]. The tip was cleaned and sharpened in vacuum using a FIM [178]. *In situ* tip conditioning was done by executing controlled contact on a hydrogen-desorbed patch of silicon [140, 155]. Bright contrast, H-functionalised AFM tips were routinely formed with controlled contact on H-terminated portions of the surface, while bare silicon AFM tips were formed using only desorbed patches (although not all controlled contacts on a desorbed patch returned a Si-tip). STHM tips were achieved by creating DBs via tip pulsing, where

the desorbed H is reported to sometimes decorate the tip's apex [4, 145, 177], providing contrast as shown in Figure 3.7 (a).

The samples used were highly arsenic-doped ($\approx 1.5 \times 10^{19}$ atoms/cm^3) Si(100). Samples were degassed at 600° C overnight followed by multiple cycles of flash annealing at 1250° C. The samples were then terminated with hydrogen by exposing them to molecular hydrogen (1×10^{-6} Torr) while the Si sample was held at 330° C for 2 min. The molecular hydrogen was cracked from H_2 gas using a tungsten filament held at 1600° C [281].

Image and data acquisition was done using a Nanonis SPM controller and software, with the imaging parameters for each of the 6 SPM analysis modes described in the text. The height setpoint reference was taken as the tip-sample separation over a H-Si atom with an imaging bias of -1.8 V and a current setpoint of 50 pA. The exact magnitude of the $\Delta f(z)$ spectroscopy changed between tip shaping events, but the general shape and behaviour for H- and Si-terminated tips (bright and dark contrast) remained consistent throughout multiple tips and tip terminations.

The defect free H-Si ball and stick model was the same as used in [140], with defects manually inserted using Avogadro [282, 283]. The geometry of the defect atoms within the lattice were optimized using molecular dynamics relaxation with a Merck molecular force field (MMFF94) [284]. Images of the lattice were colourized and rendered using Mercury [285]. Details of the probe particle simulations can be found in Supporting Information.

3.2.6 Acknowledgements

We would like to thank Moe Rashidi and Roshan Achal for valuable discussions regarding the defect origins. We would also like to thank Mark Salomons and Martin Cloutier for their technical expertise.

3.2.7 Funding

We thank NSERC, and AITF for financial support. T.D. acknowledges NSF-MIP: Platform for the Accelerated Realization, Analysis, and Discovery of Interface Materials. (PARADIM, DMR 1539918).

3.2.8 Author Contributions

J.C. collected all experimental and simulated data. Interpretation of all results was done by J.C, T.D., T.H. and R.A.W. R.A.W. supervised the project. J.C. wrote the manuscript with significant input from all authors.

3.2.9 Competing Interests

The authors declare competing financial interests. Some of the authors are affiliated with Quantum Silicon Inc. (QSi). QSi is seeking to commercialize atomic silicon quantum dot based technologies.

3.2.10 Data Availability

Data is available upon request from corresponding author.

3.2.11 ORCID iDs

Jeremiah Croshaw - https://orcid.org/0000-0001-9164-1556

Thomas Dienel - https://orcid.org/0000-0001-8146-8841

3.2.12 Preprint

A non-peer-reviewed version of this article has been previously published as a preprint: https://arxiv.org/abs/2002.09138

3.2.13 References

References for this publication are available at the end of this thesis.

3.3 Atomic defect classification of the H-Si(100) surface through multi-mode scanning probe microscopy: Supporting Information

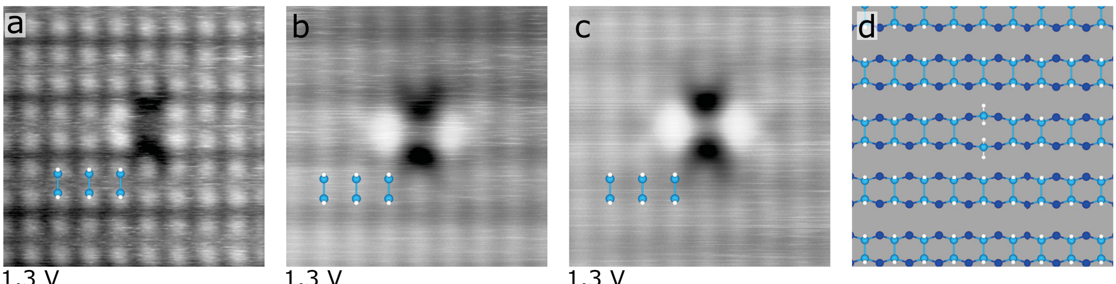

FIGURE 3.7: **Variation in dimer contrast in constant current STM topography of empty states imaging** (1.3 V, 50 pA). A dihydride pair aids to identify the dimer rows in each case. (a) Single atom contrast, where each H-Si atom is readily assignable. (b) True dimer contrast, aligned with the dihydride pair. (c) False dimer contrast where apparent dimer features appear offset from the dihydride pair. (d) The corresponding ball and stick structure for a dihydride pair. The high-resolution contrast in (a) is routinely achieved by functionalizing a dark contrast Si-terminated tip with a single hydrogen atom through the creation of a DB (H-functionalization, the reverse process is discussed in Figure 3.10). This H-functionalized tip then shows bright contrast and can be used for STHM. No correlation has been observed for the AFM contrasts and the STM dimer contrasts in (b) or (c). Each image is 3.4x3.4 nm^2.

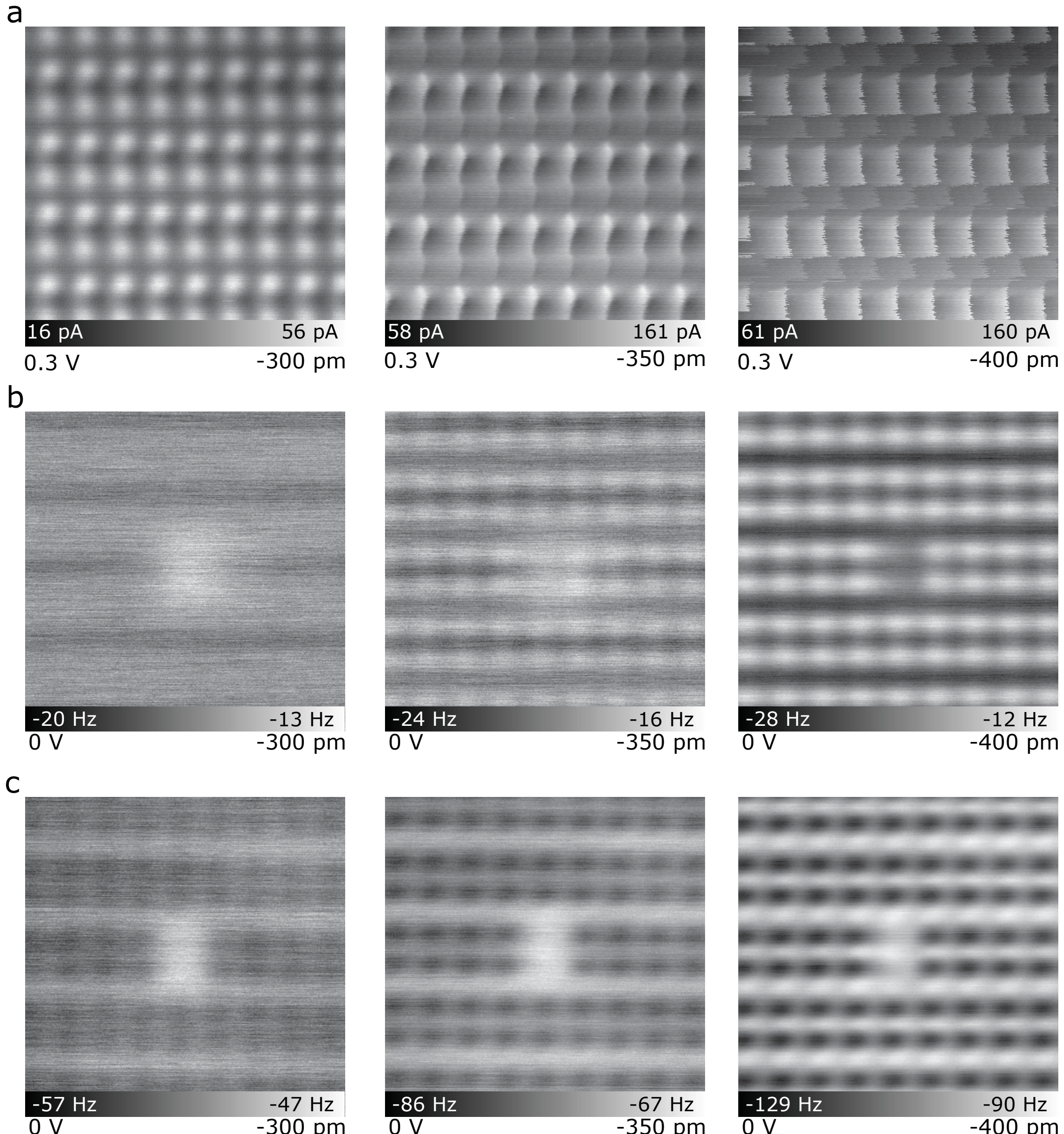

FIGURE 3.8: **Height series of constant height imaging.** (a) Constant height series of defect free H-Si(100)-2x1 with an STHM tip. (b) Constant height Δf series of a dark missing dimer with a H-terminated AFM tip. (c) Constant height Δf series of a dark missing dimer with a Si-terminated AFM tip. Each image is 3x3 nm^2 with imaging parameters indicated below each image.

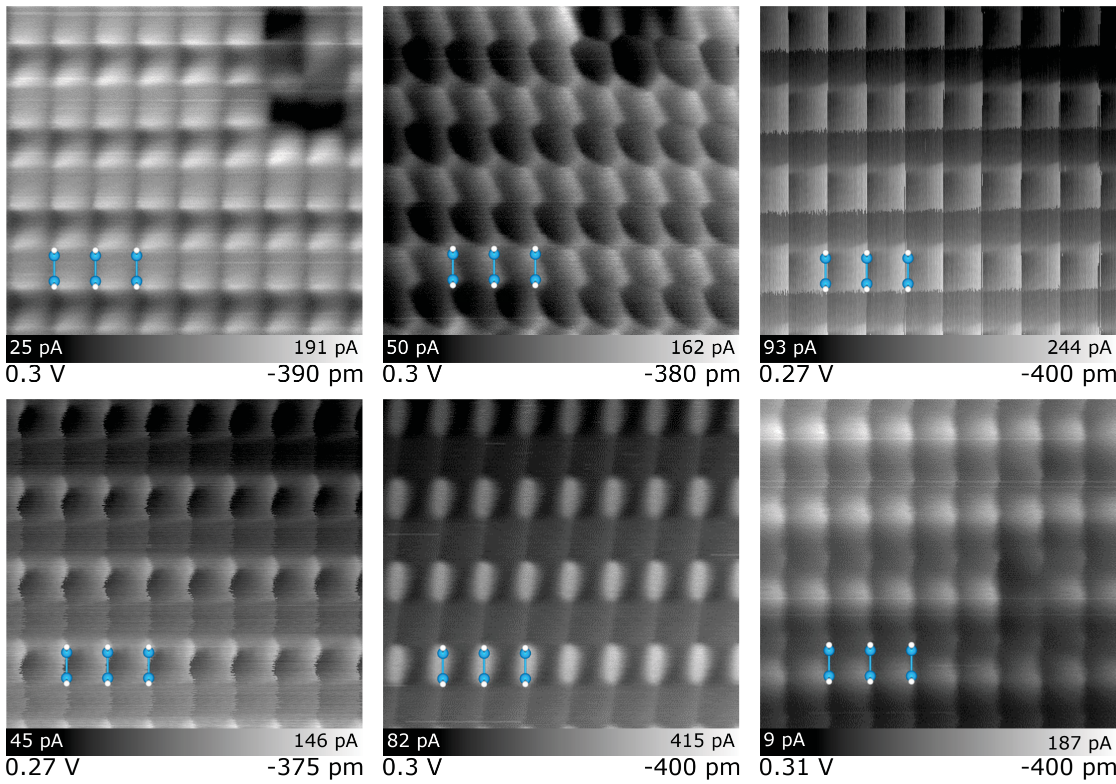

FIGURE 3.9: **STHM Images of the H-Si surface taken with different H-functionalized tips of differing flexibility.** The variation in surface character between the images highlights how asymmetries of the tip, or variations in apex coordination can affect the observed imaging. Each scan is 3.1 nm x 3.1 nm.

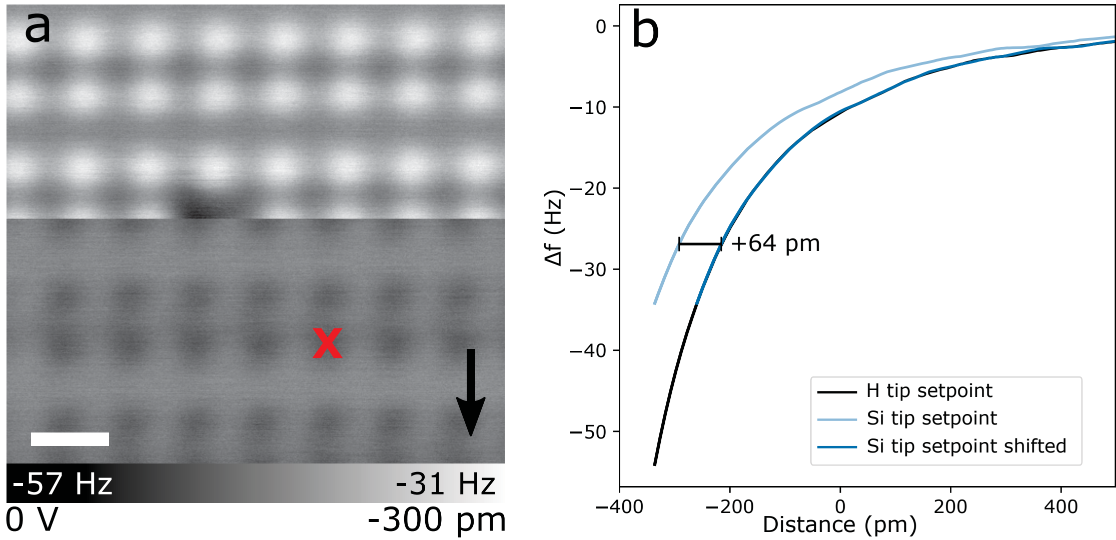

FIGURE 3.10: **Relative height difference between a Si and H apex tip.** (a) Δf map with a contrast change observed mid-scan from changing apex functionalization. An originally dark contrast silicon tip was functionalized with a hydrogen atom through the creation of a DB so that it exhibits bright contrast (top half of image). That H-functionalized tip was then scanned over a DB resulting in a H transfer from the tip to the sample and a corresponding change in contrast (silicon terminated tip for bottom half of image). (b) A Δf(z) spectroscopy was taken over a H-Si atom after the capping event (red X in (a)) and once more after resetting the height setpoint with the silicon-terminated tip (dark contrast). By comparing the curves, it is observed that the H-terminated tip sits 64 pm closer to the surface. While this height difference is roughly 2x smaller than a H-Si bond, it is important to note that this measured height is a convolution of the H-Si bond and the difference in height setpoint as a result in different density of states between the Si-terminated and H-terminated tip. The arrow in (a) indicates the scan direction, the scale bar in (a) is 500 pm. The height in (a) is the distance from a setpoint of -1.8 V and 50 pA with a H-functionalized apex. The spectroscopy curves were smoothed using a Savitzky-Golay filter to make it easier to align the plots.

3.3.1 Probe Particle Simulations

In addition to the experimental results, simulations based on the probe particle model were used to reproduce the STHM and AFM images of the observed defects. The probe particle model developed by Hapala *et al.* works by simulating a probe particle which is attached to a metal tip and allowed to distort based on interactions with the surface. These interactions are described using empirical potentials following a pairwise Leonard-Jones potential which

maps the interaction between the probe particle and the surface, and the probe particle and the metallic tip to which it is held [233]. The structure of the sample surface used in the probe particle model is generated by starting from a defect free H-Si slab from Ref. [140], adding the defects and relaxing to their respective geometry using a molecular dynamics package (Merck Molecular force field MMFF94) [284]. The resulting structures are shown in ball and stick representation throughout the paper. The imaging parameters for the simulations were kept very close to those available in the provided examples [234]. Simulations done to mimic the STHM images were performed with a flexible H atom at a tip-sample separation of roughly 780 pm defined as the distance between the surface's Si atoms and the metal apex of the tip. All H-apex AFM images were simulated using the same tip conditions as the STHM images except the tip-sample separation was increased to roughly 870 pm. The Si-apex AFM images were simulated at the same depths as the STHM images except the apex atom was replaced with a Si atom and the tip spring constant, which affects the probe particle flexibility, was increased by 40 times.

As we will discuss in the following, the simulated images show several significant successes and shortfalls in resembling the features of the experimental images. The STHM simulation images are shown in Figure 3.11. The defect free surface is shown in Figure 3.11 (a), and as can be seen, the probe particle model correctly shows a series of intersections corresponding to the position of H-Si atoms on the surface. It is important to clarify that the probe particle images show the force of interaction between the tip and surface while the STHM images show the measured tunneling current. As such, the features of these images cannot be directly compared. Since the underlying mechanism of the apparent contrast originates from the same principle, it is still useful to provide a qualitative comparison. It is difficult to compare the DB shown in (b) due to the high amount of current in the experimental images. The Si vacancy in (c) also proves difficult to compare since the structure of the Si vacancy ball and stick model did not distort under the applied molecular dynamics relaxation (see Methods). It can be expected that a more advanced modelling approach which can include charge localization and subsequent lattice distortion will be needed to more accurately match

the experimental images of charged species. The probe particle model does show some success in predicting the structure of the dihydride structures shown in (d), (e), and (f) (3x1, dihydride pair, and single dihydride respectively). Specifically, the model shows the expected distortion of the probe particle over the host dihydride atoms. As discussed previously, the slight variations between the simulated and experimental results are thought to originate from the different signals (force vs. current) measured as well as the unknown apex shape of the experimental tips. The dark and bright missing dimers shown in (g) and (h) also exhibit similar features between the simulated and experimental images. Unfortunately, the STHM images of each were taken with slightly different tips so it is difficult to provide a more detailed comparison. The siloxane dimer in (i) also shows significant similarities between the simulated and experimental images. Specifically, they both show the extension of the dimer length and the distortions (bright features) surrounding the central O atom. The raised SiH_2 and SiH_3 clusters both resemble the form of the Y shape of the SiH_2 and the X shape of the SiH_3, both centred at the position of the raised Si atom. The neutral point defect (which was simulated using a boron atom at the defect point) shows some common features but it is insufficient to confirm whether these originate from our successful prediction of the structure, or an aliasing of features from an entirely different chemical structure.

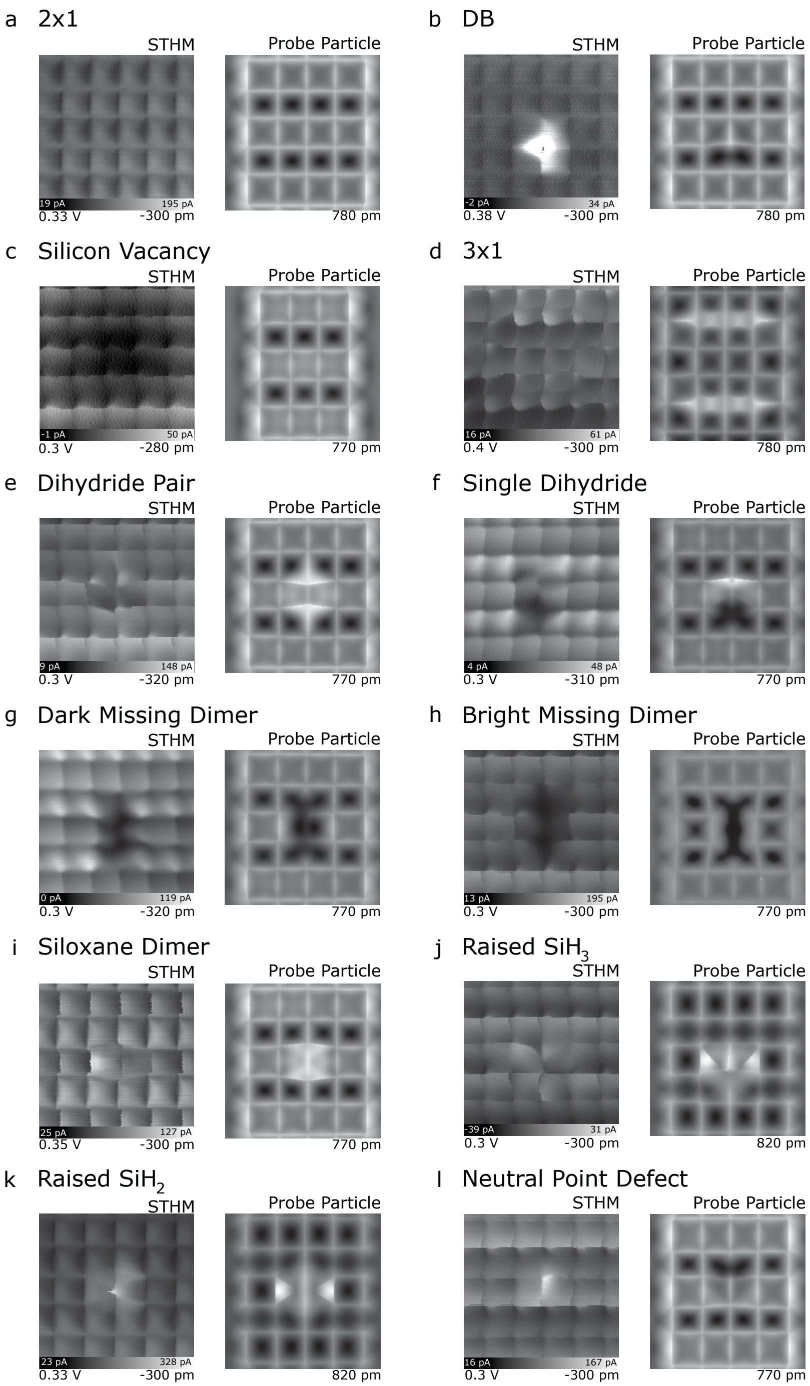

FIGURE 3.11: **Simulated STHM images in comparison with experiment** (excerpt of Figs. 3.2 and 3.3). The simulated images (right) were selected from a series of simulated heights with a flexible tip apex to best match the contrast in the experimental images (left). The corresponding distance between the tip and topmost surface Si atom is shown in the lower right of each simulated image. Each image is 2 x 2 nm^2.

The simulated H-apex AFM images are summarized in Figure 3.12. Here, the experiments and simulated data are related to force. The defect free surface shown in (a) matches reasonably well with the immediate difference being the relative sizes of the H-Si atoms. The H-Si atoms in the experimental images appear to be blurrier in comparison to the simulated images. Since both tips are assumed to have the same size of apex atom (hydrogen), it has been proposed that the difference in surface atom size comes from the flexibility of the surface atoms not modelled in the probe particle model. As shown in previous works [140], at short tip-sample separations, the interactions between the tip and sample are strong enough to move the surface atom under the influence of the tip, an effect that is not mimicked by the probe particle model. It can be suspected that this movement of the surface atoms is significant enough to cause the surface atoms to appear larger as they are imaged. In the case of the DB in (b), the simulated image does correctly show the DB as a dark centre but is missing the spherical shape of the DB. As mentioned before, we are hopeful that the inclusion of the DB orbital, charge localization, and relaxation of the DB's silicon atom into an enhanced simulation will account for these differences. The Si vacancy in (c) shows the same deficiencies in predicting the associated lattice distortion with the predicted charge localization. The dihydride species in (d), (e), and (f) (3x1, dihydride pair, and single dihydride respectively) show some success in showing the correct features associated with each dihydride Si atom, however, the experimental results fail to shown the characteristic splitting which is seen in simulated images. As mentioned previously, it is likely that this feature's absence from the experimental images is due to the flexible nature of the surface atoms, an effect which is not captured in the probe particle model. Since the dihydride Si atoms are only held by two Si atoms, it is likely that they are capable of greater flexibility than their 2x1 counterpart. Such a difference could explain the notable deviation between the positions of the inner H atoms in the experimental image when compared to the predicted H atoms of the simulated model. Nicely reproduced are the features of the dark and bright missing dimers of Figure 3.12 (g) and (h). Especially in the latter, the neighbouring dimers are simulated to be pulled towards the position of the bright missing dimer in agreement with

the experiment. A slight reduction in Δf signal of the H-Si atoms immediately to the right of the missing dimer (the scan direction influences this character) matches a similar reduction in the simulated images. This effect is easier seen in the Si-apex AFM images as will be discussed shortly. The siloxane dimer shows similar features between the experimental and simulated images as well. Both images show an increased distance between the H atoms of the dimer as well as a reduction in signal above the O atom. The effect from the O atom in the experimental image is slightly to the right of the dimer centre due to the scan direction of the image. The reverse scan direction shows the same feature on the other side of the dimer centre. The positions of the raised Si atoms in (j) and (k) relative to the underlying surface align with the simulated images, however, a notable difference is apparent in the shape of the SiH_3 and SiH_2 cluster. Again, this is thought to originate from the model not accurately accounting for flexibility in the surface atoms which would wash out any H features seen in the experimental images. Lastly the neutral point defect in panel l correctly shows a reduction in signal over the atom, but the degree of reduction is much more in the simulated model. This could be due to the model not accurately accounting for any variation in electronegativity or the structural model used being incorrect.

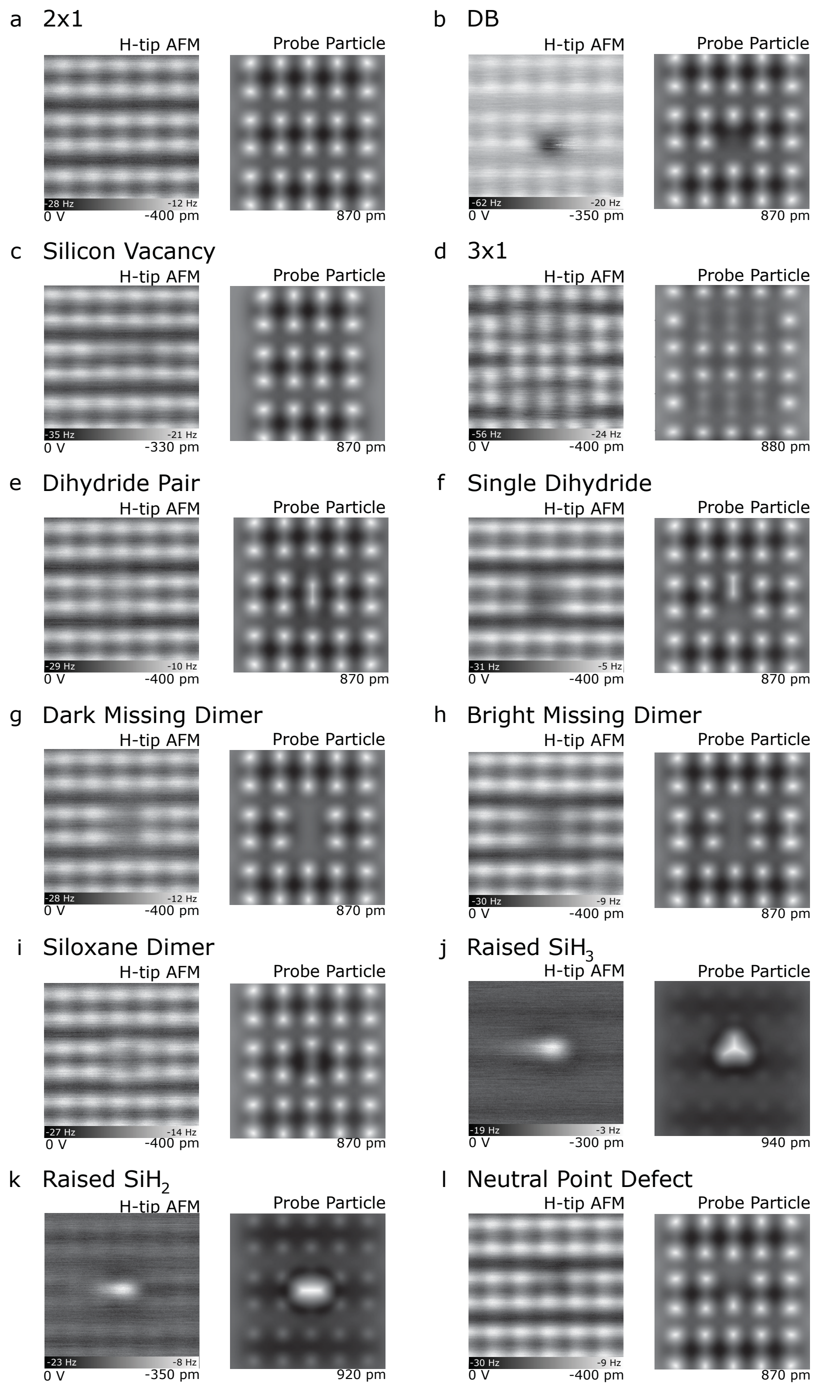

FIGURE 3.12: **Simulated H-apex AFM images in comparison with experiment** (excerpt of Figs. 3.2 and 3.2). The simulated images (right) were selected from a series of simulated heights with a flexible tip apex to best match the contrast in the experimental images (left). The corresponding distance between the tip and topmost surface Si atom is shown in the lower right corner of each simulated image. Each image is 2x2 nm^2.

The predicted Si-apex AFM images exhibit the most significant deviation from the experimental results as can be seen for the defect free surface in Figure 3.13 (a). The characteristic contrast inversion of the H-Si atoms relative to the surface is not present. Since the probe particle model only accounts for a Leonard-Jones type of interaction, it is likely that the unsatisfied orbital of the Si apex atom is contributing an additional covalent like contribution which causes the contrast inversion [149, 150]. Similar discrepancies are seen when looking at the DB in (b) and the Si vacancy in (c). An enhanced simulation approach would presumably be able to account for these differences but is beyond the scope of this work. The simulated line profile of the DB is shown in Figure 3.17 (t) and further emphasizes the discrepancy between the experimental and simulated interaction. Despite the difference in contrast between the experimental and simulated results, the probe particle model accurately predicts the atomic positions of the surface atoms as shown in the experimental images. The dihydride species of (d), (e), and (f) (3x1, dihydride pair, and single dihydride respectively) again agree very well with the experimental results. Specifically, the expected splitting of each dihydride species in (d) and (f) is well accounted for. Additionally, the observation of smaller features in the image at the position of the two outer H atoms in the dihydride pair is properly reproduced in (e). Interestingly, the simulated line profile of the dihydride pair in Figure 3.17 (f) shows the position of the inner two H atoms of the dihydride pair closer together than observed in the experimental line profile. While this difference could be attributed to the slightly asymmetric tip used to image the defect, it is also possible that the molecular dynamics optimization of the surface structure does not accurately capture the observed geometry. The dark and bright missing dimers of (g) and (h) also show strong resemblance with the experimental images with the simulated image of the bright missing dimer showing a similar reduction in signal in the H-Si atoms immediately surrounding the missing dimer. Such effects are better seen in the line profiles of Figure 3.17 (j) and (l) which show the reduced interaction at the shoulder of the defect. While the simulation does not fully align with the experimental observation, it is likely that a more robust calculation of the lattice geometry may account for such a difference. The simulation of the siloxane

dimer in (i) agrees well with the experimental images with the two outer H atoms appearing further separated than in a normal dimer as well as the presence of an additional small central feature originating from the O atom (also seen in Figure 3.17 (h)). Simulations of both raised Si structures in (j) and (k) show the expected H splitting feature which is absent in the experimental images. While it is possible that structural models for each defect is incorrect, there is also the option for these splitting features to become washed out with the inclusion of surface dynamics in the simulation (line profiles are shown in Figure 3.17 (n) and (p)). The neutral point defect of (l) correctly predicts the slight shortening of the dimer length as indicated by the position of the H-Si atom which shares a dimer with the neutral point defect, however, the absence of a stronger signal above the point defect supports the notion that either the ball and stick model, or the probe particle model contains deficiencies (Line profile is shown in Figure 3.17 (r)).

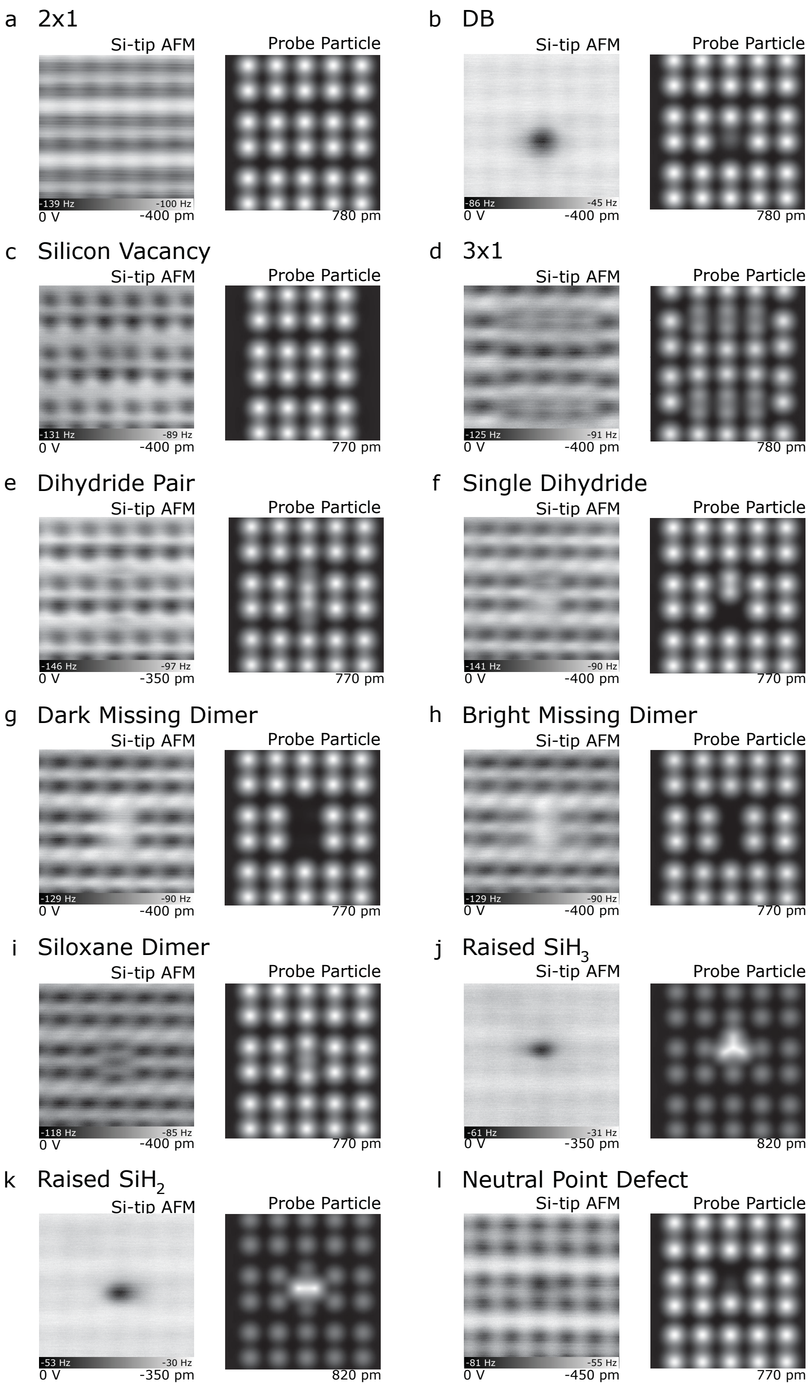

FIGURE 3.13: **Simulated Si-apex AFM images in comparison with experiment** (excerpt of Figs. 3.2 and 3.3). The simulated images (right) were selected from a series of simulated heights with a rigid tip apex to best match the contrast in the experimental images (left). The corresponding distance between the tip and topmost surface Si atom is shown in the lower right of each simulated image. Each image is 2x2 nm^2.

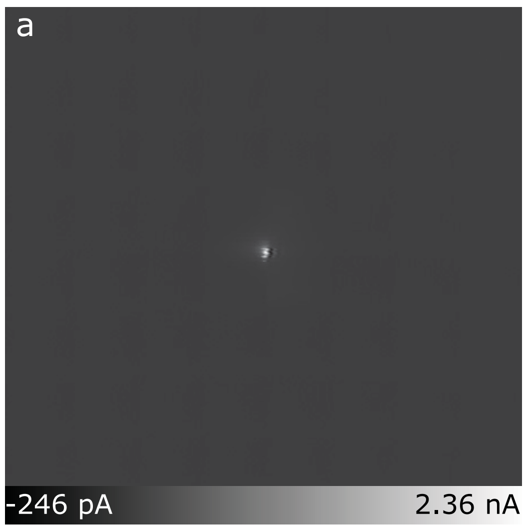

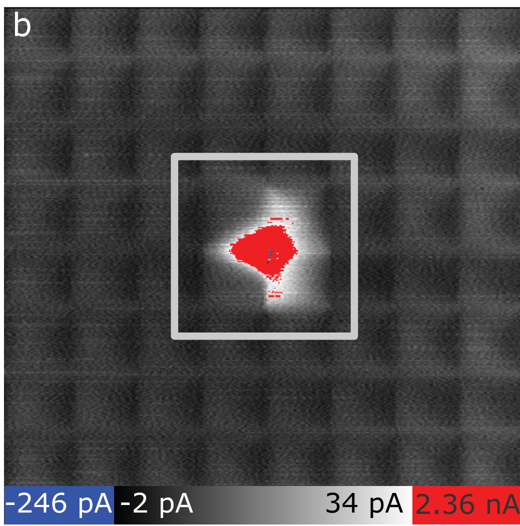

FIGURE 3.14: **Full and saturated colour scale images of the DB in STHM.** (a) Full scale STHM image of the DB from Figure 3.3a-4, with extremely localized current over the DB (constant height -300 pm, applied bias -0.38 V, image size 3x3 nm^2). (b) Colour saturated scale of the same image to highlight the H-Si atoms of the surface relative to the DB. The increased and localized nature of the current signal compared to that in Figure 3.3a-3 is a result of two properties of the H functionalization: the flexibility of the H atom at the apex and its covalent interaction with the bare Si atom of the DB. As the STHM tip scans over the DB, the increase in interaction between the surface DB and the tip leads to significant overlap of the atomic orbitals with the corresponding increase in tunneling current. Few data points close to the centre of the DB show a reversal of measured current, which we attribute to an electronics sampling error.

3.3.2 Raised Silyl Groups

The assignment of the raised SiH_2 and SiH_3 groups comes from the observation of similar imaging characteristics in the empty and filled states images of step edges. Figure 3.15 (a) shows the filled states image of a step edge with the brighter portion of the image corresponding to a terrace one atomic layer higher than the terrace in the bottom right. As can be seen, the dimer directions at each terrace are perpendicular to each other with a row of single dihydride groups on the lower terrace due the expected lattice mismatch. The key comparison which lead to the raised SiH_2 and SiH_3 groups being assigned as such is the

observation of a dark border at the boundary of the step edge and the rounding of the dimer ends best seen on the two dimers of the upper terrace in Figure 3.15 (a). The empty states image in Figure 3.15 (b) shows a different area of the surface but with a similar step edge configuration. Here, the end of the two dimer rows appear slightly larger and brighter than the remaining atoms of the higher terrace.

The characteristic dark border at the edges of terraces is also seen on smaller structures such as the ones shown in Figure 3.15 (c). Based on their size and position relative to the underlying surface, these are thought to each be two raised Si atoms which have formed their own dimer bond. If we assume that all bonds are saturated with H or neighbouring Si atoms, each structure would have an H-Si-Si-H composition. The observed dark border and rounding of the bright centre strongly aligns with the observations made at larger step edges. Similarly, the empty states image in (d) matches those features observed at the terrace edge in (b). The constant height STM image in (e) shows the onset of an STHM contrast due to the reduction in tip-sample separation over the defect. Finally, the Si apex AFM image in (f) shows a different version of the same defect where two distinct dark centres appear. By removing one of the two Si atoms, and fully saturating with hydrogen, the resulting structure would be a raised SiH_2 group that sits between two atoms of the same dimer below.

The raised Si group shown in Figure 3.15 (g) and (h) show the same characteristic dark border in filled states and a similar enhanced brightness in empty states. Based on the defect position with respect to the underlying lattice, this defect appears to be bonded to two Si atoms of neighbouring dimer rows. If we assume that all bonds are fully saturated with Si or H, the structure of the defect would be H_2-Si-Si-H_2. If we remove one of these Si atoms, and fully saturate with hydrogen, the remaining structure would match that of an SiH_3. Drawing these comparisons between the features seen at a step edge and those seen on smaller structures shown in Figure 3.15 is what lead to the classification of the raised SiH_2 and SiH_3 defects. The obvious concern to this classification is the absence of any additional hydrogen splitting in a Si apex AFM image. As mentioned in the main text, it is proposed that the absence of such features is due to the enhanced flexibility of the

raised Si groups. Since this claim cannot be further supported with more experimental work, additional theoretical work is needed which incorporates such mobility of surface atoms.

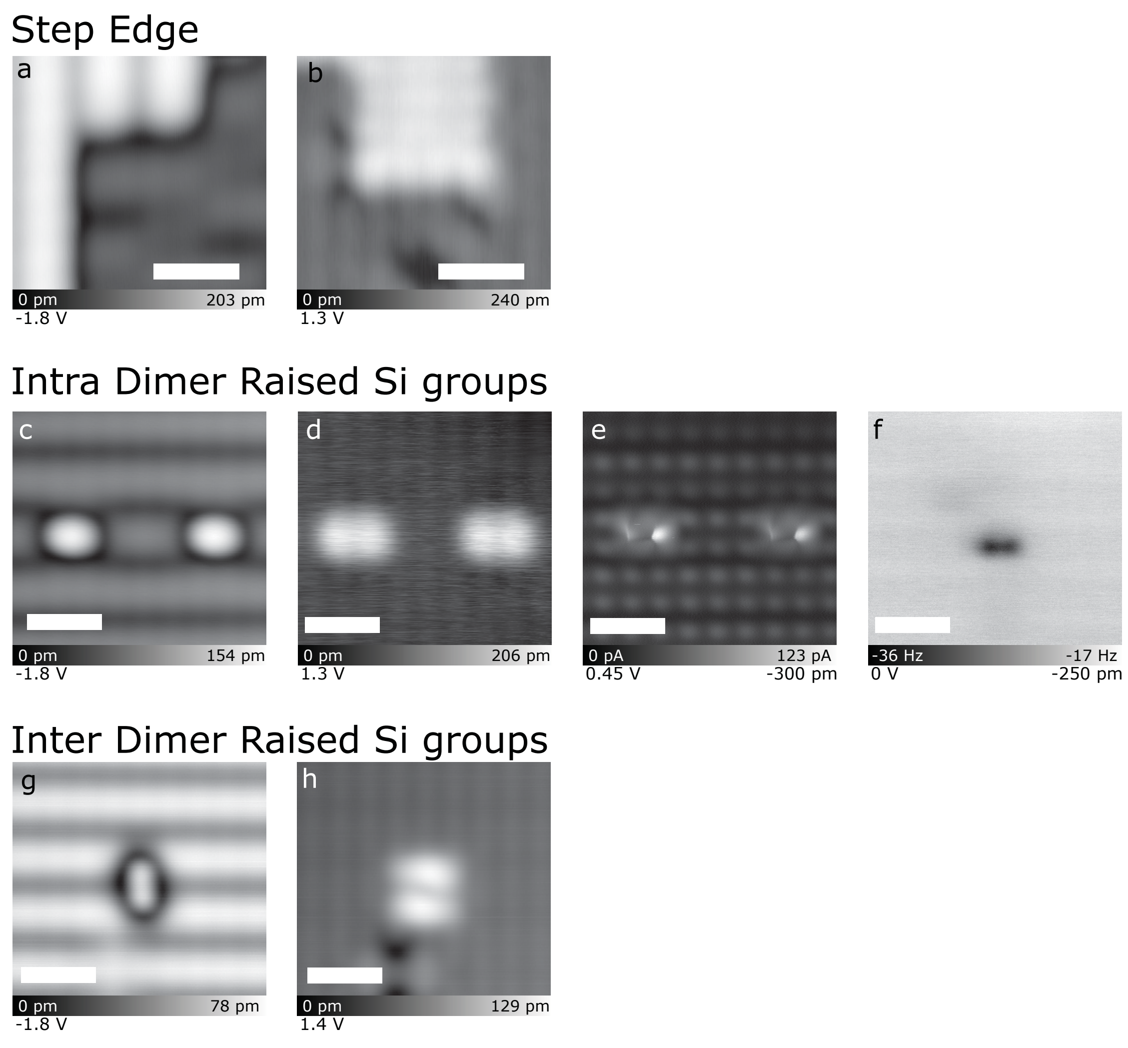

FIGURE 3.15: **Common characteristics between step edges and raised Si clusters.** (a) Filled states image of a step edge. (b) Empty states image of a step edge taken at a different surface location than (a). (c)-(e) Filled states, empty states, and constant height STM images of a larger raised Si cluster. (f) Si apex AFM image of the same cluster in (c)-(e) at a different spot on the surface. (g),(h) Filled and empty states image of a different raised Si cluster. Imaging parameters are indicated below each image. All scale bars are 1 nm.

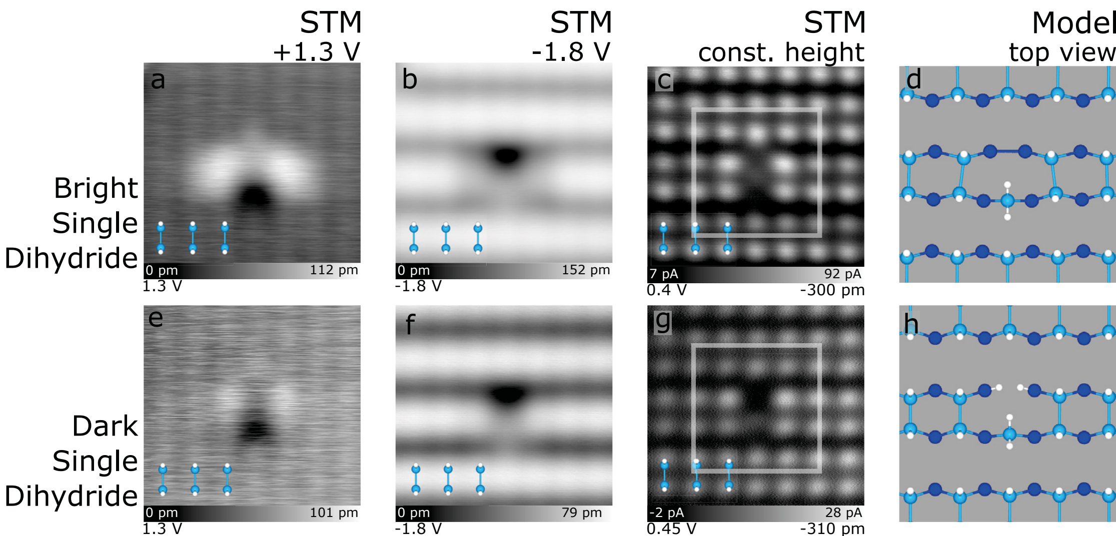

FIGURE 3.16: **Comparison between bright (top row, a-d) and dark (bottom row, e-h) variation of the single dihydride-missing atom defect.** Each image is 3.2 x 3.2 nm^2. All images were taken shortly after one another while carefully monitoring for tip changes. The additional noise in (e) is associated with the telegraph noise of a nearby DB.

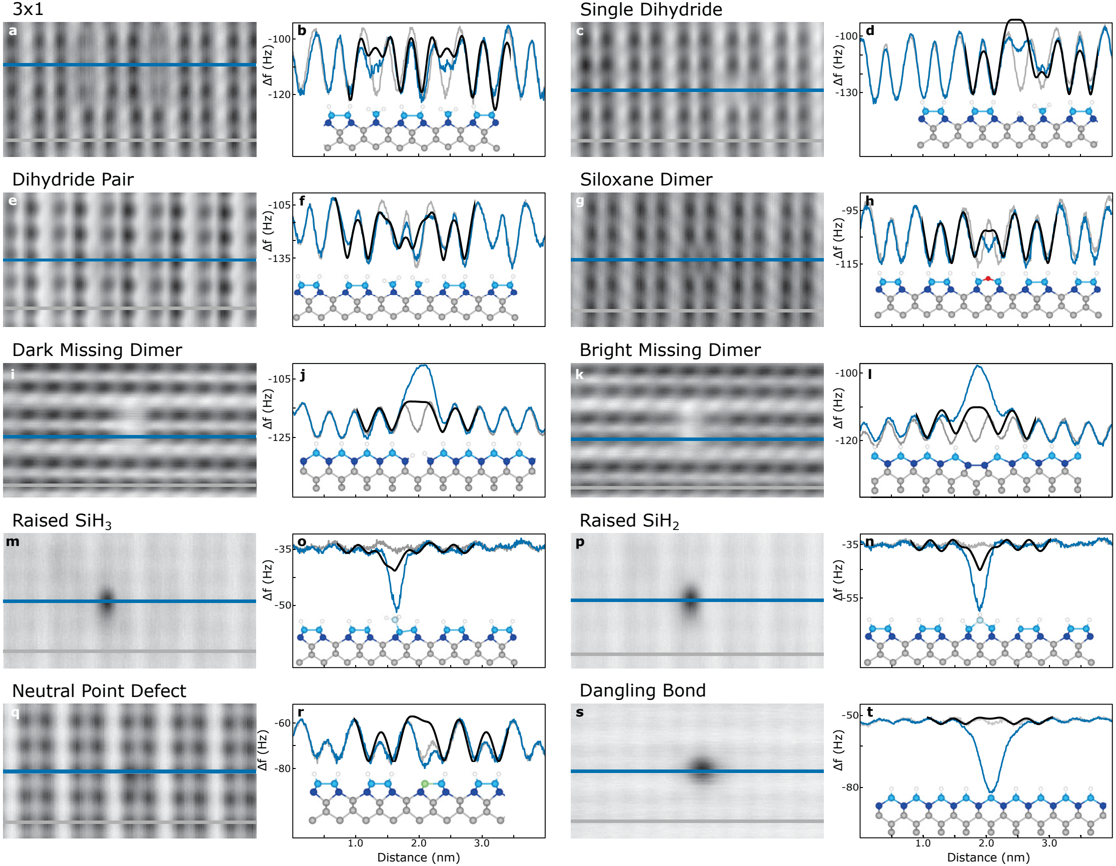

FIGURE 3.17: **Analysis of defects using Si-tip dark-contrast AFM and profile extractions with the probe particle model.** (a)-(s) The same images (left) and line profiles (right) presented in Figure 3.4 with line profiles from the Probe Particle model added in black. Simulated line profiles were taken from the simulated AFM images with a rigid tip. Profiles were inverted and rescaled to best match the experimentally observed atom positions.

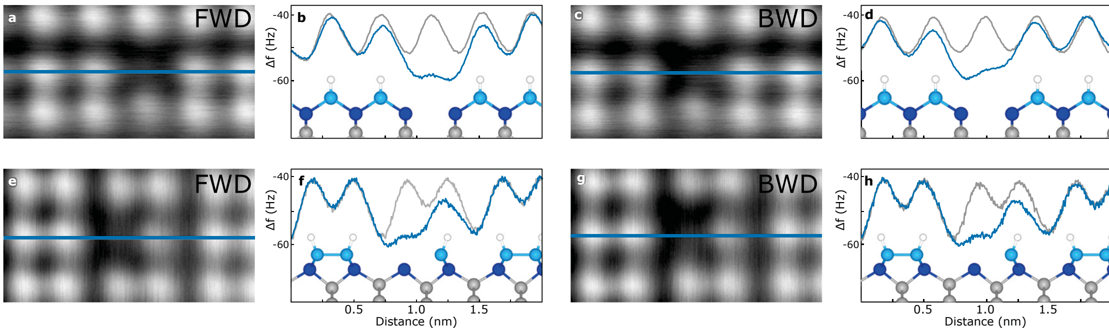

FIGURE 3.18: Each of the panels shows a line profile across the Si vacancy "I" (Figure 3.5a) imaged with H-functionalized bright contrast AFM. Direction of scan for each panel as indicated. The asymmetries in the minima at the vacancy site are likely due to a slight multi-tip made more evident by the small tip-sample separation (-400 pm).

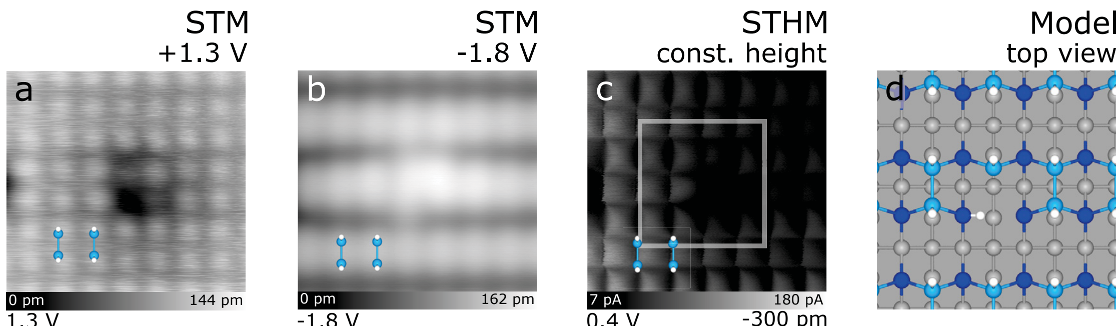

FIGURE 3.19: A possible variation of the silicon vacancy I presented in Figure 3.5. With the addition of hydrogen to the chamber during sample preparation (See Methods), it is suspected that some of the hydrogen radicals can penetrate a few monolayers into the surface, allowing them to passivate dangling bonds from Si atoms immediately surrounding a vacancy [273, 274]. Evidence of this is suggested by the vacancy shown here being similar to the one shown in Figure 3.5 (a), but with a few key differences. To first order, both display a dark depression on one side of a dimer indicating a missing silicon atom. Differences become apparent however when examining adjacent lattice sites to the missing atom. In the empty states STM image of Figure 3.5 (a), the surface hydrogen atoms around the vacancy location have similar character, displaying as darker than the surrounding surface. This is in contrast to Figure 3.19 (a) where H-Si atoms to the left of the vacancy appear unperturbed, and hydrogen atoms above and to the right are of differing character due to the presence of charge from the remaining DBs. Further differences in the appearance of this configuration are also seen in the filled state STM image of 3.19 (b) when compared to 3.5 (b), with 3.5 (b) having two maxima and 3.19 (b) only one. The normal appearance of the surface immediately to the left in 3.19 (b) supports the idea of a hydrogen penetrating the surface satisfying the left-most sub-surface dangling bond associated with vacancy (See Figure 3.19 (d)), reducing the lattice strain and making the surface hydrogen above it better match the defect-free surface. Figure 3.19 (c) shows an STHM image of the vacancy. This imaging method was used instead of a constant height image due to the tip functionalization at the time of imaging. Similar features consistent with the interpretation of the vacancy can be observed, mainly, the absence of "corners" in the STHM image above the vacancy as well as a slight negative shift in the current above the lattice intersections corresponding to the upper and right H-Si atoms.

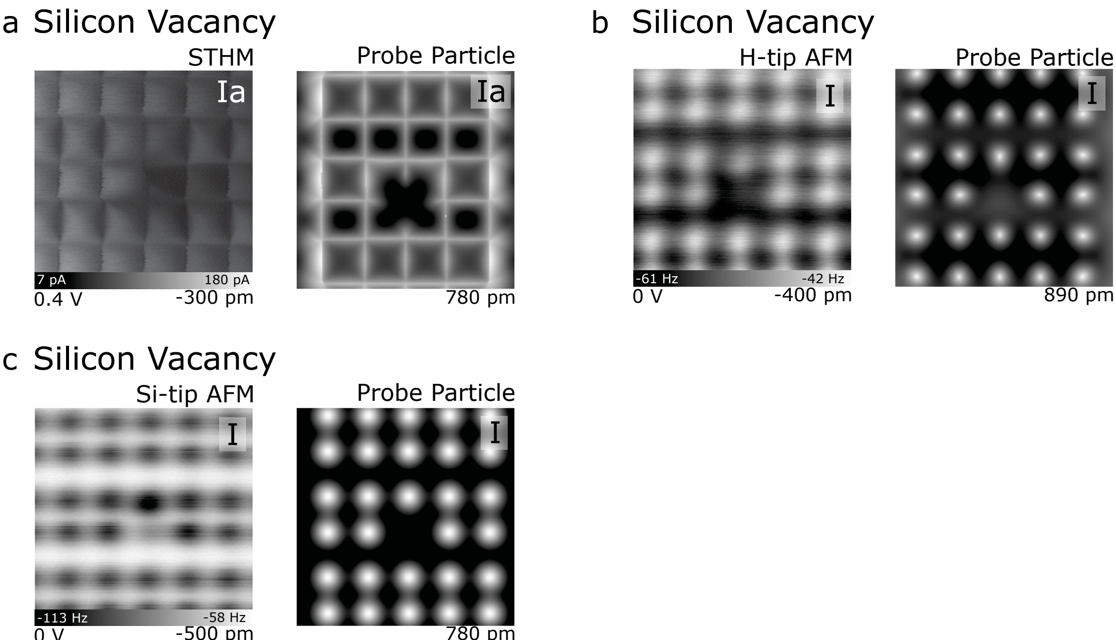

FIGURE 3.20: **Probe Particle Simulations of the Si Vacancy.** (a) STHM image of the Si Vacancy "Ia" (left) and the corresponding simulated image using the Probe Particle Model (right) with a flexible tip apex. (b) H-apex AFM image of the Si Vacancy "I" (left) and the corresponding Probe Particle Model image with a flexible tip apex (right). (c) Si-apex AFM image of the Si Vacancy "I" (left) and the corresponding Probe Particle Model image with a rigid tip apex (right). Heights for the probe particle images are the absolute separation between the topmost surface Si atoms and the metal tip. Each image is 2x2 nm^2.

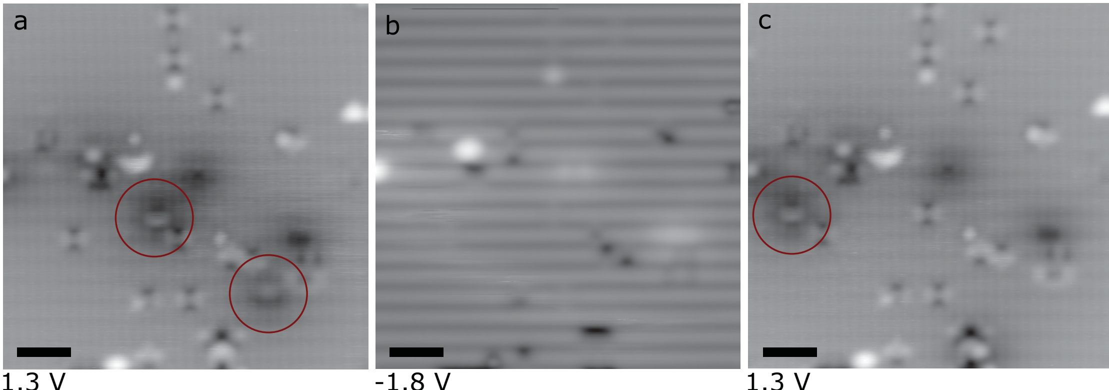

FIGURE 3.21: **Adsorbed hydrogens.** Two hydrogens are seen in (a) (red circle). (b) By scanning at -1.8V, the hydrogens are moved across the surface. This shows as streakiness in the image seen in the bottom left quadrant of the image. (c) Imaging the surface in empty states again, it can be seen one hydrogen shifted to the left side of the image and the other left the scan frame entirely. Scale bar is 2 nm.

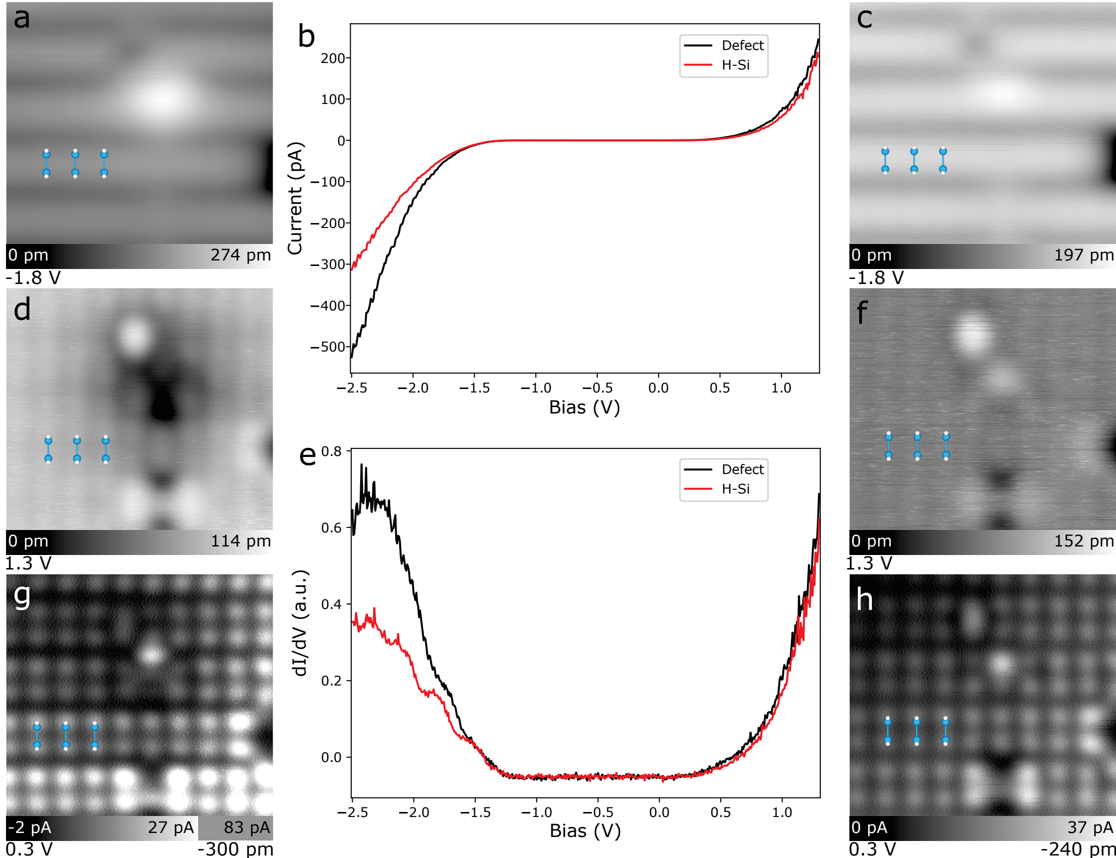

FIGURE 3.22: **Another example of the H removal from a point defect** seen in Figure 3.6. This time, the scanning bias of -1.8 V was not enough to ionize it, so an I(V) spectroscopy was done to probe higher bias values. The starting bias of the spectroscopy was -2.5 V so it is assumed the defect neutralized as the bias was increasing from -1.8 V to -2.5 V and as such, no neutralization features are seen in the curve. Each image is 3.8 x 3.8 nm^2.

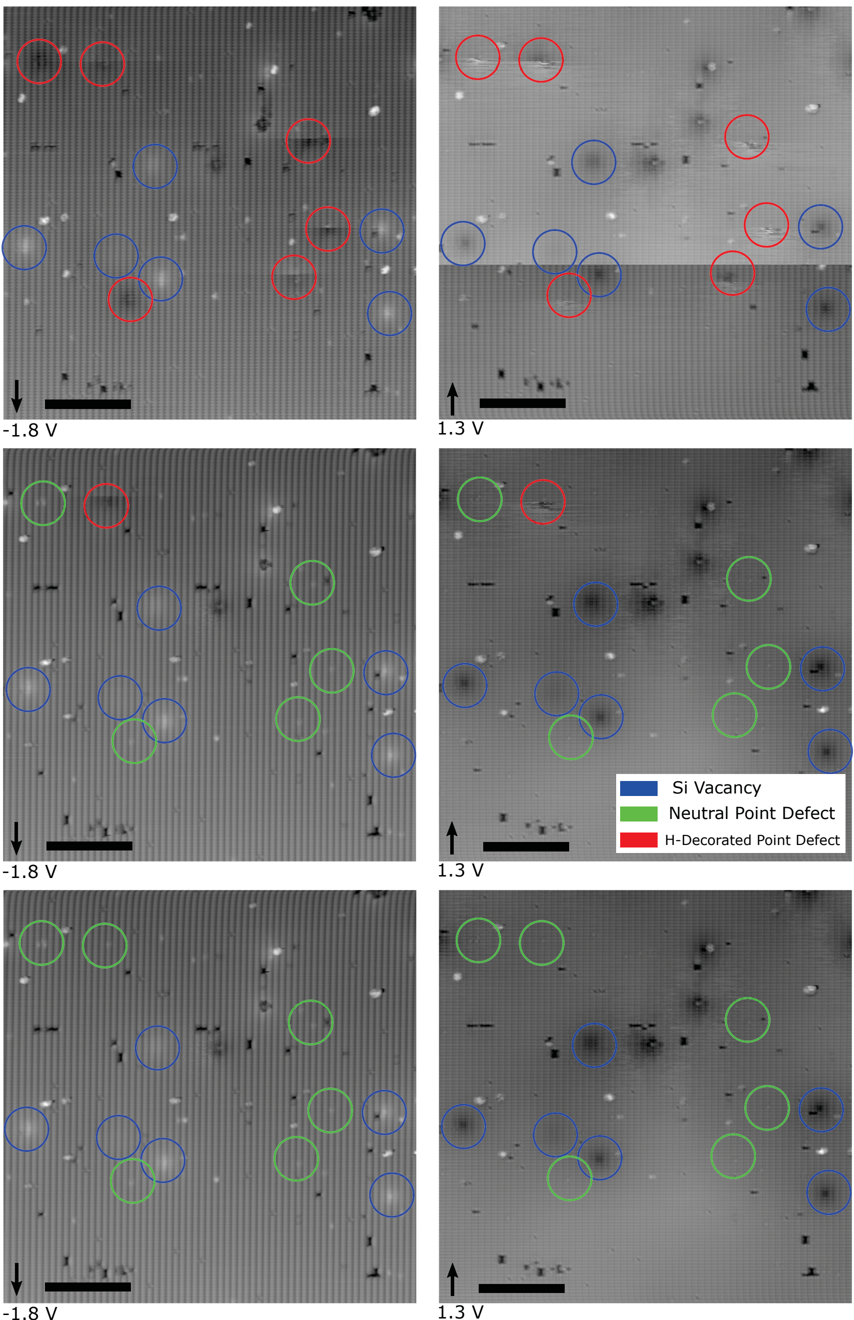

FIGURE 3.23: **Hydrogen removal from H-decorated point defects.** This was taken immediately after an approach before tip conditioning occurred so the tip apex is highly asymmetric. As images are taken at alternating bias values (-1.8 V to 1.3 V), one can observe the removal of H from the defect and the associated transition from the negative (red circle) to neutral charge state (green circle). Silicon vacancies are highlighted as well (blue circle) to provide a reference to the charge state of the defects. Scan direction is indicated by the arrows. Scale bar is 10 nm.

3.4 Unpublished Supplemental Data Regarding Defects and Imaging Modes

The following section presents data which did not fit the scope or length of the paper, but allows for a greater analysis of the data thereby providing a good foundation to potential future studies. A more thorough analysis of the tip-sample interaction with both a hydrogen and silicon terminated AFM tip is shown, better highlighting their observed properties. Line profiles of defects imaged with a Si-apex tip are also fit to extract defect feature sizes. Lastly, additional cases of each defect type are presented which further support the assigned classification made in section 3.2.

3.4.1 Apex Functionalization

The $\Delta f(z)$ spectroscopies presented in Figure 3.2 were presented to give the reader a better understanding of the overall tip-sample interaction and how these interactions translate to the observed surface features. To better understand the nature of the interaction between the apex atom and the surface, a background subtraction can be done to remove any bulk tip-sample interactions [7]. By subtracting the $\Delta f(z)$ spectroscopy taken between dimer rows (purple marker in Figure 3.2) and the spectroscopy taken above an H-Si atom (green marker in Figure 3.2), this removes much of the long range bulk interactions between the tip and sample.

Looking at the subtracted Δf spectroscopies of Figure 3.24 (a), and (b), both tip functionalizations have lost a significant amount of the longer range interactions. A slight positive increase in Δf for the Si tip is seen at around -270 pm followed by the characteristic sharp drop in Δf starting at around -350 pm marking what can be interpreted as the onset of the attractive covalent interaction. The H terminated tip shows a slight decrease in Δf at

roughly -300 pm with a large increase shortly thereafter marking the onset of the repulsive Van der Waals interaction.

By applying the Sader-Jarvis force conversion method mentioned in Chapter 2, force spectroscopies of each $\Delta f(z)$ signal can be extracted as shown in Figure 3.24 (c), and (d). Each force curve was fit with a double distance dependant function incorporating an attractive and repulsive interaction of various power dependence shown as an inset to Figure 3.24 (d). The residual sum of squares (RSS) was determined for each power combination to serve as a measurement of goodness of fit. The force spectroscopy of the Si tip (Figure 3.24 (c)) shows an early onset repulsive interaction best fit with an r^2 or r^3. The attractive potential which onsets at reduced separation appears to be best fit with an r^7. Since this interaction is understood to be covalent in nature, the fitting functions used provide very little towards a useful physical representation of the interaction and require more complicated modelling methods to convey this interaction. The force curve of the H-functionalized tip (Figure 3.24 (d)) was fit with curves better matching the expected Leonard-Jones interaction. The best fit was achieved using a 5-9 force curve although the L-J 7-13 force curve is also shown. The variation between the two seem to be well within the noise of the measurement suggesting that a significant noise reduction of the initial Δf signal using greater averaging is needed to better extract the nature of the interaction.

The potential curves calculated from the $\Delta f(z)$ spectroscopies are shown in Figure 3.24 (c), and (d). Interestingly, the Si tip shows a strong repulsive potential with a maximum of roughly 0.065 eV before the sharp attractive onset. While the origin of this feature is unknown, it is possible that it is merely an effect from scan noise which has been magnified through the conversion. The minimum value of the potential only reaches roughly -0.01 eV within the probed depths, however based on the shape of the curve, it is likely that if it was experimentally possible to probe at smaller separations, the minimum potential would continue significantly lower. The Si-tip potential was also fit with a Morse potential as shown in equation 2.12 in an attempt to better extract the covalent nature of the interaction. Similar to the Leonard-Jones fits, the Morse potential does not seem to correctly fit the shape of

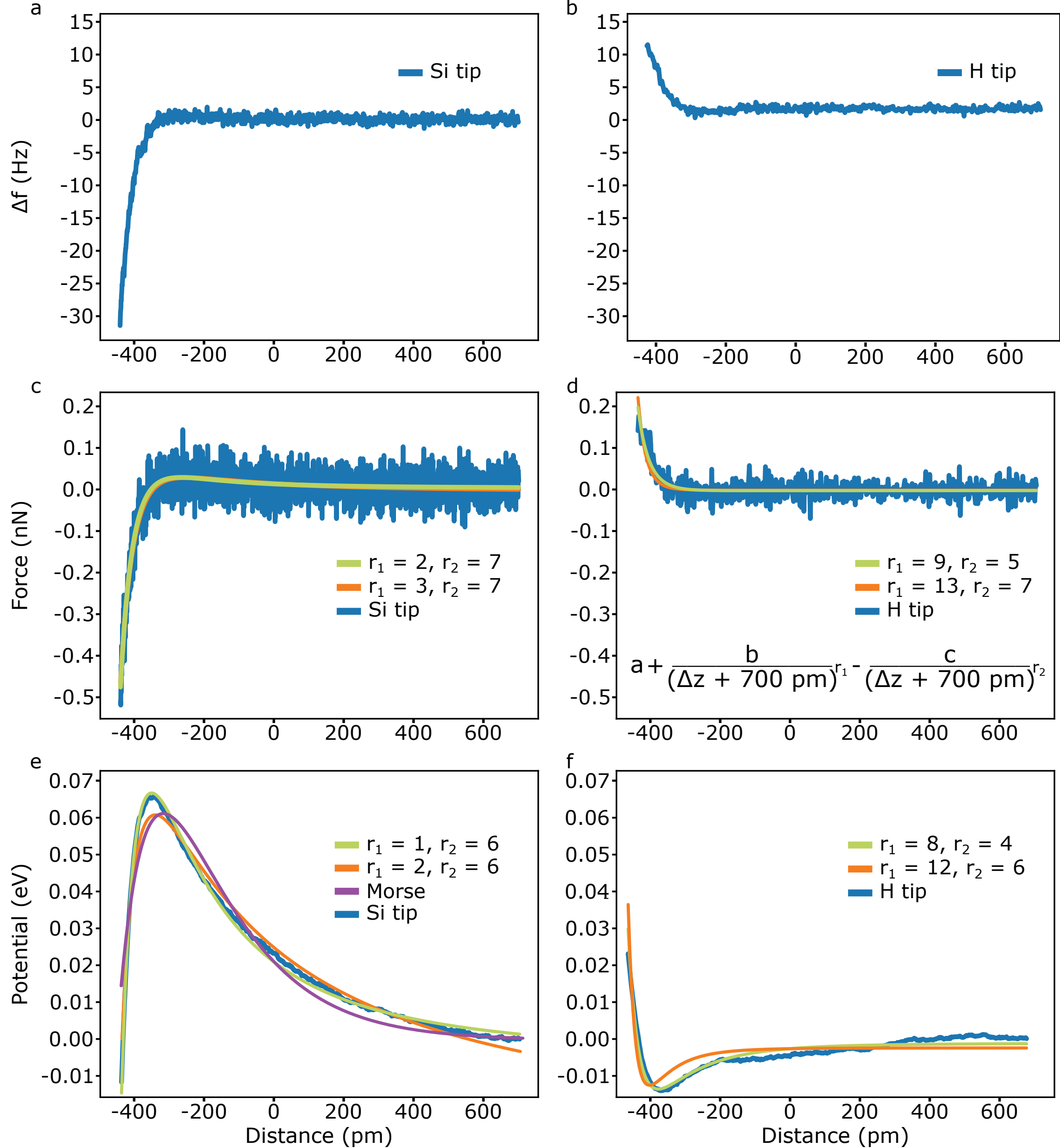

FIGURE 3.24: **Background subtraction of $\Delta f(z)$ spectroscopies.** (a) Δf (z) spectroscopy of the Si apex with inter-dimer spectroscopy subtracted from the H-Si spectroscopy. (b) Same as (a) with the H functionalized AFM tip. (c) F(z) spectroscopy of the Si terminated AFM tip as calculated using the Sader-Jarvis method described in the text. (d) Same as (c) with an H functionalized apex. Fitted curves in green and orange show a L-J tip potential as indicated in the inset of (d). Powers of r are indicated. (e) U(z) spectroscopy of the Si terminated AFM tip as calculated with the Sader-Jarvis method described in the text. (f) Same as (e) with an H functionalized apex.

the curve likely due to the absence of the short range repulsive interaction. As mentioned in Chapter 2, it is difficult to probe at further reduced separation distances as it is common for an H atom to transfer from the surface to the tip changing the tip-sample interaction. In order to better extract a functional form of the Si tip interaction with the surface, further $\Delta f(z)$ spectroscopies could be completed over DBs with varying charge states to extract any variations in the covalent or charge induced dipole interactions of the tip [7] to better separate the contributions of the tip-sample interaction. The H-terminated tip shows a characteristic minimum on the order or -0.01 eV which matches the expected strength of interaction of a Van der Waals potential. In addition, the minimum occurs at roughly -350 pm which matches the approximate distance where contrast enhancement is seen in STHM and AFM[140].

The background subtraction is a useful tool to understand the nature of the tip apex-sample interaction, however, there still remain several experimental uncertainties that warrant caution when interpreting the presented results. The primary factor is that the reported spring constant of the AFM cantilever ($k = 1800N/m$) has been reported to vary by up to 50% [286] so without experimentally determining the spring constant for each cantilever used, the calculated force curves are tarnished with a non-negligible error. In addition, the method used to fit the curves assumes that -700 pm is the equivalent 0 point in the interaction curves. This value was taken from [155] and was used because moving 700 pm in from the setpoint was usually accompanied by sudden increases in current with changes to the tip apex marking what is interpreted as a tip-sample contact. While a useful average, this value will vary significantly between tips of the same and different functionalizations. Qualitative observations show that this value of 700 pm will vary by up to 200 pm depending on the tip structure, tip functionalization, and sample properties.

The final experimental consideration which prevents an accurate physical interpretation of the tip-sample interaction is the possibility of a multiple atom apex. Such a case is presented in Figure 3.25 where the single DB imaged in filled states STM (Figure 3.25 (a)) does not show the double feature associated with a multi-tip. Looking at the constant height Δf

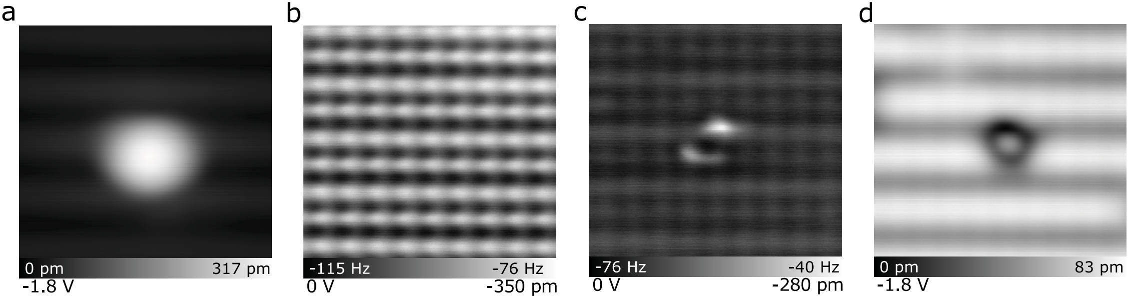

FIGURE 3.25: **Multi contrast AFM functionalization.** (a) Filled states image of a DB imaged with a multi-apex tip. (b) AFM image of the H-Si(100)-2x1 surface with a multi-apex tip. (c) AFM image of a raised SiH_3 species highlighting the multi apex functionalization. (d) Filled states image of the raised SiH_3 species from c. Each image is 4 x 4 nm^2.

measurement in (b), the H-Si surface appears to be imaged with both a Si and H tip that are shifted by roughly 1 Å. When looking at the AFM measurement of a raised Si defect in Figure 3.25 (c), (filled state STM in (d)) it is clear that the tip apex consists of a cluster of atoms, one of which consistent with a Si-apex, and the others consistent with a H-apex. Although this shows an extreme case, it is not uncommon for single tip apexes to feature a secondary atom on the apex. Such an apex does not always have a significant effect on imaging the surface, but will have an effect when analyzing the nature of the interactions as probed with $\Delta f(z)$ spectroscopies.

In order to overcome such limitations imposed by the unknown apex structure, significant statistics would be needed using various cantilevers, tip structures, and surface features. These resulting measurements would then give a more comprehensive understanding of the influence of the cantilever, tip, and sample on the measured interactions. Such an endeavour would likely require measurements from multiple users over many years of experiments and as such is outside the scope if this thesis.

3.4.2 Defect Feature Fitting

Since the dark contrast AFM images taken with a Si-terminated tip apex showed such strong contrast with the substrate and high visibility of each atom of the surface, it was useful to extract the geometry of these surface features. For each of the defects presented in Figure 3.4, the line profiles were fit with Gaussian curves to extract the position of each atom, and subsequently the distance between them.

The 3x1, single dihydride, and dihydride dimer structures are shown in Figures 3.26, 3.27, and 3.28 respectively. Each show the extracted geometry of the defect free surface in grey with the dimensions listed above (b) and (d) of each Figure. Compared to the predicted distance of of 3.5 Å between H atoms within a dimer pair and 4.2 Å spacing between the H atoms of neighbouring dimers in adjacent dimer rows [140], it can be seen in Figure 3.26 that the intradimer spacing is roughly 0.1 nm smaller at roughly 0.34 nm while the interdimer spacing is approximately 0.1 nm larger[1]. When looking at the same dimensions of Figure 3.28, the intradimer spacing is smaller still at roughly 0.32 nm while the interdimer spacing is larger at roughly 0.44 nm. Since both of these images were taken with different tips, it appears that the tip apex has a notable effect on the measured dimensions of the surface.

The effect of the tip structure on the extracted feature size is further observed when comparing the values from the forward and backward scans. Because the apex atom is not always perpendicular to the surface, its reactivity to atoms of the sample can vary depending on their orientation, this effect is most prominently seen in the dihydride pair case in Figure 3.28 where the measured position of each H-Si atom varies depending on which side of the dimer it is on. For this effect to be completely absent from the scans, the apex atom would need to be completely perpendicular to the surface with a very slow scan speed (the scan speed here was $\sim$ 10 nm/s) to eliminate any directional hysteresis.

[1]It is worth noting that the absolute value extracted from the fits is dependent upon a user controlled calibration of the piezo controllers.

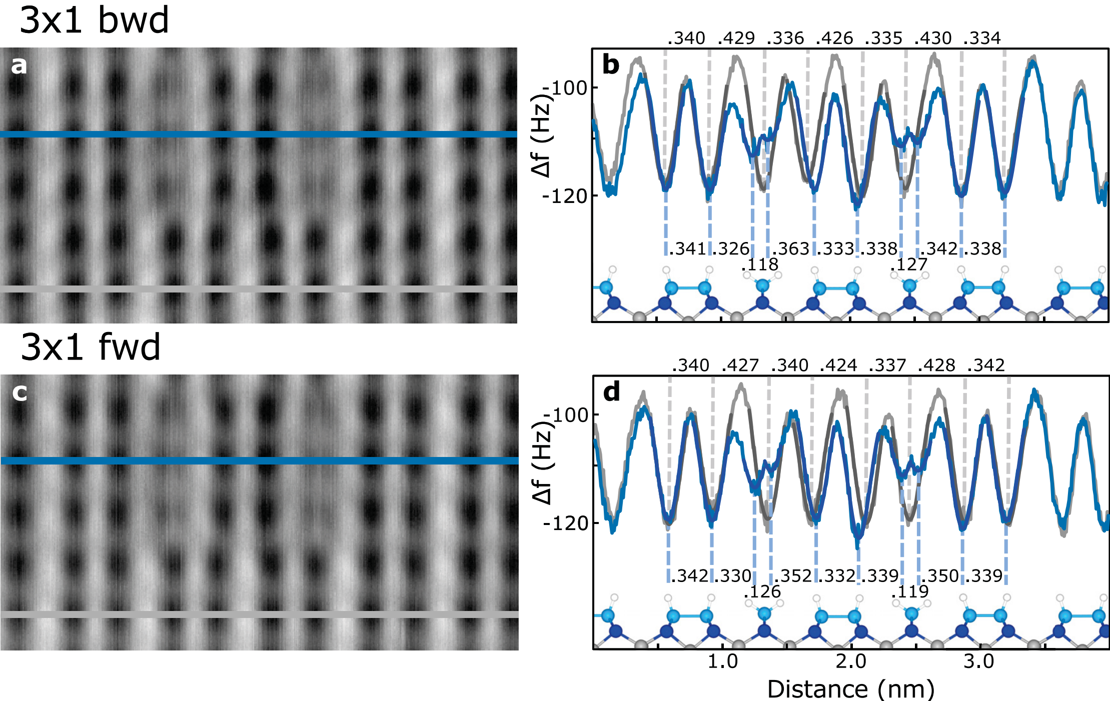

FIGURE 3.26: **3x1 feature sizes.** (a) The backward AFM scan of a 3x1 defect. The horizontal lines correspond to the cross sections taken in (b). (b) Cross sections with a ball and stick model below. Each peak was fitted to a Gaussian distribution with the mean used to calculate the distance between peaks. Errors from each fit are $\leq \pm$ 0.005 nm. (c) The forward AFM scan of (a). (d) Corresponding cross sections of (c). Imaging parameters are the same as Figure 3.4.

When looking at the 3x1 dihydride structure (Figure 3.26), the dimensions of the splitting due to each H atom of the SiH_2 cluster are seen to be roughly 0.12 nm. This is much smaller than the expected positions of each H atom when compared to the ball and stick models suggesting that the splitting over each dihydride species may be a convolution of the Si atom and each H atom. Centred between each dihydride is the newly formed dimer structure which matches the dimensions of dimers along a defect free line.

The single dihydride structure (Figure 3.27) shows a larger variation in forward and backward scans when measuring the splitting feature. Since both the single dihydride and 3x1 defects were imaged with the same tip, this suggests the difference in chemical structure surrounding

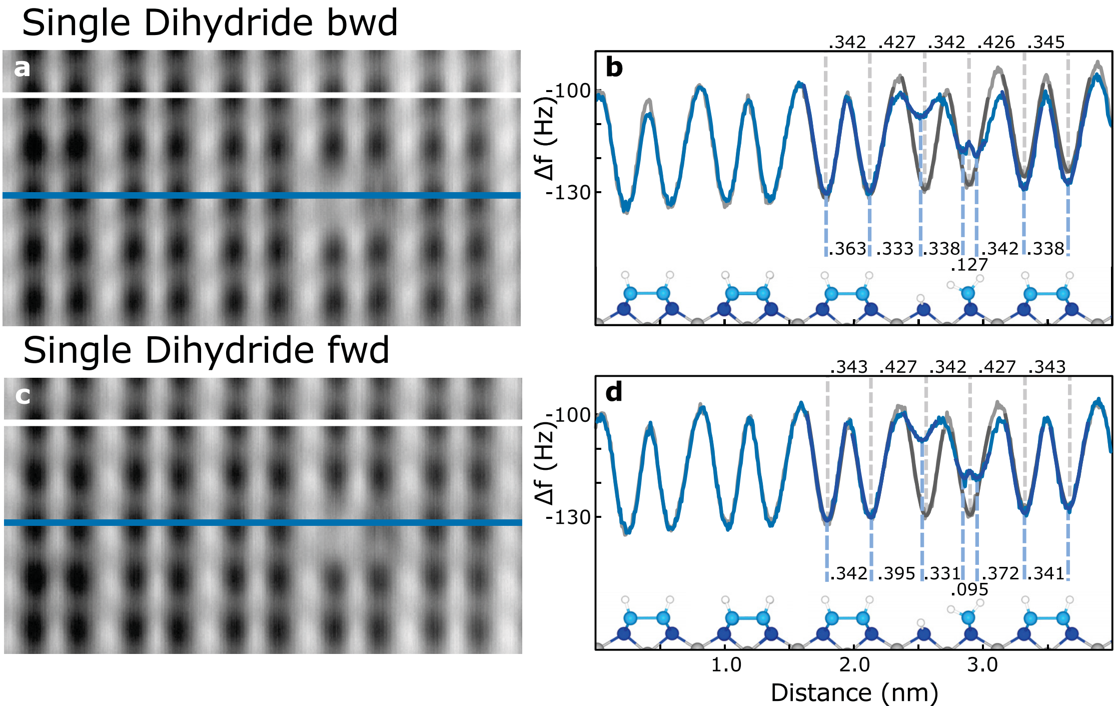

FIGURE 3.27: **Single dihydride feature sizes.** (a) The backward AFM scan of a single dihydride defect. The horizontal lines correspond to the cross sections taken in (b). (b) Cross sections with a ball and stick model below. Each peak was fitted to a Gaussian distribution with the mean used to calculate the distance between peaks. Errors from each fit are $\leq \pm$ 0.005 nm. (c) The Forward AFM scan of (a). (d) Corresponding cross sections of (c). Imaging parameters are the same as Figure 3.4.

the two dihydride defects has an impact on the observed defect structure.

As discussed in section 3.2, the dihydride pair shown in Figure 3.28 did not exhibit the dihydride splitting seen in the other dihydride defects. When looking at the spacing between the inner H atoms, this distance was observed to decrease from roughly 0.32 nm to 0.30 nm as would be expected from the tilted geometry of the SiH_2 species.

The missing dimers in Figures 3.29 and 3.30 were measured along the dimer rows where H atoms have a predicted spacing of 3.9 Å. Since the tip apex will always probe the H-Si atoms with the same orientation, any variation between the extracted distances between the H-Si

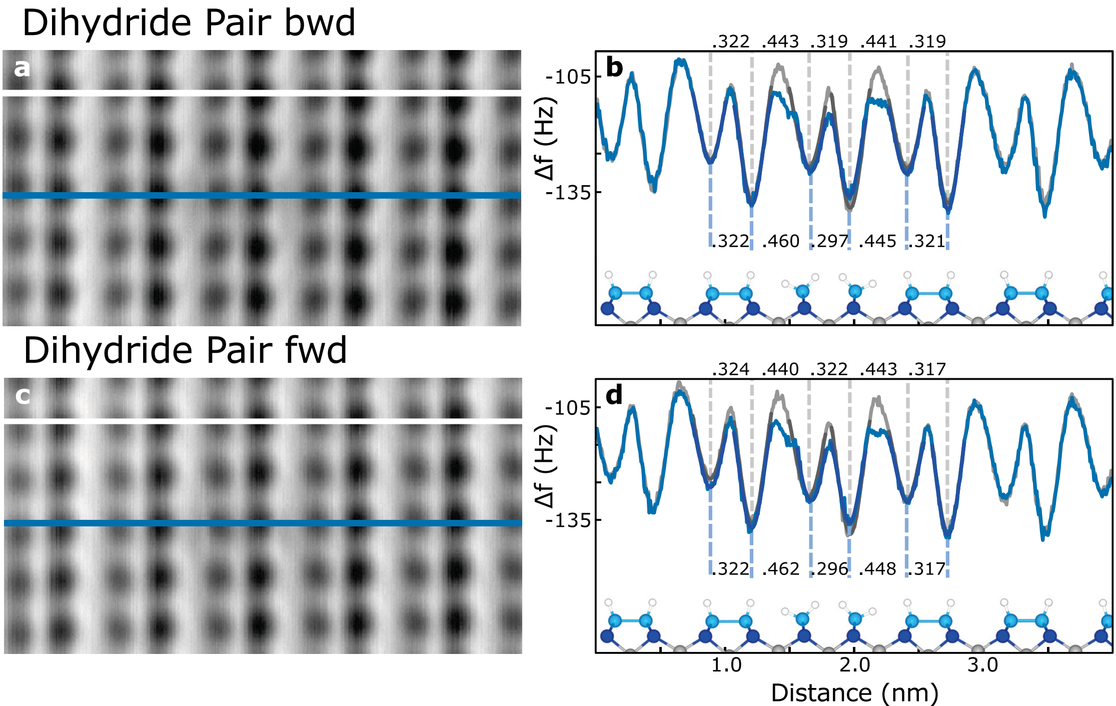

FIGURE 3.28: **Dihydride pair feature sizes.** (a) The backward AFM scan of a dihydride pair defect. The horizontal lines correspond to the cross sections taken in (b). (b) Cross sections with a ball and stick model below. Each peak was fitted to a Gaussian distribution with the mean used to calculate the distance between peaks. Errors from each fit are $\leq \pm$ 0.005 nm. (c) The Forward AFM scan of (a). (d) Corresponding cross sections of (c). Imaging parameters are the same as Figure 3.4.

atoms is a result of noise in the Δf signal and subsequently the fits. The atoms neighbouring the missing dimer do have a directional dependence and show a notable difference in the forward and backward scan directions. Such an effect is emphasized when comparing the relative Δf signal of the two shoulder minima surrounding the missing dimer. In both the bright and dark missing dimer case, the shoulder to the right of the missing dimer is higher than the left, whereas in the forward case, they are more closely matched highlighting the asymmetries of the tip apex structure.

When looking at the distance between these two shoulders, both the bright and dark missing dimer show a distance of roughly 0.86 nm. These are both slightly larger than the defect free

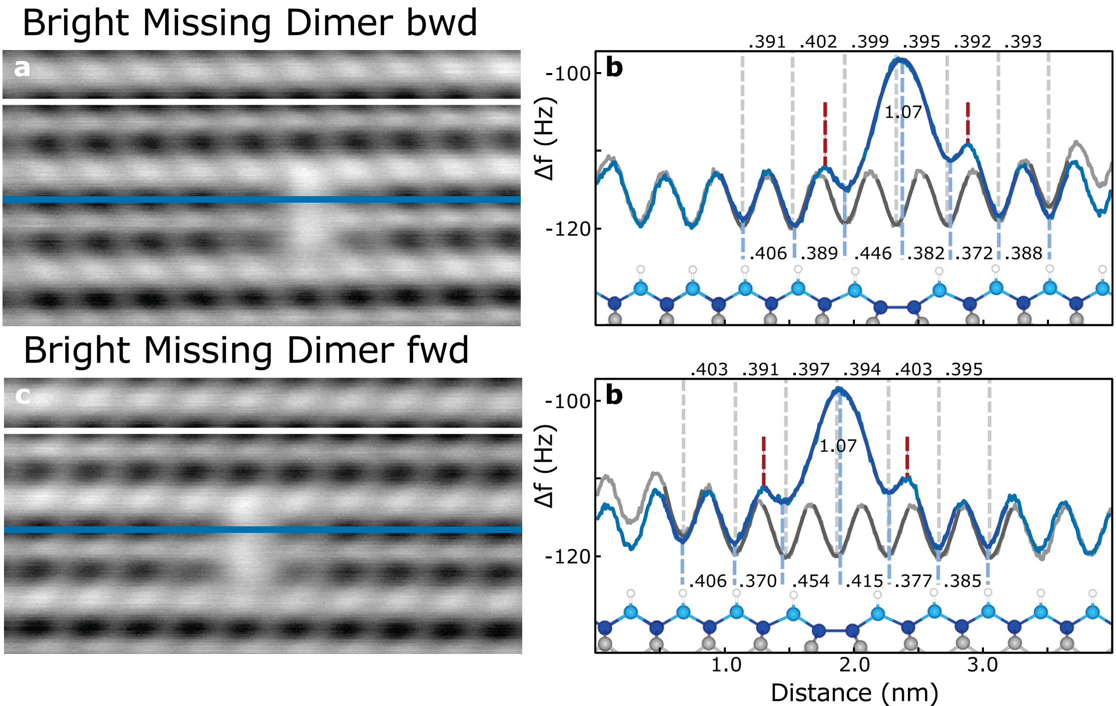

FIGURE 3.29: **Bright missing dimer feature sizes.** (a) The backward AFM scan of a Bright missing dimer defect. The horizontal lines correspond to the cross sections taken in (b). (b) Cross sections with a ball and stick model below. Each peak was fitted to a Gaussian distribution with the mean used to calculate the distance between peaks. Errors from each fit are $\leq \pm$ 0.005 nm. (c) The Forward AFM scan of (a). (d) Corresponding cross sections of (c). Imaging parameters are the same as Figure 3 of the paper.

line of roughly 0.80 nm. The difference between the bright and dark missing dimers becomes apparent when looking at the distance between the peaks just off the shoulders marked in red. The bright missing dimer is smaller by about 0.1 nm. This matches the expected trend of the ball and stick models in which the atoms of the bright missing dimer are pulled closer together due to lattice strain. The suspected reason that this reduction in distance is not seen in the shoulder minima is likely due to an overlap of the missing dimer signal which would also explain why the depth of the shoulder minima does not match the defect free lines as well as the dark missing dimer. Interpretation of the features of both the bright and dark missing dimers would greatly benefit from further experimental and theoretical studies.

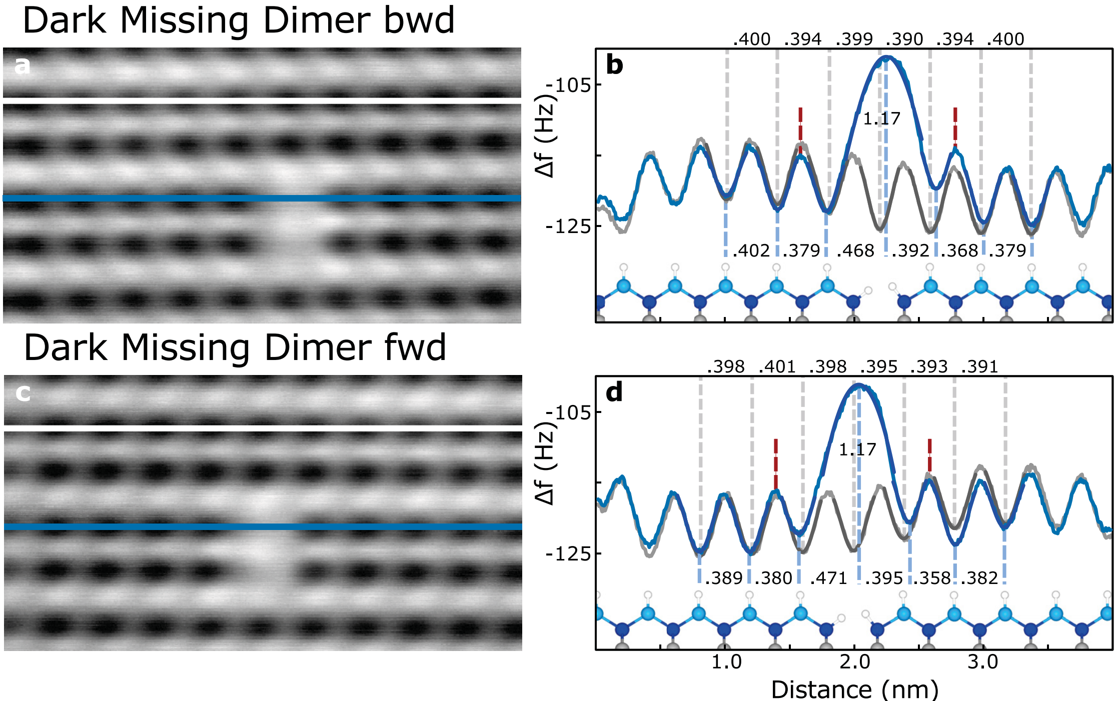

FIGURE 3.30: **Dark missing dimer feature sizes.** (a) The backward AFM scan of a dark missing dimer defect. The horizontal lines correspond to the cross sections taken in (b). (b) Cross sections with a ball and stick model below. Each peak was fitted to a Gaussian distribution with the mean used to calculate the distance between peaks. Errors from each fit are $\leq \pm$ 0.005 nm. (c) The Forward AFM scan of (a). (d) Corresponding cross sections of (c). Imaging parameters are the same as Figure 3 of the paper.

The siloxane dimer of Figure 3.31 shows the expected stretching of the defect dimer length. The defect dimer length is roughly 0.44 nm with the distance between the H-Si atom and the O atom at roughly 0.22nm. Again there is a slight hysteresis when comparing the forward and backward directions. Although it is tempting to try to extract some relative height of the oxygen compared to the H atoms, the measured difference in Δf is a combination of the difference in height, but also variations in the covalent and dipole interactions between the H and O atoms.

The Si Vacancy I is presented in both directions in 3.32. Along the dimer rows (Figure 3.32 (a)-(d)), the difference between minima surrounding the defect are roughly the same

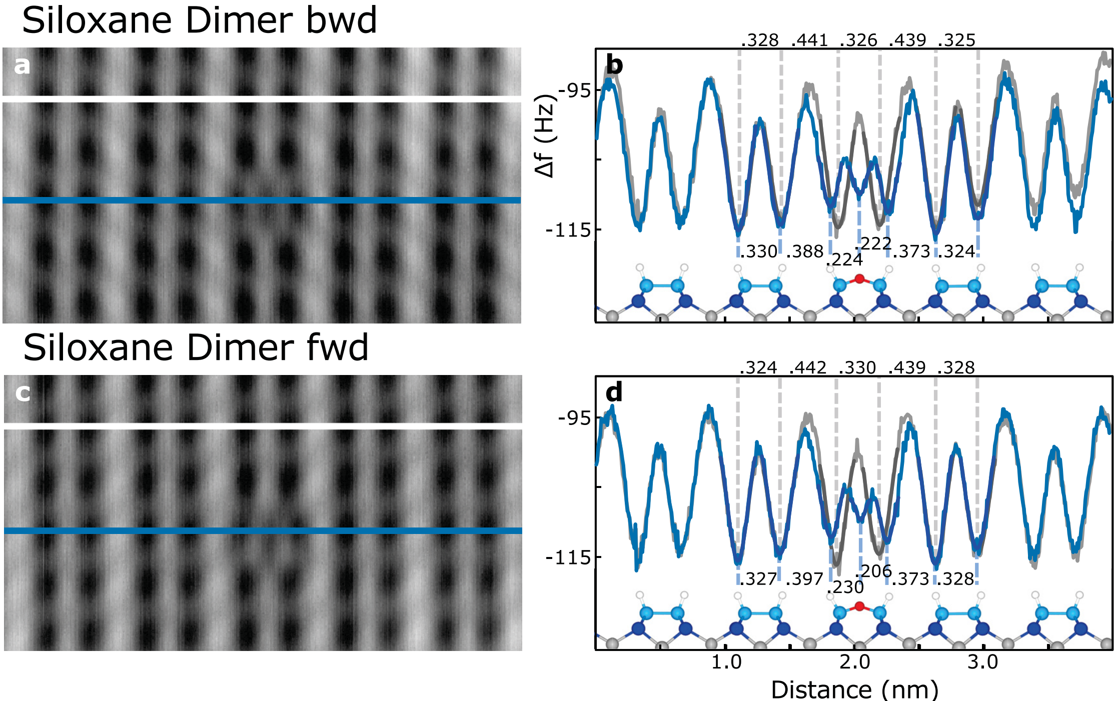

FIGURE 3.31: **Siloxane dimer feature sizes.** (a) The backward AFM scan of a siloxane dimer defect. The horizontal lines correspond to the cross sections taken in (b). (b) Cross sections with a ball and stick model below. Each peak was fitted to a Gaussian distribution with the mean used to calculate the distance between peaks. Errors from each fit are $\leq \pm$ 0.005 nm. (c) The Forward AFM scan of (a). (d) Corresponding cross sections of (c). Imaging parameters are the same as Figure 3 of the paper.

as the defect free line. When measured across the dimer row however (Figure 3.32 (e)-(h)), the distance between the H-Si atom of the defect and the nearest dimer is roughly 0.02 nm longer than the defect free line. This supports the claim made that the vacancy is a source of lattice strain, pulling in surrounding atoms. The Si vacancy II (Figure 3.33) shows a similar lattice strain effect with the distance between two neighbouring H atoms above the defect reduced to 0.34 nm compared to the expected defect free distance of 0.40 nm.

Lastly, the neutral point defect shows a similar reduction in lattice spacing with the dimer distance dropping to 0.26 nm from the defect free 0.31 nm (again notice that the defect free spacing of H-Si atoms has changed with the intradimer spacing reduced to 0.30 nm and the

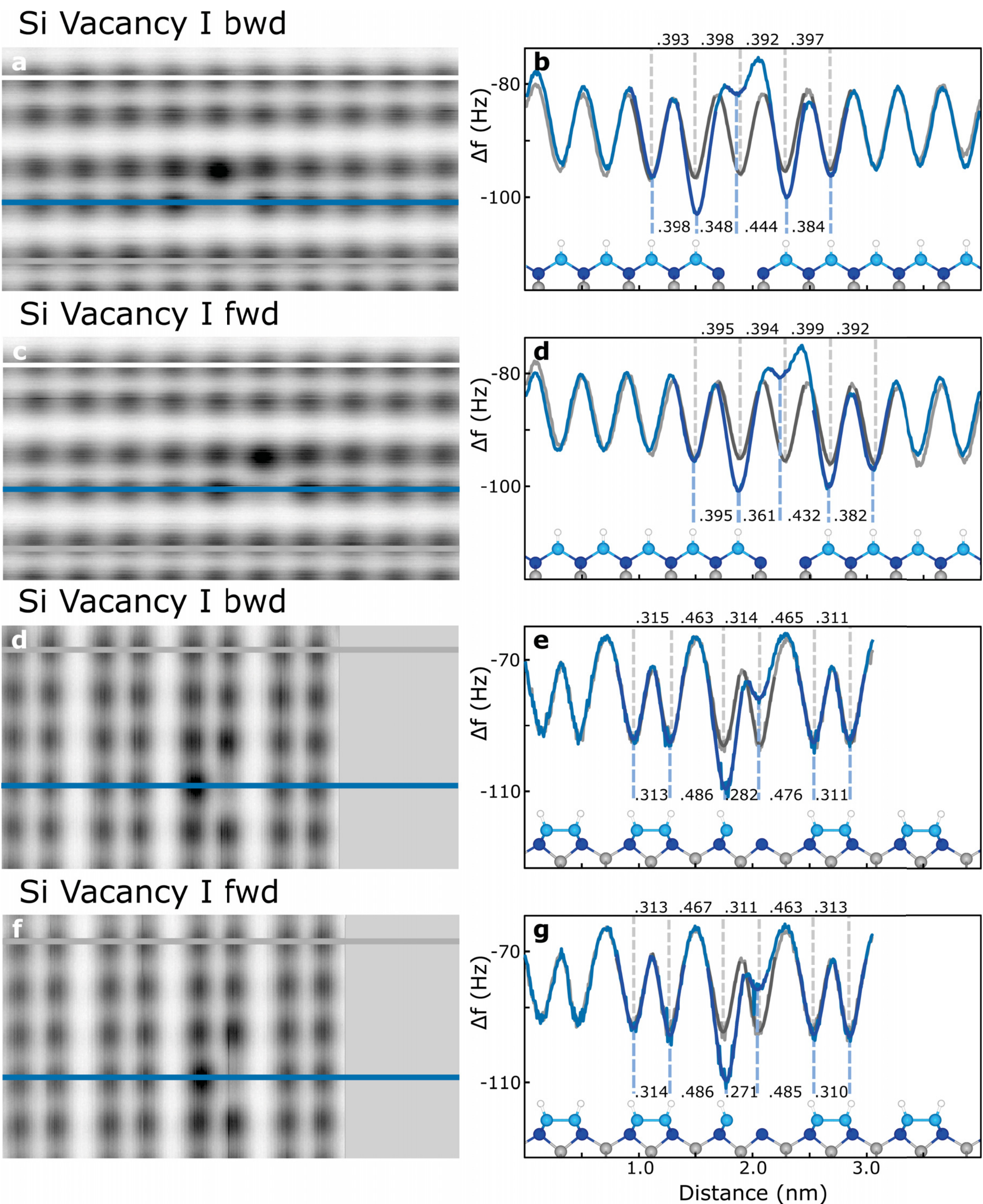

FIGURE 3.32: **Silicon Vacancy I feature sizes.** (a) The backward AFM scan of a silicon vacancy I defect. The horizontal lines correspond to the cross sections taken in (b). (b) Cross sections with a ball and stick model below. Each peak was fitted to a Gaussian distribution with the mean used to calculate the distance between peaks. Errors from each fit are $\leq \pm$ 0.005 nm. (c) The Forward AFM scan of (a). (d) Corresponding cross sections of (c). Imaging parameters are the same as Figure 3.4.

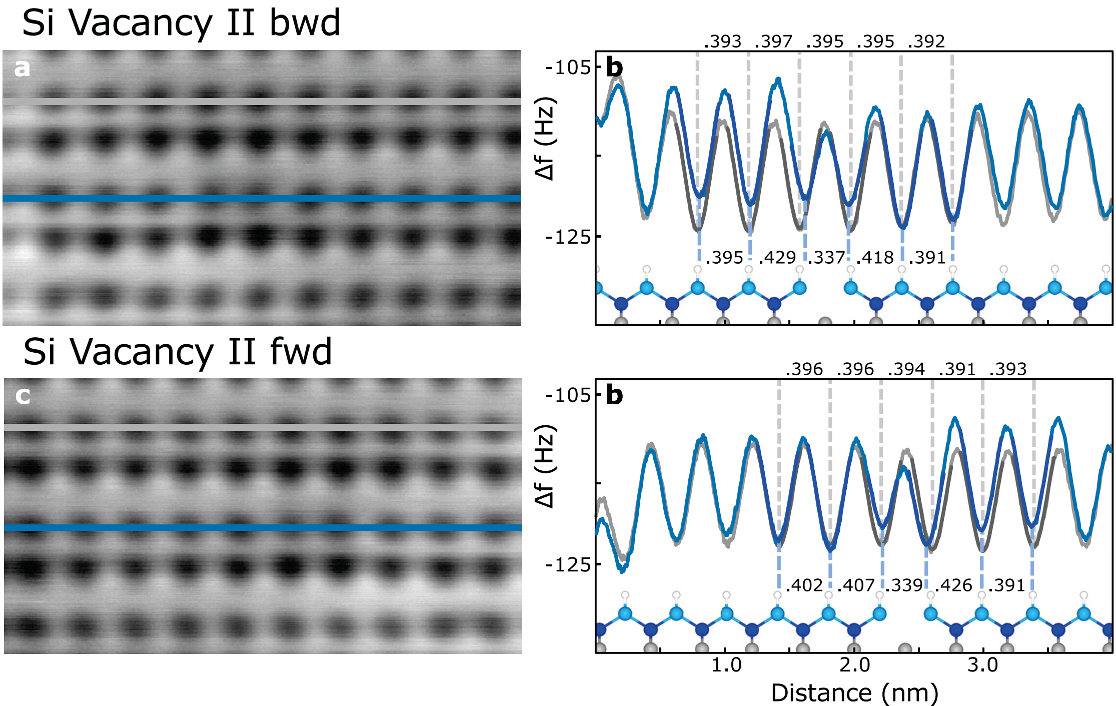

FIGURE 3.33: **Silicon vacancy II feature sizes.** (a) The backward AFM scan of a silicon vacancy II defect. The horizontal lines correspond to the cross sections taken in (b). (b) Cross sections with a ball and stick model below. Each peak was fitted to a Gaussian distribution with the mean used to calculate the distance between peaks. Errors from each fit are $\leq \pm$ 0.005 nm. (c) The Forward AFM scan of (a). (d) Corresponding cross sections of (c). Imaging parameters are the same as Figure 3.4.

interdimer spacing increased to 0.49 nm. This is a result of using a Si tip different from Figures 3.26 and 3.28). This reduction in dimer length supports the claim that the neutral point defect is made from an atom different from Si with a larger electronegativity thus decreasing the bond length.

As mentioned previously, the measured distance between atoms is dependent on tip, direction, and scan speed. In order to better provide useful defect dimensions for theoretical modelling, a larger defect data set is likely needed allowing for feature averaging with multiple tip functionalizations and shapes.

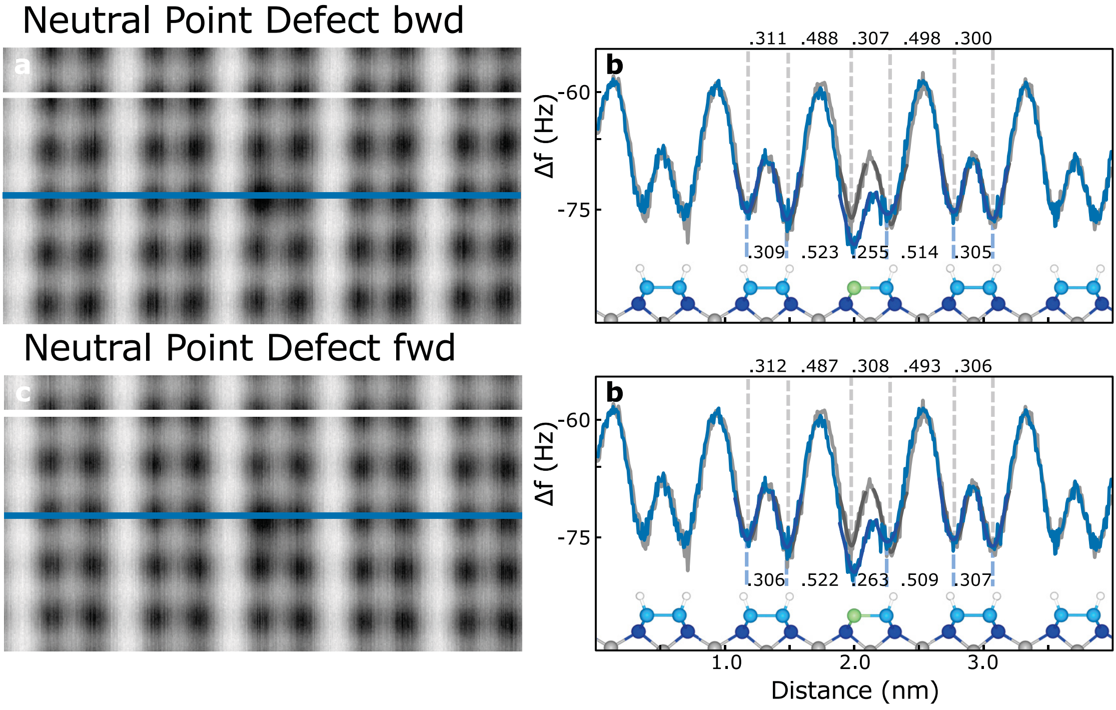

FIGURE 3.34: **Neutral point defect feature sizes.** (a) The backward AFM scan of a neutral point defect. The horizontal lines correspond to the cross sections taken in (b). (b) Cross sections with a ball and stick model below. Each peak was fitted to a Gaussian distribution with the mean used to calculate the distance between peaks. Errors from each fit are $\leq \pm$ 0.005 nm. (c) The Forward AFM scan of (a). (d) Corresponding cross sections of (c). Imaging parameters are the same as Figure 3.4.

3.4.3 Additional Defect Information

The following subsection will present several images collected for various defect types which either did not contribute enough to the content of the publication or were too noisy. They did however aid in the development of understanding the classification and behaviour of the defects and will likely provide useful information for further studies so it is beneficial to present them now.

3.4.3.1 Dihydrides

The dihydride feature of the H-Si(100)-2x1 surface was the most common defect feature found when scanning the surface. Although understood by comparing theoretical simulations with STM images, the presence of two separate atoms at the position of each host Si atom was not observed until imaged in AFM with a Si terminated tip. The characteristic splitting is easily observed in the 3x1 structure where the SiH_2 atoms are surrounded by dimers on all sides as shown in Figure 3.35 (a),(b), and (c) (empty states STM, H apex AFM, and Si apex AFM respectively). The dihydride dimer (in surrounding grey box) experiences an asymmetric chemical environment where each SiH_2 structure experiences a repulsive tilt resulting in the outer H atoms in the pair preferentially tilting towards the surface making the defect almost indistinguishable from neighbouring H-Si dimers using a Si tip. This image was the first taken which confirmed that even though the SiH_2 cluster of a 3x1 structure and a dihydride dimer are chemically the same, their geometric position relative to the surface greatly affects how each atom is imaged. It is also worth mentioning that based on the H-apex AFM image in Figure 3.35 (b), this tip shows a notable asymmetry when imaging the H-Si atoms so it would be thought of as a "poor" tip, but it can also appreciably differentiate between the H_2Si species of the dihydride pair and the defect free H-Si atoms highlighting that it is important to explore various tip shapes even if they do not produce the most symmetric images.

The struggle to understand the difference between dihydrides of a dihydride pair and 3x1 structure resulted in the imaging of several different dihydride pairs with varying Si-apex tips. Four such images are presented in Figure 3.36. It is interesting to compare empty states STM images on the left to the dark contrast AFM images on the right. Figures 3.36 (a), (b), and (c) show the "true dimer" contrast in the STM images while (d) shows the "false dimer" contrast in the STM images. This further highlights the point made in Section 3.3 that it is difficult to identify the type of tip apex from the STM contrast. Additionally, it is worth pointing out that only Figure 3.36 (a) shows the smaller distortion from the outer

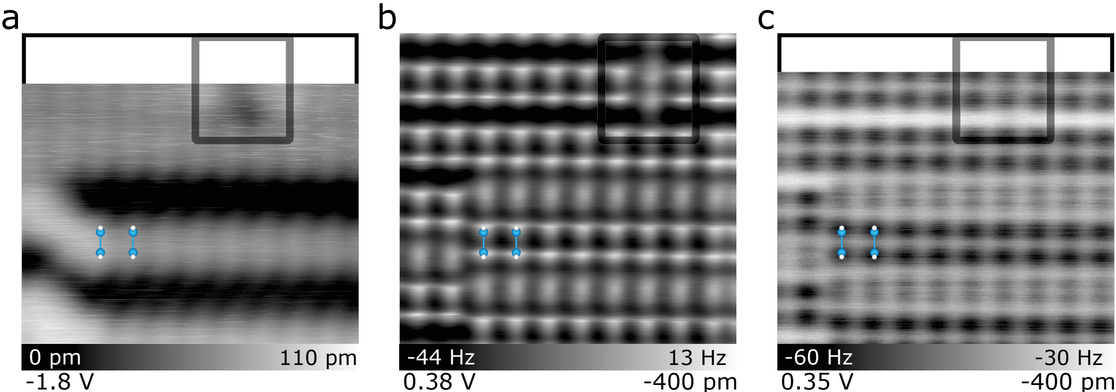

FIGURE 3.35: **Dihydride features of the surface.** (a) A patch of 3x1 with a dihydride pair indicated by the blue arrow. (b) The H functionalized AFM image. The difference between the SiH_2 of the dihydride pair and 3x1 features are clearly seen when compared to the defect free surface. (c) The dark contrast image showing SiH_2 feature of the 3x1 structure is visible but the dihydride pair appears very similar to the H-Si atoms of the surface.

H atoms of each SiH_2 cluster. Since it is assumed that each of the four tips presented are terminated with a Si apex, the cause of this difference must be due to a different reactivity of each tip due to variations in the overall structure of the apex cluster.

When creating the catalogue, it was also important to provide evidence against classifications that were thought to be incorrect. One such published classification claimed that the dihydride pair or "bow-tie" structure was actually two phosphorus atoms at the surface [287] each with their own hydrogen atom. By removing all H atoms of the structure and then adding them again using tip controlled repassivation [4, 177], the "bow-tie" structure could be expected to either return to its "bow-tie" shape if it were phosphorus atoms, or shift to an H-terminated dimer if it were Si atoms. Figure 3.37 (a) shows a dihydride pair (black box) and the same area in (b) after the defect was erased supporting the claim that the dihydride pair is actually made from two SiH_2 clusters. It was also observed that the desorption of hydrogen from a dihydride species required a greater bias pulse than a normal dimer. So much so that such a pulse would always result in a neighbouring H atom being removed first. It is suspected that this is due to the higher degrees of freedom offered by the absence

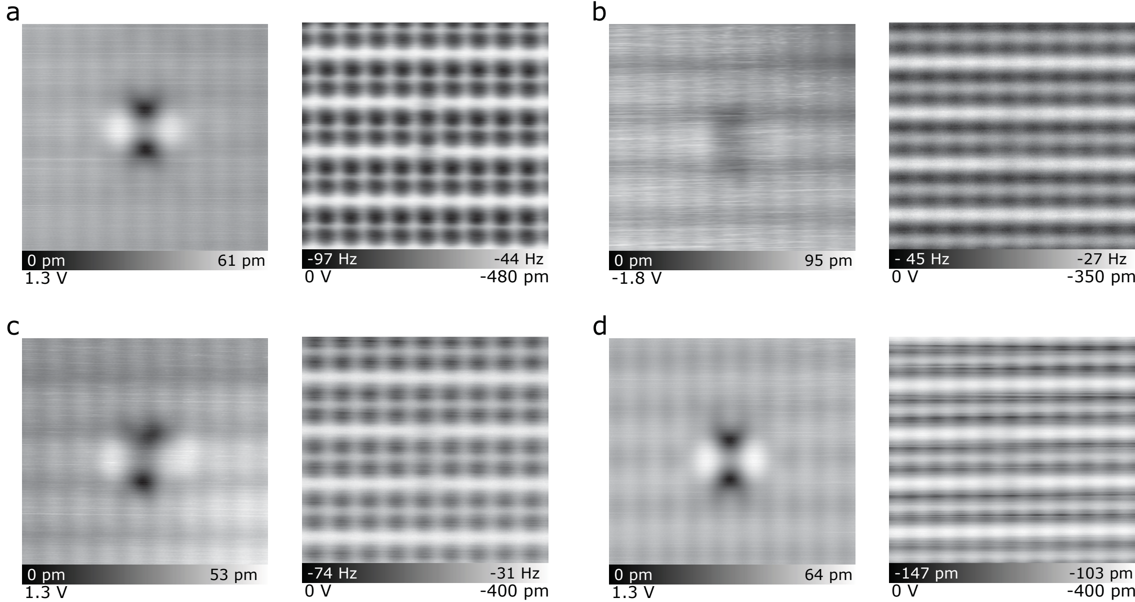

FIGURE 3.36: **Dihydride pairs imaged with dark contrast.** (a-d) Dihydride pairs imaged with unique Si apex tips. AFM images are right and empty states STM images are left. Imaging parameters are indicated below each image. Each image is 3.8 x 3.8 nm^2.

of a dimer bond allowing more of the pulse energy to be transferred into the motion of the SiH_2 cluster rather than breaking the Si-H bond. This is similar to the observed trend that fabricating DB pulses at room temperature require a larger pulse amplitude compared to low temperature. In order to ensure that the dihydride species was fully desorbed, a small patch was removed shown in Figure 3.37 (c) in which hydrogen atoms were incrementally added shown in Figure 3.37 (d)-(j).

In addition to H desorption, the manipulation of a dihydride structure was also observed using a physisorbed H atom [6, 177] shown in Figure 3.38[2]. The adsorbed H atom is first observed in Figure 3.38 (a) marked by the blue arrow with two dihydride pairs above (red arrow), and a bare dimer structure below (black arrow). The constant height STM image is

[2]A recent study [220] suggests that such an H atom may actually be chemisorbed with a Si atom and that the negative charge originates from a subsurface DB although this is inconsistent with our experimental observations

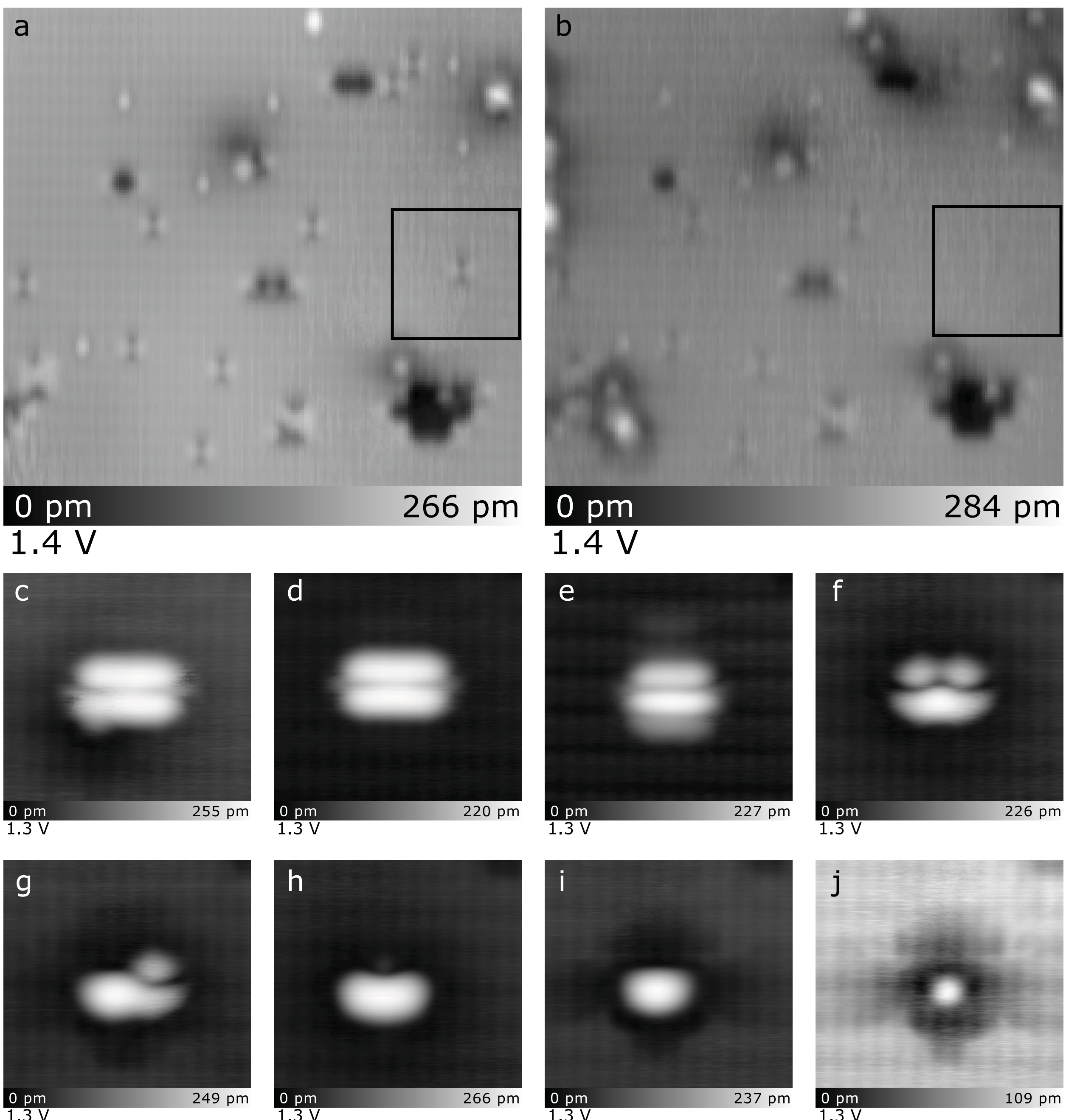

FIGURE 3.37: **Erasing a dihydride pair.** (a) The empty states image of the surface with a dihydride pair highlighted by the bounding box. (b) The same surface with the dihydride pair erased. The additional surface DBs were created for tip functionalization needed for DB erasure. (c-j) The incremental erasure of the DB patch made over the dihydride. Imaging parameters are below each image. (a-b) are 20 x 20 nm^2 with a 5 x 5 nm^2 bounding box. (c-j) are 5 x 5 nm^2

shown on the right which suggests that the H atom preferentially sits between two adjacent dimer rows. By scanning at a bias of -1.8 V, the hydrogen atom can often be moved away from the tip (as shown in Figure 3.21). In this instance, the adsorbed H atom became trapped next to the two dihydride pair structures shown in Figure 3.38 (b). The constant height image on the right suggests the H atom is now positioned between two atoms of the same dimer. Such a position is thought to be more unstable than that shown in Figure 3.38 (a) since it is very rarely observed. By scanning at higher positive bias values (Figure 3.38 (c)), sharp changes in contrast near the dihydride pairs were observed. Subsequent imaging at non perturbative bias values shows that the left dihydride pair was shifted down a dimer row with the adsorbed H atom now just out of frame (as indicated by the circular streakiness above the two dihydride pairs.)

The last point of interest regarding dihydrides is in a common variation of the single dihydride. Much like etch pits, which are just larger extensions of missing dimers, a single dihydride can often be seen in larger clusters such as that shown in Figure 3.39. Interestingly, such single dihydride clusters are often seen in groups of three like this hinting at some unknown preference for Si atoms to be etched from the surface in clusters of 3.

3.4.4 Missing Dimers

The classification of the missing dimers was a point of contention since the differences between them are so minute. Looking at Figure 3.40 (a), it can be seen that two distinct variations are observed. Minor differences can even be seen when looking at the filled states images in (b) with very little distinction available in the constant height STM images in (c). Another anecdotal observation about such missing dimer clusters is that clusters that are formed across several dimer rows (as shown in Figure 3.40) were always observed to alternate between bright and dark species, never two bright species next to each other[3]. While it is difficult to confirm the reason without theoretical simulations, one suggested reason is that the formation

[3] This point does not claim that they would never sit next to each other, only that it was never observed.

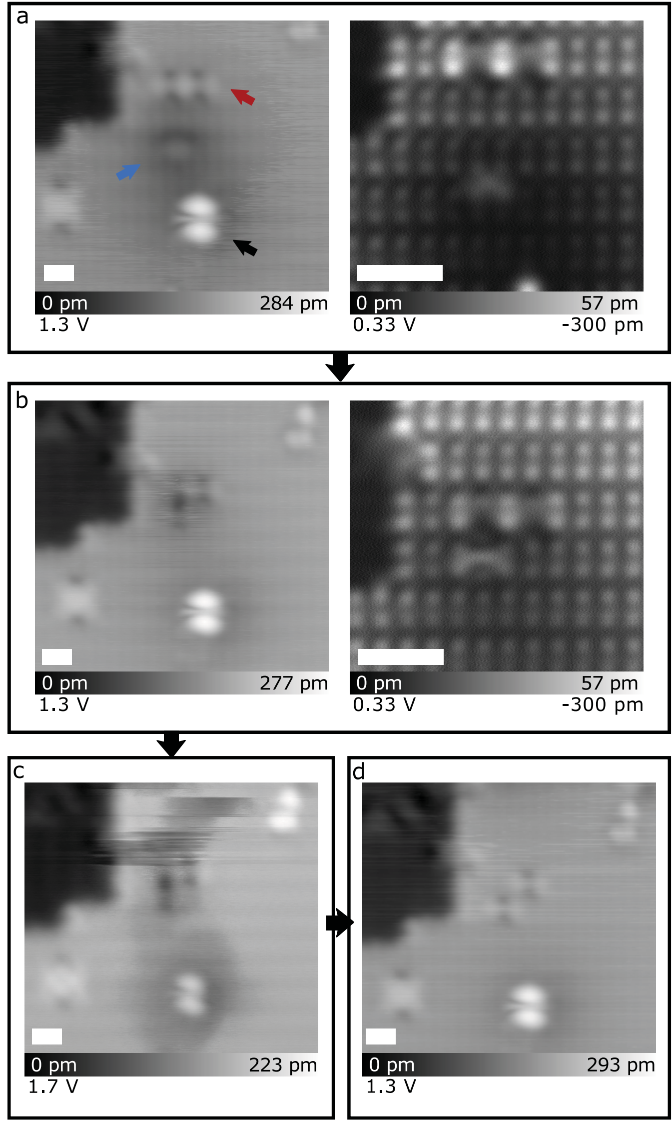

FIGURE 3.38: **Dihydride pair shifting.** (a) An absorbed hydrogen (blue) next to two dihydride pairs (red) and a bare dimer (black). The constant height image shows the that position of the hydrogen appears to be between two dimer rows. (b) The adsorbed hydrogen has been pushed closer to the two dihydride pairs. The constant height image appears to show the hydrogen between two Si atoms of the same dimer. (c) The surface when scanned at a more positive sample bias (1.7 V). The sharp steps in contrast indicate changes to the distribution of surface atoms. (d) The redistribution resulted in the left dihydride shifting one dimer row lower. An Adsorbed hydrogen is suspected to be just off frame at the top of the image. All imaging parameters are indicated below each image. Scale bar is 1 nm.

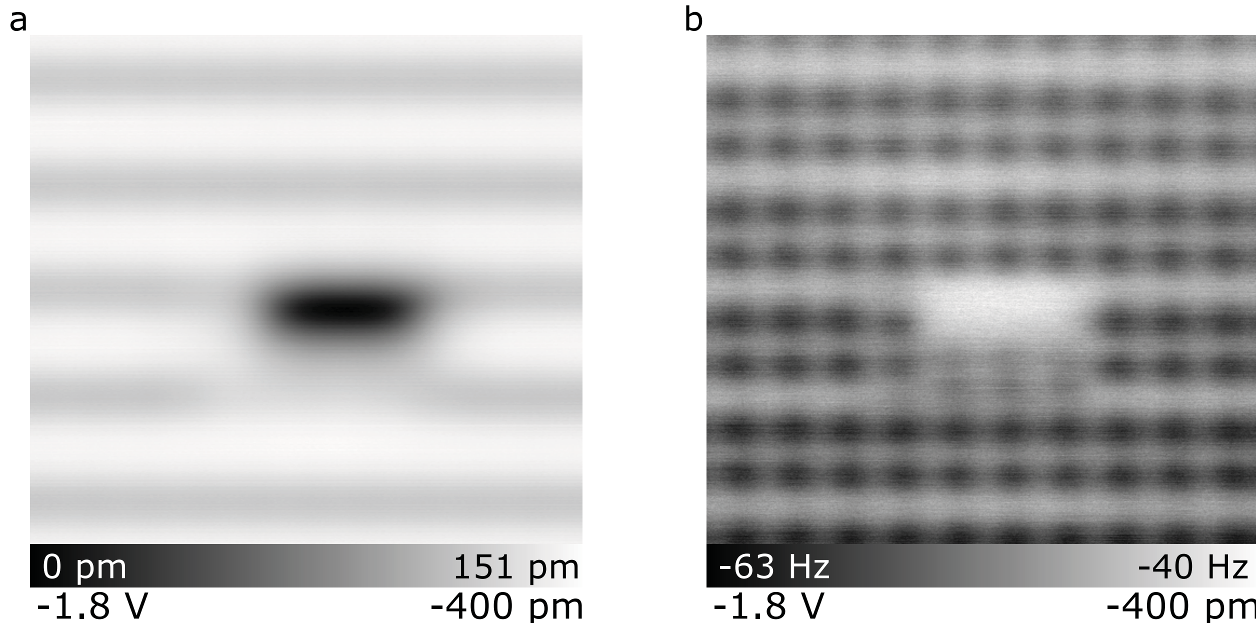

FIGURE 3.39: **Triple single dihydride.** (a) The empty states image of the commonly found triple grouping of a single dihydride. (b) The Si apex AFM image showing the characteristic splitting above the dihydrides. Each image is 4 x 4 nm^2.

of two bright dimers next to each other is likely prohibited due the higher energy cost from the increased lattice strain.

The dark missing dimer was also seen to quite often cluster next to a siloxane dimer as shown in Figure 3.41. Such a combination is estimated to make up roughly 20% of dark missing dimers observed on the surface. Although the reason for these two defects to preferentially form next to each other is unknown, it is likely that additional H atoms on the surface from the adsorption of the initial water molecule contribute to making it energetically favourable to remove the neighbouring Si atoms during hydrogen termination. The scans shown in Figure 3.41 also highlight the difference in imaging quality when using a hydrogen functionalized tip. Figure 3.41 (a),(b), and (c) show the empty, filled, and constant height scans using a tip of standard quality while Figures 3.41 (d),(e), and (f) show an H functionalized tip. As mentioned in Chapter 2, the difference in contrast in the empty and filled states images comes from a different tip density of states offered by hydrogen functionalization while the difference in constant height contrast originates from the flexible H atom of the apex tracing

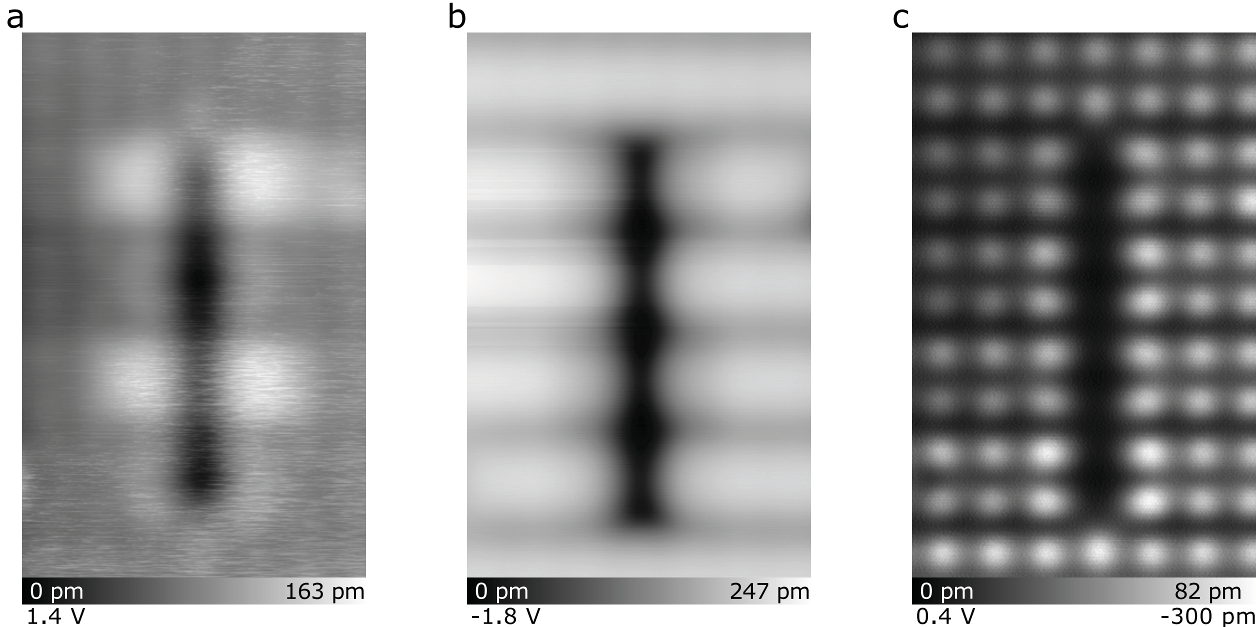

FIGURE 3.40: **Bright and dark missing dimers.** (a) The filled state image of 4 missing dimers across 4 dimer rows. Two bright and two dark missing dimers are seen allowing for a more direct comparison of their empty states features. (b) The filled states image. (c) The constant height image of the same feature. Imaging parameters are indicated below each image. Each image is 2.5 x 4.2 nm ^{2}.

corrugations of the surface through tip apex-sample repulsion.

3.4.5 Siloxane Dimer

The elucidation of the third atom in the siloxane dimer demonstrated the usefulness in imaging with different tip apex atoms. Previously referred to as a "split dimer", the origin of this defect was previously unconfirmed with some groups referring to it as a dihydride pair. It wasn't proposed to originate from water contamination until a study of the chlorinated Si surface looked at the effects of water contamination as mentioned in section 3.2. Attempts to reproduce the results seen in [271] weren't as successful due to the introduction of additional unknown surface contaminants which reduced the overall quality of the surface as shown in Figure 3.42. In this case, a clean Si(100) surface was prepared and allowed to sit in the load lock for several seconds. The base pressure of the load lock was roughly 1×10^{-9} Torr, which

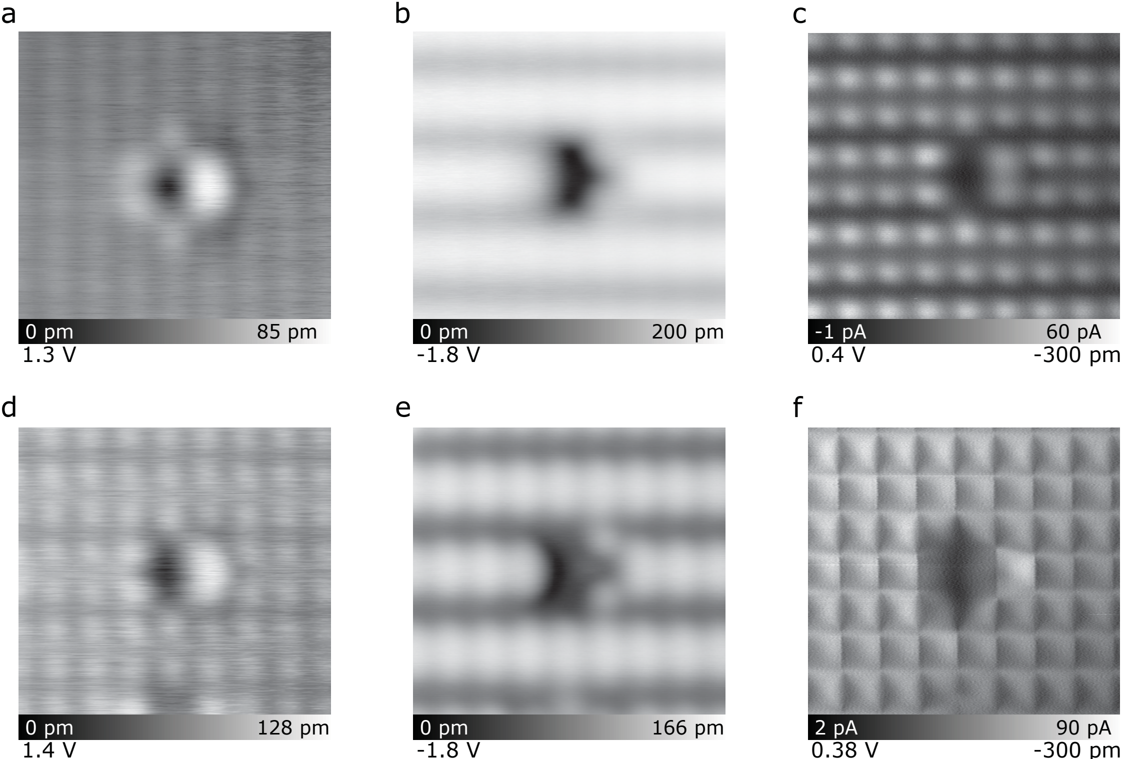

FIGURE 3.41: **Missing dimer with a siloxane dimer.** (a) The empty states imaging of a commonly found defect combination, namely a dark missing dimer and a siloxane bridge. (b-c) The filled states and constant height images respectively. (d-f) Images of the same defect imaged with an STM tip functionalized for STHM. The different surface features extracted between the two data sets further demonstrate the dependence on the tip density of states.

was thought to be high enough to introduce contaminants from the air but not enough to completely dirty the sample. After sitting in the load lock, the sample was returned to the vacuum chamber and subsequently terminated with hydrogen. After scanning the surface, it was clear that a significant number of siloxane dimers were present on the surface (Figure 3.42), but the number of additional surface contaminants make it difficult to get a clean image of the surface. Further studies which leak in water vapour could be done, but would require the system to be immediately baked to remove any subsequent water contamination.

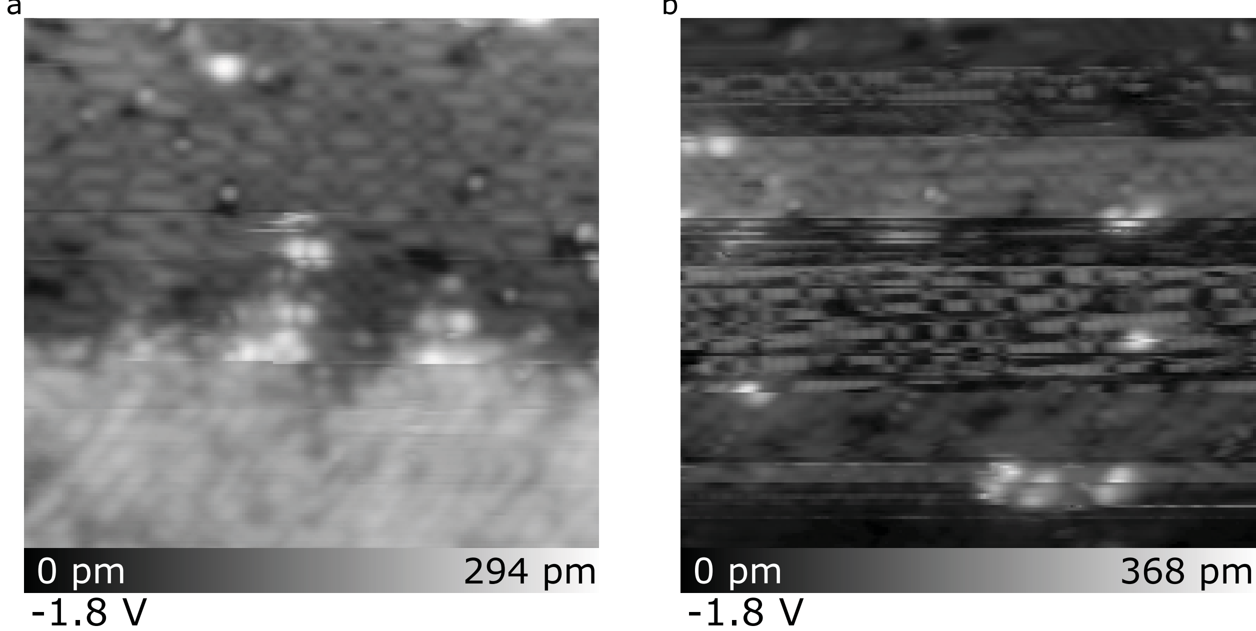

FIGURE 3.42: **Oxygen contamination.** (a) shows a portion of a hydrogen terminated surface with several siloxane dimers from water contamination. The bottom portion of the surface is desorbed patch. (b) shows a different area of the surface with siloxane dimers present. The constant change in imaging contrast is due to tip-sample contacts associated with a "dirty" sample.

3.4.6 Neutral Point Defect

It was originally thought that the charged variation of the neutral point defect was similar to that of a Si vacancy. It wasn't until the observation of the irreversible transition to the neutral point defect was it confirmed to be something different. While the origin is still unknown, a recent theoretical study [220] suggests that the neutral point defect exists in a structure similar to a dihydride pair except one of the H atoms is removed leaving a Si atom with one H atom and a negatively charged DB. Transitioning to the neutral point defect is proposed to occur by removing the H atom of the same Si atom with the DB leaving a Si atom with two DBs and a SiH_2. The proposed species would then exist in a single negative charge state. While additional experimental studies are needed to support these claims, it is likely that such an interpretation is incorrect. The claim that the observed neutral point defect exists as a negatively charged species with a gap state is unsupported by experimental evidence. The absence of any charge induced band bending when imaging at positive sample

biases suggests the species is neutral. In addition, KPFM studies done by Huff *et. al.* [6] extracted a contact potential difference map over a neutral point defect with no observed effect on the CPD . Since the theoretically proposed species is expected to hold a gap state, it should therefore also have significant current in the band gap of the crystal much like a DB on a Si dimer. Looking at the spectroscopy in Figure 3.22, it doesn't appear that such a signal exists furthering the claim that such species is neutral. Lastly, it is unlikely that the proposed DB_2Si H_2Si structure of the neutral point defect would exist in a stable state. It is more likely that such a the system should transition to the more stable H-Si-Si-H dimer. While interesting and useful, the theoretical claims made in [220] would require experimental verification not currently available to support their claims.

Since the charged point defect often transitions to the neutral point defect by scanning at negative sample bias or with reduced tip-sample separation, it is difficult to study it with all imaging modes available, specifically AFM. Figure 3.43 shows a rare image of the charged species in filled (a), empty (b), and constant height STM (c). It is interesting to note the similarities between the constant height STM images in (c) and Figure 3.38 (b), suggesting that the additional H atom may be positioned within the dimer structure. Comparing the charged to the neutral variation of the point defect (as shown in Figure 3.22), it is clear that the position of the bright spot in the constant height STM images shifts closer towards the centre of the dimer, potentially due to the removal of the H atom within the dimer.

The neutral point defect has also been observed to sit next to other defects such as the dihydride pair in Figure 3.44. While this does not provide any further evidence to the origin of the defect, it does confirm that such a defect only affects 1 atomic site.

It is clear that further work is needed to identify the origin of the neutral point defect. The claim made in section 3.2 that the neutral point defect is a contaminant boron atom was due to the observation that further manipulation to the neutral point defect cannot be done via additional pulses (to potentially liberate a bonded H atom). Since the species sits where a Si atom would, and appears to be neutral, it would suggest a trivalent species. Since

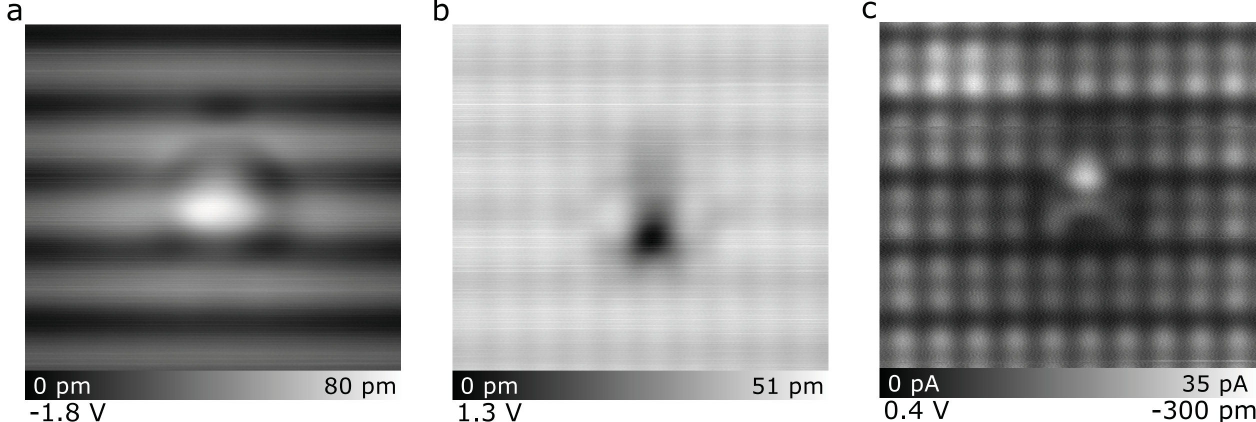

FIGURE 3.43: **The charged point defect.** (a) shows another example of the charged point defect before it is neutralized as imaged in filled states. (b) shows the same area in empty states with (c) showing the constant height image. Imaging parameters are indicated below each image. Each image is 4 x 4 nm^2

boron is more electronegative than Si (resulting in a shorter bond length as shown in Figure 3.34), and boron atoms have been observed to migrate to the surface during sample flashing, the origin of the neutral point defect was assigned to boron. Further investigations with crystals of varying boron concentrations and flashing procedures are needed to extract any correlation between the defect origin and boron.

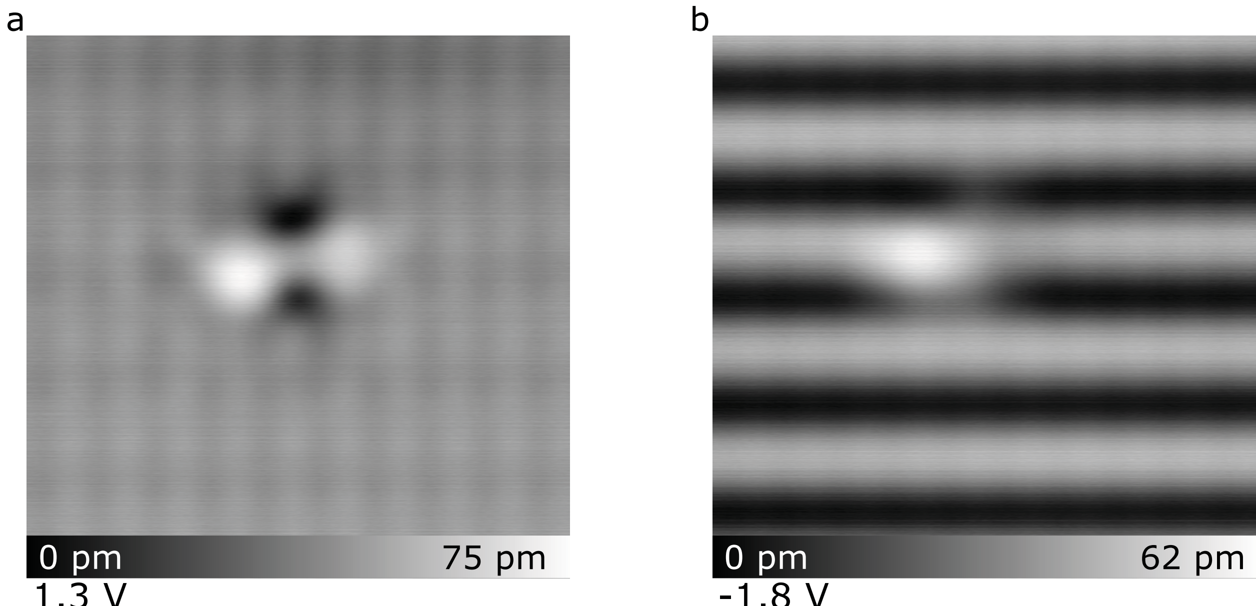

FIGURE 3.44: **Neutral Point defect with a dihydride pair.** (a) shows the empty states image of a neutral point defect imaged next to a dihydride pair defect. (b) shows the corresponding filled state image.

Chapter 4

Defect Identification and Segmentation Through Machine Learning

The push to develop "beyond CMOS" devices has led to the need to find alternative methods of fabrication capable of addressing size scales not presently achievable with traditional fabrication techniques. Scanning Probe Microscopes offer a fabrication method capable of Å resolution but with the added cost of extensive user interaction and slower fabrication speeds. The push to fully automate the fabrication of such "beyond CMOS" devices using a scanning probe has thus been an area of great interest. By fully automating device fabrication using a scanning probe microscope, it would allow for the parallelized operation of many scanning probes making it possible to match throughput of current semiconductor fabrication standards.

As discussed in Chapter 2, many initial automating schemes were attempted with minimal success. The complexity of the surface in addition to the somewhat random behaviour of the scanning tip made it difficult to predict and control when scanning the sample. It

wasn't until automated fabrication schemes were coupled with machine learning techniques that significant progress was observed. Since then, machine learning has been applied to a number of scanning probe applications as highlighted in section 2.3.1.

Prior to the incorporation of machine learning into the automated patterning of DBs, a partially automated system was in place. In this system, a user would input the desired pattern and align the pattern to the surface. The surface would have to be pre-scanned to ensure that there were no unwanted defects that would prevent the DBs from being successfully patterned or prevent the DB device from operating correctly. This initial scanning of the surface to locate a viable area to pattern the DB device is the most time consuming portion of the fabrication procedure owing to the slow scan speed, random distribution of defects, and extensive user interaction needed to assess the surface quality. The work shown here demonstrates how locating a viable area for DB patterning can be automated via the incorporation of machine learning into DB device fabrication. By employing a convolutional neural network to identify and locate 6 different defects on the surface, it is possible to assess the quality of the surface for DB fabrication. Once the locations of each of the defects on the surface are known, an algorithm determines the best spot to place a predefined DB pattern such that the distance between the pattern and the defects is maximized.

As mentioned, the work presented in the published paper was chronologically completed before the work in Chapter 3. Through the extensive data labelling, a better understanding of how diverse the defects of the H-Si(100)-2x1 surface were which lead to the development of the defect catalogue. This enhanced understanding of defects was only applied to a second round of data labelling which increased the diversity of defects understood by the neural network. The work involving the expansion of the training data is included in this chapter after the original publication and demonstrates significant improvements made to the abilities of the neural network.

4.1 Deep Learning-Guided surface Characterization for Autonomous Hydrogen Lithography

Reproduced in accordance with the IOP Publishing Author Rights Policy. Online version available (https://iopscience.iop.org/article/10.1088/2632-2153/ab6d5e) [1]

Mohammad Rashidi[1,4], Jeremiah Croshaw[1,4,5], Kieran Mastel[1], Marcus Tamura[1], Hedieh Hosseinzadeh[2], and Robert A. Wolkow[1,2,3,5]

[1] Department of Physics, University of Alberta, Edmonton, Alberta, T6G 2J1, Canada

[2] Quantum Silicon Inc, Edmonton, Alberta, T6G 2M9, Canada

[3] Nanotechnology Research Centre, National Research Council Canada, Edmonton, Alberta, T6G 2M9, Canada

[4] MR and JC contributed equally to this work.

[5] Authors to whom any correspondence should be addressed.

Email: croshaw@ualberta.ca and rwolkow@ualberta.ca

Keywords: convolutional neural network, hydrogen terminated silicon, scanning probe microscopy, surface dangling bonds, automated fabrication, hydrogen lithography

Supplementary material for this article is available in section 4.2.

4.1.1 Abstract

As the development of atom scale devices transitions from novel, proof-of-concept demonstrations to state-of-the-art commercial applications, automated assembly of such devices must be implemented. Here we present an automation method for the identification of defects prior to atomic fabrication via hydrogen lithography using deep learning. We trained

a convolutional neural network to locate and differentiate between surface features of the technologically relevant hydrogen-terminated silicon surface imaged using a scanning tunneling microscope. Once the positions and types of surface features are determined, the predefined atomic structures are patterned in a defect-free area. By training the network to differentiate between common defects we are able to avoid charged defects as well as edges of the patterning terraces. Augmentation with previously developed autonomous tip shaping and patterning modules allows for atomic scale lithography with minimal user intervention.

4.1.2 Introduction

With the miniaturization of complementary metal-oxide-semiconductor technology approaching its fundamental limit, attention has been focused on developing alternatives built at the atomic level [221, 288, 289]. If these devices are to be commercially viable, they must be built in a way that allows parallelized and automated fabrication. Scanning Probe Microscopy (SPM) has provided a means for several different varieties of atom-scale device fabrication including memory systems using a Cu/Cl system [49] or dangling bonds(DBs) on hydrogen terminated silicon (H-Si) [4], spin-based logic using Fe atoms on a Cu(111)surface [42], single-atom transistors using phosphorus dopants in silicon [48], and binary atomic wires and logic gates using DBs on the H-Si surface [46]. Despite the progress made in the design of these and other device concepts [49, 290–292], reliable device fabrication is usually limited by patterning accuracy or variability in the fabrication process. DBs on the H-Si surface have been shown to be rewritable [4, 147, 177] as well as stable at room temperature [57, 163] making them an excellent candidate for atom scale devices.

The H-Si surface has found applications in the study of surface chemistry including self-directed growth of ordered multi-molecular lines [293, 294] and reaction energetics [295]. The controllable desorption of hydrogen from the H-Si(100)-2x1 surface using the probe tip of a scanning tunneling microscope (STM) [159], allowed for more precise studies of surface chemistry [296] including fabrication of rudimentary devices [297, 298]. With the continued

study of DBs on H-Si surfaces, more complex and functional devices have been developed; however, complete automation of the hydrogen lithography process has been limited by three major factors. First, the probe requires continuous monitoring to ensure an atomically sharp patterning condition. This step was recently automated using machine learning [155]. Second is automated hydrogen lithography error detection and correction through recently realized controlled hydrogen repassivation techniques [147, 177]. Third is the automated characterization and localization of defects on the H-Si(100)-2x1 surface to assign an ideal patterning area by avoiding certain charged and uncharged defects which is the subject of the present work.

Defects found on hydrogen-terminated samples can take the form of sub-surface or surface charge centers which can affect the operation of nearby electric field sensitive atomic devices [6], or as non-charged surface irregularities which limit the space available for patterning. Manually locating and characterizing defects is quite labor intensive and depends on the random distribution of these defects and the cleanliness of the terminated sample. Initial attempts to automate surface defect recognition relied on fast Fourier transforms [64]; however,the characterization of defects was limited to a few of many different species. More recently, machine learning has been applied to assist in classification and analysis of surface structures using SPM [193, 209, 210, 212, 299], but it has yet to be applied to surface features of the H-Si(100)-2x1 surface. Here, we implement an encoder-decoder type convolutional neural network (CNN) [300–302] to locate and classify features on the surface. By using semantic segmentation [303, 304], the neural network is trained to recognize a variety of charged and uncharged defects commonly found on the H-Si(100)surface. After implementing the model with existing patterning [4], and probe tip forming suites [155], full automation of the patterning process is achieved.

Crystalline silicon is tetravalent and forms a diamond lattice; each silicon atom shares four bonds, two above and two below the atom. At the (100) surface, two of these bonds are unsatisfied so the crystal reorganizes to a lower energy configuration. The addition of atomic hydrogen to the silicon surface during the annealing process results in the formation of one

of three possible phases. The likelihood of forming such phases can be controlled by the annealing temperature at which the sample is prepared. On a silicon surface with (100) orientation, the 2x1 phase forms at $\sim$ 377° C, the 3x1 phase at $\sim$ 127° C, and the 1x1 phase below $\sim$20° C [163, 229, 266]. The most commonly used for DB patterning is the 2x1 reconstruction where each surface atom pairs with a neighbouring surface atom to create a dimer pair. The dimer pairs are assembled in rows which run parallel to each other across the surface. The unsatisfied bond of each silicon atom can either be terminated with hydrogen or left vacant creating a DB. Although the preparation of the H-Si(100)-2x1 phase is well understood, some surface defects decorate the otherwise perfectly clean, defect-free surface. We are able to image the defects as well as clean H-Si(100) using a STM.

In order to train the CNN to recognize these surface defects, they must be labeled in a pixel-wise manner in the STM images. Our neural network is trained with seven different classes of defects. The first is regular, clean H-Si(100)-2x1 (Figure 4.1 (a)). There are two types of charged defects labeled 'type 2' [6, 249] (Figure 4.1 (b)), the origin of which is yet to be confirmed, and 'DB' or DB [159, 173] (Figure 4.1 (c)). The remainder of the known surface defects are understood to exist in a neutral charge state and consist of diversely reconstructed H-Si, adatoms, and adsorbed molecules. Figure 4.1 (d) shows a 'dihydride' in which two silicon atoms each bind to 2 hydrogen atoms instead of forming a dimer pair [258]. Figure 1 (e) shows a 'step-edge' which is a drop in the surface height by one atomic layer. Dimer rows run perpendicular to the original direction above the step and the boundary of the step edge is often marked with 1x1 or 3x1 reconstruction [260, 305, 306]. Figures 4.1 (f)-(j) show several different defects that either appear too infrequently in our training data to properly train the neural network, or are found too close to each other to properly segregate during data labelling (Figure 4.1 (k)). Defects of this type were assigned the label 'clustered'. It is hoped that future implementations of the network will allow for further segregation of the 'clustered' class into individual defect classes. Figure 4.1 (l) shows the final label class, an adsorbed species, molecule, or cluster of atoms of unknown origin labeled as 'impurity'. These defects are thought to be something other than H-Si and can usually be reduced by

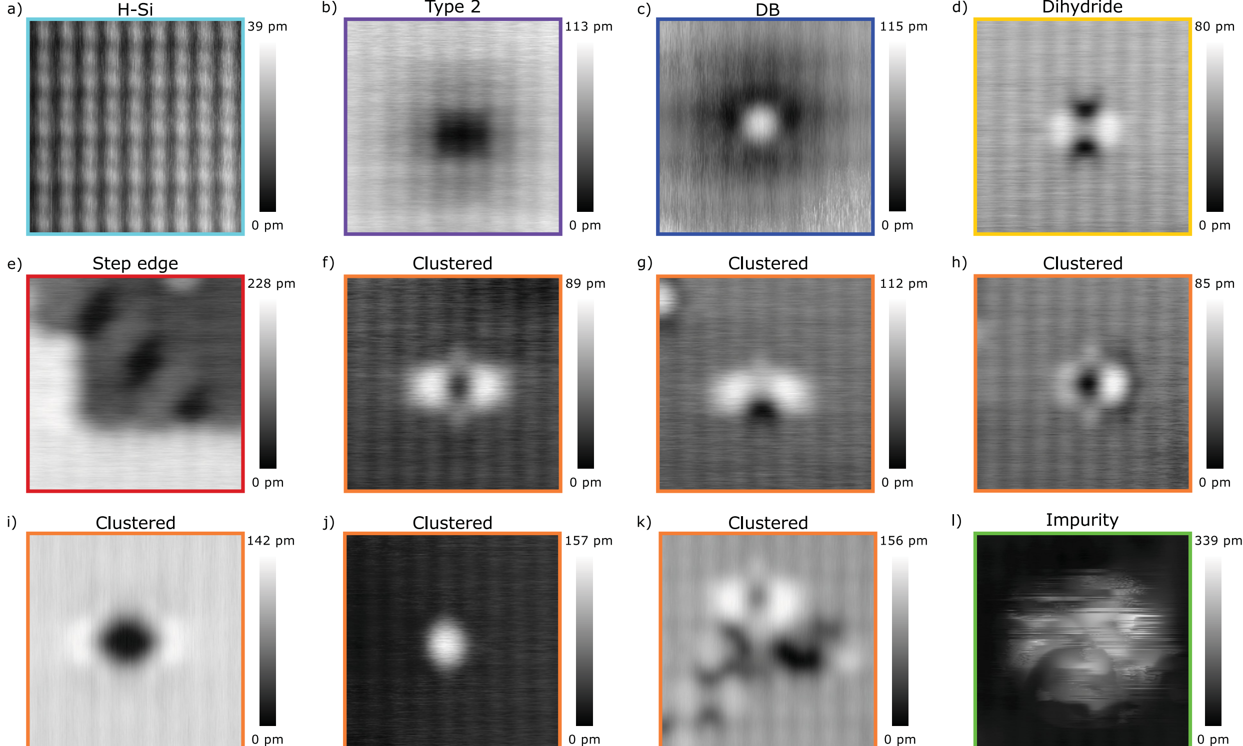

FIGURE 4.1: **Defect classes:** empty state images of various defects found on a typical H-Si(100) surface labeled with their appropriate class. Each image is 4x4 nm^2 taken with a STM with a sample bias of 1.4 V and a tunneling current of 50 pA. The coloured borders match the assigned contour colours of Figure 4.3. A normalized version is shown in Figure 4.5.

eliminating any potential contaminants during sample preparation. Further discussion on the origins and structure of these defects including an investigation of individual defects of the 'clustered' class will be presented in a future work [2].

4.1.3 Methods

All experiments were performed using an Omicron Low Temperature STM operating at 4.5 K and ultrahigh vacuum (4×10^{-11} Torr). Tips were electrochemically etched from polycrystalline tungsten wire and resistively heated in ultrahigh vacuum to remove surface adsorbates and oxide, and sharpened to a single atom apex using field ion microscopy [178]. In situ

tip processing was performed by controlled tip contact with the surface [140, 144, 177]. Tip shaping parameters were the same as in [155].

Samples used were highly arsenic doped (1.5×10^{19} atoms cm^{-3}) Si(100). Samples were prepared by degassing at 600° C overnight followed by flash annealing at 1250° C. The samples were then terminated with hydrogen by exposing them to atomic hydrogen gas at 330° C. It should be noted that these sample preparation guidelines were only loosely followed for all samples shown in this paper in order to ensure that a significant number of surface defects were present on the sample.

Image and data acquisition was done using a Nanonis SPM controller and software. All training data was acquired at an imaging bias of either 1.3 or 1.4 V with a tunneling current of 50 pA. An empty states imaging bias was exclusively used due to the enhanced contrast around certain defects. Specifically, distinctions between charged and uncharged defects as well as dihydrides are much easier to notice when analyzing the empty states rather than the filled states images as shown in Figure 4.6. The patterning automation routine was programmed in Python and Labview using the Nanonis programming interface library.

The CNN was implemented using Keras(2.1.3)with TensorFlow backend. Data was labeled using LabelMe software [307].

4.1.4 Results and Discussion

Neural network architecture

The architecture of the CNN was implemented to support semantic segmentation of the images. Semantic segmentation allows for both the localization and classification of objects in images. This can be used in many applications where the network must make a distinction between different objects in an image including use in self-driving cars [183–185] and medical image analysis [186–188]. In our case, a distinction is made between the pixels that make up each of the labeled defects. We trained various CNN architectures(Figure 4.10) and

implemented the one that shows the greatest performance in defect recognition (Figure 4.2) (Labeled model 8 in the SI). An encoder-decoder type architecture is used which allows for higher order feature extraction while minimizing the number of trainable parameters [300, 302, 308]. Each encoder layer consists of two sets of a convolutional layer(3x3 kernel), batch normalization layer, and a 'relu' activation layer followed by a maxpooling layer(2x2 kernel). The number of convolutional filters doubles with each encoder layer starting with 32 filters reaching a maximum of 128 filters. Following the encoder layers, a series of decoder layers are applied to bring the output of the network to a size which matches the input. Each decoder layer consists of an upsampling layer(2x2 kernel), convolutional layer(3x3 kernel), batch normalization layer, another convolution layer(3x3 kernel) and batch normalization layer followed by a relu activation layer. The final output layer consists of a convolutional layer which uses 7 filters(3x3 kernel) followed by a softmax activation which produces a one to one mapping of the surface for each of the labeled classes.

Data set and training

The network training data set was compiled from 28 images(100x100 nm^2 with a resolution of 1024x1024). Each of the 28 images were divided into 64 smaller images(128x128). Each of the smaller images in the training set were rotated by 90°, 180°, and 270° as well as flipped along its axis and subsequently rotated increasing our training data by a factor of 8. Images were divided into training, testing, and validating images at a ratio of $\sim$ 2/3:1/6:1/6, respectively (corresponding to 9560:2384:2393 images). Although all images used in the training set are of the same size, the network was designed to take images of varying sizes as inputs. The only restriction to the input images is that they all have the same resolution of 1024 pixels/100 nm. This ensures that each convolutional filter will extract the same feature profiles on a variety of STM images. We utilized the Adam optimization algorithm [200] with learning rate of 0.01. Subsequent model retraining was done using a learning rate of 0.001 which very slightly improved network performance in this case. The networks were trained using a categorical cross entropy loss function. The network quality was assessed using a soft Dice

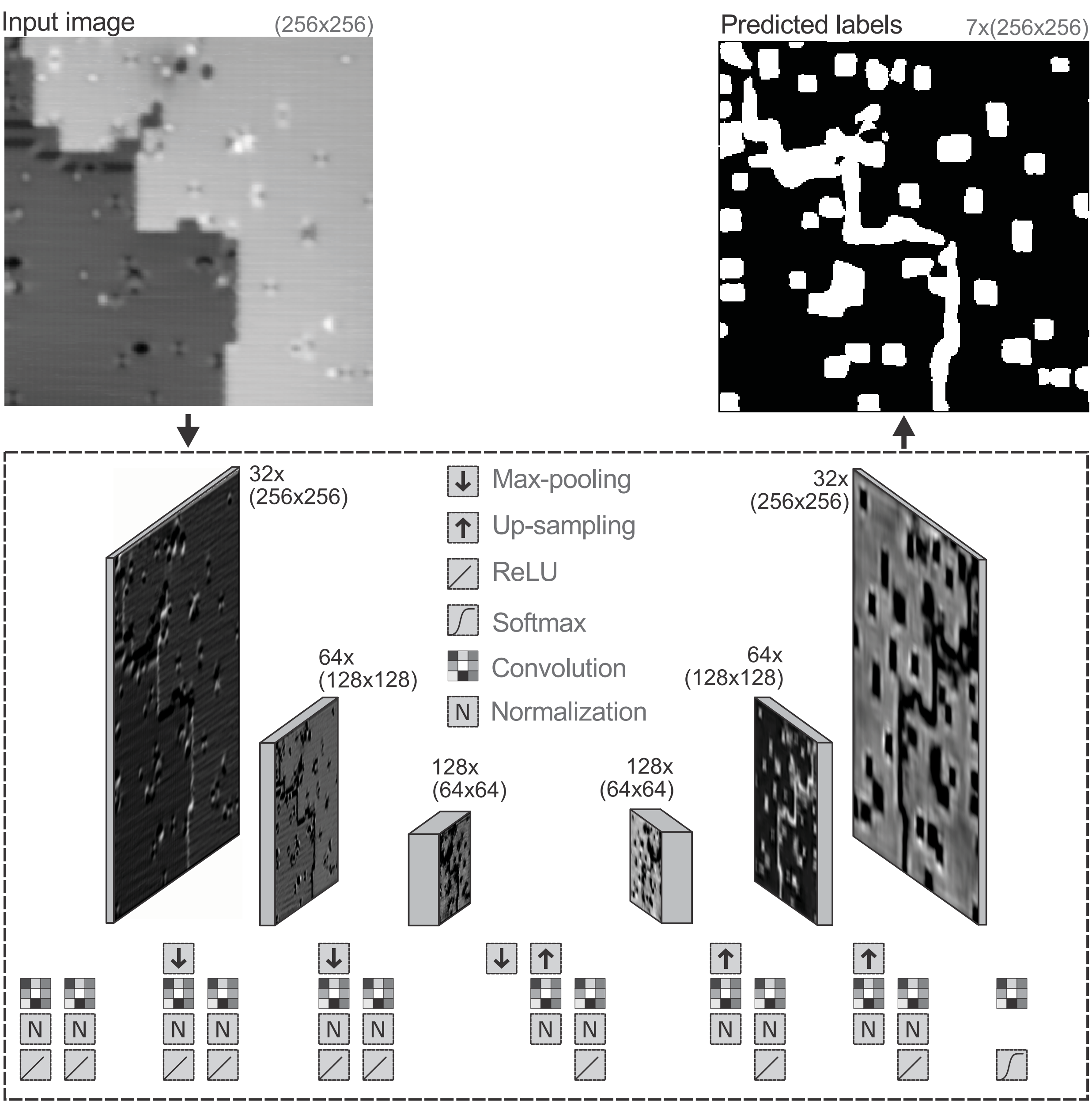

FIGURE 4.2: **A representation of the CNN architecture used in this study.** This architecture is selected by comparing the performance of different CNNs (table 4.1) as well as traditional machine learning methods (We include in the SI, our attempts at using SIFT features [205] [56] to classify surface defects.) It consists of 3 convolutional encoder layers followed by 3 convolutional decoder layers. The final set of images is passed through one final convolutional layer followed by a softmax activation giving 7 separate images corresponding to each of the 7 labels. The output displayed here marks the clean H-Si in black.

loss function, to reduce the effect of the large class imbalance found in our training data [309].

Neural network performance

A subset of the outputs of our fully trained model can be seen in Figure 4.3. The clean H-Si label was left out because of overlapping boundaries with the defects. More examples of the predicted label outputs including clean H-Si can be seen in Figures 4.7 and 4.8. The overall Dice score of the model is recorded at 0.86 which was calculated as a weighted average of the Dice score for each label. A full confusion matrix showing all individual Dice scores including other network architectures can be seen in Figure 4.11. A large portion of the 0.14 inaccuracy can be attributed to the fact that we had multiple users labelling data without a standardized defect size in place. This effect can be seen when comparing the labeled test data set with the predicted labels(Figure 4.9). The edges of the labeled data are straight, while the predicted label edges show a much rougher border.

One would expect that if each of the defect types were traced with a constant label size, the predicted edges would better replicate the labeled edges. This effect can be seen in the confusion tables(Figure 4.11). Lower scores are observed for defects with a high edge-to-surface pixel ratio (type 2, DBs, dihydrides) compared to defects with a lower edge-to-surface pixel ratio (H-Si). For our purposes, this does not present an issue as the size of the defects are much larger than the variation in the predicted defect edges.

Augmentation with scanning probe lithography

With the successful development of the neural network, it was implemented in the automation of hydrogen lithography. Figure 4.4 summarizes the current automation process. The user inputs a pre-designed pattern they wish to create (inset of Figure 4.4 (b)) and scales the coordinates of the scanner with the surface lattice parameters such that the DB pattern aligns with H-Si atoms on the surface. The user initiates the program and the SPM controller takes a scan of the sample with a resolution matching the training data. The image is fed to the

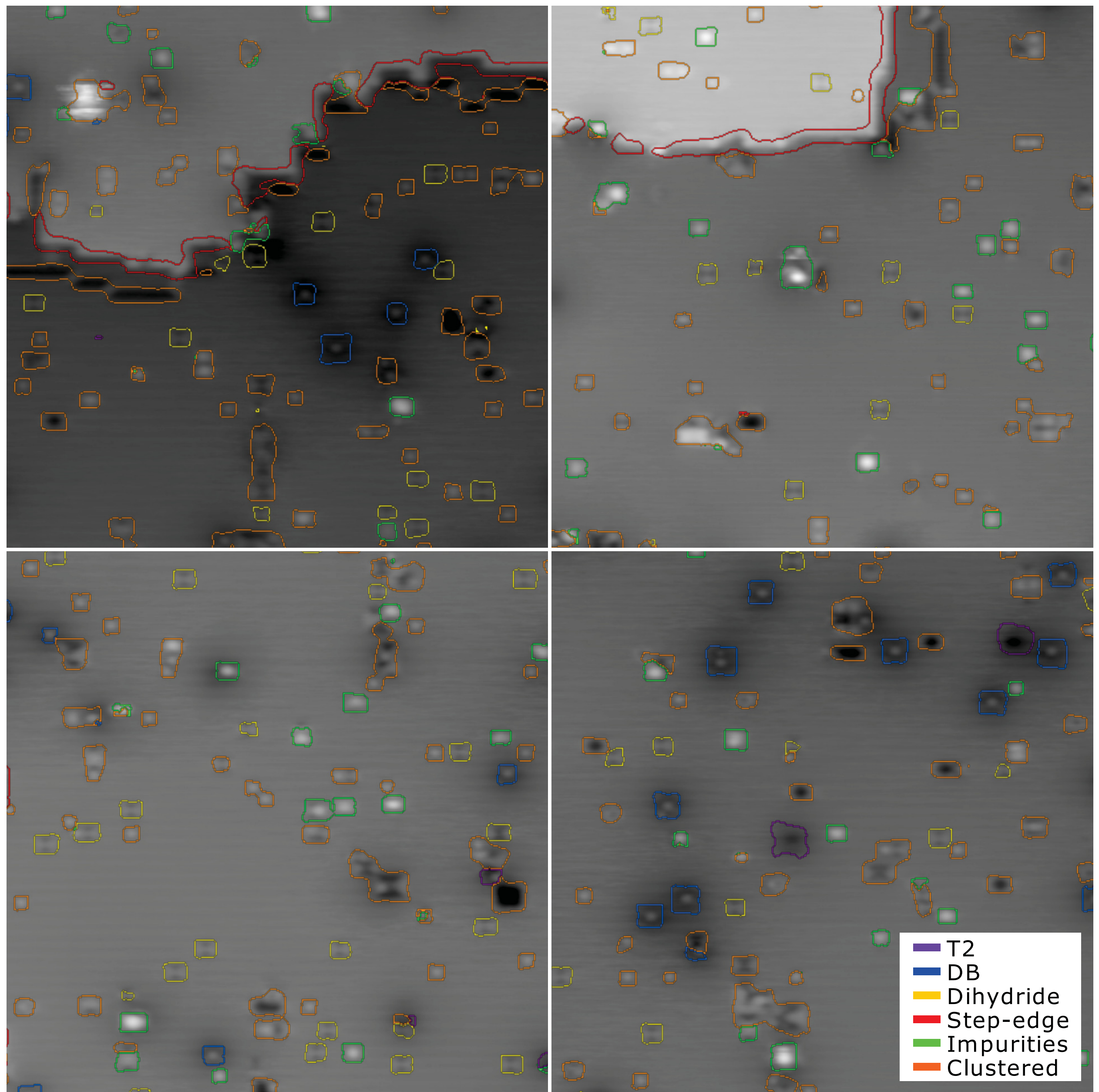

FIGURE 4.3: **Traces of the predicted labels of the CNN and the original input images** (constant current of 50 pA and sample bias of 1.4 V). Each image is 40 x 40 nm^2.

neural network and an output image containing each of the defects is returned. In order to decrease the local electrostatic interactions of local charge defects with the DB pattern [6], an effective radius of 5 nm is applied to all type 2 defects on the surface. This increased spacing does not need to be applied to DBs since they are now routinely erasable. The same radius is applied to step-edges as well to allow space to ensure all subsequent DB patterns are made on the same step terrace. The program then identifies the area on the sample furthest from any defects that would support the pattern (white box in Figure 4.4 (a)). Once found, a smaller scan of the viable area is taken to confirm the dimer direction matches that of the pattern. If not, the pattern is aligned with the next best viable area until the dimer direction is correct. The smaller scan is then used to shift the pattern such that each DB lies directly above their corresponding H-Si atom on the surface. The program begins patterning by positioning the tip above the specified H-Si atoms and applying an initial bias pulse of 1.8 V with a pulse width of 10 ms. If the DB creation is unsuccessful, the pulse bias is increased by 0.1 V intervals(up to a max of 2.5 V) until the DB is created. The tip continues this process for all desired DBs until the pattern is complete (Figure 4 (b)). Tip shaping takes place if the DB is not successfully created after the bias pulse has reached its maximum value. A full flow chart of the patterning program can be seen in the SI(Figure 4.12) as well as additional patterning examples (figures 4.14–4.17). The same procedure could be applied to more complicated fabrication schemes.

4.1.5 Conclusion

Continuing on the path to fully develop atomically-precise fabrication tools, we have successfully implemented a routine that can assess the quality of a sample, identify a suitable area that is free of defects, and execute a hydrogen lithography procedure. The routine is based on a CNN which uses semantic segmentation to locate and differentiate between certain charged and uncharged defects that inhibit the manufacturing process or potentially alter the operation of patterned devices. We have demonstrated the applicability of our

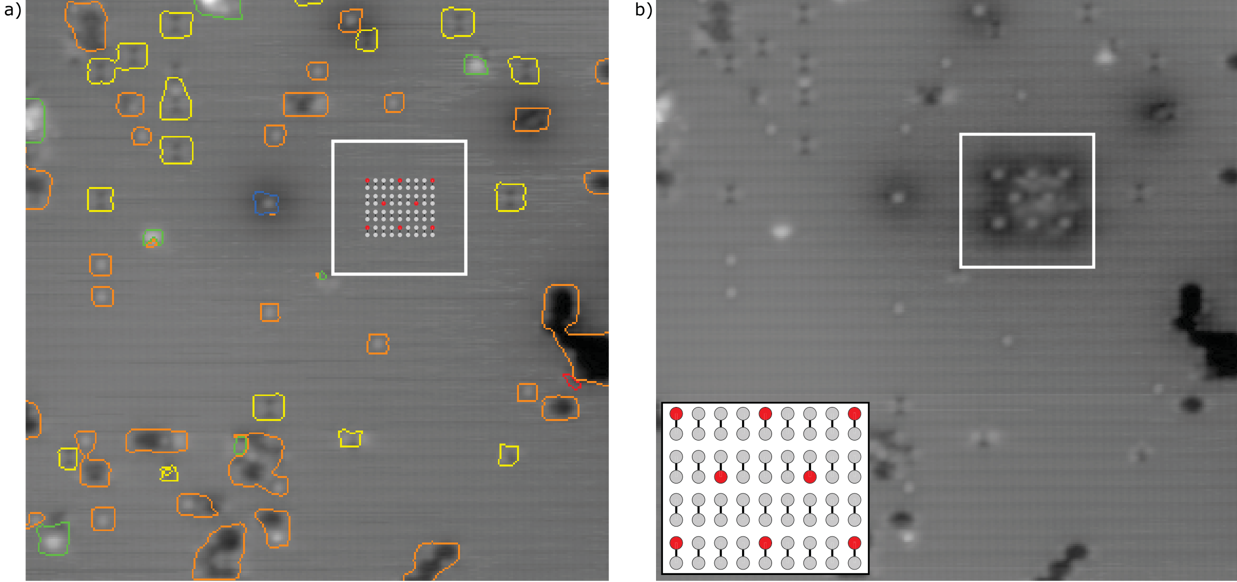

FIGURE 4.4: (a) A trace of the defects from the CNN analysis of the scan image shown. The white square shows the area furthest from defects for the corresponding pattern. (b) The resulting surface after patterning the device shown in the inset.

approach by training the neural network with images of defects commonly found on the H-Si(100)-(2x1)surface. Hydrogen lithography was shown by patterning an 8 DB structure on the H-Si surface. It is envisioned that defect-free regions adequate for fabrication of functional logic or memory units comprised of roughly one hundred atoms will exist and that interconnections between such units will be custom routed so as to avoid defects. In this way, defect-free surface areas will be connected to form larger, effectively defect-free circuit blocks. In addition to avoiding defects, erasure of certain defects identified using the neural network is expected to become fully automated in future works. The techniques shown here are applicable to any type of device fabrication or lithography using any form of SPM as well as subsets of semiconductor device fabrication where the quality of the materials used must be assessed to optimize the fabrication process.

4.1.6 Acknowledgements

We thank NSERC, AITF, and Compute Canada for financial support. We would also like to thank Mark Salomons and Martin Cloutier for their technical expertise and to Thomas Dienel and Taleana Huff for valuable discussions.

4.1.7 Author contributions

MR and JC developed the code. JC, MR, KM, MT, and HH identified and labeled the defects. RAW supervised the project. JC and MR wrote the manuscript with input from all authors.

4.1.8 Competing interests

The authors declare competing financial interests: a patent has been filed on this subject. Some of the authors are affiliated with Quantum Silicon Inc. (QSi). QSi is seeking to commercialize atomic silicon quantum dot based technologies.

4.1.9 Data availability

Data is available upon request from the corresponding authors.

4.1.10 ORCID iDs

Jeremiah Croshaw https://orcid.org/0000-0001-9164-1556

4.1.11 References

References for this publication are available at the end of this thesis.

4.2 Deep Learning-Guided surface Characterization for Autonomous Hydrogen Lithography: Supporting Information

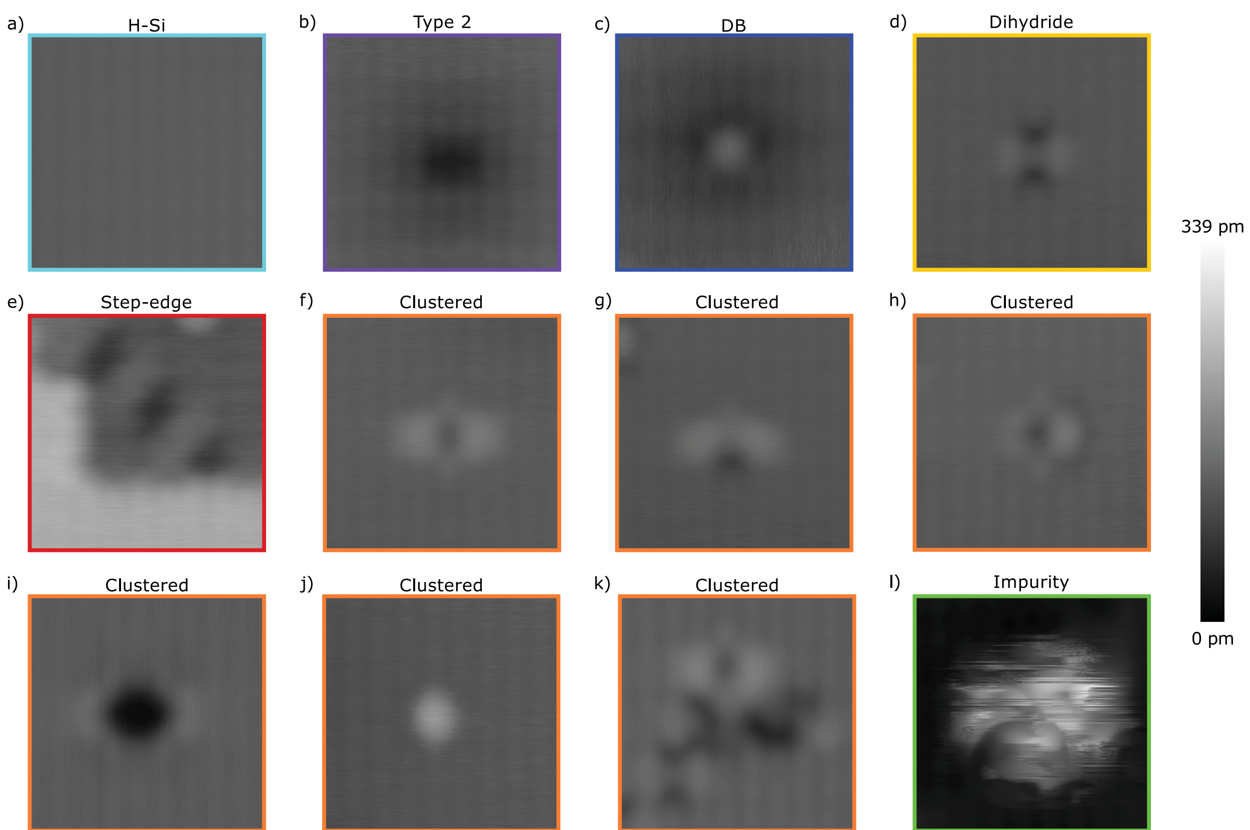

FIGURE 4.5: Normalized images of the defects found in Figure 4.1. (a)-(k) have been normalized so that the H-Si surrounding the defect is at the same relative height. (l) has been left unmodified. All images now use the same height scale.

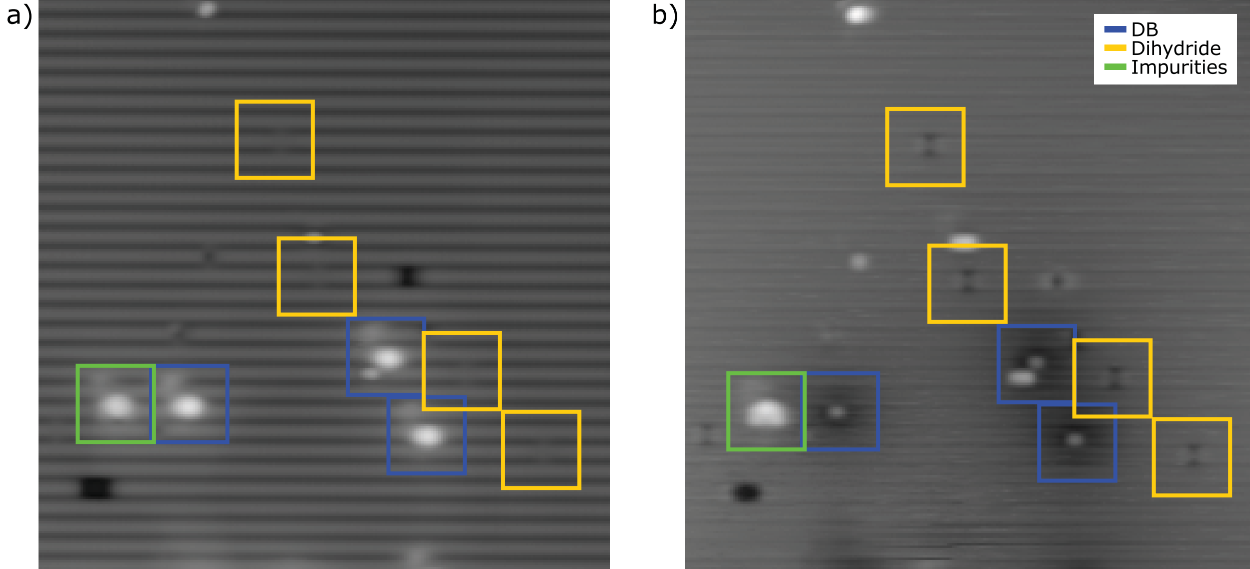

FIGURE 4.6: (a) A filled states (-1.8V) and (b) empty states (1.3 V) image of the surface. Specific defects were manually identified to show the difference in defect features when imaged at either bias. Imaging at 1.3 V offers an advantage in that it easily distinguishes between charged and uncharged species (as observed when comparing the impurity with the DBs), as well as more easily highlights dihydrides when compared to the regular 2x1 surface.

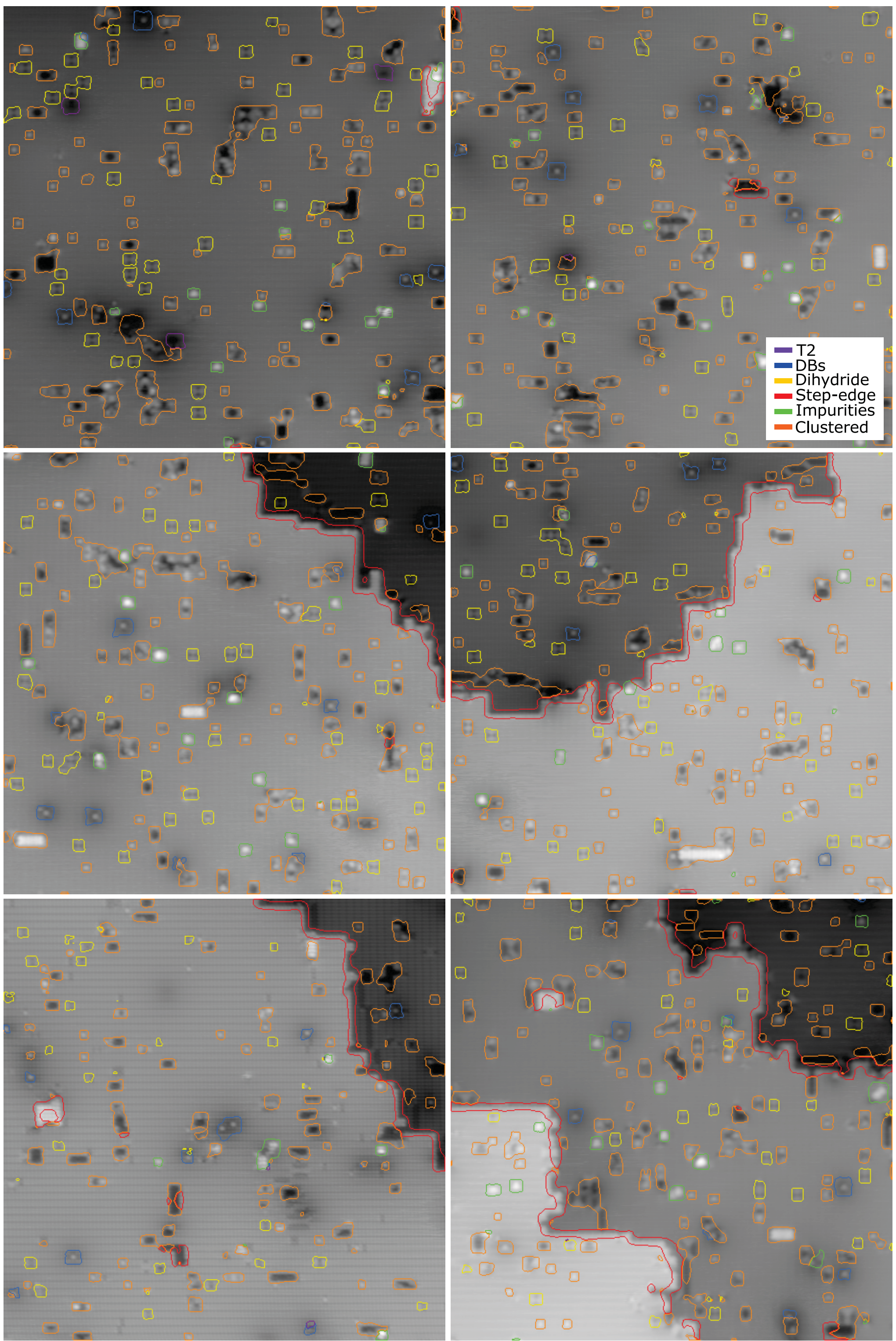

FIGURE 4.7: **Surface scans and six of the labeled outputs from the neural network.** Each image is 50 x 50 nm^2 and was taken at a sample bias of 1.3 V and tunneling current of 50 pA. The surface shown in the bottom left was imaged using a rare tip contrast that the network was not very familiar with. A decrease in the accuracy of defect segmentation compared to the other five images can be seen.

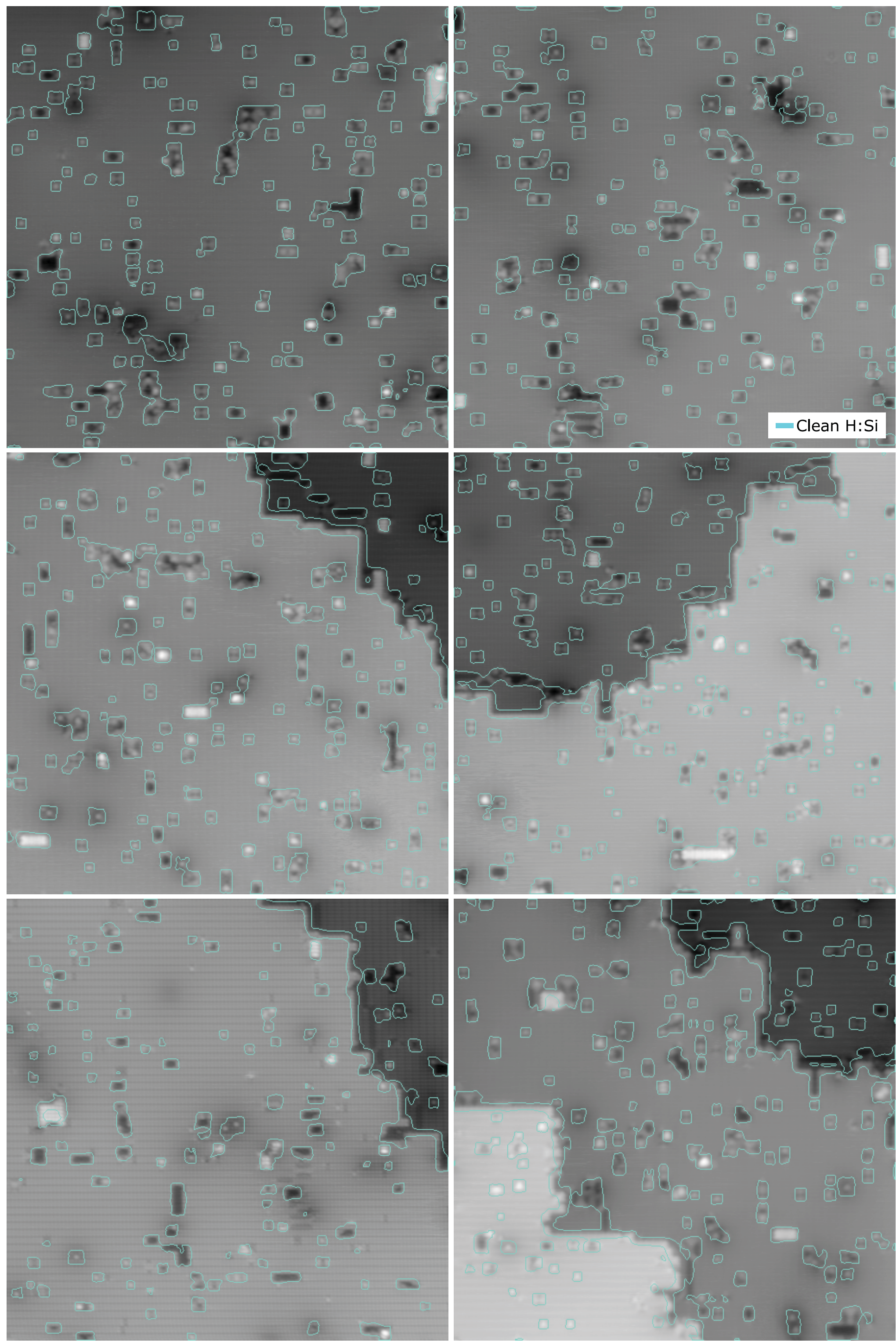

FIGURE 4.8: **Surface scans and one of the labeled outputs from the neural network.** Each image is 50 x 50 nm^2 and was taken at a sample bias of 1.3 V and tunneling current of 50 pA. The surface shown in the bottom left was imaged using a rare tip contrast that the network was not very familiar with. A decrease in the accuracy of defect segmentation compared to the other five images can be seen.

FIGURE 4.9: **Heat maps from a random selection of the test data set.** True pixels are yellow while false pixels are purple. Each image is 12.5 x 12.5 nm^2.

4.2.1 Neural Network Architecture

A variety of neural network architectures were trained to find a configuration which gave the best Dice score of the Test and Validation data. Figure 4.10 shows the architectures of

10 of these models. These 10 models were chosen from the many more that were trained to highlight their superior performance or unique architecture. Models 1 through 5 where designed based on the U-net [308] model. Comparing the dice scores found in Figure 4.11 or Table 4.1, it can be seen that the implementation of skip layers did not increase the dice scores of the networks. Model 6 was based off the network presented in [212]. Models 7-9 were modifications of this network style with the addition of convolutional filters. Model 10 was a modification of model 1 without any downsampling layers. The removal of these layers made training the network much more time consuming which necessitated the removal of four convolutional layers. The two networks with the best Dice score were models 8 and 9 which used double convolution style encoder/decoder layers. Model 9 had the advantage of a quicker image processing time, however given that the current time scale to acquire an image is roughly 10 minutes, the additional 5 seconds saved will not significantly decrease the fabrication time. As a result, model 8 was chosen due to the slightly better performance at classifying T2s, DBs, dihydrides, impurities, and clustered defects as shown in the confusion tables of Figure 4.11. Interestingly, the dice score for each defect remained relatively constant for each defect type lending to the discussion in the main text suggesting that the edge-to-surface ratio of the defects in combination with the large class imbalance place an upper limit on the dice scores achievable with this data set.

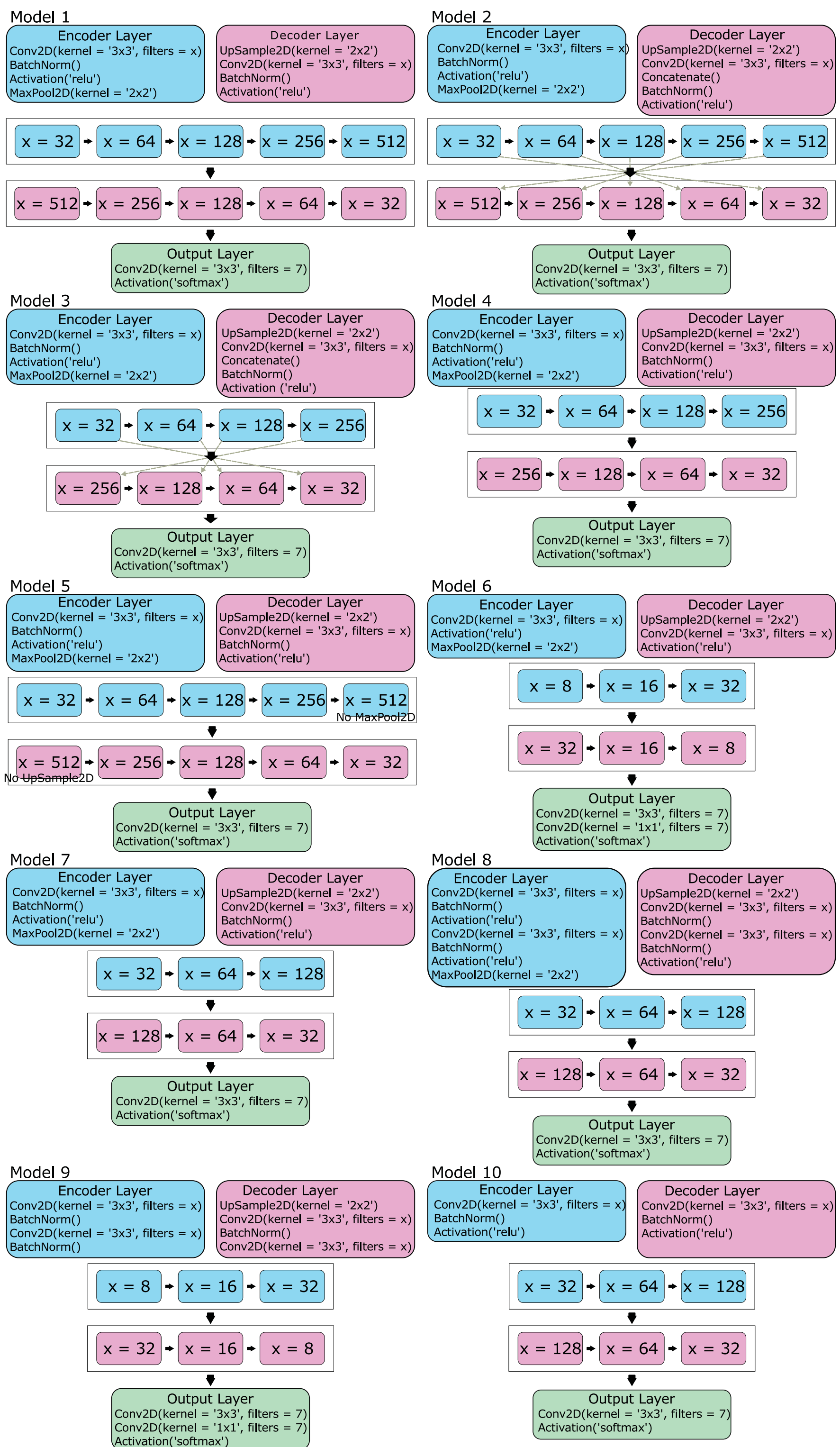

FIGURE 4.10: **Architectures of each of the 10 models tested**. Each model shows the variation in the encoder, decoder, and the output layers between each model.

Model #	Convolution Layers	Pooling Layers (one direction)	Trainable Parameters	Dice Score (Test Data)	Dice Score (Val Data)	Load and Analyze Time (s)
1	11	5	5,500,999	0.860	0.856	12.1
2	11	5	7,071,719	0.843	0.853	15.5
3	9	4	1,759,207	0.865	0.860	12.6
4	9	4	1,369,159	0.858	0.854	10.7
5	11	4	5,500,999	0.828	0.826	12.6
6	8	3	21,487	0.860	0.855	6.0
7	7	3	335,431	0.867	0.863	9.5
8	13	3	735,175	0.868	0.862	14.8
9	14	3	45,639	0.868	0.864	9.7
10	7	0	335,431	0.857	0.852	16.5

Table 4.1: Parameters of each of the tested models highlighting key features of their architecture as well as classification performance.

FIGURE 4.11: **Confusion matrices showing labelling accuracy of the test data set for each of the 10 models.** Each entry represents the Dice score for the actual label in the column being identified as the predicted label along the row.

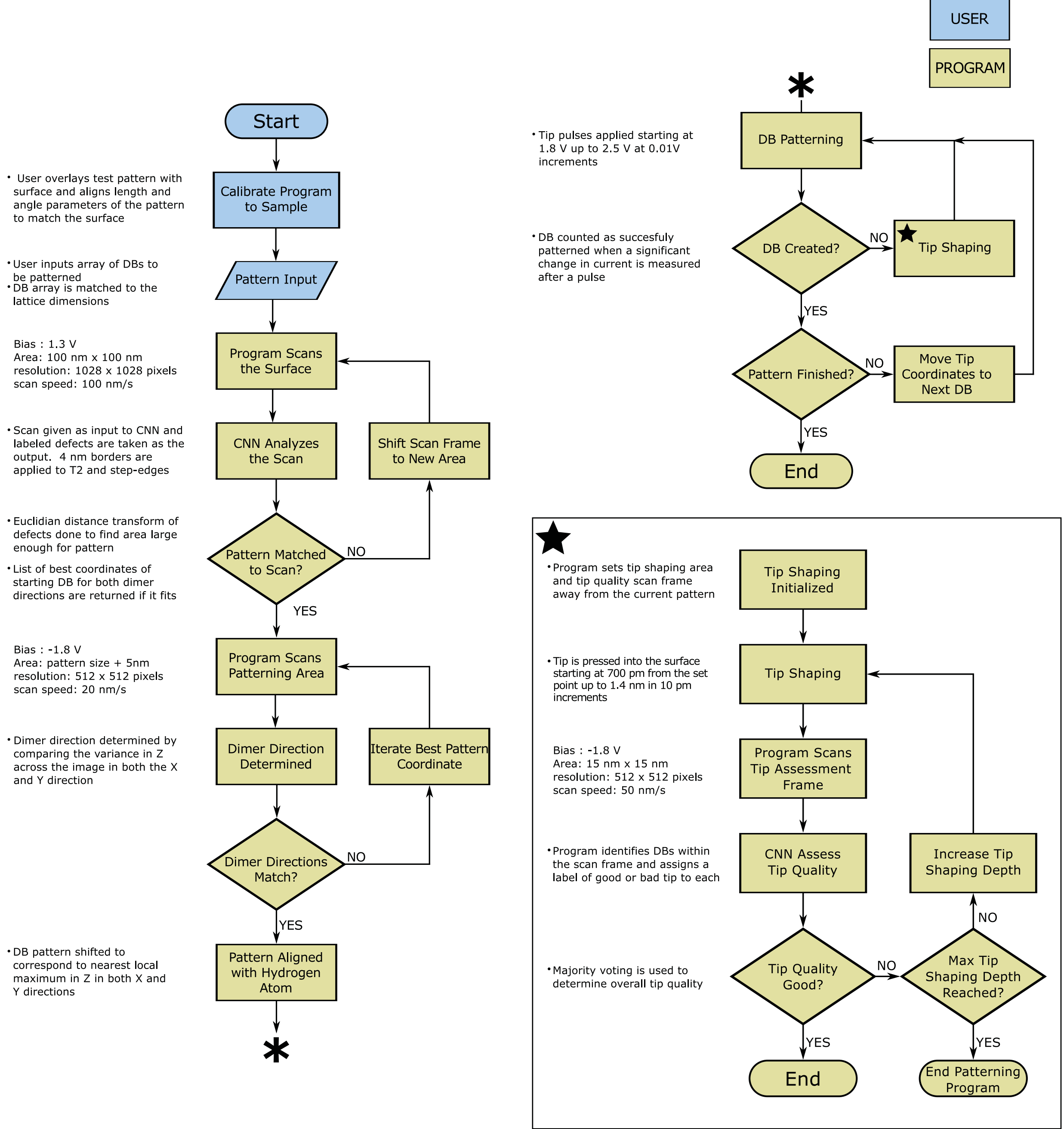

Figure 4.12: Decision tree summary followed in the lithography automation suite.

4.2.2 Scale Invariant Feature Transform Classification

In addition to neural networks, an attempt to classify surface defects using scale invariant feature transform (SIFT) descriptors [205] was also made. Training data was created from the already labelled data by taking 20 x 20 pixel cutouts of each the 6 defect types see in Figure 4.13 (a). Valid keypoints and descriptors for each defect were calculated using the SIFT library from the OpenCV package [310]. Only 64% of the defects returned valid keypoints and descriptors. Visual inspection of the images which failed to return valid SIFT keypoints shows that these defects were taken from larger images with multiple step edges resulting in very little contrast in the defect image. After splitting the defects into training and testing data (0.67:0.33), the descriptors were clustered using a mini batch k-means method using 500 clusters. From there, the frequency of descriptors in each image belonging to these clusters where counted. These frequencies were normalized using a standard scaling method and were used as features to train a random forest classifier. An overall accuracy of 68% is achieved on the test set with the full confusion table presented in Figure 4.13 (b). Even if this accuracy could be improved to a level comparable with the neural network approach, in order to achieve a similar resolution in defect segmentation, a sliding window approach is needed. Unfortunately, the SIFT algorithm available through OpenCV is a relatively slow process. Using a sliding window approach with a window size of 20 x 20 pixels, it takes roughly 2 hours to analyze a 50 x 50 nm image compared to the 15 seconds needed using neural networks with the same computational power.

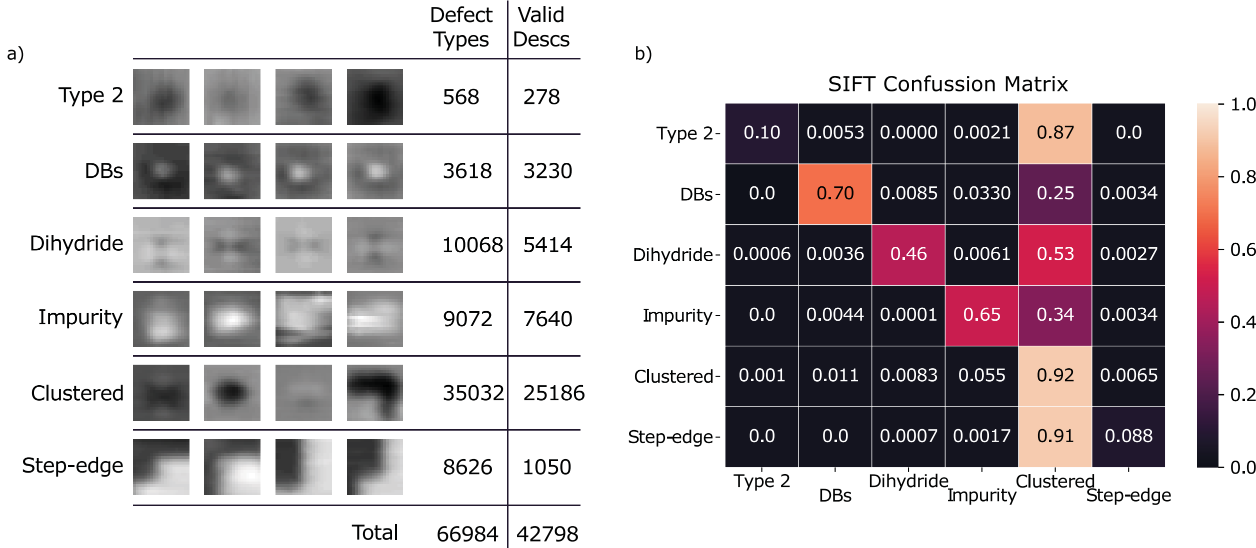

Figure 4.13: **Scale invariant feature classification.** (a) A sub-sampling of the images used to create the training data set for SIFT classification. The number of images used for each defect is also listed as well as the number of images for each defect which produced a valid descriptor using sift classification. (b) The confusion matrix of the defect classification using SIFT descriptors and the random forest classifier

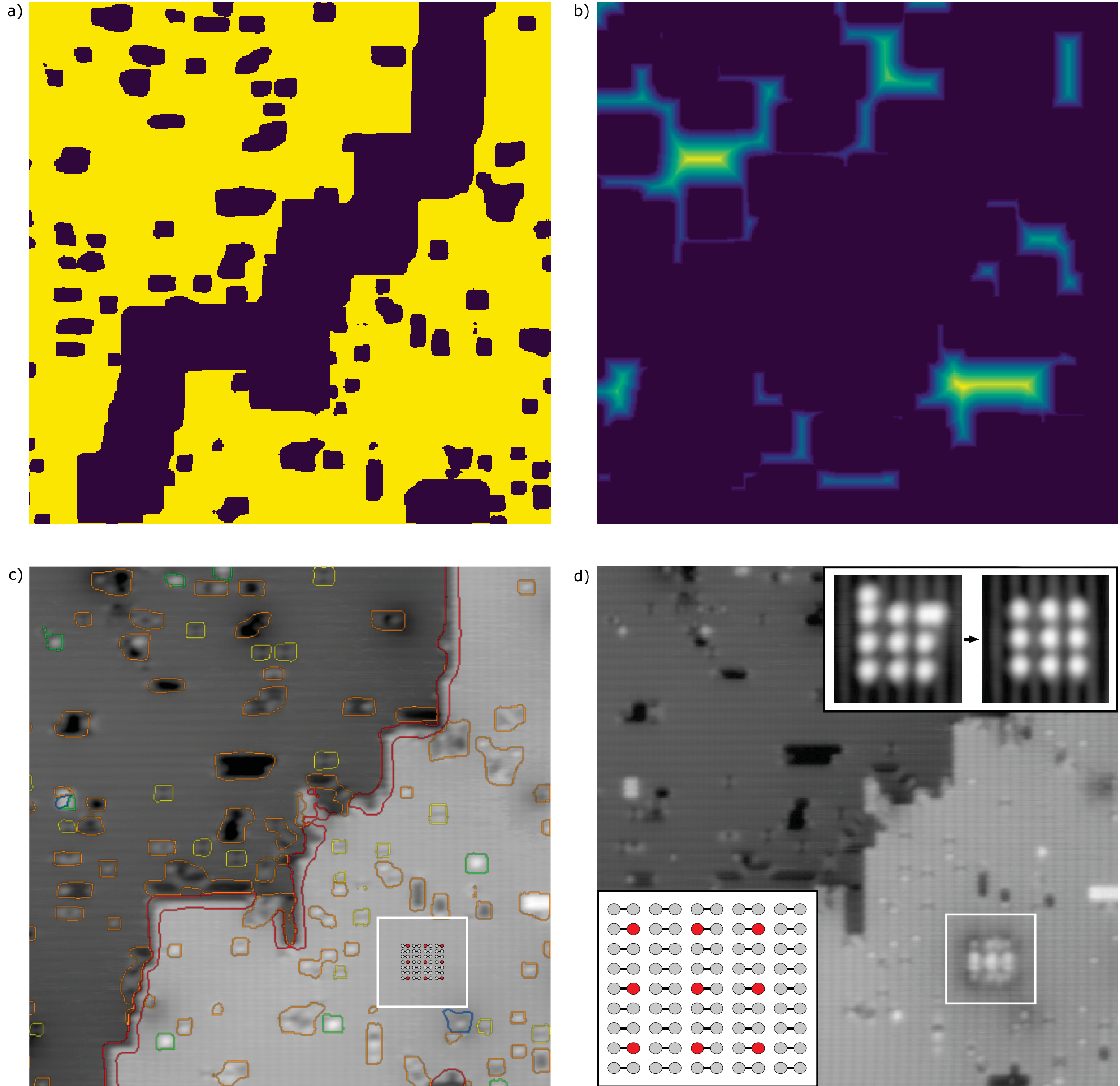

FIGURE 4.14: **An outline of the fabrication procedure.** (a) A trace of the surface defects (purple) with the added effective thickness surrounding the step-edge present in this image. (b) A mapping of the best spot to place the pattern. The best fits are in yellow with the top left corner of the pattern corresponding to the brightest spot in the image. (c) Alignment of the pattern with the surface showing the segmentation of defects as returned by the network. (d) The resulting surface after hydrogen lithography. The inset in the upper right shows the initial pattern with a minor mistake and the manually corrected pattern. The images are 40 x 40 nm^2 and acquired at an imaging bias of 1.3 V and a constant current of 50 pA.

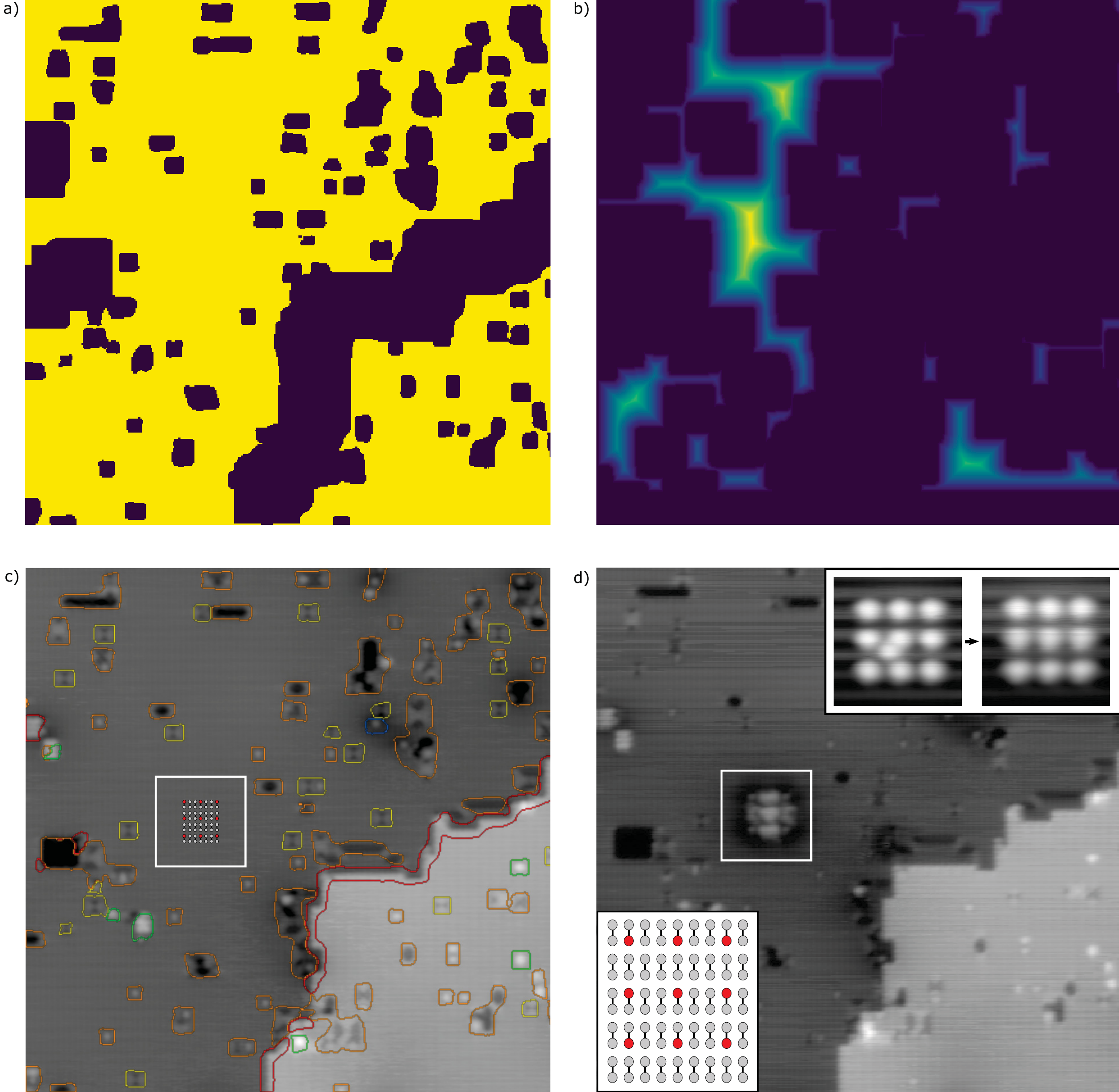

FIGURE 4.15: **An outline of the fabrication procedure.** (a) A trace of the surface defects (purple) with the added effective thickness surrounding the step-edge present in this image. (b) A mapping of the best spot to place the pattern. The best fits are in yellow with the top left corner of the pattern corresponding to the brightest spot in the image. (c) Alignment of the pattern with the surface showing the segmentation of defects as returned by the network. (d) The resulting surface after hydrogen lithography. The inset in the upper right shows the initial pattern with a minor mistake and the manually corrected pattern. The images are 40 x 40 nm^2 and acquired at an imaging bias of 1.3 V and a constant current of 50 pA.

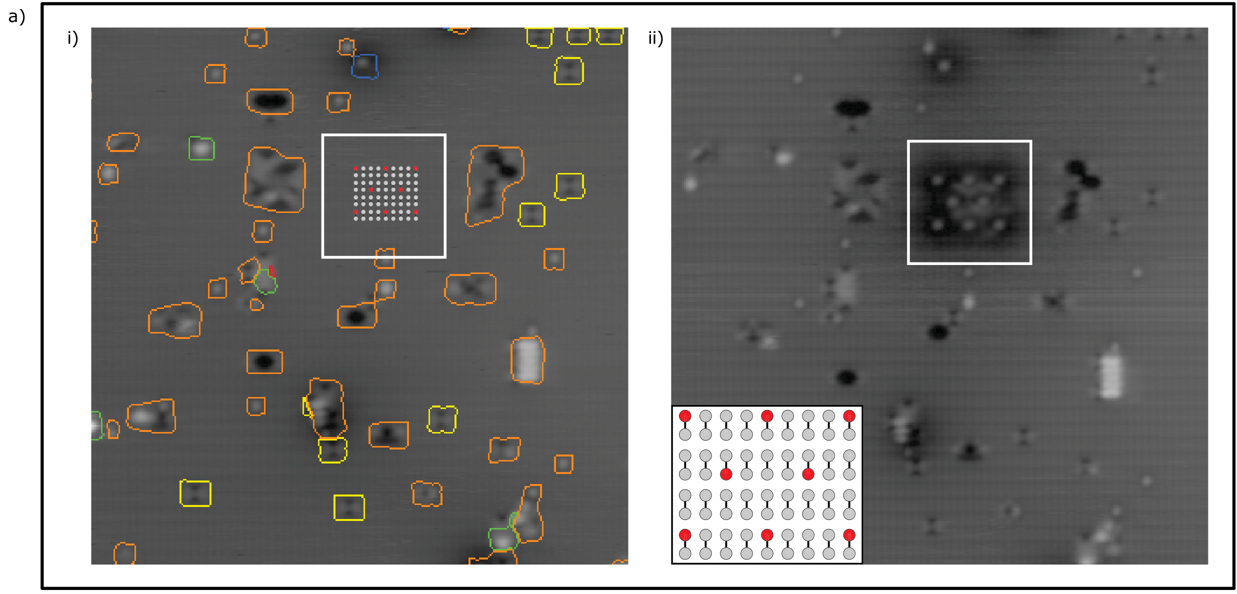

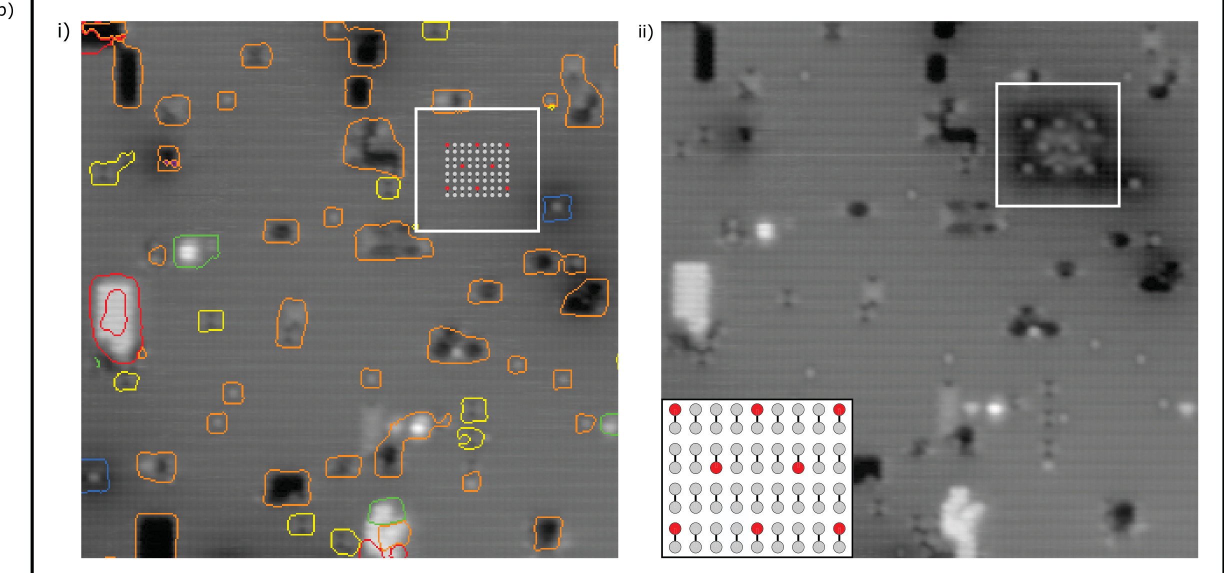

FIGURE 4.16: **Pattern patterning following defect classification**(a) A trace of the defects from the CNN analysis of the scan image shown. The white square shows the area furthest from defects for the corresponding pattern. (b) The resulting surface after patterning the device shown in the inset. The images are 30 x 30 nm^2 and acquired using a sample bias of 1.3 V and a setpoint current of 50 pA.

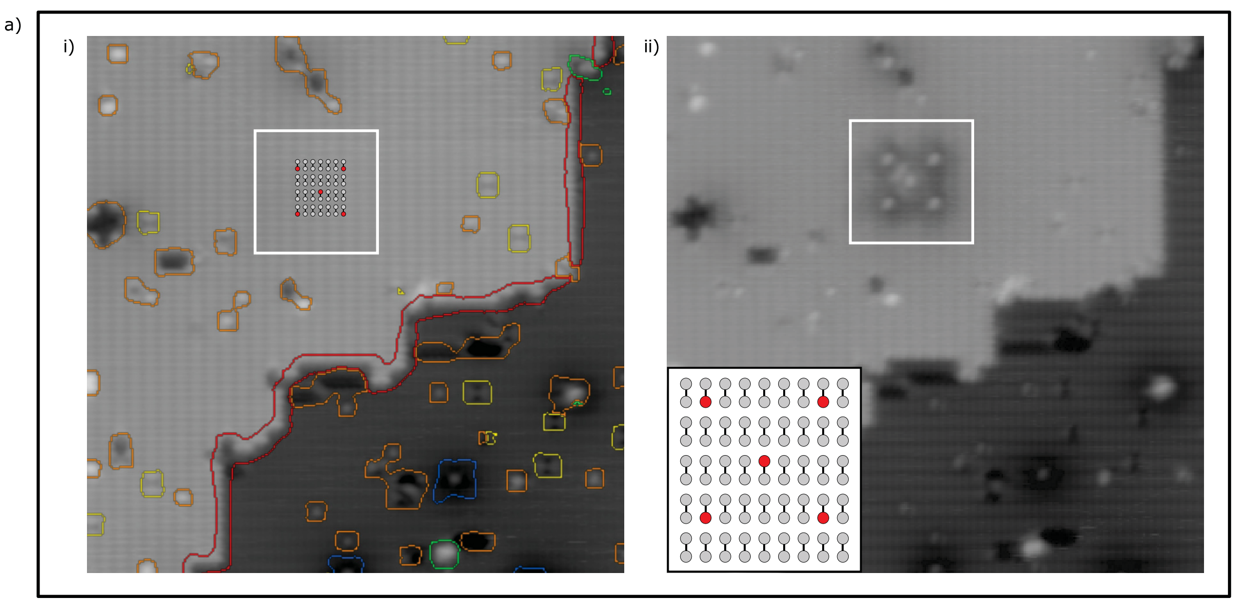

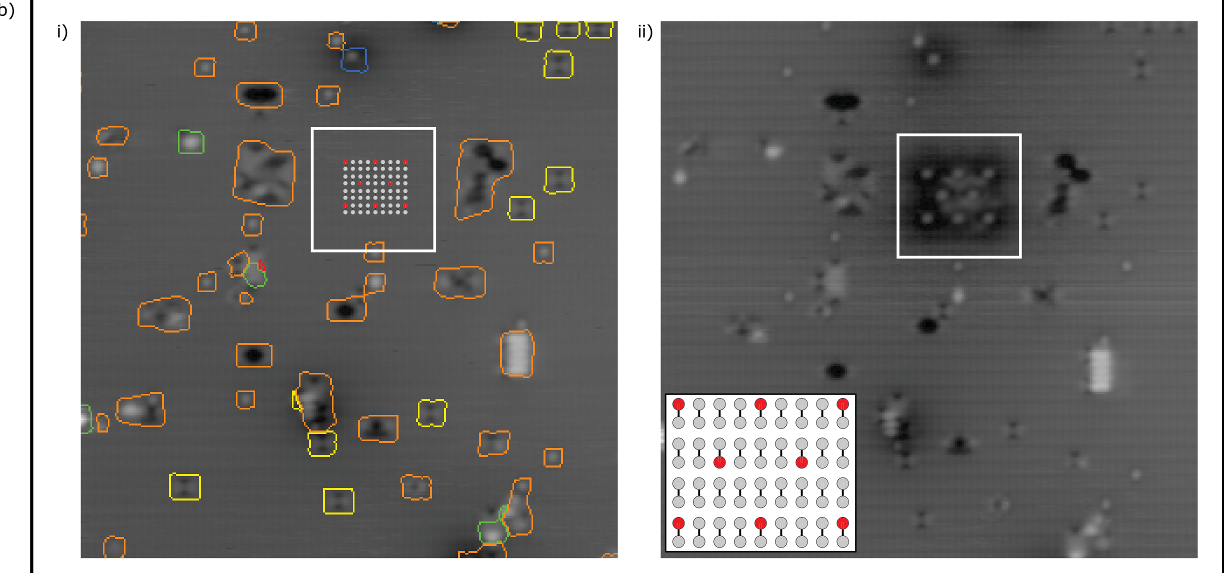

FIGURE 4.17: **Pattern patterning following defect classification**(a) A trace of the defects from the CNN analysis of the scan image shown. The white square shows the area furthest from defects for the corresponding pattern. (b) The resulting surface after patterning the device shown in the inset. The images are 30 x 30 nm^2 and acquired using a sample bias of 1.3 V and a setpoint current of 50 pA.

4.3 Unpublished Supplemental Data Regarding Defect Classification using Machine Learning

The development of the neural network used in the previous sections allowed for the full automation of device fabrication by learning to distinguish between 6 different defect classes. Following the development of the network in combination with the defect catalogue of Chapter 3, it was clear that the capabilities and applications of the neural network could be enhanced by updating the training data to better reflect the improved understanding of surface defects present on the surface. By expanding the number of classes and improving the quality of labelled data, a more powerful and robust neural network was developed. This enhanced network is shown below.

4.3.1 Expanding Defect Classes

Several modifications were made to the labelled data to improve the subsequent performance of the neural network. The number of defect classes were expanded to 14 to include several new defects identified from the work in Chapter 3. Figure 4.18 shows an example of each of the new classes. The single dihydride, 1x1, 3x1, siloxane dimer, raised silyl, etch pit, and missing dimer have all been added by further segregating the clustered class of the previous model. Unfortunately, segregating the type 2 class into a Si vacancy and charged point defect class (shown in Figure 4.18) did not provide enough unique examples of the charged point defect for the model to accurately learn it. The same can be said for the missing dimer class which is a combination of both the bright and dark variation. A notable exclusion from the defect classes is the neutral point defect which appeared in very low quantities throughout the data set. This is likely due to the fact that the point defect was still in the charged variation since the surfaces used for the data set images were never scanned at the appropriate transitioning biases. In order to enhance the data set to include the neutral point defect, additional studies will likely need to be done to identify a surface annealing

Defect	Count	Pixels (million)	Average Size (pixels^2)	% of Data Set
H-Si	-	74.0	-	82.1
DB	3679	1.8	495	2.0
Si Vacancy	1109	0.5	492	0.6
Dihydride Pair	9867	2.2	225	2.5
Single Dihydride	1358	0.3	221	0.3
1x1	2018	0.7	351	0.8
3x1	1022	0.5	456	0.5
Siloxane Dimer	12568	1.8	140	2.0
Raised Silicon	7591	1.7	219	1.8
Etch Pit	6147	1.9	312	2.1
Gunk	1089	0.6	544	0.7
Step Edge	283	1.4	4784	1.5
Missing Dimer	3807	0.8	220	0.9
Unknown	6271	2.0	318	2.2
TOTAL	56809	90.2	675	100

Table 4.2: Updated Defect Data Set Specifications. Defect count shows the unique labels in the 86 images used for the data set.

procedure which maximizes their concentration followed by preliminary surface scans at -1.8 V to ensure that all point defects have transitioned to their neutral state.

Further specifications of the labelled data is shown in Table 4.2 which highlights the fraction of the completed data set that each defect class represents. The data set was created from 43 surface scans (100 x 100 nm^2, 1024 x 1024 pixels^2) using both the forward and backward scans to double the number of images available giving the total 90.2 million pixels shown in Table 4.2. Images were cropped into 128 x 128 pixel sections, flipped and rotated creating a total of 44032 images which were divided into train, test and validation data sets at a ratio of 2/3, 1/6, and 1/6 respectively increasing the size of the data set by roughly 30 000 images compared to that used in the previous section. In addition to the inclusion of the new defect classes, the labelled data was also refined by a single labeler to establish a more uniform label size for each defect.

Several variations of the models presented in the previous section were explored when training with the updated data set. Primarily based on models 8 and 9, the version which showed the

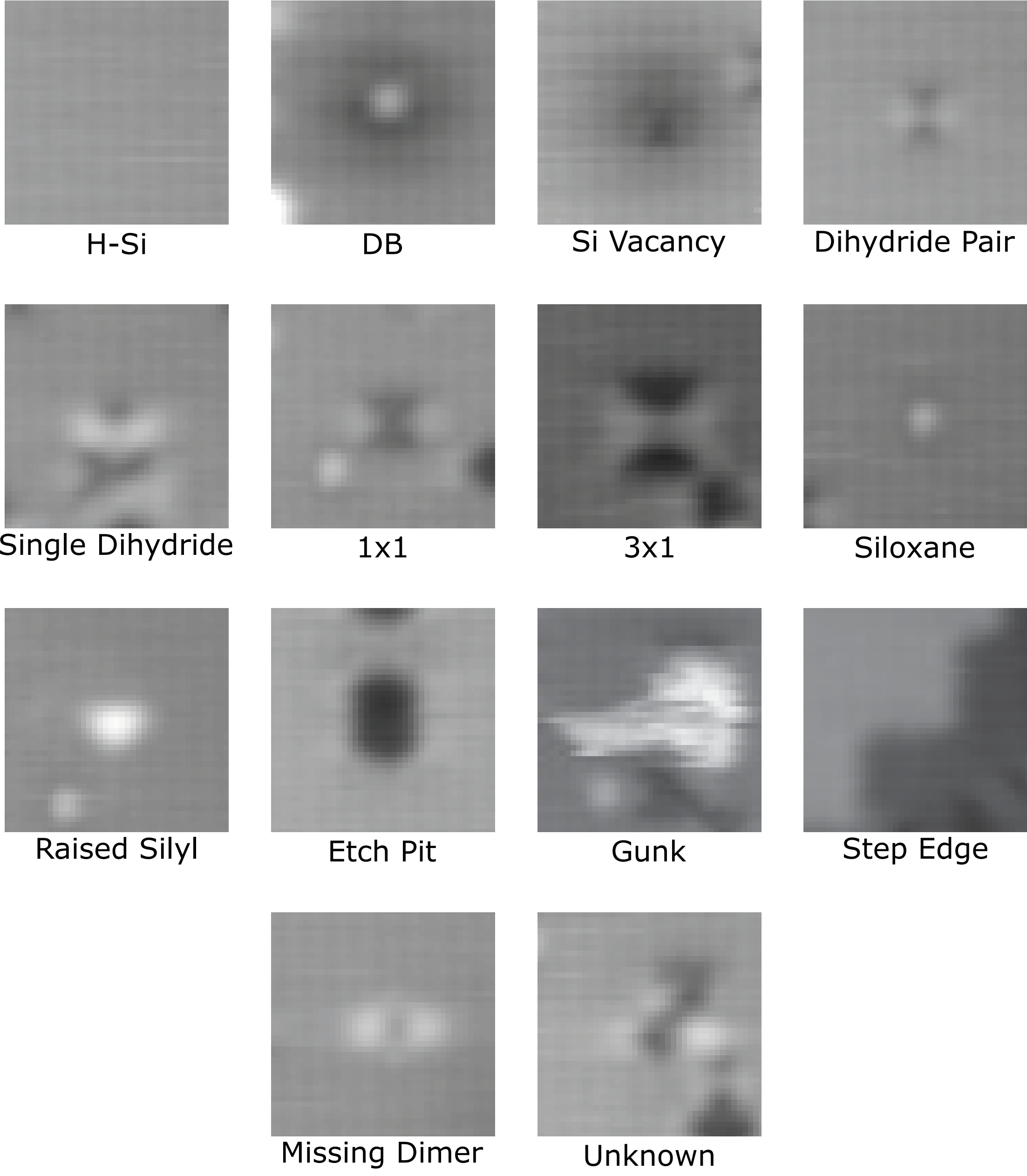

FIGURE 4.18: **Expanded defect classes for defect segmentation.** Each image shows an example of the new defect labels classes. Further information regarding each defect is discussed in the text of Chapter 3 and 4. Each image is 3.5 x 3.5 nm^2.

greatest accuracy was a variation of model 8 in which the number of convolution filters for each layer was doubled (64, 128, 256) (giving a Dice = 0.90). Attempts to include a weighted training set were also done to try and account for the large class imbalance, however, the resulting accuracy was less than the unweighted training (Dice = 0.78-0.88). Interestingly, networks which were trained with a weighted data set were able to more confidently assign defects as such however, they also misclassified defects as H-Si more than those trained with an unweighted data set. The confusion matrix for the best performing model trained with the updated data set is shown in Figure 4.19. Comparing this to the confusion matrix in Figure 4.11, all defect classes show significant improvement. Most notably, the Si Vacancy (Type 2) has improved from a Dice score of 0.13 to 0.42. It is speculated that this improvement is due to a combination of correcting mislabelled data as well as using a more standardized label size. Much like the neural networks trained using the original data set, the overall dice score per label seems to be correlated to the number of examples available for each defect type in the training data. It is therefor suggested that for further improvements to be made to the accuracy of the neural network, the data set should be updated so as to reduce the class imbalance seen.

A segmented surface as predicted using the updated model is shown in Figure 4.20. As shown, the model appears to accurately predict a vast majority of the defects. A few mistakes can be seen where the model incorrectly classifies the defects as H-Si as well as dividing a single defect into two defects. Both issues will likely resolve with a more balanced data set[1] with the latter issue easily corrected using a post prediction filter which applies a majority voting filter to single defects which are predicted as multiple classes.

[1] It is worth noting that performance decreases when the defect is imaged within the telegraph noise associated with a neighbouring charged species due to their absence in the data set

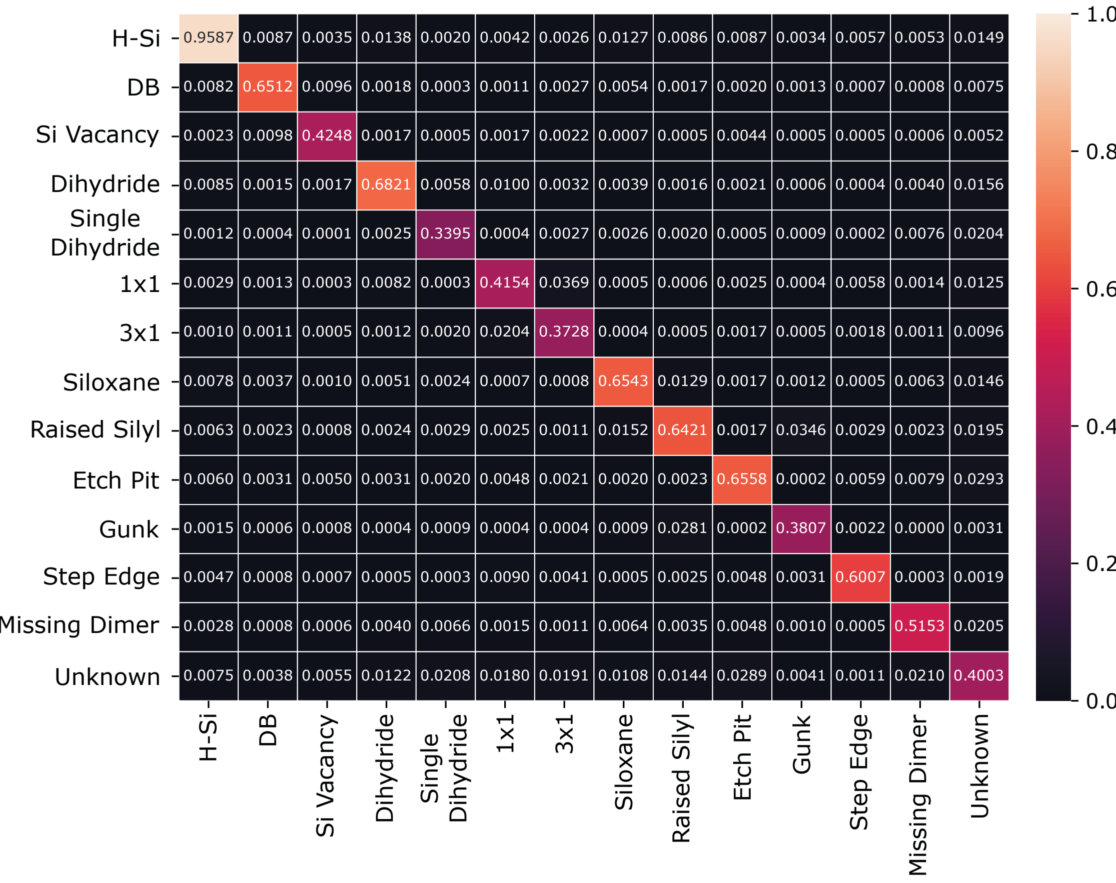

FIGURE 4.19: Confusion Matrix showing the Dice score of the updated neural network applied to the validation data.

4.3.2 Automated Quality Assurance and Defect Exploration

With the notable improvement to the accuracy and range of the neural network, it opens up further applications. In addition to being used for DB fabrication as discussed previously, the added number of classes allow the network to autonomously assess the quality of the surface. Such an example is shown in Figure 4.21 which shows 4 images of samples prepared using 4 variations of the preparation procedure. Each sample has been assessed for DBs, siloxane dimers, etch pits, and dihydrides; all an indication of sample quality. Figure 4.21 (a) shows a typical surface prepared with a base pressure in the high 10^{-11} Torr range (a good surface

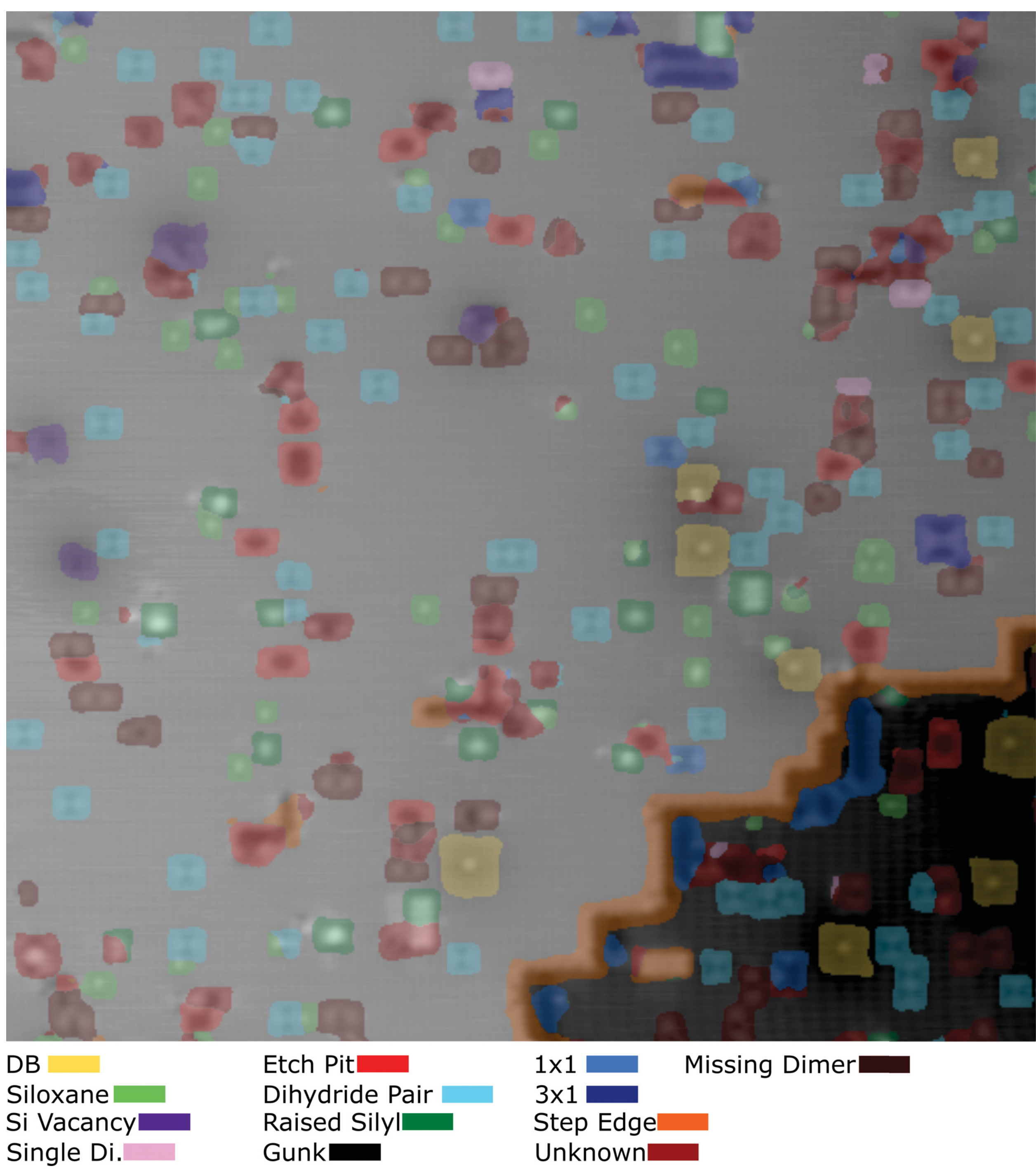

Figure 4.20: **A surface scan with defects as predicted by the updated model.** Corresponding colours as indicated below. Image is 50 x 50 nm^2 with an imaging bias of 1.3 V.

is prepared in the low 10^{-11} Torr range) which presents with the usual number of defects expected on a poorly prepared surface. The surface in Figure 4.21 (b) was allowed to etch for roughly 10 minutes longer than the usual 30-120 seconds explaining the larger concentration of etch pits seen. Figure 4.21 (c) shows a surface that was prepared in a chamber with a base pressure in the low 10^{-11} Torr range but that hasn't been baked for several months explaining the above average concentration of siloxane dimers (water contamination). This surface also has a higher concentration of DBs suggesting that the surface was annealed at a temperature higher than the traditional 330° C. The final surface shown in Figure 4.21 (d) was annealed at a temperature lower than the traditional 330° C resulting in the observed increase in dihydride species. It is envisioned that such an analysis could be coupled to an automated surface preparation system in which parameters (annealing temperature, etch time, H_2 pressure, etc.) could be tuned and subsequently correlated to a change in the observed concentration of defects. Since the analysis would no longer be reliant on a human user, the quantity of surfaces analyzed is only dependant on the scan speed of the system which could be further improved by parallelizing scanning probe systems.

One of the biggest limitations to semantic segmentation is the cost associated with developing a data set for training a neural network. This requires an initial understanding of the different classes and a significant amount of time spent labelling the data set. If an additional class is needed, the entire data set must be relabelled by hand. This puts a limitation on the ability to expand a neural networks knowledge as further discoveries about the data set are made. By combining supervised learning techniques with unsupervised learning techniques, it enables computer algorithms to further learn and distinguish between defects that were not labelled in the initial data set.

The combination of supervised and unsupervised techniques for segmentation of surface defects has been previously shown by Maksov *et al.*[311] and Ziatdinov *et al.* [223] . In both cases, neural networks were trained to distinguish between a clean and defected surface(WS_2 and H-Si(100)-2x1 respectively). These neural networks were able to learn such a distinction in both cases with a very small data set. By collecting more images of the surface and allowing

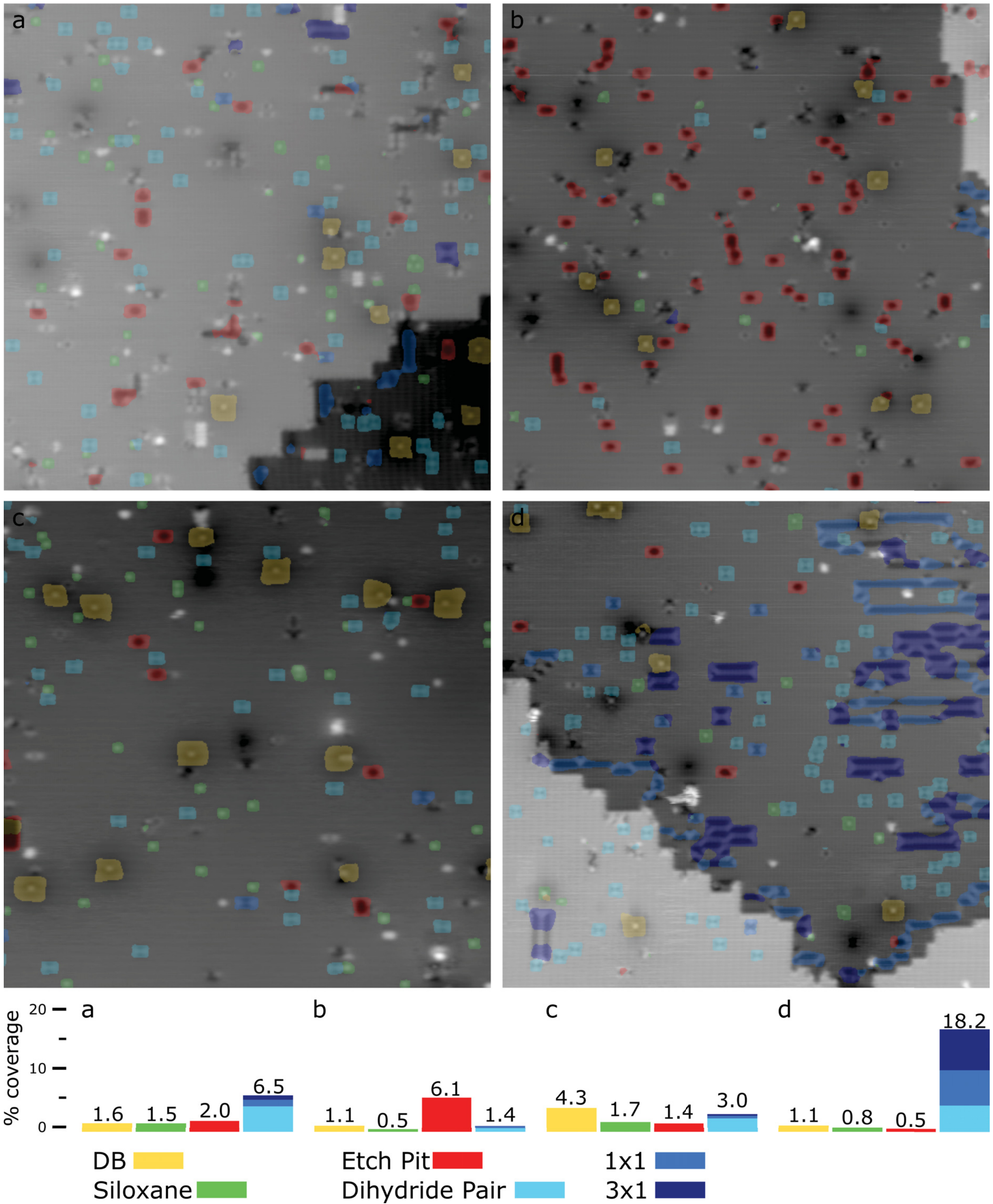

FIGURE 4.21: **Autonomous surface quality assessment.** (a)-(d) Surfaces prepared with varying preparation parameters (as described in the text) to emphasize the variability in surface defects. The corresponding histograms showing the calculated concentration of DBs, siloxane dimers, etch pits, and dihydride species for each surface is shown at the bottom of the figure. Each image is 50 x 50 nm^2 and acquired at a sample bias 1.3 V.

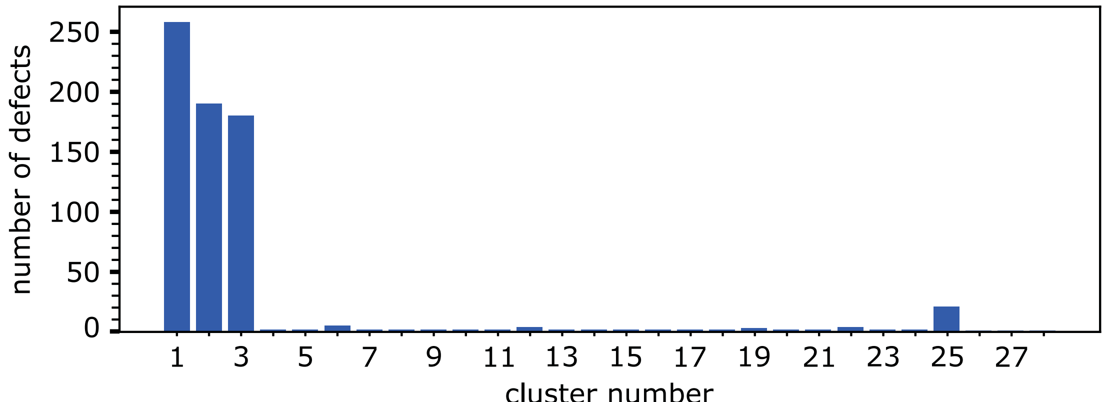

FIGURE 4.22: **Mean shift clustering of unknown defects.** Histogram showing the number of defects assigned to each class using mean shift clustering. All clusters other than 1,2,3, and 25 only have 1 or 2 defects assigned to each class.

the trained neural network to segment between the clean and defected surface, a collection of unlabelled defects was acquired. These defects were then used in an unsupervised learning technique allowing the algorithm to learn how to distinguish between the several varieties of defects based on differences in extracted surface features. This achieves the same result as a purely supervised technique but requires much less time spent creating a full data set.

As a proof of concept, a similar method was applied to the unknown class in the updated labelled data. By applying a mean shift clustering algorithm [207] to the data in the unknown class, the algorithm was able to distinguish differences in the defects and cluster those which shared common features. Figure 4.22 shows the results of the sklearn MeanShift algorithm applied to the unknown data set. As can be seen a total of 28 clusters were identified with 90 % grouped into the first 3 clusters. The remaining 10 % are distributed among the remaining 25 clusters as is often observed in unsupervised clustering with imbalanced data sets[223].

Looking at images from each class in Figure 4.23, it appears that cluster 1 and cluster 2 both consist of a new type of defect not known at the time of relabelling the data. The defect in cluster 1 shows a triple single dihydride as shown in Figure 3.39. A small number

of defects which do not match this classification are also seen in cluster 1 (see the 5th image in the top row for cluster 1). This will likely require the unsupervised learning algorithm to be supplemented with manual defect classification as suggested in [223] to ensure that defects which appear to share similar features are segregated appropriately. The defects shown in cluster 2 make up a previously unidentified defect. This defect appears to be made of 2 neighbouring missing dimers with one brighter and one darker edge. Just based on the images presented in Figure 4.23, it appears the brighter side is made of a raised Silicon atom however a complete analysis using multiple imaging modes as discussed in Chapter 3 is needed to confirm this. Like cluster 1, cluster 2 also shows a few additional defects suggesting that some user interaction is still needed to confirm classifications.

The defects shown in cluster 3 show a greater variation in shape between defects. All defects appear to show a similar bright feature relative to the substrate but the shape and position of this bright feature varies throughout the images. It is difficult to say with only the empty states images if these defects are variations of the raised silicon defect or another surface contaminant requiring the application of multiple imaging modes to provide further analysis to these defects. Future implementations of the training data would benefit from including both empty and filled states imaging allowing for more features to be learned for each defect class.

The defects in cluster 25 all show a very similar imaging contrast suggesting the model has clustered these defects based on the surface contrasts rather than the shape of the defect. Further work that could be explored to mitigate this issue is to allow the clustering algorithm to group defects based on some extracted features[205, 206, 223] of the image instead of the entire image. By providing the clustering algorithm with pre-filtered images, it allows the algorithm to emphasize certain features that are important to classification while ignoring those that aren't.

The last set of images in Figure 4.23 shows one image each from clusters 4 to 15. As can be seen, the defects in each image all show significant differences which resulted in the creation

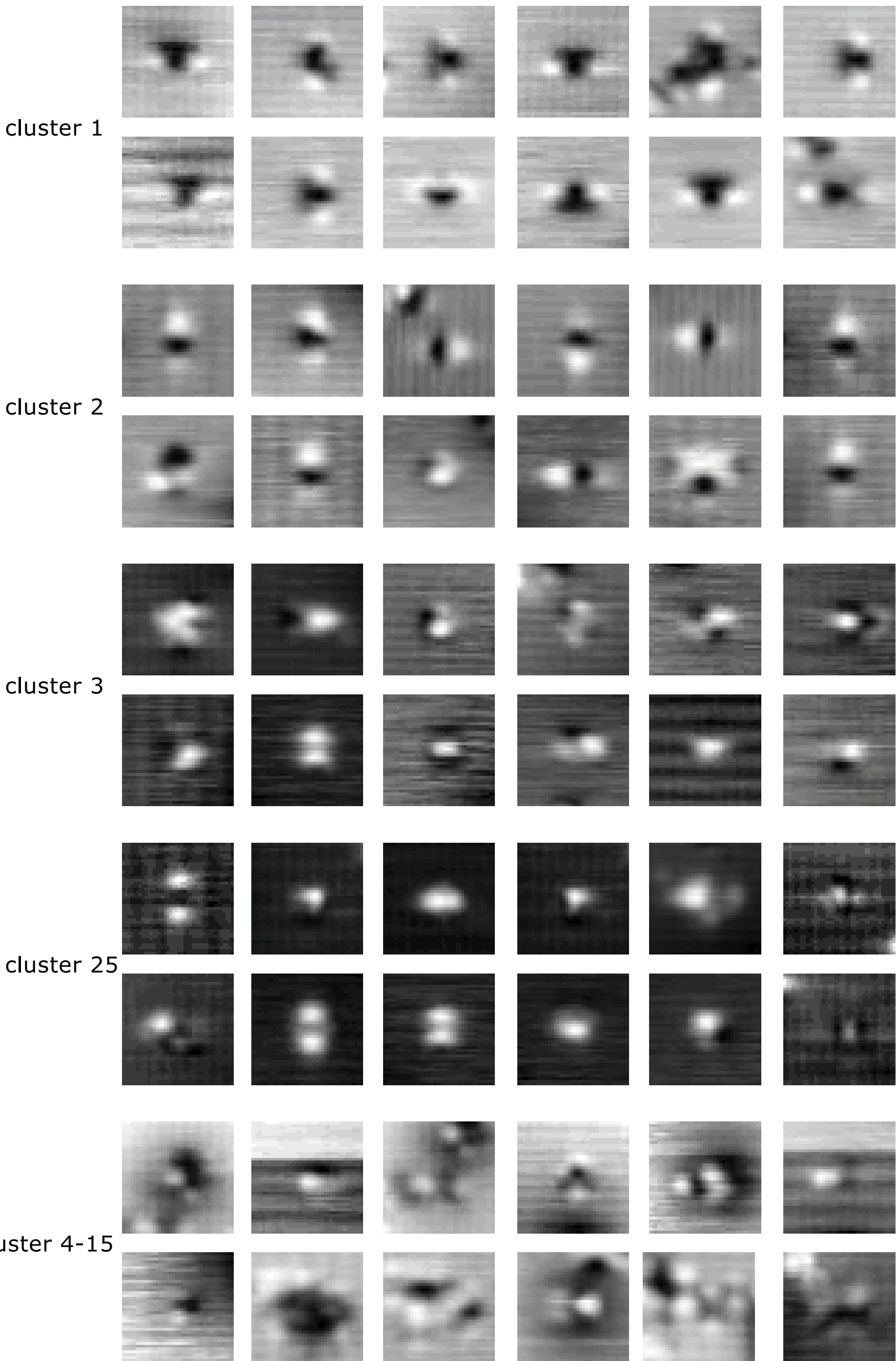

FIGURE 4.23: **Defect clusters of the Unknown class.** Random images taken from each cluster as calculated using a mean shift algorithm. Each image is 3.2 x 3.2 nm^2. All images shown for cluster 4-15 are from different clusters within this range.

of a unique cluster for each image. As the data set is expanded and number of unknown defects is increased, it is anticipated that a distinction can be made between defects which are novel species and those which are merely a unique combination of known defects.

By combining the results of the unsupervised learning with the previously labelled data set, the defects in cluster 1 and 2 could be included as their own class. The number of defects available in the labelled data set could then continue to be updated in this way as a larger data set is collected with unknown defects clustered into unsupervised groups and added to the labelled data set. As mentioned previously, the assignment of the newly clustered defects to their own class will require some interaction from a user to confirm that the defects are in fact of the same origin. This technique would still drastically improve the efficiency of the refinement of the neural network as a user will no longer need to manually relabel the entire data set whenever a new class is to be added. By combining the supervised and unsupervised techniques in such a way, it drastically streamlines the quality assessment and analysis of surface defects allowing for the autonomous study of the desired surface.

Chapter 5

Charge Distributions within Dangling Bond Structures

One of the most significant, often ignored realities of developing atom scale electronics is that they must still work with current technological infrastructures such as power supplies, wireless transmission, and cooling systems. While these systems can be modified to accommodate the shrinking of logic devices, the point remains that atom scale devices will still need to communicate with systems outside their native operating environment. As such, the development of what can be called a "macro-to-atom" system is needed to manipulate and couple the device to external controls.

The transistors of a Si wafer that make up an integrated circuit are coupled to external systems using interconnects. A series of alternating layers of a low permittivity dielectric (such as SiOF or SiCOH) and rows of metal lines (such as Cu, surrounded by dielectric) are stacked on top of the Si wafer. Vertical interconnect accesses (vias) made from metal are used to connect each layer allowing for unique access to the source, drain, and gate of each transistor. Current semiconductor technology featuring 7 nm node[1] dimensions is fabricated

[1] The node size in in reference to an arbitrary scaling factor in transistor design commonly used in the semiconductor industry.

using interconnects that are 28 x 14 nm[312]. If these same technologies were to be applied to the development of atom scale devices, it becomes clear that a significant reduction in interconnect size is still needed.

Modifications to the lithography process, such as using electron beam lithography can reduce feature sizes down to roughly 10 nm, however the size of such structures still needs to be reduced by a factor of 10 if they are to be used to address individual atoms of a surface [313]. This brings to light the need for an intermediate device connection where structures of roughly 100 to 10 atoms in width can be coupled to single atom devices. With the ultimate goal being the ability to create smaller wires, there are important limitations that need to be addressed to understand the viability of such a route. First, one must consider if it is physically possible to pattern the desired structures, second is the limitation in operating power and speed set by fundamental physical concepts as determined by the size and resistance of the structures.

Current lithographic processes involve material deposition and etching using a combination of resists and masks to create latent images of the desired circuits. These patterns in the resist are then washed away using a chemical or ion etching procedure leaving the desired structure behind. In actuality, it is a much more complex and intricate process better explained in such resources as [314] or [313]. If for example, the desired circuit was to pattern a series of copper wires leading to a device, it becomes apparent that the size limit of these wires is given by the diffraction limit of the light. The minimum feature size (CD, critical dimension) is proportional to the wavelength of light used (λ) given approximately as

$$CD = k_1 \cdot \frac{\lambda}{NA} \tag{5.1}$$

where NA is the numerical aperture. So as we decrease λ or increase NA ($NA = nsin\theta$), we can decrease our feature sizes. It is important to note however that changing these values

also limits the depth of focus (DF) of our system.

$$DF = k_2 \cdot \frac{\lambda}{NA^2} \tag{5.2}$$

Additioanl resolution can also be achieved by diffraction cancellation in which the effect of nonlinear beam spreading is reduced [315].Current lithographic techniques involving extreme ultraviolet (EUV, 13.5 nm) light sources have been able to a achieve feature sizes of 10 nm [33]. Feature sizes could possible be reduced further by using X-ray sources or electron beam lithography, however, significant changes to the lithography infrastructure is need before these can be implemented.

As discussed previously, a viable alternative to traditional lithography techniques is the use of probe based lithography. By using the sharp tip of a scanning probe system (such as an STM or AFM), it is possible to manipulate surface materials so as to fabricate the desired structures. A plethora of techniques have been developed for scanning probe lithography which can best be classified by the dominant tip-surface interaction such as thermal, mechanical, bias, current, and thermochemical lithography. An excellent review which covers these methods and more can be found in [58]. The most applicable to the research conducted in this thesis is bias-SPL. By applying a bias pulse above the surface of interest, it is possible to create what are essentially 1-D wires from either metal atoms(Gold Atoms on NiAl(110) [316, 317],Cu chains on Cu(111) [318] [319]), or Si DBs (by selectively removing hydrogen atoms from an otherwise hydrogen terminated surface) [159]. The newly created DBs could then themselves act as a conducting wire, or react with further materials such as gaseous phosphine (PH_3) creating lines of dopants [320].

Although, the realization of the “macro-to-atom” connection can be made using probe based lithography, it is important to understand limiting factors in their applicability. If one considers the copper wire interconnects of a traditional integrated circuit, two of the main limiting factors in operation are power consumption ($P = I^2R$), and the clocking speed

limited by the RC time constant ($\tau = RC$). Following procedures outlined in [26] we can estimate τ for a copper interconnect using parallel plate capacitance (C_{eff}) given as

$$C_{eff} = 2\epsilon_o\epsilon_r L\left(\frac{T}{X} + \frac{W}{H}\right), \tag{5.3}$$

resistance (R) given as

$$R = \rho\frac{L}{TW}, \tag{5.4}$$

combining to give

$$RC \approx 2\epsilon_o\epsilon_r\rho\frac{L^2}{TW}\left(\frac{T}{X} + \frac{W}{H}\right), \tag{5.5}$$

where ϵ_0 and ϵ_r are the vacuum and relative permittivity respectively, ρ is the resistivity, L is the length of wire, T is the height of the wire, W is the width of wire, X is the horizontal wire separation, and H is the vertical wire separation. Using a rough order of magnitude calculation where $T \approx 0.36\mu m$, $X = W = H \approx 0.23\mu m$, ρ =17 $n\Omega \cdot m$ (Cu), and $\epsilon_r \approx 3.6$ (fluorinated SiO_2) gives an $RC/L^2 \approx 34\ ps \cdot mm^{-2}$ where lengths on the order of mm give the observed GHz clocking rates seen in modern systems.

So the question that presents itself, is how will these atomic wires (metal or DB/dopant) respond? To make an order of magnitude approximation, let's assume copper and silicon DB wires with a resistance similar to bulk Si ($\rho_{Si} \approx 42\mu\Omega \cdot m$ with n $\approx 10^{19}/\text{cm}^3$), a wire size on the order of 0.4 nm, and a wire spacing of 10 nm. If we ignore any current leakage between the wires and the bulk[2] and assume vacuum above the wires (we can then approximate ϵ_r to be ~ 6, a split between Vacuum and Si), equation 5.5 becomes

[2] An effect which would decrease the operating speed of the device

$$RC \approx 2\epsilon_o \epsilon_r \rho L^2 \left(\frac{1}{XW}\right) \tag{5.6}$$

giving RC/L^2 $\approx$ 4.5 x 10^5 $ps \cdot mm^{-2}$ for Cu and $\approx$ 1.1 x 10^9 $ps \cdot mm^{-2}$ for Si. If these wires extend on the order of μm's that puts the clocking rate on the order of THz for Cu and 1 GHz for Si roughly matching the upper limit of CPU speeds found in modern computers.

The concept of power consumption through these atom sized wires presents an interesting challenge to calculate, since there currently does not exist a working prototype to extract operating specs from. Let us instead consider a simple schematic where a "larger" 200 nm wide Cu wire is coupled to a smaller atom sized wire of roughly μm length. The question then becomes, does this smaller segment of wire introduce a significant increase in power consumption compared to an unbroken larger metal wire.

If these wires are expected to carry the same current (let's say 1 mA) then it's a simple comparison of resistance to extract the power usage. The resistance per mm for the large copper, small copper, and small Si wires can be written as

$$\begin{aligned} R/l &= \frac{\rho}{A} \\ R_{CuL}/l &= \frac{17n\Omega \cdot m}{0.23\mu m \cdot 0.36\mu m} = 2.05 \times 10^2 \Omega/mm \\ R_{CuS}/l &= \frac{17n\Omega \cdot m}{0.4nm \cdot 0.4nm} = 1.06 \times 10^8 \Omega/mm \\ R_{SiS}/l &= \frac{42\mu\Omega \cdot m}{0.4nm \cdot 0.4nm} = 2.63 \times 10^{11} \Omega/mm \end{aligned} \tag{5.7}$$

It becomes very clear that if we assume that smaller wires are expected to run the same current as their larger counterparts, the power consumption would make these devices prohibitively expensive even if we assume the atomic wires will run for shorter lengths on the chip. Thankfully, these atom size devices are expected to require a significantly lower current supply to operate. The single atom transistor from Chapter 1 by Fueschle *et al.* [48] was shown to draw roughly 1×10^{-7} A in the on position. If we assume a similar current

requirement for the small Si and Cu wires, we can estimate the power consumption of our wires

$$\begin{aligned} P/l &= I^2 R/l \\ P_{CuL}/l &= (1mA)^2 \left(2.05 \times 10^2 \Omega/mm\right) = 2.05 \times 10^{-4}\,\mathrm{W/mm} \\ P_{CuS}/l &= (100nA)^2 \left(1.06 \times 10^8 \Omega/mm\right) = 1.1 \times 10^{-6}\,\mathrm{W/mm} \\ P_{SiS}/l &= (100nA)^2 \left(2.63 \times 10^{11} \Omega/mm\right) = 2.6 \times 10^{-3}\,\mathrm{W/mm} \end{aligned} \tag{5.8}$$

These approximations suggest that as long as the smaller wires are capable of operating with lower current requirements, they will not introduce any significant limitations in energy consumption, especially when considering that these smaller wires will only need to extend *um*'s in length compared to the *mm*'s of longer wires. While to a first order, these calculations appear to suggest that atomic wires provide a valuable avenue for the macro to atom configuration, there have been a lot of liberties taken in these calculations which still require experimental verification, the most important being a measure of the conductivity through Si DB lines.

Two probe measurements have been carried out on the hydrogen terminated Ge(100)-2x1 surface however this experiment only confirmed the presence of a gap state capable of carrying current [321]. For extractions of specific values of surface conductivity one has to look at 4 probe surface conductivity measurements which can extract the conductivity per unit square[3]. Work by Just *et. al.* determined the surface conductivity of the unterminated Si(100)-2x1 surface to be $1.6 \pm 0.4 \times 10^{-4}$S/square. If we approximate this value to a single DB wire (assuming a sheet thickness of 1 nm), we get a resistance per wire length of $R_{Si}/l = 1.6 \times 10^{10}\,\Omega/\mathrm{mm}$, slightly better than the resistance calculated for bulk Si. It is important to state that since this calculation of resistivity came from an unterminated surface, the actual resistivity of a DB wire on an otherwise hydrogen terminated surface may be significantly

[3]the square (□) is commonly used in surface conductivty measurements. It references a square area of the surface with the resistance across a 1 nm x 1 nm area of the surface measuring the same as a 1 m x 1 m area.

different. The development of such systems capable of measuring the conductivity of a Si DB wire are currently underway, however, numerical values are unavailable at the time of writing this thesis [322].

Until such measurements can be taken, it is useful to study the properties of DB wires and structures to extract information regarding the structural and electrical behaviour with the addition of charge. The overall ground state of DB wires has been extensively theoretically studied with significant deviations in the expected conductivity depending on the observed ground state of the wire [323–331]. Experimental studies have been limited to STM and H-apex AFM which have failed to conclusively identify their ground state, and charged behaviour. The work that follows incorporates the use of a Si-apex tip which is capable of distinguishing between the positive, neutral, and negative charge state of a DB through variations in the $\Delta f(V)$ signal of an AFM. The capability allows for the observation of charge distributions within a DB wire providing insights into the structural reordering of DB wires needed for theoretical and experimental calculations of their conductivity.

5.1 Charge Distributions in Silicon Atomic Wires

A preprint of this paper is available here [3].

Jeremiah Croshaw[1,2], Taleana Huff[3], Mohammad Rashidi[1], John Wood[1], Erika Lloyd[1], Jason Pitters[3], Robert Wolkow[1,2,3]

[1] Department of Physics, University of Alberta, Edmonton, Alberta, T6G 2J1, Canada

[2] Quantum Silicon Inc., Edmonton, Alberta, Tt6G 2M9, Canada

[3]Nanotechnology Research Centre, National Research Council Canada, Edmonton, Alberta, T6G 2M9, Canada

5.1.1 Abstract

Using a non-contact atomic force microscope (nc-AFM), we examine the continuous DB wire structures of the hydrogen terminated silicon (100) 2x1 surface. By probing the DB structures at varying energies using the gating effect of an AFM tip, we identify the formation of previously unobserved ionic charge distributions correlated to the net charge of DB wires and their predicted lattice distortion. Performing spectroscopic analysis, we identify higher energy configurations corresponding to an alternative lattice distortion as well as tip-induced charging effects. By varying the length and orientation of these DB structures, we further highlight key features in the formation of these ionic surface phases.

5.1.2 Introduction

The development of novel "beyond CMOS" devices has led to the design and implementation of device components made of few to single atoms[46, 48, 221, 288, 332–335]. Due to their decreased size, the charge distribution of such devices can no longer be treated as an ensemble average, instead requiring discreet addressment. The atomic force microscope (AFM) has been proven to be a useful tool for the detection of discrete transitions between charge states in both molecular[112–114, 336, 337] and atomic structures[108, 236, 338], including silicon dangling bonds (DBs)[6, 46, 155]. In particular, DBs on the otherwise hydrogen terminated Silicon (H-Si) (100)-2x1 surface have recently been shown to behave as quantum dots capable of holding 0, 1, or 2 electrons (rendering the DB in a positive, neutral, or negative charge state)[168, 173, 174, 248]. Enabled through atomically precise lithography [1, 4, 5, 145, 147, 177], patterned DB systems are capable of representing binary logic through charge state manipulation within many-dot structures[6, 46, 55, 155]. Missing from these studies, however, has been exploration of the positive DB charge state and a look at charge arrangement in continuous (made with no intervening H-Si atoms) DB structures.

In this work we further our understanding of continuous DB structures at previously unexplored energies within the bulk Si band gap as enabled by AFM. Due to the anisotropy of the (2x1) reconstruction [125, 168, 173, 339], these DB structures are either patterned along a single dimer, creating what is commonly referred to as a bare dimer [84, 247, 262, 340], or along the same side of a dimer row creating a DB wire[269, 323]. DBs within a bare dimer are separated only by the shared dimer bond forming a pi bond[341–344] while DBs within a DB wire are separated by a second layer back bonded Si atom. This difference in bonding leads to distinct differences in their atomic and electronic properties. By using a charge sensitive Si-functionalized probe[2], we are able to clearly distinguish between the positive, neutral, and negative charge states of DBs within bare dimers and DB wires, yielding insights into the association of DB charging with lattice distortion. We identify the formation of an ionic charge distribution within bare dimers and DB wires with the latter only visible when accompanied by changes in the overall charge state. Through spectroscopic analysis, we identify the formation of both higher energy ionic configurations attributed to an alternative lattice distortion[345] as well as higher order charge distributions within DB wires, with differences observed for DB wires of varying lengths.

5.1.3 The Single DB

The native charge state of the DB can be modified by either varying the crystal doping level or the electrostatic environment surrounding the DB[6, 46]. Using a degenerately n-doped crystal (see methods), Kelvin probe force microscopy (KPFM) reveals the transition bias between the neutral and negative (0/-) charge state and the positive and neutral (+/0) charge state of the DB to be 0.2-0.4 V below the Fermi level[6, 46, 155] and at the onset of the valence band[167] respectively. Due to the location of the (+/0) charge transition, it is difficult to detect with KPFM as high currents in the expected bias range make it difficult to maintain tip integrity or distinguish the DB charging from higher bulk current contributions[7]. By raising the electrostatic potential surrounding the DB [6], these charge transitions can be

shifted in energy to a more mid gap region allowing for both charge transitions to be detected with KPFM. Figure 5.1 (a) shows a $\Delta f(V)$ spectroscopy of a DB—which was positioned on the edge of a 14 DB cluster (shown in the supporting information in Figure 5.8)—highlighting the positive (purple), neutral (orange), and negative (blue) charge state. The (+/0) charge transition can be seen at V_s = -0.8 V with the (0/-) charge transition occurring over V_s = 0.7 - 0.8 V, roughly 1.2 V higher than previously reported[6, 46, 155] (The corresponding I(V) spectroscopy and STM images can be seen in Figure 5.9). The slanted nature of the KPFM charge step is not seen in other single electron charging systems such as molecules on an insulating substrate[114, 346] and is thought to be a result of a current induced averaging of the charge state based on the competing emptying and filling rates of the DB [167, 347].

Constant height Δf maps of the DB in the positive (+), neutral (0), and negative (-) charge state relative to the H-Si surface can be seen in Figure 5.1 (b),(c), and (d) respectively. Matching the trend seen in the $\Delta f(V)$ spectroscopy, the (+) DB appears brighter than the surrounding H-Si atoms, the (0) DB shows similar contrast to the surrounding H-Si atoms, and the (-) DB appears as much darker than the surrounding H-Si atoms. In addition to the change in charge state, there is also a predicted lattice distortion [155, 174, 348] which raises position of the (-) host Si atom by roughly 30 pm giving the DB a more sp^3 character and lowering the position of the (+) host Si atom by roughly 40 pm giving the DB a more sp^2 character[174]. This lattice distortion is shown with Figures 5.1 (b)-(d) with the horizontal black line showing the relative shift from the (0) Si atom position in grey. It is difficult to extract such lattice features as the measured Δf signal is convoluted with the changing covalent and charge induced dipole interaction of the surface DB with the neutral DB of the Si terminated tip [139, 143, 146, 149, 150].

5.1.4 The Bare Dimer

Consistent with observations of the unterminated 2x1 surface [135, 245, 349–353], bare dimers are predicted to undergo a lattice distortion putting one atom in a raised (sp^3) electron-rich

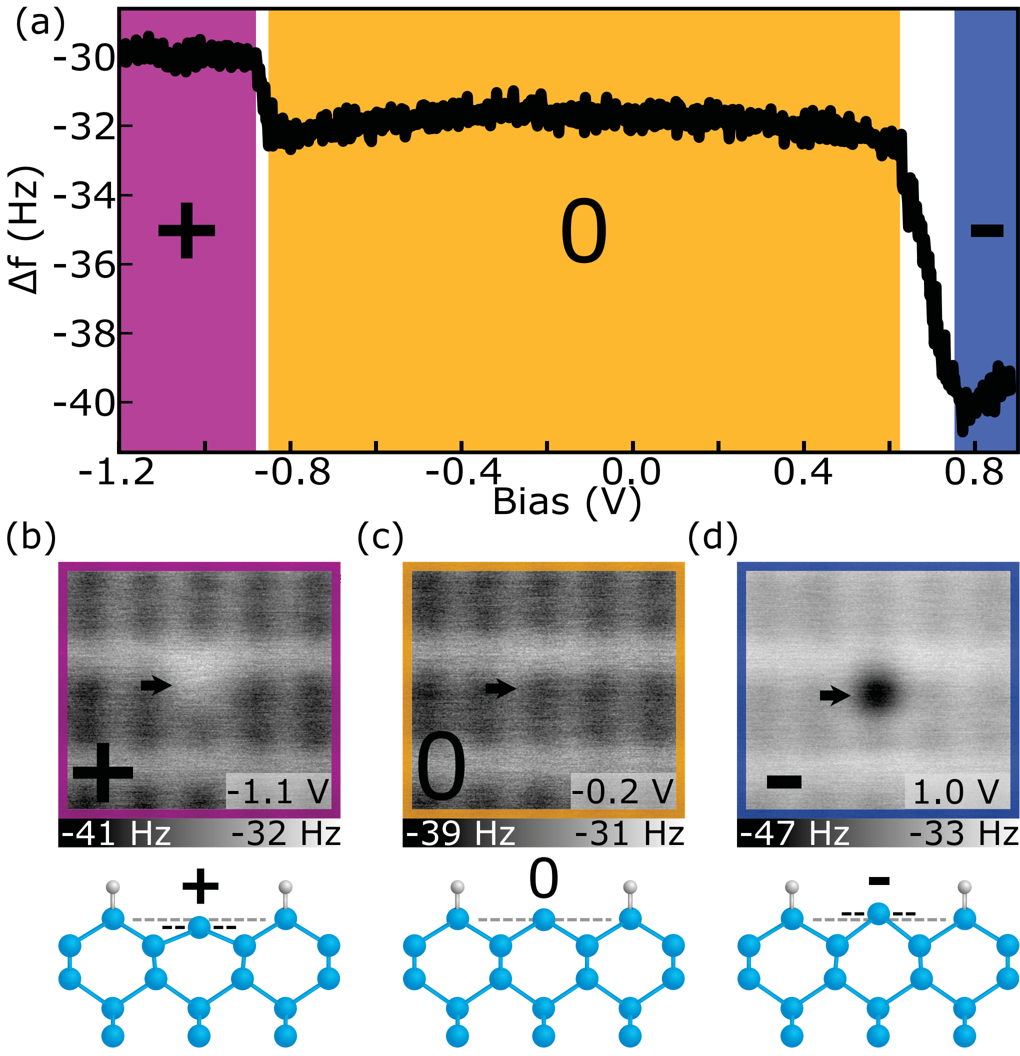

FIGURE 5.1: **Three Charge States of the Si DB.** (a) $\Delta f(V)$ spectroscopy over a Si DB showing the (+/0) and (0/-) charge transition (occurring at roughly -0.9 V and between 0.7-0.8 V respectively). (b),(c),(d) Constant height Δf images of the DB in the positive (+), neutral (0), and negative (-) charge state respectively with the corresponding ball and stick model of the Si DB in each charge state. The black dashed line highlights the vertical height shift of the charged host Si atom relative to the neutral state with dimensions listed in the text. Each image is 2.1 x 2.1 nm^2 with bias values as indicated. All measurements performed at -300 pm from the height set point (see methods).

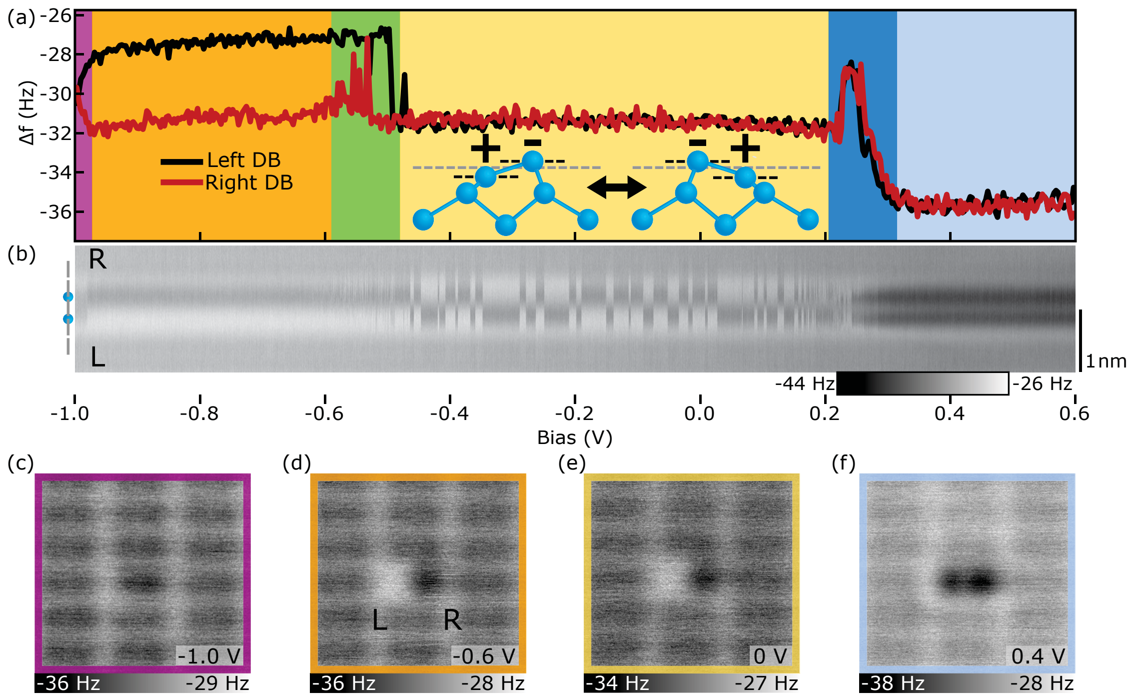

FIGURE 5.2: **Charge Distributions of the Bare Dimer.** (a) $\Delta f(V)$ spectroscopy over the right (red) and left (black) DB of the bare dimer. The inset shows the buckled geometry of the bare dimer in the two degenerate charge configurations (+- or -+) (dimensions taken from ref [355]). (b) $\Delta f(V)$ line scans over the bare dimer with the position of the bare dimer within the line scans is indicated to the left of (b). 50 line scans at bias increments of 0.02 V from -1.0 to 0.6 V are shown. Scale bar is 1 nm as indicated on the right of (b). (c)-(f) Constant height Δf of the bare dimer imaged in four of the six regions as indicated by the coloured border and bias. All measurements performed at -300 pm from the height set point (see methods). Corresponding band diagrams are shown in Figure 5.11.

(-) state, and the other in a lowered (sp^2), electron-deficient (+) state[329, 344, 354]. Figure 5.2a shows the $\Delta f(V)$ spectroscopy of each DB in a bare dimer (labelled left and right) revealing six distinct regions. $\Delta f(V)$ line scan maps along the bare dimer were also taken in which 50 line scans were acquired at bias intervals of 0.02 V within the full bias range (the corresponding $I(V)$ spectroscopy and $I(V)$ line scan maps are shown in Figure 5.10).

At biases lower than -0.98 V (purple), the bare dimer appears to be in a symmetric configuration with both sides of the bare dimer appearing neutral also shown in the constant height Δf image of Figure 5.2 (c). Increasing the sample bias between -0.98 V and -0.6

V (orange), the bare dimer reorders to the expected ionic (-+,ud) configuration with the right DB appearing negative and the left DB appearing positive as supported in Figure 5.2 (d). At -0.6 V to -0.5 V (green), the tip becomes resonant with the pi state[341–344] of the bare dimer possibly allowing charge to quickly transfer between sides of the bare dimer as indicated by the spikes in signal in the $\Delta f(V)$ spectroscopy of Figure 5.2 (a) as well as the streakiness seen in the line scans of Figure 5.2 (b). Between -0.5 V and 0.2 V (yellow), the $\Delta f(V)$ spectroscopies show that both DBs appear negative, however looking at the line scans in Figure 5.2b and the Δf map of Figure 5.2 (e), it is clear that the bare dimer is still in an ionic configuration except now the bare dimer readily switches between the (-+) and (+-) configuration likely facilitated by the newly accessible pi state. The reason both DBs in the $\Delta f(V)$ spectroscopies appear negative is due to a localized attractive interaction between the DB and the tip causing the negative DB within the bare dimer to "follow" the tip [146, 155] creating a tip-induced charging. Such an effect isn't seen in the line scans of Figure 5.2 (b) because the tip is not localized over a single DB for a long enough time for a tip induced charge redistribution to occur.

At higher bias values between 0.2 V and 0.3 V (dark blue), the bare dimer becomes resonant with the pi* state[342, 343] as indicated by the peaks seen in the $\Delta f(V)$ spectroscopy. Looking at the line scans in Figure 5.2 (b), it appears that the DBs experience this increase in Δf simultaneously suggesting that this peak is a measurement artifact, i.e, electron dynamics are occurring at a faster rate than the AFM is capable of sampling. Similar features are also seen in the $I(V)$ plots in Figure 5.10 corresponding to resonant tunneling through the pi* state. Above bias values of 0.3 V (light blue), both DBs in the bare dimer appear to be in a negative charge state as supported by Figure 5.9 (f). It is unclear if the bare dimer is in a 2e$^-$ (- -) charge configuration due to electron injection from the tip, or is switching between a degenerate 1e$^-$ (0-/-0) charge configuration at rates faster than the sampling of the AFM. Since the origin of the characteristic butterfly shape [84, 247] of the bare dimer in STM images (Figure 5.10) is attributed to a flipping of between two degenerate states [247], it is more likely that the bare dimer exists in a 1e$^-$ (0-)/(-0) configuration. Further insights

into the charge configuration below -0.98 V and above 0.2 V may be offered by time resolved techniques [7, 167] and warrant further investigation.

5.1.5 DB Wires

DB wires are predicted to undergo a similar distortion attributed to a Peierls effect [356–358] thus reducing the overall energy of the DB wire. STM observations of such reorderings have been reported through variations in the height of DBs within a wire as explained through a similar Jahn-Teller distortion[269] through the pairing of second layer Si atoms. DBs which are raised through the pairing of second layer Si atoms exhibit more sp^3 qualities, creating a more electron-rich state, while DBs which are lowered through the pairing of second layer Si atoms exhibit more sp^2 qualities, creating a more electron-deficient state[269, 357, 359]. This resulting lattice shift is predicted to create an almost ionic charge redistribution throughout the wire via an up-down(sp^3-sp^2) pairing of DBs within the wire. More recent theoretical studies suggest that spin ordering through electron-electron interactions is the more stable ground state configuration compared to a charge reordering from electron-phonon interactions [325, 329, 344, 345, 360]. Wires are predicted to align in an antiferromagnetic fashion at finite length with the non-magnetic (ionic) ordering becoming more stable at longer wire lengths due the additional stability of longer ionic configurations[325, 345]. The conductivity through such wires is predicted to vary drastically depending on the established ordering of the wire used in the calculation with spin or charge ordered wires developing a semiconducting gap [323, 325–327, 329, 330, 345] that undistorted wires do not possess [324, 328, 330, 331]

Using KPFM, it is revealed that with a net neutral charge, DB wires do not exhibit any charge reordering. Only through the addition of a negative charge (or positive charge shown in Figure 5.12) does the DB wire reorder into the theoretically predicted ionic distribution likely facilitated by an additional polaronic effect [357, 360–362] as shown in Figure 5.3. Figure 5.3 (a) shows the $\Delta f(V)$ spectroscopy taken over the second DB in a five DB wire (indicated by the black arrow in Figure 5.3 (b)-(e)) revealing four distinct charge distributions. Between

-1.1 V and -0.5 V (purple), the DB wire exists in an overall neutral charge state with each DB in the wire showing a neutral charge in Figure 5.3b (insights into the predicted spin ordering require a spin sensitive probe and are currently outside our abilities). Between -0.5V and 0.25 V (orange), the DB wire enters a net 1e$^-$ charge state resulting in an ionic charge redistribution and corresponding lattice distortion (-+-+-, ududu) as shown in Figure 5.3 (c).

As the bias is increased between 0.25 V and 0.4 V (blue), the 5 DB wire is shown to periodically enter an alternative net 1e$^-$ (0-+-0, dudud) charge distribution shown in the top half of Figure 5.3 (d). Such a charge configuration is predicted to have a higher overall energy[345] than the (-+-+-, ududu) configuration and is therefore less stable when imaged. Although the outer atoms in this charge configuration are expected to be in a more electron-depleted sp^2 configuration, the rigidity of the end H-Si atoms in combination with the crystal doping level prevent the formation of positive DBs at the ends of the wire [325, 345]. Increasing the bias between 0.4 V and 0.8 V (green), the 5 DB wire enters a higher order charge state (multiple e-). Looking at the Δf map of Figure 3.4 (e), the DB wire appears to be in a (-0-0-) charge state, however, when probed with larger tip-sample separations as shown in Figure 5.13, the DB wire appears to be in a (-000-) charge configuration with the central DB appearing negative only at reduced tip heights. As with the $\Delta f(V)$ spectroscopies of the bare dimer, such an effect can be explained by the attractive interaction between the tip and surface DBs resulting in a localized tip induced charging of the central DB.

Extending these measurements to DB wires of varying length, the same charge reordering is seen for DB wires with a net 1e- charge. Odd DB wires, shown in Figure 5.4 (a), are observed in a lower (udu) and higher (dud) energy configuration associated with ionic pairing within the structure. Each of the line profiles in Figure 5.4 is an averaging of multiple line scans in either configuration taken from full line scan maps in Figure 5.5. Like the 5 DB wire, the 3 and 7 DB wires show a lower energy (-+-, udu) and (-+-+-+-, udududu) charge reordering respectively. In the higher energy configuration each host Si atom switches its orientation resulting in (0-0, dud) and (0-+-+-0,dududud) configurations respectively. As predicted in

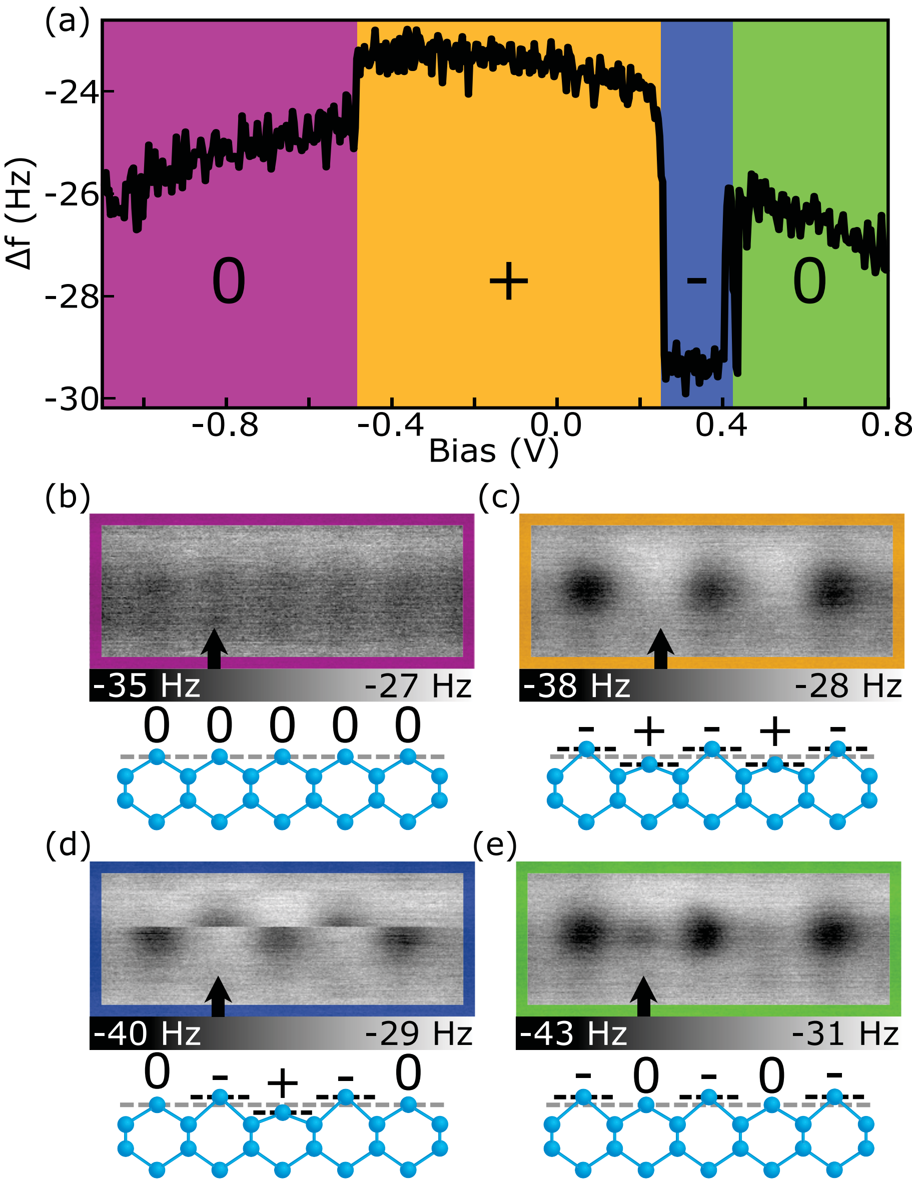

FIGURE 5.3: **Charge Distributions of the 5 DB Wire** (a) $\Delta f(V)$ spectroscopy over the second Si DB (marked with a black arrow in (b)-(e)) of the 5 DB wire showing four distinct charge regions (The $\Delta f(V)$ spectroscopy of all 5 DBs within the wire is shown in Figure 5.14). (b)-(e) Constant height Δf image of the neutral, lower energy $1e^-$, higher energy $1e^-$, and higher negative charge configuration respectively. Each ball and stick model shows the expected trends in lattice distortion as calculated in Ref [345] and [359]. Bias values for (b)-(e) are -0.7 V, -0.2 V, 0.2 V, and 0.8 V respectively. Height setpoint of (a) is -200 pm, (b)-(e) is -250 pm. All images are 1.0 x 2.5 nm^2.

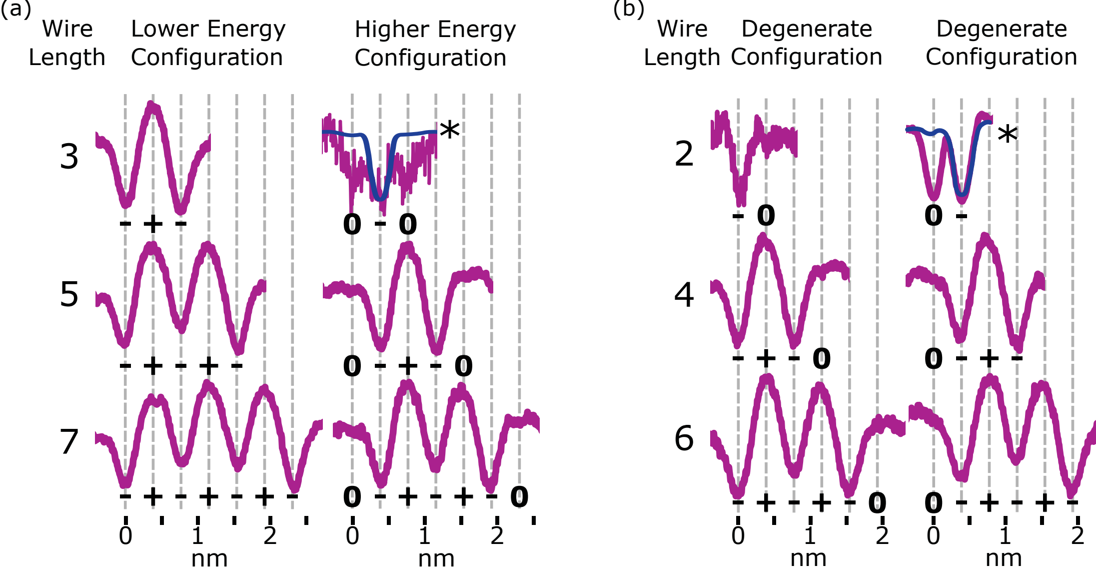

FIGURE 5.4: **DB Wire Charge Distributions** (a),(b) Line profiles of odd and even length DB wires from 2 to 7 DBs in lower energy and higher energy (degenerate for even length DB wires) charge configuration as indicated. Each profile shown is an average of 20-50 individual line scans from Figure 5.5 except the higher energy configuration (0-0) of the 3 DB wire and degenerate (-0) configuration of the 2 DB wire which were only visible for 1 and 6 line scans respectively. The blue lines show the expected configuration for each as described in the text.

Ref. [345], the energy difference between the (udu) and (dud) states of the 3 DB wire is larger than the energy difference between these states in the 5 and 7 DB cases. As a result, the higher energy (0-0, dud) configuration of the 3 DB wire is less stable and was never observed for a complete line scan. The line scan presented in Figure 5.4 (a) only showed a momentary excitation as the tip scans over the centre DB. As a result, the line profile appears much noisier (due to reduced averaging) with each DB appearing negative. The blue line profile was drawn to show the expected configuration if the structure was stable enough to be completely imaged by the tip. The transition of the middle DB in the 3 DB wire from the (+) to (-) charge state is also seen in the $\Delta f(V)$ spectroscopies shown in Figure 5.14.

Unlike the odd length DB wires, the even length DB wires demonstrate two degenerate

configurations when in the net 1e$^-$ charge state resulting in an (ud) or a (du) pairing. Figure 5.4 (b) shows line profiles of both degenerate distributions for DB wires of length 2, 4, and 6. Much like the odd wire case, DBs which are raised through second layer pairing (sp^3) are imaged as negative while DBs which are lowered through second layer pairing (sp^2) are imaged as positive if they sit within the wire and neutral if they sit at the ends of the wire. The ionic distributions in the 2, 4, and 6 DB wires are therefore observed in a (-0/0-, -+-0/0-+-, and -+-+-0/0-+-+-) charge distribution respectively as shown in Figure 5.4 (b). In the 2DB wire case, the predicted barrier between degenerate configurations is much lower than that of the longer DB wires [269, 363], so it toggles more easily between each configuration. As a result, the 2 DB wire configuration was most often imaged in a (–) configuration as the negative DB "followed" the tip during scanning. The left configuration (-0) appeared for only a few line scans resulting in greater noise seen in the line profile with the right configuration (0-) never appearing due to an additional electrostatic perturbation from subsurface charges[5, 6]. The blue curve has been drawn to highlight the expected configuration.

The energy at which each wire transitions from the net neutral to net negative (1e$^-$) charge state depends on the wire length with longer wires ionizing at lower sample biases as predicted in Ref [325, 345]. Figure 5.5 highlights the first ionization bias for DB wires length 2 to 7, along with the second ionization bias where a wire can facilitate an additional negative charge. The 2 DB wire is ionized at the largest sample bias around -0.08 V while the 7 DB wire is ionized at -0.5 V. As the DB wires length is increased from an odd to an even DB number, a slight increase in the first ionization energy is observed. This effect is seen if one compares the first ionization energy of the 3 DB wire to the 4 DB wire and the 5 DB wire to the 6 DB wire. Since the odd and even DB wires possess the same number of positive and negative DBs, we speculate that this increase in ionization energy is due to the additional lattice strain associated with having a down (sp^2) atom at the end of the wire without the energy lowering effect of a Coulombic contribution through ionic pairing. Increasing the wire length further from an even to odd wire creates an additional ionic (+-,du) pair which lowers

the ionization energy of the wire. The opposite trend was predicted in [325, 345] which we attribute to their models accounting for a fully ionic configuration for even length wires resulting in a lower energy configuration due to the added Coulombic interaction. The first ionization energy of DB wires is plotted for wires up to 15 DBs in length shown in Figure 5.6. At a DB wire length of 9 to 15 DBs, this ionization energy is found to reach a minimum value of roughly -0.55 V suggesting the added Coulombic contribution across the wires is screened at these higher lengths. The slight increase in bias of the first ionization events as DB wires are increased in length from an odd to an even number of DBs is evident up to the longest chain measured. Line scans of DB wires of length 8 to 15 are shown in Figure 5.15.

A similar trend can be seen when looking at the secondary ionization energy transitioning to a multiple negative charge state in DB wires as shown in Figure 5.6. As the sample bias increases and the DB wire is forced to accept an additional charge from the tip, the DB wires redistribute their charge so that the separation between negative charges is maximized. This is most easily observed for the 4 and 5 DB wire case which now contain two negative DBs located at the wire edges with all middle DBs imaged in the neutral charge state. The 6 and 7 DB wires also readjust to hold a negative charge in both wire ends. The 7 DB wire easily accommodates the addition of the negative charge by neutralizing the centre DB leaving two (-+-, dud) clusters at the ends of the wire. The 6 DB wire appears to be in a more frustrated configuration with both outer DBs appearing negative and the two inner DBs showing a switching behaviour similar to the 2 DB case. It is likely that this DB cluster is switching between a degenerate (-+-00-/-00-+-) charge distribution as the tip scans over the wire although confirmation of such a configuration is outside the available sampling rates.

As the DB length is increased, the DB wires can more easily accommodate a greater number of charges. Since this added charge introduces an additional polaronic effect [357, 360–362], the DB wires are able to reorder into a greater number of configurations which are stabilized by this added charge. Figure 5.7 shows select Δf maps of DB wires length 8 to 15 at 0 V. At this bias, the 8 DB wire has transitioned from the (ud) configuration expected for even wires and instead features two (-+-) clusters at either end. The (ud/du) configuration for

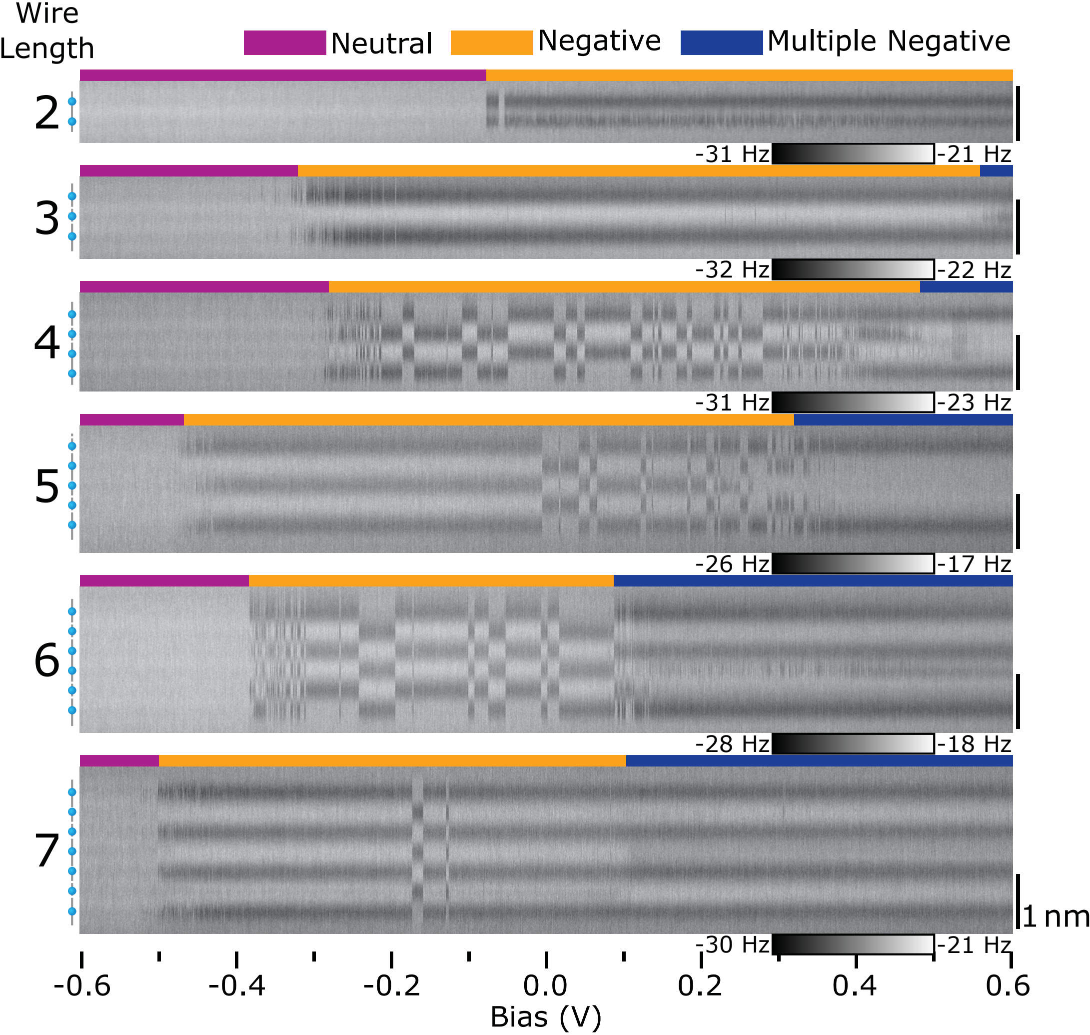

FIGURE 5.5: **Charging of DB wires** Linescans of DB wires length 2 to 7. Bias increments are 0.02 V with 50 line scans taken at each bias. Purple indicates the bias window when the DB wire is neutral, yellow indicates a single negative charge in either the lower or higher order (odd) or degenerate (even) configuration, and blue indicates an observed charge greater than -1. The position of each DB in the DB wires are indicated to the left of each line scan in blue. Linescans taken for DB wires of length 2,4,6 and 7 were taken at -250 pm, 3 was taken at -300 pm, 5 was taken at -200 pm. These heights were selected for each wire to minimize the effects of tip induced switching. The onset of the first ionization event did not vary with decreased tip height as shown in Figure 5.13.

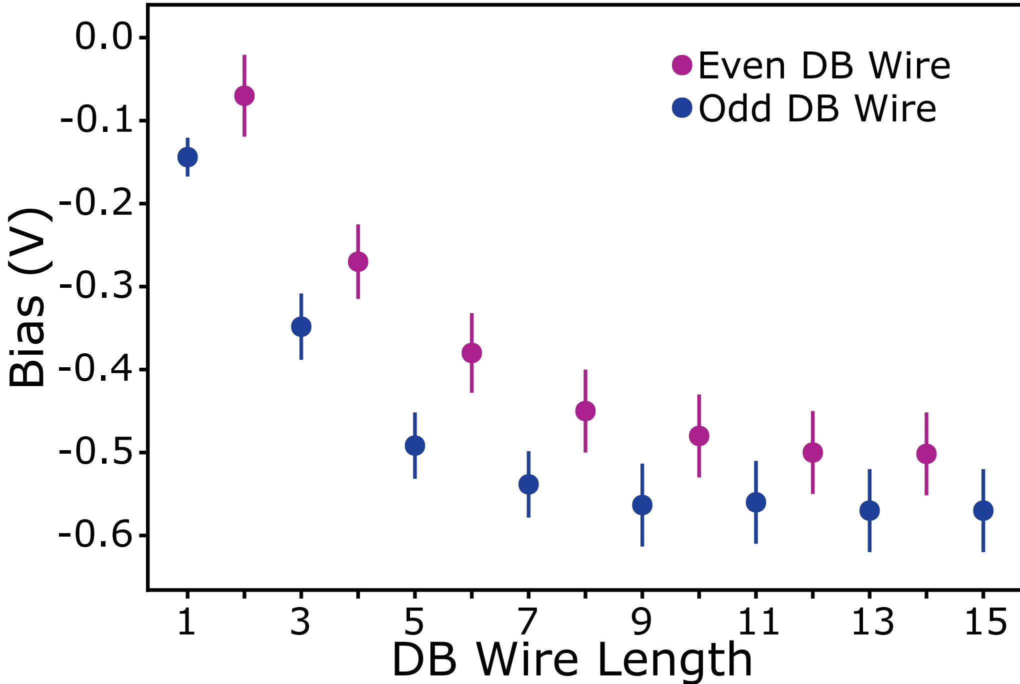

FIGURE 5.6: **Charging Voltage of DB wires.** Bias at which the DB wire transitions from the neutral to negative charge state. Error bars account for variations in charging energy between the $\Delta f(V)$ spectroscopies (Figure 5.14) and line scan images (Figure 5.13 and Figure 5.15) taken at varying tip heights.

the 8 DB wire can be seen in the line scans of Figure 5.15 at bias values lower than the configuration seen in Figure 5.7 (a), suggesting that the configuration shown in figure 5.15 (a) is a higher energy configuration. The 9 DB wire of Figure 5.7 (b) is shown to switch between two configurations mid-scan. The position of the (-+-) cluster on the left side of the 9 DB wire shifts one lattice site with the middle DB appearing negative only when the (-+-) cluster is at the end of the DB wire. Its appearance is very similar to the 5 DB wire at reduced tip-sample separation suggesting this DB may only be negative due to a tip interaction. The right side of the 9 DB structure does not appear to switch with the left side of the wire which supports the claim that the added polaronic effect from additional charge

can stabilize the wires into higher energy configurations, allowing for the wires to decoupling into smaller subunits. The 10 DB wire (Figure 5.7 (c)) again features (-+-) clusters at the edges of the wire with the central two DBs appearing negative.

The line scans in Figure 5.15 again reveal that this is a higher energy configuration compared to the (ud/du) configuration expected with even length DB wires. The shape of the two central DBs appears much more asymmetric compared to all other negative DBs seen suggesting that this is likely a single negative DB which switches between the middle left and middle right DB due to a tip induced charging (like the 2 and 4 DB wire cases), resulting in a net charge of $3e^{-}$ for the 10 DB wire at 0 V. The 11 DB wire (Figure 5.7 (d)) shows both (-+-) clusters at the ends of the wires with 2 negative DBs separated by a neutral DB giving the structure a charge of $4e^{-}$.

The DBs of length 12 to 15 show similar trends as observed in DB wires of previous lengths. The 12 and 15 DB wires (Figure 5.7 (e),(h)) both show a switching of the charge configuration within the wire with a decoupling of the left and right sides. The 13 and 14 DB wires (Figure 5.7 (f),(g)) appear to be in a stable configuration with the centre DB imaging very similar to that of the 5 and 9 DB wire suggesting it is negative due to a tip induced charging. The full line scans for the 8 to 15 DB wires presented in Figure 5.15 clearly indicate that an increased wire length allows for a greater degree of charge distributions within the wires. The increased length means that charges are more effectively screened along the wires resulting in a decoupling of the wire into smaller subunits. As the tip bias is increased, the structure of the DB wire can reconfigure due to the stabilizing polaronic effect from charge injection from the tip. Since the DB wires appear to more easily switch between the various configurations, it makes it difficult to assign a single lattice configuration as was done for DB wires of shorter length.

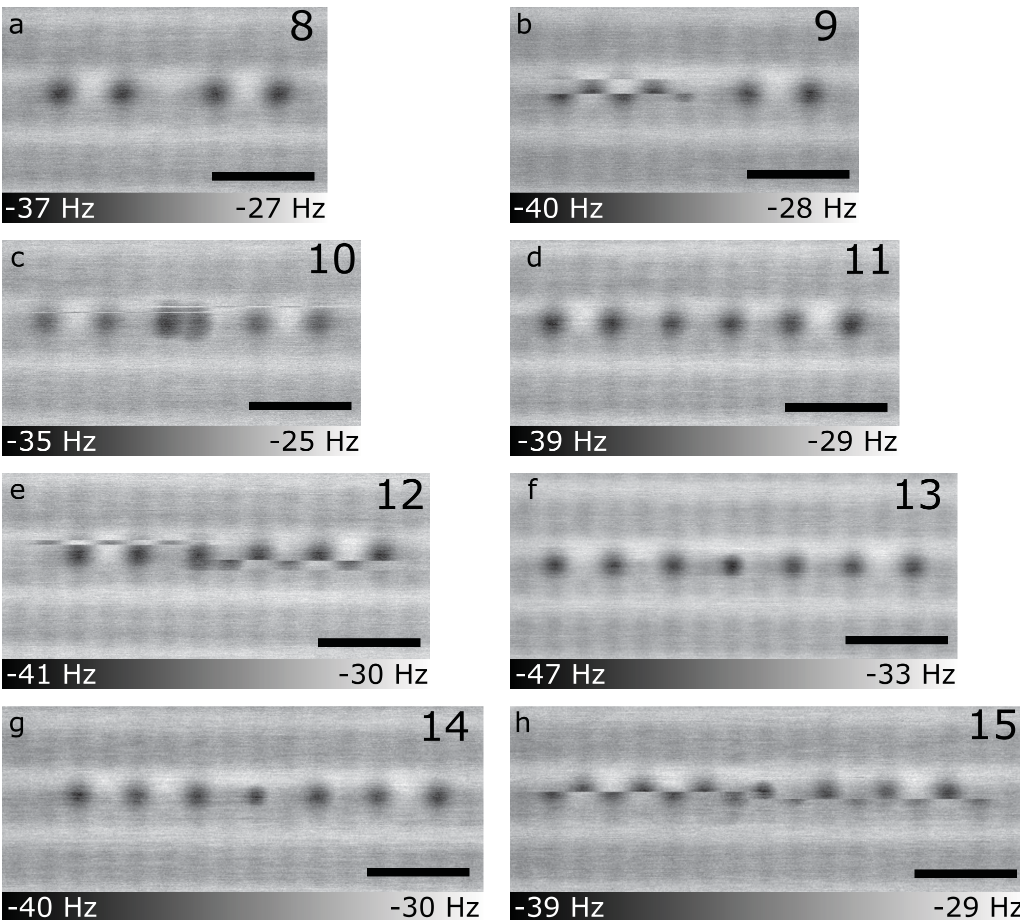

FIGURE 5.7: **DB Wires of Longer Length.**(a)-(h) $\Delta f(V)$ maps of DB wires of length 8 to 15 as indicated in the top right of each image. All images are taken at 0 V and -300 pm. Scale bar is 1nm.

5.1.6 Conclusion

By using a Si terminated tip capable of distinguishing between the three different charge states of surface Si DBs, we were able to demonstrate how charges distribute throughout DB structures at varying probe biases. We were able to confirm the buckling and subsequent charge redistribution of a net neutral bare dimer as well as identify the pi and pi* states through $\Delta f(V)$ spectroscopy. Additional charge distributions observed in the bare dimer warrant further time resolved study. Examining DB wires, we were able to report that the predicted charge redistributions and subsequent lattice distortions are only favoured when the entire DB structure is negatively charged. The net neutral charge state of the DB wire reveals no such charge redistribution implicating a possible spin ordering may be present. Further measurements using spin sensitive microscopy is needed to support this claim. When ionized to the $1e^-$ charge state, the DB wires were observed to hold two different lattice distributions corresponding to a lower energy (udu) and higher energy (dud) configuration in odd DB wires and a degenerate (ud) and (du) configuration in even DB wires, with the ionization bias dependent on the wire length. KPFM imaging of DB wires shows that additional ionization events of the DB structures breaks the ionic up-down pairing resulting in higher order charge distribution, supplied by charge injection from the probe tip. These higher order charge distributions are likely to contribute to the observed character in STM images. These results provide useful experimental evidence of the ordering of such structures, which can provide insights into further theoretical and experimental studies, including their expected conductivity and potential applications in atomic electronics.

5.1.7 Methods

Experiments were performed using an Omicron qPlus LT AFM [90, 96, 279] and an Omicron LT STM system operating at 4.5 K and 3×10^{-11} Torr. STM tips were fabricated from polycrystalline tungsten wire by electrochemical etching followed by resistive heating and

field-evaporation to clean and sharpen the tip using a field ion microscope (FIM)[178]. AFM tips used a third generation Giessibl tuning fork with a focused ion beam (FIB) mounted Tungsten tip ($f_0 \sim 28$ kHz, Q-factor $\sim$ 16k-22k)[280]. The AFM tip was cleaned and sharpened in-situ via controlled tip contacts with hydrogen desorbed patches of Silicon until it returned characteristics corresponding to a Si terminated tip[2, 147]. DB structures were created via controlled bias pulses [4, 145, 159]. The bias ranges for each set of measurements were chosen to capture as great a bias window as possible while trying to prevent any unwanted tip changes due to high tunneling current through the valence and conduction band of the crystal. The AFM measurements taken in this work were taken over several months, so while each tip shows the desired Si tip contrast of the surface, the exact reactivity of the tip varies between some data sets. Samples were degenerately arsenic-doped ($1.5 \times 10^{19}\,\text{cm}^{-3}$). Samples were degassed at 600° C overnight followed by multiple annealing flashes at 1250° C. The samples were subsequently hydrogen terminated by exposing the system to molecular hydrogen (1×10^{-6} Torr) for two minutes while holding the sample at 330° C. A tungsten filament held at 1,600° C was used to crack the hydrogen [248, 281]. Images and data were collected using a Nanonis SPM controller, with additional custom-built LabVIEW controllers. The height setpoint references in constant height measurements are relative to a tip-sample separation distance initialized with a tunneling current feedback of 50 pA and sample bias of -1.8 V with the tip positioned over a H-Si atom.

5.1.8 Acknowledgements

We would like to thank Thomas Dienel and Roshan Achal for the valuable discussions regarding these results. We would also like to thank Mark Salomons and Martin Cloutier for their technical expertise. We thank NSERC, Compute Canada, and AITF for support.

5.1.9 Author Contributions

JC collected all experimental data except Figure 5.12 which was collected by TH. The manuscript was written by JC with input from all authors. TH, MR, JW, and EL further supported the development of this manuscript with additional experimental data not shown. JP and RAW supervised the project.

5.1.10 References

References for this publication are available at the end of this thesis.

5.2 Charge Distributions in Silicon Atomic Wires: Supporting Information

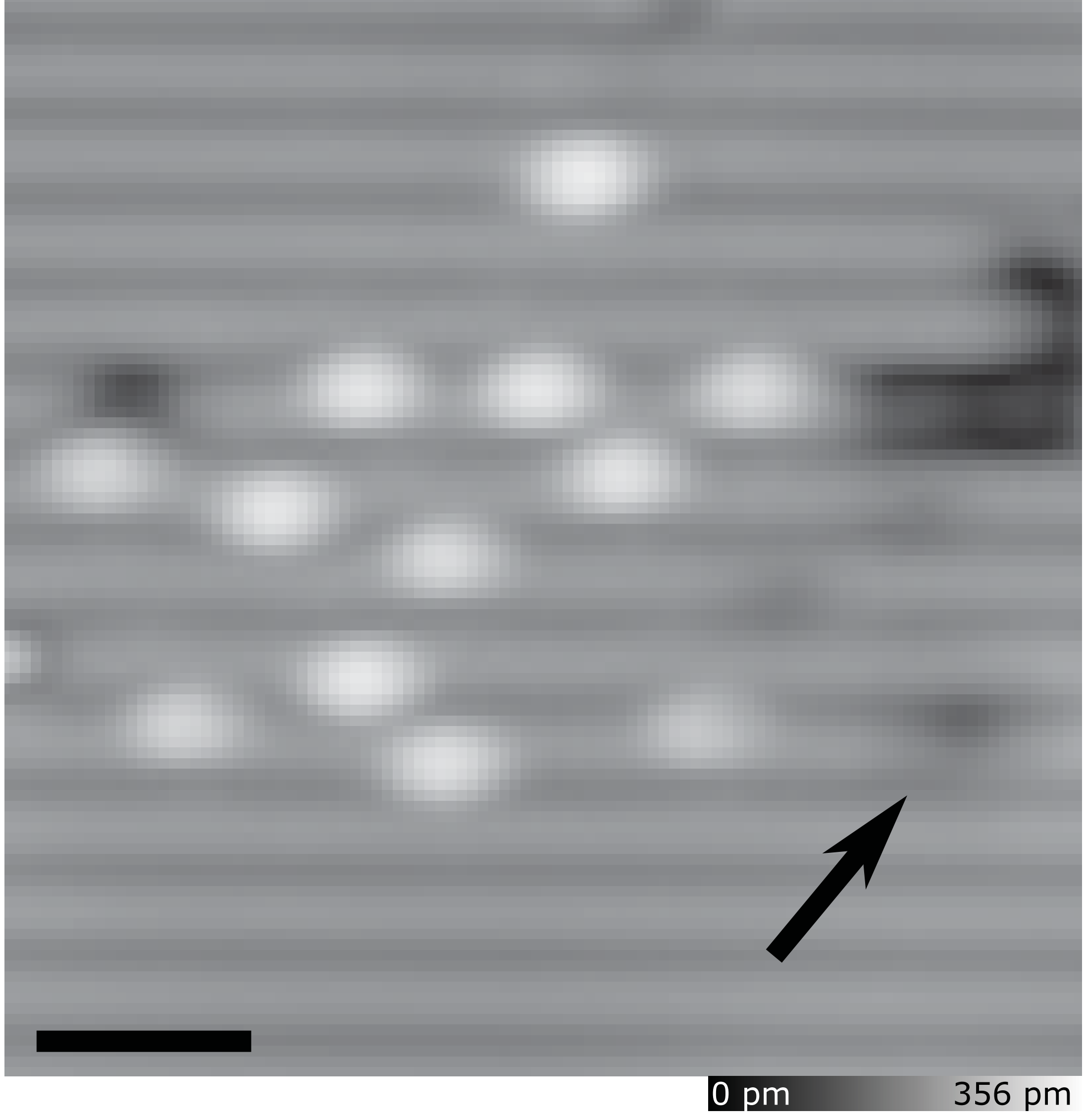

Figure 5.8: **Cluster of Surface DBs.**Filled states image of the area surrounding the DB from Figure 5.1 (marked by black arrow). Scale bar is 2 nm.

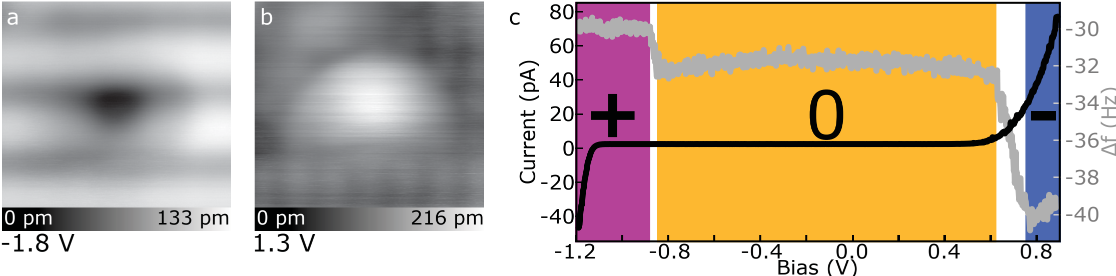

FIGURE 5.9: **STM measurements of the DB.** (a) The filled states image of the DB. (b) The empty states image of the DB. Sample biases are indicated in the lower right of each image. Each image is 2.6 x 2.6 nm^2(c) $I(V)$ spectroscopy of the DB compared to the $\Delta f(V)$ spectroscopy from the main text. The empty and filled states images in (a) and (b) better match the characteristics of a DB on a p-type sample suggesting the nearby electrostatic perturbations have significantly changed modified the emptying and filling rates of the DB[7, 167] rendering it positive at -1.8 V and neutral at 1.3 V as opposed to the expected neutral (-1.8 V) and negative (1.3 V) commonly found on n-type samples[174].

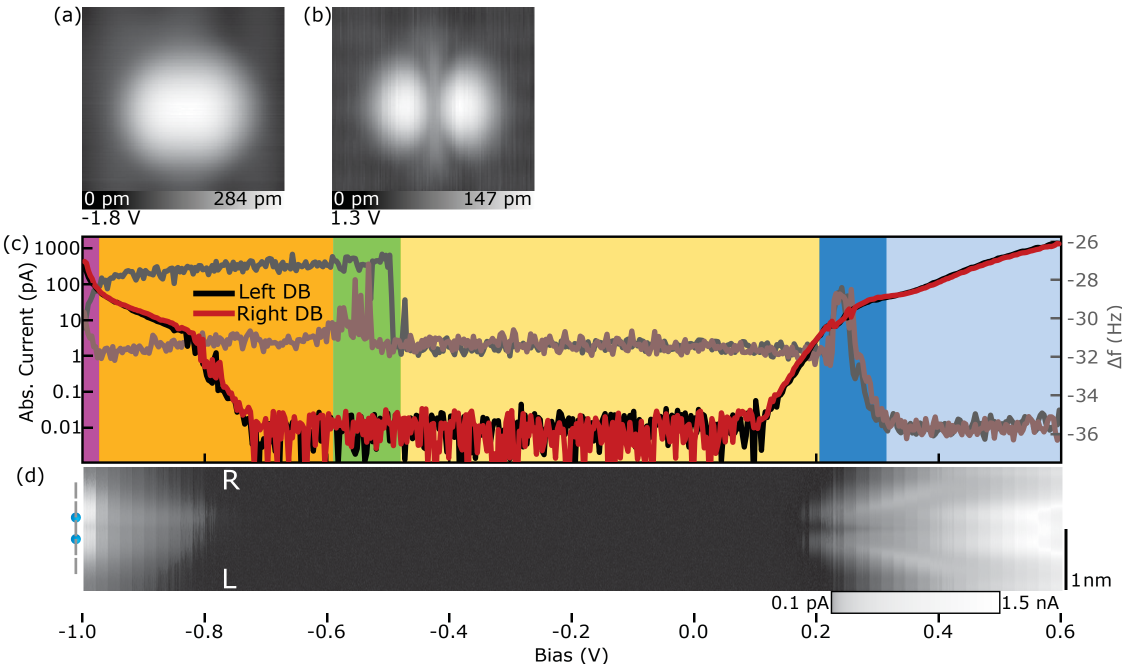

FIGURE 5.10: **Bare Dimer $I(V)$ Spectroscopy and STM Images**(a) filled (-1.8 V) and (b) empty (1.3 V) states STM image of the bare dimer structure.(c) $I(V)$ spectroscopy of the bare dimer compared to the $\Delta f(V)$ spectroscopy from the main text. (f) $I(V)$ line scan maps simultaneously measured with the $\Delta f(V)$ line scan maps in Figure 5.2 (f). The position of the bare dimer in the line scans is indicated on the left of (d) with the grey line added to orient the structure. 50 line scans at bias increments of 0.02 V are shown. The current scale in (c) and (d) is plotted logarithmically to highlight low current features at the onset of the conduction and valence band. Relative heights for each are -300 pm. The scale bar for the line scans is 1 nm as indicated on the right (d).

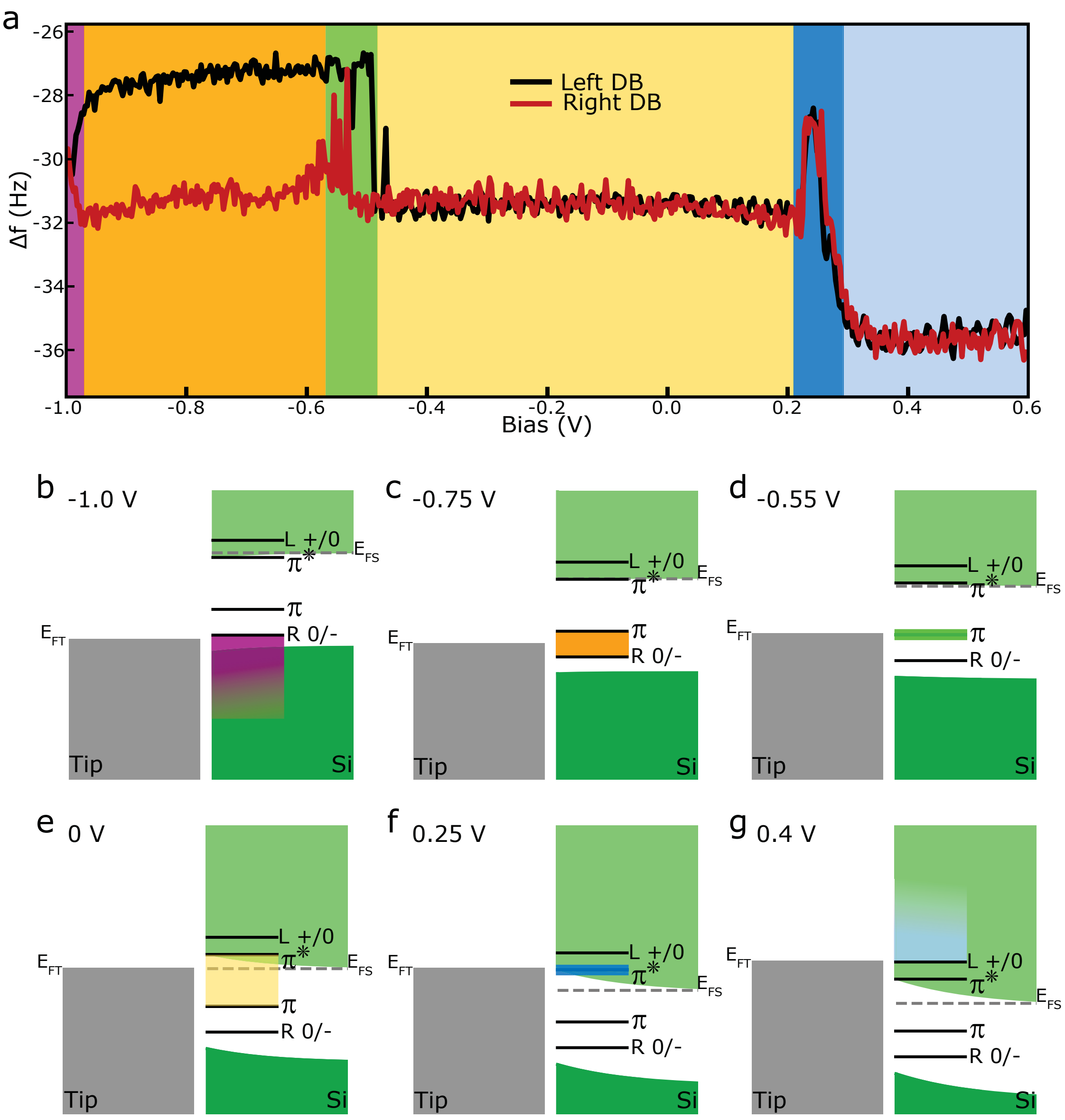

FIGURE 5.11: **Band Diagrams for the Associated $\Delta f(V)$ Spectroscopy of a Bare Dimer.**(a) The $\Delta f(V)$ (left axis) and $I(V)$ (in grey, right axis) spectroscopy of a bare dimer as shown in Figure 5.2 of the main text. (b)-(g) The associated predicted band diagrams of the bare dimer system at bias values indicated in the lop left of each panel. The band diagrams were calculated using semi-tip[131].

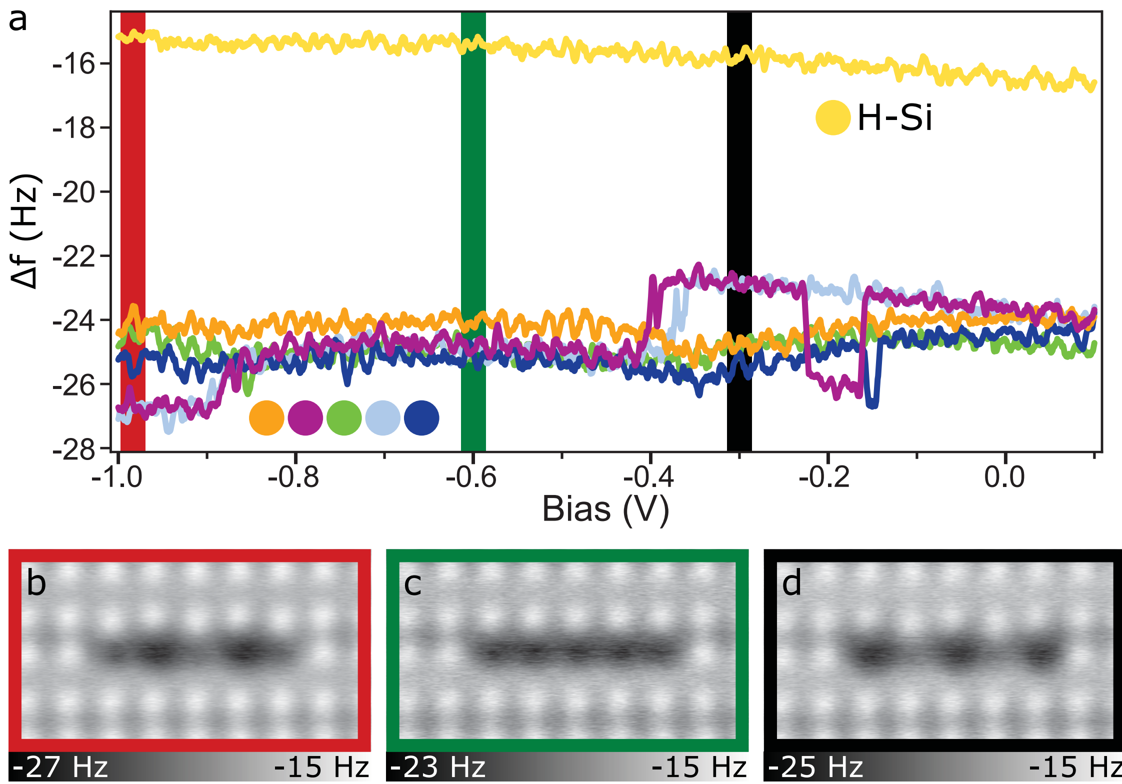

FIGURE 5.12: **Net Positive Configuration of a 5 DB wire as probed with an H terminated tip.** (a) $\Delta f(V)$ spectra taken over each DB in the 5 DB wire as indicated in the lower left, as well as over the hydrogen surface in yellow (tip height = -280 pm). A Savitsky-Golay filter of order 9 was applied to allow easier differentiation of the curves. (b-d) Constant-height Δf AFM images of the wire with bias values as indicated in (a). Each image is 1.9 x 3.4 nm^2 with a relative tip height of -310 pm. The presence of a net positive lattice distribution in DB wires was not as easily observed for results presented in the main text due to an increase in current from the valence band at the onset net positive charge transition associated with a different alignment of the DB energies with the Fermi level of the crystal from varying sample preparation [281]. The net positive distribution can be seen for the 5 and 7 DB case in Figure 5.14 but is short lived due to the onset of tunneling current (not shown). Further studies on p-type crystals using a Si terminated AFM tip would be useful to better demonstrate the net positive redistribution of DB wires.

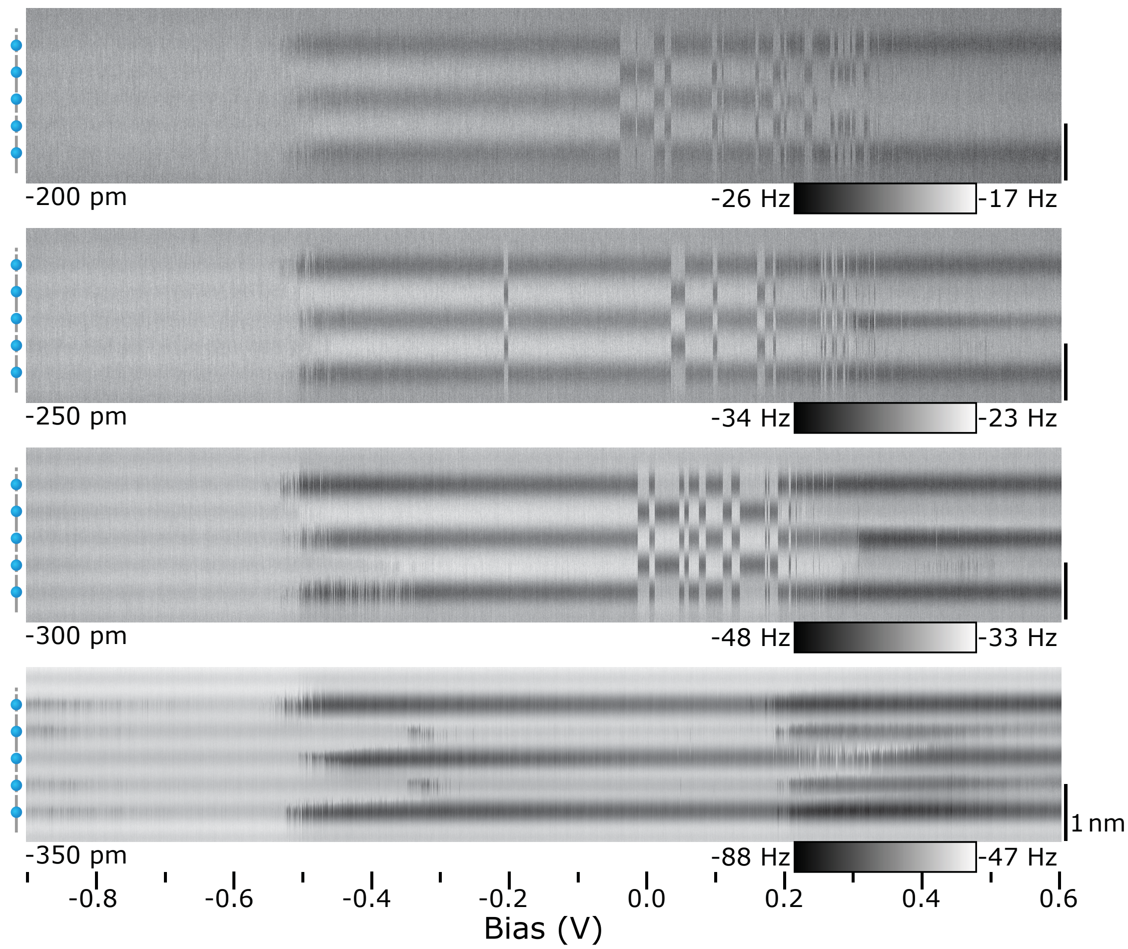

FIGURE 5.13: **Charge Distributions with Tip Height**. Line scans of a 5 DB wire. Bias increments are 0.02 V with 50 line scans taken at each bias. Each image is taken at a different relative depth as indicated in the bottom left of each set of scans. The streakiness of the centre DB at -350 pm is dependant on scan direction which in this case is top to bottom.

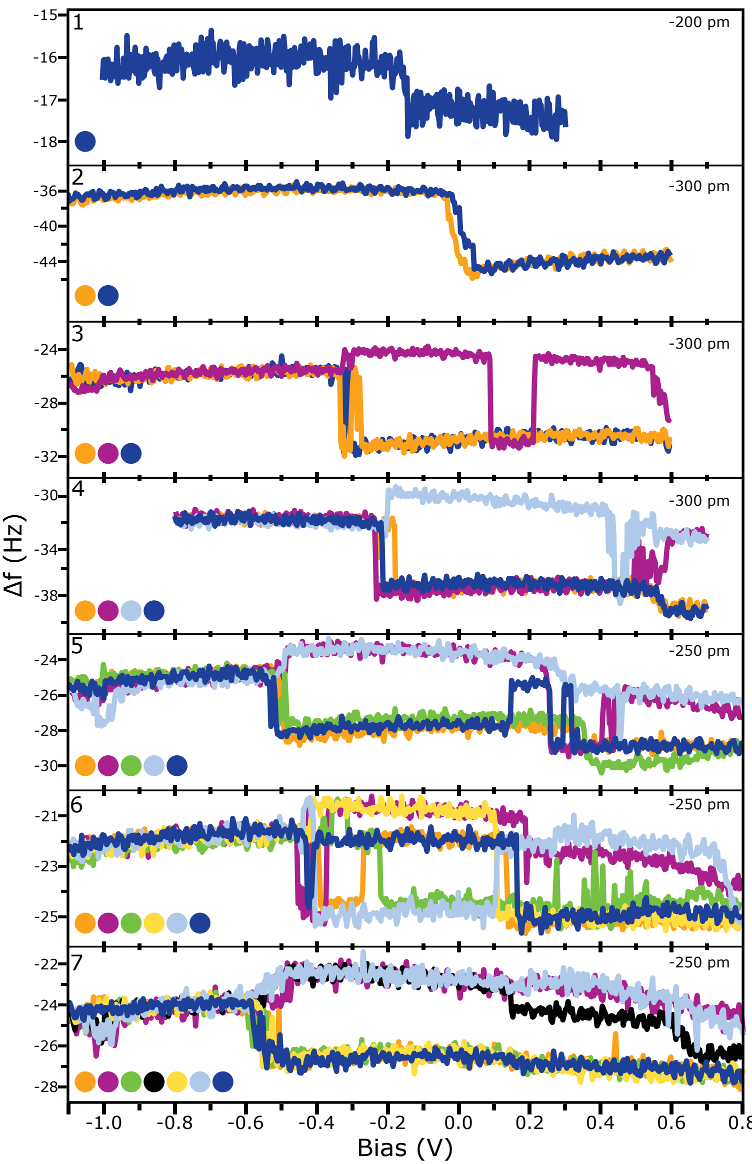

FIGURE 5.14: **KPFM Spectroscopy of DB Wires.** $\Delta f(V)$ spectroscopy over DB wires length 1 to 7 as indicated in the top left of each panel. Spectroscopy colors are shown in the bottom left of each panel. The height of each spectroscopy is indicated in the top right and was chosen to highlight the charge switching of each DB without significant influence from the tip. Note that the centre DB of the 3 DB wire briefly enters a (-) charge state as mentioned in the text. Since neither the left or right DB enter the expected neutral state, the middle DB is thought to only enter this higher energy state due to the sustained interaction with the tip as discussed in the main text.

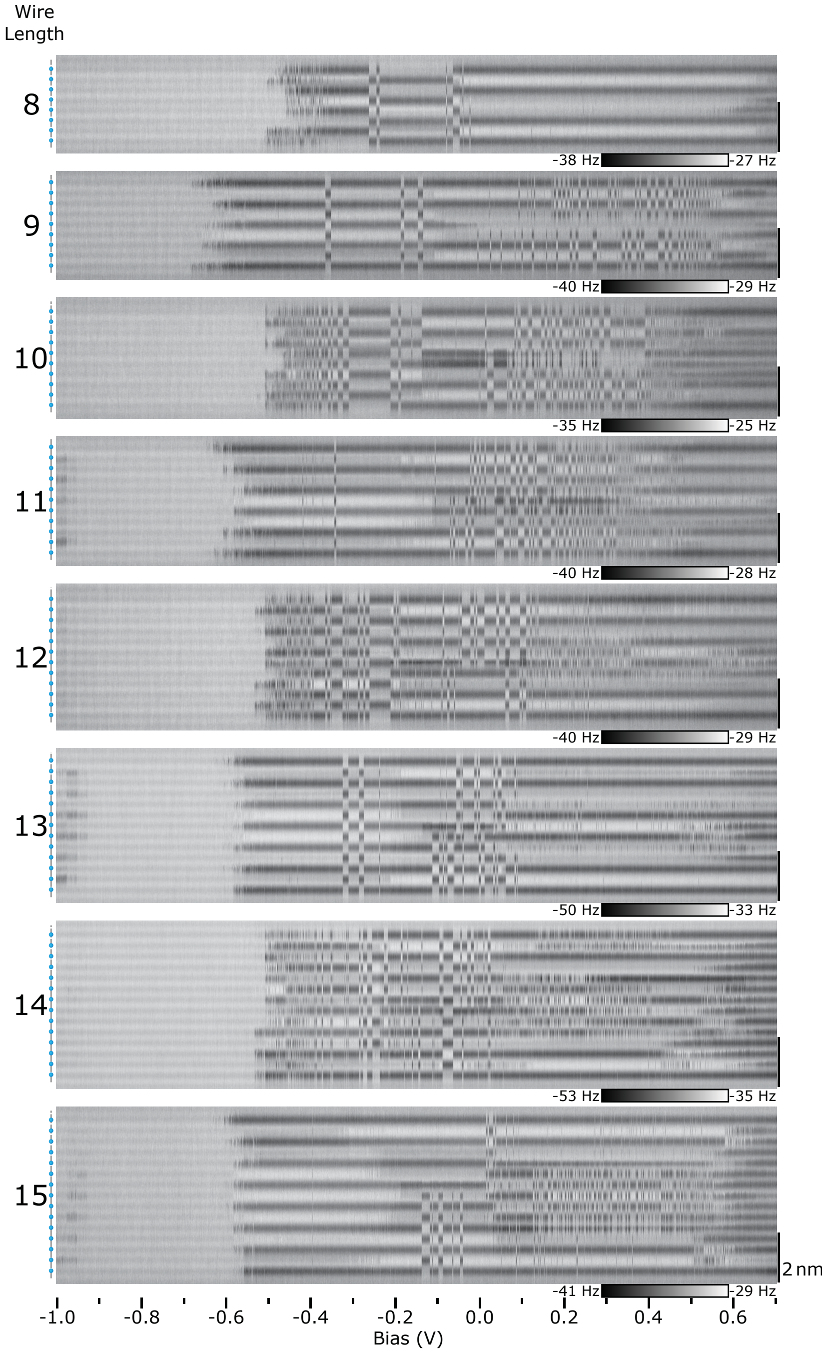

FIGURE 5.15: **Charge Distribution Among Longer Wires.** Line scans of DB wires length 8 to 15. Bias increments are 0.02 V with 50 line scans taken at each bias. All line scans were taken at a relative height of -300 pm. The position of DBs within the DB wires is indicated to the left of the line scans in blue.

5.3 Unpublished Supplemental Data Regarding DB structures

DB wires have been an area of great interest in the Wolkow group. DB wires were first rigorously studied by Wood *et. al.* [364, 365] which looked at the filled and empty electron DOS of such structures. Work by Achal *et al.* published the commonly observed behaviour of DB wires reacting with H_2 in vacuum with no energy barrier as predicted and observed in Ref [363] and references therein. Using a charge detection scheme similar to what was later used by Achal *et al.*, Lloyd [169] was able to confirm that DB wires up to 5 DBs in length all have a single negative charge in a relatively unperturbed states. It wasn't until work by Huff [175] that DB wires were observed at energies within the Si band gap using KPFM. Presented in Figure 5.12 (and [175]), this work identified multiple negative charges within a single DB structure seemingly clashing with the previous observations made by Lloyd. The application of constant height imaging at the onset of the conduction and donor bands as shown in Figure 5.16 allowed for the first correlation between charge induced band bending and transitions between distinct charge reconfiguration within DB wires.

Figure 5.16 (a) shows a current trace along a DB wire with bias values increasing after 50 line scans resulting in the step like increase in current. By correlating the current signal to the structure of the DB wire as shown in Figure 5.16 (b)-(e), key insights can be gained regarding the overall charge structure. Transitioning from what is now understood as the (-+-+-) state to the (0-+-0) state, there is an increase in current associated with the increase in sample bias. Transitioning from the (0-+-0) to the (-000-) state, there is a significant drop in current seen in Figure 5.16 (a) and (e), due to a charge induced band bending from the increase in net negative charge of the DB structure. This increase in negative charge bends the Si electron energy bands up (higher in energy) reducing the overlap between filled states of the tip and empty states of the sample resulting in this decrease in current. Since this same charge induced band bending did not occur for the (-+-+-) to (0-+-0) transition, it

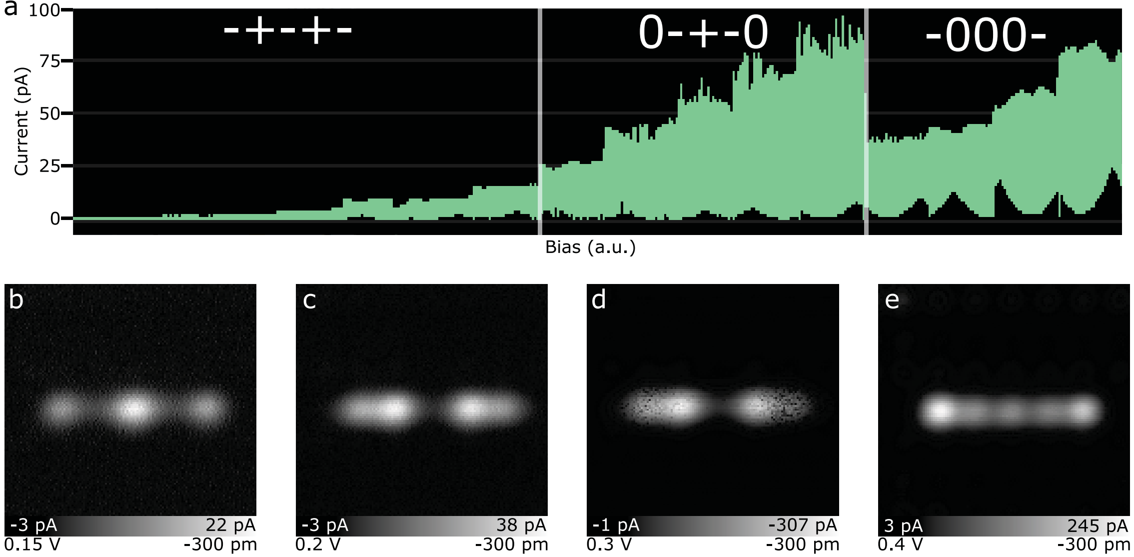

FIGURE 5.16: **The bare dimer anti-node.** (a) shows a comparison between the KPFM spectroscopies of a lone bare dimer and the perturbed bare dimer. (b) shows how features of the perturbed bare dimer are extracted to show an unperturbed bare dimer with no switching.

was thought that although the number of negative charges within the structure changed (as indicated by KPFM experiments shown in [175]), the overall charge of the structure did not change. Only after the application of a Si terminated AFM probe was the distinction made between the three charge states of DBs within wires confirming that both the number of negative DBs within a wire could changed with increasing bias and that this change did not modify the net charge of the structure due to the observed formation of positive DBs within in the wire.

The works shown in this section aim to further the understanding of DB wires and bare dimers. A brief theoretical overview of the Hubbard Model will be presented which can be used to develop an intuition of the underlying physical phenomenon responsible for the observed ordering of DB structures. Additional I(V) spectroscopies from the data presented in Sections 5.1 and 5.2 in addition to additional experiments which were thought to be outside the scope of the previous sections are also presented to further support our experimental

understanding and provide useful information for future experiments.

5.3.1 The Hubbard Model

The Hubbard model [366] presents a simplified description of electron-electron interactions within a lattice. It is dependent upon a hopping integral t and an on-site interaction term U. It is written as

$$\hat{H} = -t \sum_{i,\sigma} \left(\hat{c}^{\dagger}_{i,\sigma} \hat{c}_{i+1,\sigma} + \hat{c}^{\dagger}_{i+1,\sigma} \hat{c}_{i,\sigma} \right) + U \sum_{i} \hat{n}_{i,\uparrow} \hat{n}_{i,\downarrow} \tag{5.9}$$

where $\hat{n}_{i\sigma} = \hat{c}^{\dagger}_{i,\sigma} \hat{c}_{i,\sigma}$ is the spin-density operator for spin σ on the i-th lattice site and the total density operator is $\hat{n}_i = \hat{n}_{i,\uparrow} + \hat{n}_{i,\downarrow}$. Looking at this Hamiltonian, it is clear that a single lattice site could exist in one of four states; an electron empty site, a singly occupied site with a spin up electron, a singly occupied site with a spin down electron, and a double occupied site with a spin up and spin down electron. The likelihood of formation for each of these states depends on the ratio of t and U for the given system. In a 1-D lattice, t could be decreased by increasing the distance between lattice sites while U is found to depend on a combination of the electron affinity and ionization energy for a specific atom. In general U increases as we decrease the atomic period and increase the atomic group (move towards the top right corner of the periodic table).

If we consider a system where $U/t \gg 1$, the system behaves as isolated magnetic moments with very little, if any correlation between lattice sites. If we increase t, but also keep U relatively large, it can lead to doninant contributions from magnetic correlations such as ferromagentic and antiferomagnetic alignments. Finally, as we decrease U, it becomes possible for electrons to transition on the same site. For a 1/2-filled system, this results in an alternating empty-filled lattice distribution[367].

Theoretical work done by Lee and Cho [368] develop an understanding between the observed ordering of one-dimensional dangling-bond wires with varying U and t parameters for the C(100), Si(100), and the Ge(100) surface. To summarize, they calculate a value of U for C (3.45 eV), Si (1.71 eV), and Ge (1.36 eV) as well as a value of t (C (1.04 eV), Si(0.75 eV), and Ge (0.63 eV)). The change in U is directly attributed to the changing localization associated with the 2p, 3p, and 4p character of the C,Si, and Ge DBs respectively. The hopping parameter t is determined from the estimated bandwidth from the non-magnetic,non-ionic band structure of a DB wire.

In calculating the magnitude of the energy gap associated with an anti-ferromagetic or ionic ordering in C, Si, and Ge, they find that the anti-ferromagnetic gap is larger than the ionic gap in C while the ionic gap is larger than the anti-ferromagnetic gap in Ge while Si shows a slight preference to an anti-ferromagnetic ordering. Looking at the trend of U/t for C (3.32), Si (2.28), and Ge (2.15), it is more apparent why the C and Si atoms are predicted to undergo an anti-ferromagnetic ordering while Ge is predicted to undergo the ionic (Peierls/Jahn-Teller) ordering.

The explanation of the anti-ferromagnetic ordering for C is not explained by the Hubbard model alone and requires an additional term

$$\hat{H}_{spin} = -\Sigma_{i \neq j} J_{ij} \hat{S}_i \cdot \hat{S}_j \tag{5.10}$$

commonly referred to as the Heisenberg Hamiltonian [367] where $\hat{S}$ is the spin operator and J is the spin exchange constant. For $J > 0$ spins align parallel, and when $J < 0$ spins align anti-parallel (thought of as the difference between the singlet and triplet state energy $(E_s - E_t)$). For the anti-ferromagnetic configuration then J must be negative with $|J| = 4t^2/U$ when used with a Hubbard Model[367]. If the lattice is allowed to move under a Peierls distortion, an additional displacement term should be added to Equation 5.10 to

account for a modified spin coupling [369, 370]. The electron-phonon coupling seen for Ge can be captured by a Peierls contribution given as

$$\hat{H}_{e-ph} = \Sigma_i \left(\frac{\hat{P}_i^2}{2M} + \frac{K}{2} \left(\hat{u}_i - \hat{u}_{i+1} \right)^2 \right) \tag{5.11}$$

where $\hat{u}$ and $\hat{P}$ are the displacement and momentum operators respectively with the phonon frequency defined as $\omega_0 = \sqrt{K/M}$.

Now applying this to our experimental results we can gain a better appreciation for the respective orderings seen for bare dimers and DB wires. Predicted by Lee *et al.*[344], the bare dimer undergoes a charge ordering while the 2 DB wire undergoes an anti-ferromagnetic ordering. Understanding the surface geometry for bare dimers and DB wires, it is clear that DB wires would have a larger t value due to their increased separation. In addition to this increased t, they should also have a larger U which prevents the onsite pairing seen in the bare dimer case. As discussed, the Hamiltonian which describes the Si surface should also include a Peierls contribution, which accounts for a different electron-phonon contribution between the two different configurations, and an N-nearest neighbour Coulombic contribution [371] which accounts for the ionic attraction between (+) and (-) DBs. Foregoing the addition of separate terms, it may be more appropriate to consider a U_{eff} in which the on-site pairing term is lowered through this lattice distortion and Coulomb attraction[4]. This would give a bare dimer a lower U_{eff} than a 2 DB wire due to the closer spacing between DBs and the different distorted lattice geometry of a bare dimer.

Now comparing U_{eff}/t for the DB wire and bare dimer, it is easier to understand why the bare dimer would prefer an ionic distribution while the DB wire would prefer an anti-ferromagnetic distribution[5]. Once charged however, the DB wire is observed to undergo an ionic distribution. This is because the DB wire system is not isolated as the Hubbard model

[4] Reminder that the dimer bond is roughly 2.25 Å and DBs in a wire are spaced by 3.84 Å.

[5] As mentioned in section 5.1, the non-magnetic Si terminated AFM tip does not offer any indication into a potential spin ordering and warrants further investigation

would suggest. It is coupled to both the tip and the Si bulk. This coupling allows for the addition of electrons to the DB wire either by insertion from the donor/conduction band or AFM tip. We could represent this by an additional U_{Si} and U_{tip} term in the Hubbard model. Once aligned to the appropriate bias, it becomes energetically favourable for the DB wire system to accept an additional electron making the on-site pairing the dominant contribution.

5.3.2 The Bare Dimer

In addition to the single bare dimer structure as shown in Figure 5.2, additional variations of the bare dimer structure were also studied. Figure 5.17 shows a perturbed bare dimer where an additional DB has been patterned on the top side of the dimer immediately to the right of the bare dimer. As can be seen from the $\Delta f(V)$ spectroscopies in Figure 5.17 (a), this additional DB acts as a perturber to the bare dimer. The rapid switching associated with the π state can be seen at around -1.0 to -0.8 V with the ionization step associated with the (0/-) transition of the single DB at roughly -0.2 V. The position of the third DB is made clear when comparing Figure 5.17 (c) and (d) highlighting the large negative shift in Δf above the third DB. A slight change in Δf can also be seen in the spectroscopies over the top and bottom DBs of the bare dimer as well due to the added Coulomb contribution from this third DB. The most significant difference from the single bare dimer case of Figure 5.2 is the absence of any π^* signal and the subsequent charging step. As a result, the bare dimer is always imaged with the top DB of the bare dimer in the (+) state and the bottom DB of the bare dimer in the (-) state. It is interesting to note that the only time the bottom DB of the bare dimer switches to a suspected (+) state is when in resonance with the π state. Unlike the single bare dimer which was shown to switch between the (-+/+-) configurations above the π state, the perturbed bare dimer does not. This suggests that although the single DB is neutral at these energies, there must be an additional perturbation from either charge polarization or lattice distortion which keeps the bare dimer in this configuration. It is also

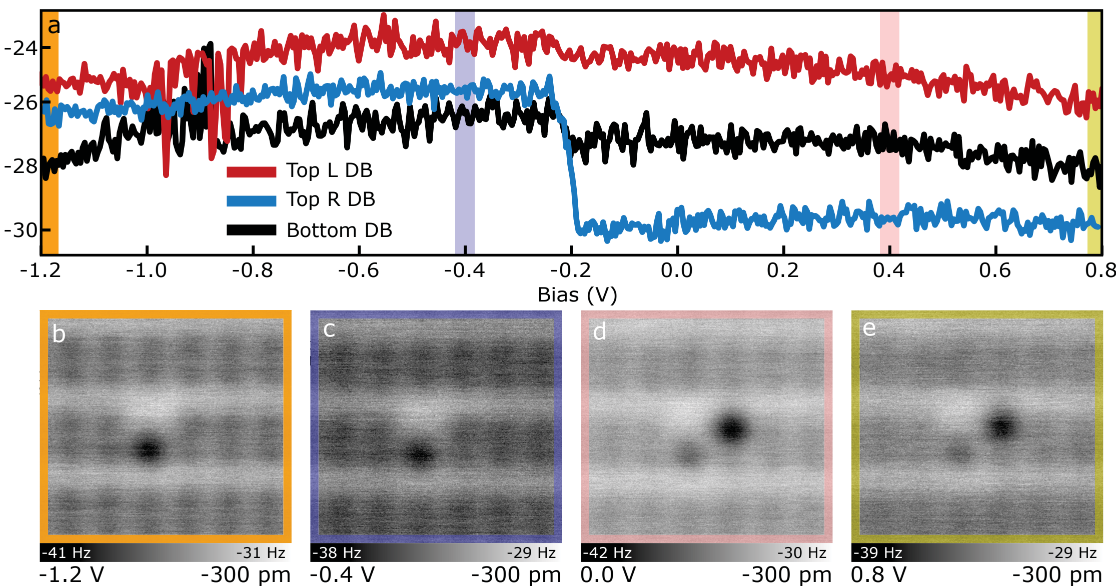

FIGURE 5.17: **A perturbed bare dimer** (a) The $\Delta f(V)$ spectroscopy of a bare dimer with an additional DB patterned on the top half of the adjacent right dimer row. (b)-(e) Δf images of the DB cluster at 4 different bias ranges as indicated by the coloured borders matching the vertical lines in (a).Each image is 2.3 a 2.3 nm^2.

interesting to note the difference in Δf signal between the negative DB of the bare dimer and the single DB. Since the two main contributions towards the attractive interactions of a Si tip and a surface DB are the covalent and Coulombic contributions, such a difference is attributed to either of these effects. This could be manifest through the slightly different electrostatic environment of the two negative DBs, or differing covalent character due to the differing chemical environment attributed to the shared dimer bond and slight difference in lattice distortion.

Following the measurements of the perturbed bare dimer, this same DB structure was made symmetric again by patterning a fourth DB making two neighbouring bare dimers. The spectroscopies in Figure 5.18 (a) show the expected π state extending over a larger bias range of roughly -1.1 V to -0.7 V. As explained previously using I(V) spectroscopies [323] such a broadening is due to a potential hybridization of the neighbouring π bonds. In the

bias range of -0.6 V to 0.4 V, the spectroscopy reveals that three of the bare dimers are in the negative charge state while one remains in the positive state. Looking at the Δf images in Figure 5.18 (c) and (d), it is clear that bare dimers are now aligned in the commonly observed p(2x2)configuration (comparable to the lattice order seen on the unterminated surface). The reason for three negative DBs instead of two in the spectroscopies is attributed to the tip induced charging shown for the single bare dimer case discussed in Section 5.1. The reason that all four do not appear negative is likely due to a higher flipping barrier due to the neighbouring bare dimer which would also need to flip to maintain the surface phase. To confirm this claim, additional experiments would need to be taken with increasingly longer bare dimer structures (like in [350]). The decrease in Δf associated with passing the π^* bond has returned and can be seen at roughly 0.4 V (although the shape of the spectroscopies do not exactly match the single bare dimer case). Looking at the Δf image in this bias range in Figure 5.18 (e), this charging step moves the bare dimers into what appears to be a quadruple negative structure. As suggested in the section 5.1, this configuration likely involves electron dynamics that are too fast to be observed with AFM.

Since the perturbed bare dimer structure appears to be unable to flip between the two (-+/+-) configurations, further examination may provide useful insights into the characteristic butterfly shape [247] of the bare dimer in empty states imaging. Figure 5.19 (a)-(c) show the filled state STM image of the single, perturbed, and double bare dimers respectively. The empty states images of the same structures are shown in Figure 5.19 (d)-(f). The characteristic butterfly shape of the single bare dimer is clearly seen with the bright central node appearing horizontally between the two DBs of the bare dimer. The perturbed bare dimer does not show such a feature with the two DBs of the bare dimer appearing asymmetric matching the observed asymmetry in charge states shown in Figure 5.17. The double bare dimer then reveals the distinct central node feature again.

The origin of this central nodal feature is explained by Engelund *et al.* [247] who attributes the origin of this node to a degenerate switching between the two states. In this work they

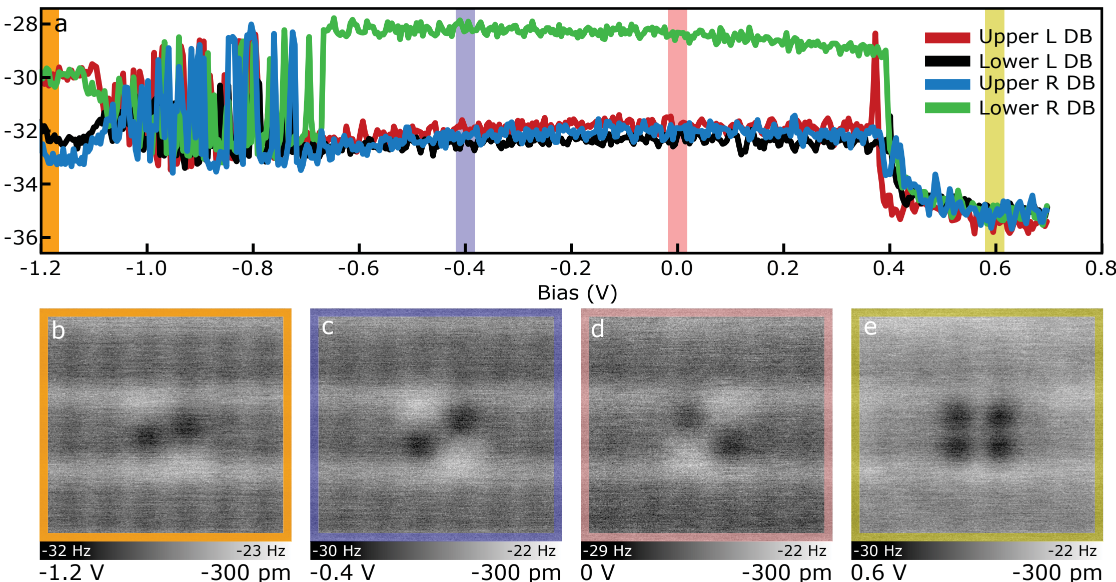

FIGURE 5.18: **A double bare dimer** (a) The $\Delta f(V)$ spectroscopy of a double bare dimer structure. (b)-(e) Δf images of the DB cluster at 4 different bias ranges as indicated by the coloured borders matching the vertical lines in (a).Each image is 2.3 a 2.3 nm^2.

distinguish between two methods of switching, a current-induced fluctuation or a thermally-induced fluctuation. The current induced fluctuation is described as an n=1 process (n = electrons) meaning that an electron must be injected into the DB structure from the tip to cause the central butterfly node. The thermal (n=0) transition is also simulated which shows an absence of any central butterfly node. We can compare these two transition mechanisms to experimental evidence presented in Figure 5.19. The n = 1 transition can be associated with the bare dimer entering a negative charge state as shown in the single and double bare dimer case which both reveal the butterfly shape when imaged at 1.3 V (Figure 5.19 (d), (f)) It is impossible to observe a current signal of the thermal transition due to this transition only occurring below 0.2 V, however, by taking the perturbed bare dimer image, such a transition could be extrapolated. Figure 5.19 (g) shows the empty states STM image of the bare dimer which has been cropped and mirrored to remove the perturbing bare dimer and then flipped and duplicated to give a representation of an STM image of the superposition

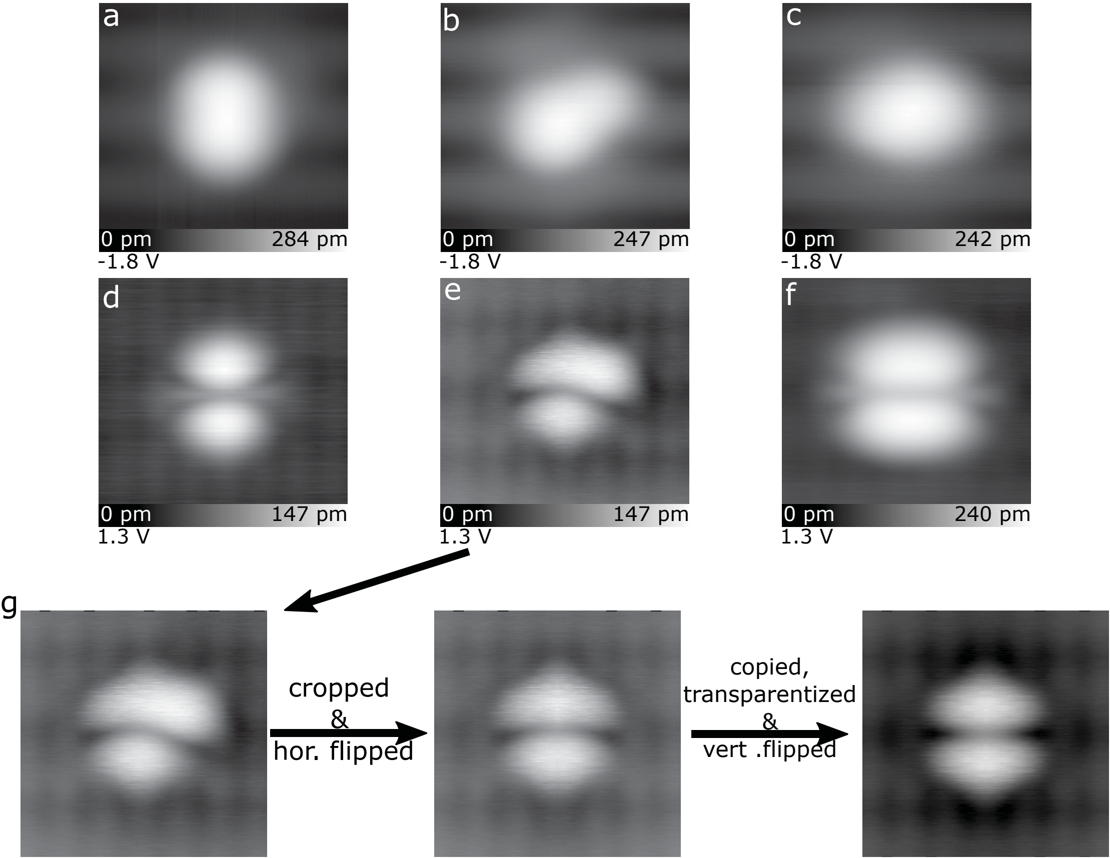

FIGURE 5.19: **the butterfly shape of the bare dimer** (a)-(c) The filled states STM image of the single, perturbed, and double bare dimer respectively. (d)-(f) The empty states STM image of the same structures. (g) The perturbed bare dimer which has been vertically cropped and then mirrored to remove the single DB. The image was then flipped and overlaid with the unflipped image to present a superposition of the bare dimer as if it were imaged as a superposition of the two potential states. Each image is 2.3 a 2.3 nm^2.

of the two degenerate states of the bare dimer.

Comparing these two images to the theoretically simulated thermal and current induced images in [247], both the experimental thermal and current induced images strongly match their theoretical counterparts. The bare dimer which undergoes current induced transitions shows the central butterfly node while the bare dimer which undergoes thermal induced fluctuations does not. It would be useful to provide corresponding AFM data for bias values

around 1.3 V, however, the tip-sample separation needed to provide useful AFM contrast at these bias values results in high current which often damages the tip or surface. These results provide useful insights into the STM features seen in DB structures suggesting that the average charge state of the DBs within the structures have a significant impact of the STM image, but as mentioned in the previous section, they require further time-resolved experimental studies.

In addition to a bare dimer which can be perturbed by a single DB, Figure 5.20 shows a 5 DB wire which has been perturbed by a bare dimer patterned at the location of the second DB. Although full spectroscopies were not taken for this structure, three different bias regions were explored in AFM revealing the unique charging behaviour of the structure. The filled states image is shown in Figure 5.20 (a). Figure 5.20 (b) shows the DB structure at -0.8 V with only the bare dimer in its (-+) configuration visible. All other DBs are neutral. At -0.4 V, (Figure 5.20 (c)), the right 3 DBs of the DB wire enter the net negative (-+-) charge state with the left most DB still appearing neutral. Only when the bias is further increased does the last DB appear negative (Figure 5.20 (d)). Since the positive charge of the second DB of the wire is now cancelled by the additional negative charge of the bottom bare dimer atom, for the full 5 DB wire to enter the (-+-+-) charge configuration, the net charge of the DB wire/bare dimer structure must increase to $2e^-$. This increase in net charge is what causes the 5 DB wire to decouple into the two sub-units shown.

5.3.3 Additional DB wire observations

Although the majority of the DB wire data in the previous sections only show the Δf signal, all the measurements simultaneously recorded the tunneling current which can give insights into the correlation between charge state and tunneling current. The I(V) spectroscopies of the DB wires of length 2 to 7 are shown in Figure 5.21. These measurements were taken simultaneously to the Δf measurements of Figure 5.14 allowing for a direct comparison between charge state and tunneling current. Looking at the magnitude in current for each

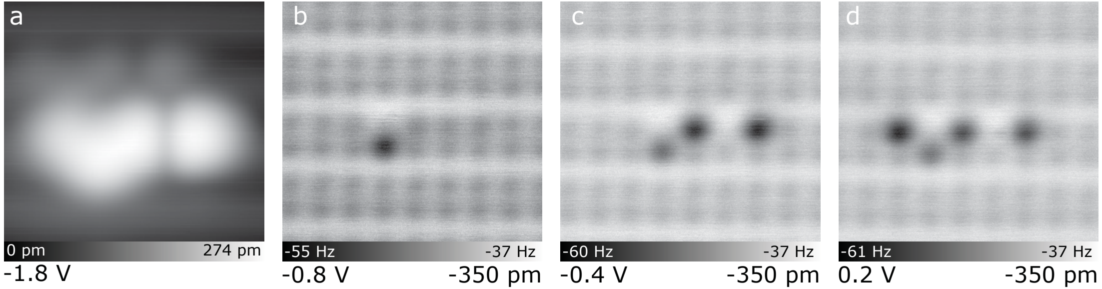

FIGURE 5.20: **DB wire decoupling with bare dimer.** (a) The filled states STM image of a 5 DB wire with a bare dimer patterned at the position of the second atom. (b-d) Δf images of the same structure at -0.8 V, -0.4 V, and 0.2 V respectively. Each image is 3.1 x 3.1 nm^2

DB wire highlights the limitations of using current as the main signal for DB structures in energies near the band gap. The only region where a useful signal can be extracted is roughly between 0.2 V and 0.8 V. Any lower and we are in the band gap, and any higher and we reach tip damaging currents. Additionally, the filled states bias has a more drastic increase in tunneling current as demonstrated with the 7 DB wire increases from 0 to 1.6 nA in less than 0.1 V (at roughly -1.05 V). Despite this, the current signal does still provide some useful insights. Looking at the 2 and 3 DB wires, the onset of empty states current begins at roughly 0.4 V reaching 100s of pA by roughly 0.6 V. The 4 DB wire shows an initial increase in current similar to the 2 and 3 DB cases, but experiences a significant drop until it begins to rise again at 0.6 V. This sudden drop and increase marks the 4 DB wire transitioning between the net 1e$^-$ charge state and the 2e$^-$ charge state corresponding to a transition between the degenerate (-+-0/0-+-) state to the (-00-) state (similar to Figure 5.16). The 5 DB wire shows a similar shape however, the charging features are only seen over the middle left and middle right DBs (and at much lower max current). From the KPFM measurements in Figure 5.14, we can attribute this feature happening above two of the five DBs due to a localized tip induced effect. The data presented in Figure 5.16 which also measures a 5 DB chain shows a much more dramatic increase which suggests that the local Fermi level (from different dopant profiles [281]) will have an effect on the stability of the

different charge configurations of 5 DB wires. This is supported in [365] which show varying features in constant current STM images of DB wires fabricated on Si surfaces with different dopant profiles.

The 6 and 7 DB wires shown in Figure 5.21 show the onset of empty states current starting at roughly 0.6 V matching the onset of current of the 4 and 5 DB wires in the $2e^-$ charge state. From the $\Delta f(V)$ spectroscopies of Figure 5.14, we know that the 6 and 7 DB wires exist in a $2e^-$ charge state at these bias values resulting in the delayed onset of current from charge induced band bending.

In addition to spectroscopies, an image of the current signal can also be taken of DB wires as long as the probe biases allow for a signal to be measured. Figure 5.22 shows several images taken of DB wires length 3 to 7 at varying bias values. These images were taken using an STM only tip on a different sample and machine and so the bias values at which each charge configuration appears is slightly different than that presented earlier. Looking at column i in Figure 5.22, it shows the lowest available bias in which a signal can be extracted in empty states. The 3, 4, and 5 DB wires appear in their lowest (or degenerate) configuration ((-+-),(0-+-), and (-+-+-) respectively) while the 6 DB wire appears to switch rapidly between its two degenerate states and the 7 DB wire appears to be in the higher order (-+-0-+-) charge state.

Without going into detail on all remaining images, it is worth while to emphasize a few points from this data set. First, it is interesting to note that the conductivity (measured current) through the DB wire depends on the charge state of the DB. As an example, compare the (-+-+-) charge state of Figure 5.22 (c)-i with the (0-+-0) charge state of (c)-ii. In (c)-i, the central DB is in the (-) charge state and has a higher current signal. The central DB in (c)-ii is in the (+) charge state and has a significant reduction in current. The neutral DB in either case has an observed conductivity somewhere between the (+) and (-) charge state (This trend is how the configuration of the 4 DB wire in Figure 5.22 was assigned as such). Second, the 4 DB wire shown in Figure 5.22 (b)-i sits in the (0-+-) charge state. Despite the

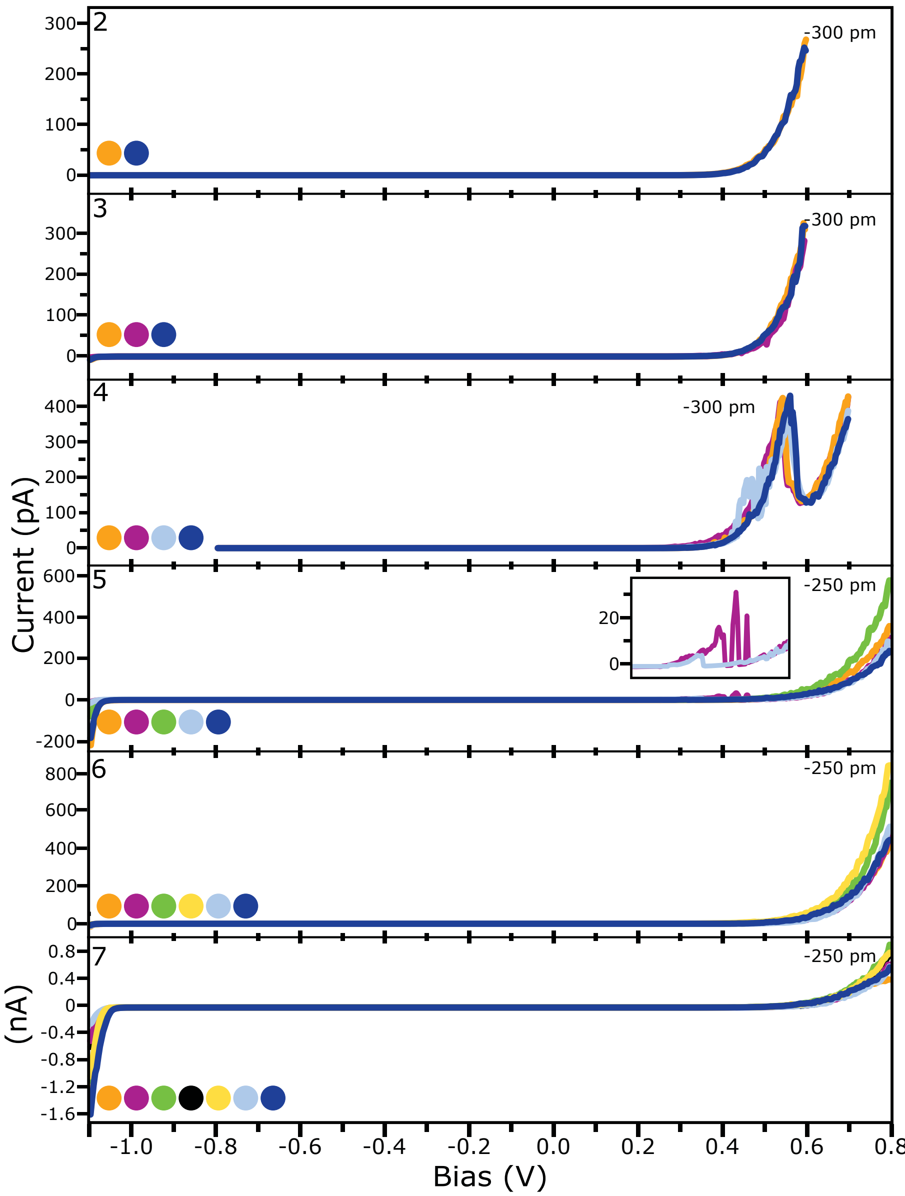

FIGURE 5.21: **I(V) spectroscopy of DB wires**. Spectroscopy over DB wires length 2 to 7 as indicated in the top left of each panel. Current signals were acquired simultaneously with the Δf spectroscopies shown in Figure 5.14. The inset in the 5 DB wire shows a zoomed view highlighting the sharp changes in current associated with lattice switching.

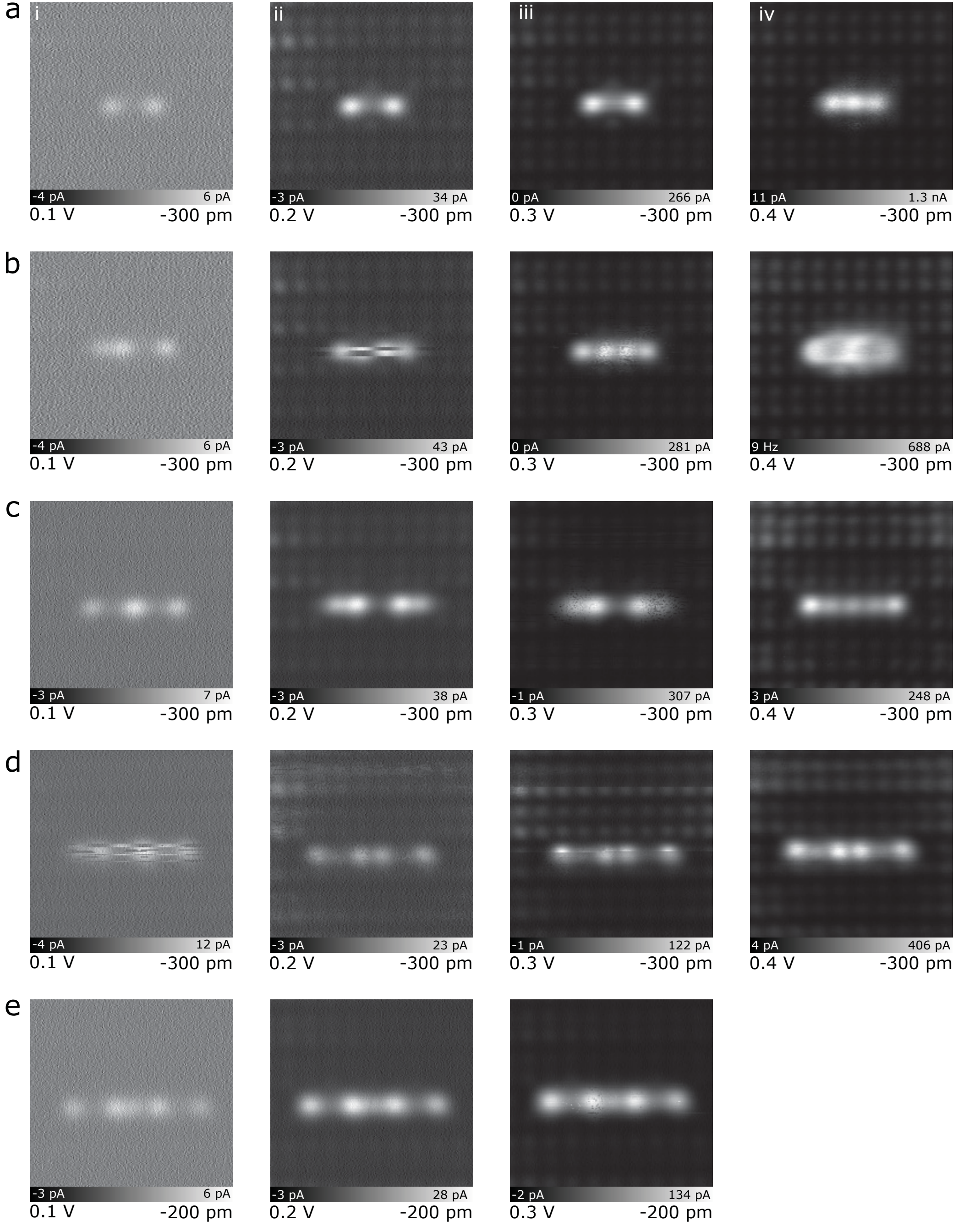

FIGURE 5.22: **Constant height STM measurements of 3-7 DB wires at various bias values.** Each image is 3 x 3 nm^2.

middle left and far right DB both existing in the negative charge state, the middle left DB appears slightly larger with a slight increase in measured current (the same can be observed between the two outer DBs and the middle DB of the 5 DB wire in (c)-i) Since these DBs are observed to exist in the same charge state (from KPFM), the difference in measured current can be explained by a difference in DB energy within the negative charge state (resulting in a different overlap in states with the tip and different emptying pathways into the bulk Si). This misalignment is attributed to the end states of the DB wires which are bonded to a more rigid H-Si atom. These H-Si atoms remove some of the available lattice movement preventing the end DBs from distorting to the same degree as the central DBs within a wire. The degree to which the lattice distortion effects the energy level of DBs on the surface still requires theoretical simulations.

Lastly, looking at the DB wires of higher energy in columns iii and iv, there are sharp changes in the current signals (similar to a telegraph noise [166]) associated with the rapid switching of DB wires between different charge states. Such a feature is perhaps most evident in the 5 DB case in Figure 5.22 (c)-iii where the DB wire switches between the net $1e^-$ and $2e^-$ charge states. Since the sampling rate of the current channel is notably higher than the Δf channel, the current signal is able to detect such features that may go unnoticed using Δf alone.

Figure 5.23 shows the same Δf measurements that are shown in Figure 5.13 but with the simultaneously acquired current signal. At a tip height of -200 pm, the empty states current signal appears to be fairly smooth across a single line scan with the peaks in current corresponding to the two negative DBs at either end of the wire. As the height is reduced to -250 and -300 pm, a sharp step in current can be seen over the middle DB. Since the onset of this current appears as a step-like onset as the tip scans across the DB, it is attributed to a tip induced charging where the negative charge of this DB is only held when the tip is directly over it with the charge state quickly changing again as the tip passes over the middle DB. At -300 pm, this central line increases in width due to the increased interaction with the tip. At -350 pm between 0.2 V and 0.6 V, all DBs within the wire appear to be

in a negative charge state. Looking at the current signal, this can be attributed to a tip induced charging event in which the charge state of each DB is locally manipulated as the tip scans across it. Looking at the DBs in position 2 and 4 in the current signal at -350 pm, they posses the most drastic step-like features from the tip induced transition between the (0) and (-) charge states.

The current signals of all the line scans in Figures 5.5 and 5.15 are shown in Figure 5.24 and Figure 5.25. In addition to the current signal, these line scans are presented in their full bias range giving insights to bias ranges not presented previously. One of the most interesting details is the presence of charge localization at the onset of the net positive charge state ($\sim$ -1.0 V). This can be seen for the 3, 5, and 7 DB wires in Figure 5.24 which appear to be in a (+-+), (+-+-+), and (+-+-+-+) charge configuration respectively. As the bias is decreased further, the charge configurations are no longer observed likely due to the onset of tunneling current from the filled states. Since the cause of this large onset in current has been attributed to varying dopant distributions [347], it explains why the positive charge state was so easily seen in Figure 5.12 and not here. This further supports the idea that further studies are needed with varying dopant profiles (including p-type) to gain a better understanding of the correlation between DB wire charging and the Si Fermi level. The positive charge step isn't seen for the 2, 4, and 6 DB wire cases (The 4 DB wire case did not cover a wide enough bias range) likely due to the same reason the negative ionization step appears at more positive biases than the odd length DB wires (as shown in Figure 5.6).

In addition to the AFM charging features, the current signal also reveals interesting patterns at larger negative biases (-1.1 V) which appear to alternate between a high and low current states. From the corresponding Δf signal, it appears that the DBs within the wire at roughly -1.1 V all appear to be neutral in charge. We can correlate the positions of these minima and maxima in current signal with the position of the (-) and (+) DBs of the net 1e$^-$ state of DB wires. This further suggests that DBs which are imaged in the same charge state using KPFM, may have varying energy alignments with respect to the Si bulk resulting in this variation in tunneling current.

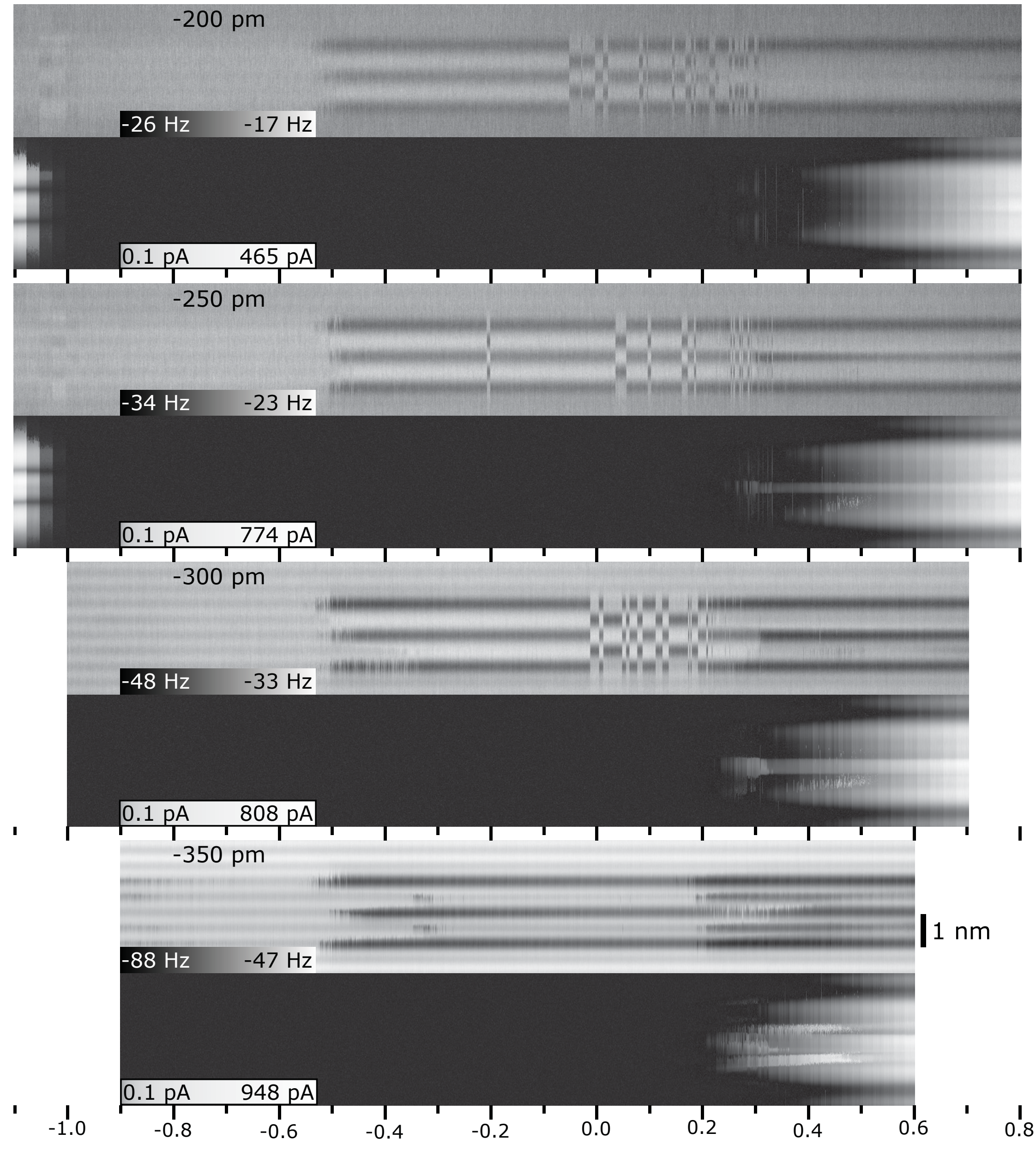

FIGURE 5.23: **Charge distribution with tip depth.** Line scans of a 5 DB wire with measured current signal. All other parameters are the same as Figure 5.13.

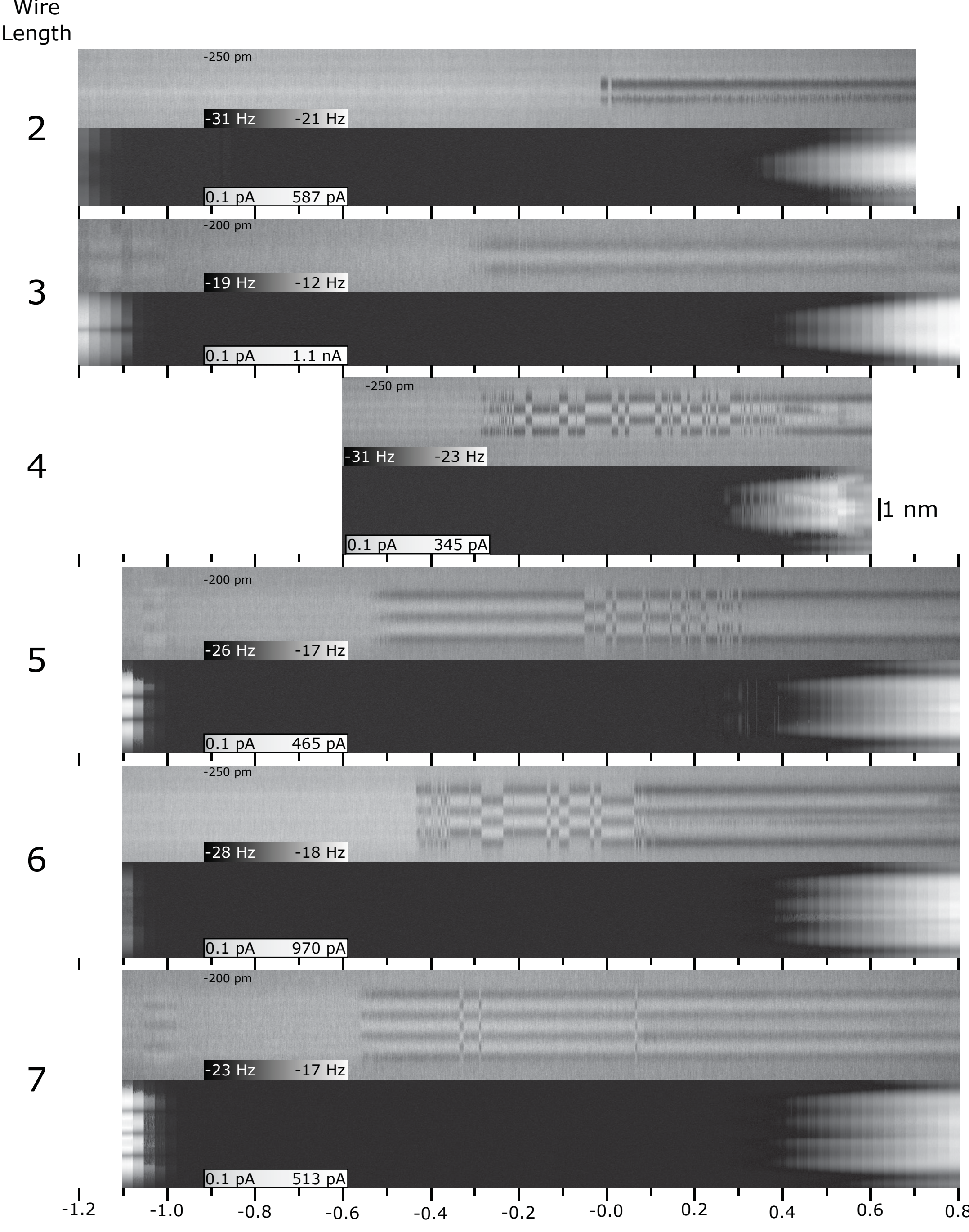

FIGURE 5.24: **Charging of DB Wires with Current Signal**. Line scans of DB wires length 2 to 7 as shown in Figure 5.5. The bias range has been extended to cover the full range available. Current line scans have been plotted using a log scale. All other parameters as indicated in Figure 5.5.

The DB wires of length 8 to 15 shown in Figure 5.25 do not probe far enough into the filled states to provide further information regarding the current signal, but they do provide further evidence of charge redistribution in the net positive charge state of the wires. Specifically DB wires of length 9, 11, 13, and 15 show some evidence of charging features (seen at -1.0 V) not seen in the even DB wire cases.

With this new appreciation for the relation between the charge states of the DB wire and features in the measured conductivity of the wire, it may be useful to look at constant current empty and filled states images of the DB wires. Figure 5.26 shows the empty and filled states images of DB wires length 2 to 7 and 15 as well as the filled states images of DB wires length 2 to 15. Starting with the filled state image of the 3 DB wire (marked 3 in the top right of the panel), we observe a reduction in height above the middle DB with an increase in height above the outer DBs in the filled states image. As we increase the DB wire length, we can see similar minima and maximum in height across the DB wires in filled states with the most prominent maxima occurring at the wire ends. With our understanding of charge distribution using KPFM, we can correlate these height maxima to the positions of negative DBs (when the wire is in the net $1e^{-}$ charge state) with the largest peaks at the end corresponding to the positions where the DBs are most often negative (as observed in Figure 5.25). The most prominent minima across DB wires corresponds to the position of the most commonly seen positive DB wire which appears as part of the (-+-) cluster at the wire ends (again shown in Figure 5.25). It is important to note that just like the AFM scans, the charge states within DB wires will likely switch between (+),(0),and (-) depending on competing emptying and filling rates of the DB wire, tip and Si bulk, so the observed features within empty (and filled) states wires are due to an averaging over many charging events and can merely be correlated to the DB charge states in the net $1e^{-}$ charge state of the wire, not attributed to them.

In the empty states image, the 3 DB wire appears to be fairly homogeneous with a secondary node below the middle DB in the wire and a slight cure seen along the bottom of the wire. Unfortunately, not all DB wires were imaged in empty states, but from those that were (2-7,

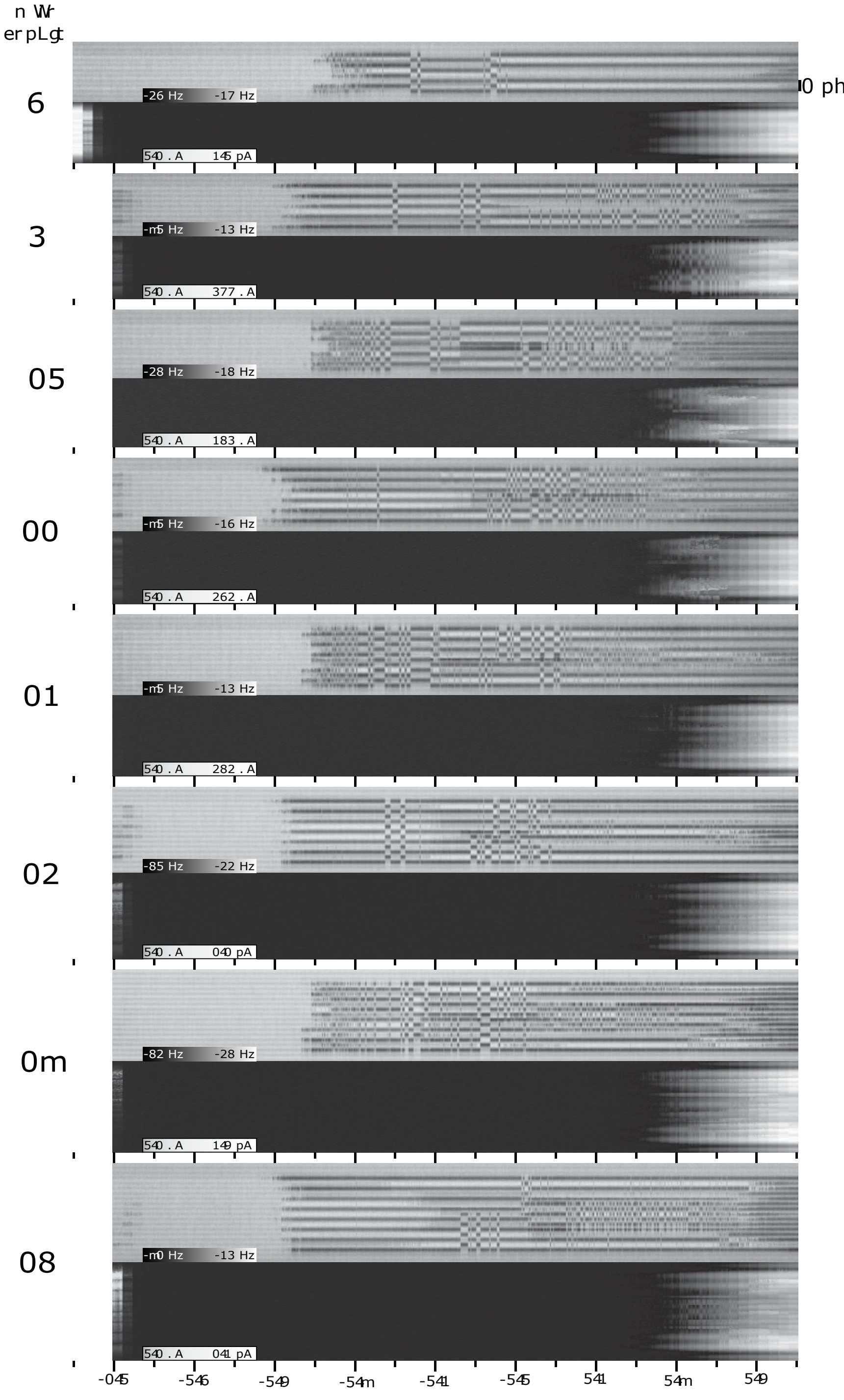

FIGURE 5.25: **Charge distributions among longer wires with current signal.** Same parameters as Figure 5.15 with current signal plotted in log scale.

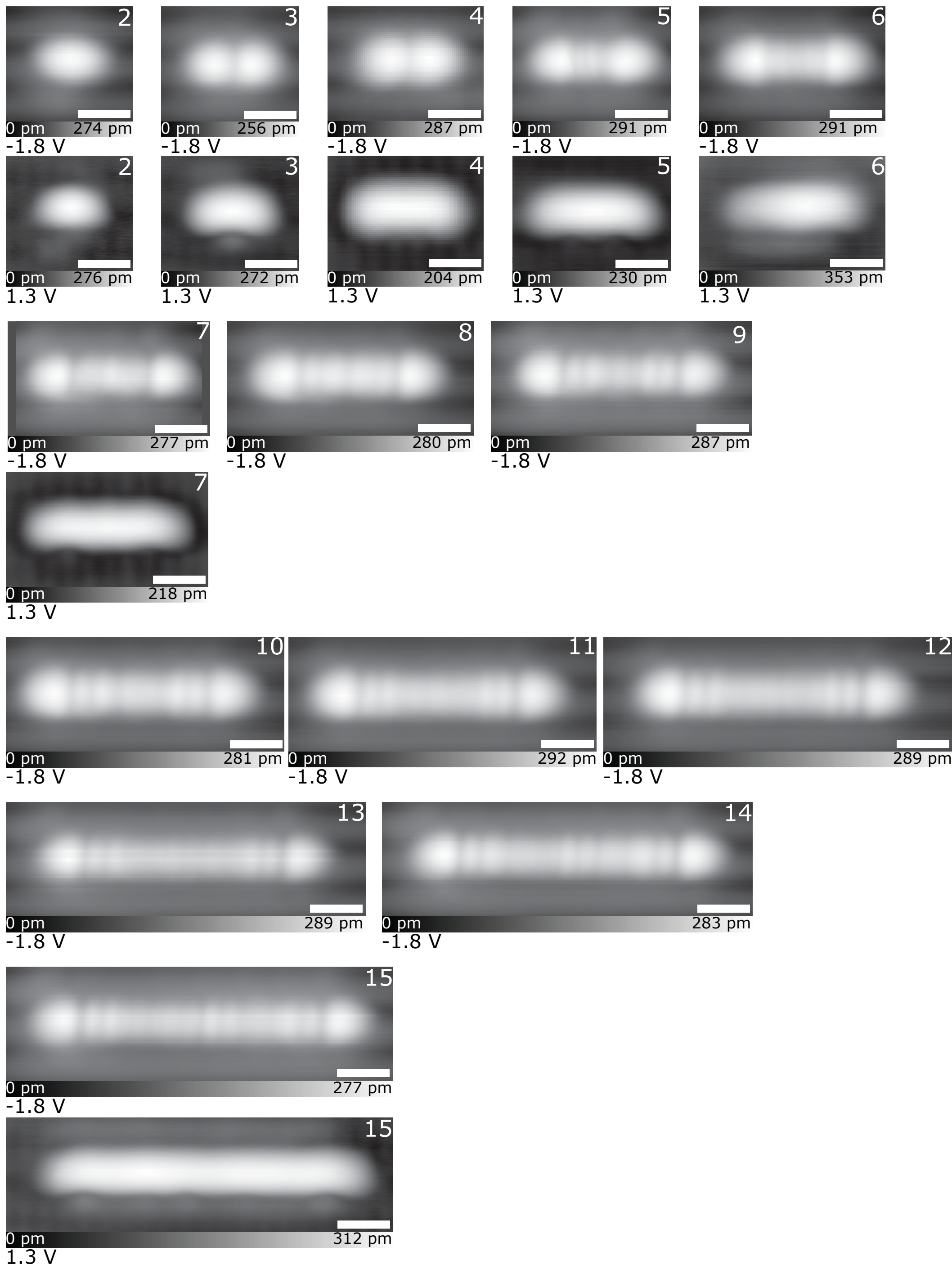

FIGURE 5.26: **Filled and some Empty States STM images of DB Wires**. Imaging bias in the bottom left of each image indicate if it is empty (1.3 V) or filled (-1.8 V) images. The length of each DB wire is indicated in the top right of each image. Scale bar is 1 nm

and 15) a similar slight curve is seen along the bottom of the wires at the ends which again corresponds to the position of the positive DBs in the (-+-) clusters. The 15 DB wire is particularly interesting since it also shows a hint of some secondary nodes along the bottom of the wire. One final thing to note is that these STM images were taken with a Si-terminated apex which is difficult to get in a perfect AFM and STM imaging condition. As such, a secondary feature can be seen slightly above and to the left of the DB wires (especially for the wires length 7 to 15). For the 4 and 5 DB wire, this feature was distracting from the main features of the DB wires so the filled states images were taken from a different data set which used an STM only tip. Looking at the height scale of the 4 and 5 DB wires in empty states compared to the others, it is clear that the tip character plays a significant role in the conductivity. Further investigations of such features within both the filled and empty states images of DB wires using different tip contrasts as shown in Figure 3.7 may be useful. In addition, these features have been found to vary with changing dopant profiles [365] likely due to the varying emptying and filling rates of the DBs[7] within the wires also warranting further investigation.

Since the even DB wire exist in a degenerate configuration at the net 1e$^-$ charge state, a reasonable study would be to see if these structures could be polarized like the DB pairs studied in [46]. Since the (-+-) cluster of a 4 DB chain has a net negative charge, patterning a DB on the left and right of the 4 DB wire may cause enough of a perturbation to push the (-+-) cluster to the opposite end of the wire. Figure 5.27 shows such an experiment where a single DB was patterned on the left (Figure 5.27 (a)) and right (Figure 5.27 (b)) side of a 4 DB wire with two intervening H-Si atoms. Looking at the filled states images of column i, we can see a distinct asymmetry in the height minima of the 4 DB wire when under perturbation. When the DB is left of the wire, this minima appears on the right of the wire. When the DB is right of the wire, this minima appears on the left side of the wire. Correlating the position of the minima to the positive DB, we can see the Coulombic interaction of the single DB does have an effect. It is important to note that since there is a significant tunneling current, these features are expected to be an averaging of the configuration of the DB wire. The

empty states images in column vi reveal a similar perturbation with the location of a more pronounced curve underneath the wire as well as the location of the smaller secondary node corresponding to the expected position of the (+) DB within the wire under perturbation.

The AFM images are shown in columns ii-v at varying biases. The single DB did not transition to the negative charge state until very near 0 V (As will be shown in Figure 5.27) so it was difficult to measure the polarizability at 0 V as was done in Ref. [46]. Once the single DB charged, the 4 DB wire can be seen to switch between configurations during image acquisition suggesting that it is more difficult to polarize a DB wire compared to a DB pair or that the tunneling current between the tip and DB wire present at non-zero biases caused a significant perturbation of the wire. To better understand the relation between the polarizability of a 4 DB wire with bias, a full set of line scans was taken at biases between -0.6 V and 0.5 V. For each set of 50 line scans, the charge configuration of the DB wire was grouped into one of six different configurations and represented as a percentage. This was done for each bias interval of 0.02 V allowing average population to be calculated as a function of bias.

The results are shown in Figure 5.28, where the 4 DB wire with a single DB on the left side is shown in (a) and (b) (bwd and fwd), the right side in (c) and (d), and the unperturbed wire in (e) and (f). Both the forward and backward scans of the tip are shown to highlight that minimal hysteresis is evident with scan direction. Looking at Figure 5.27 (a), there are 6 unique charge configurations listed. The bold atom indicates the state of the perturbing DB (1 is negative, 0 is neutral), while the non-bolded set of 4 numbers corresponds to the 4 DB wire (1 is negative, 0 is either neutral or positive). Scanning from -0.6 V up to roughly -0.25 V, the DB wire and single DB are both uncharged. Once we reach -0.25 V to -0.05 V, the 4 DB wire becomes net negative switching between the (-+-0) and (0-+-) configurations (written as 1010 and 0101 respectively). A slight preference is given for the (0-+-) state in green matching the expected polarization from the single DB. In the small range of roughly -0.1 V to 0 V, the single DB is in a negative charge state with the DB wire in the net neutral state as indicated by the slight rise in the purple curve. Above 0 V, both the single DB

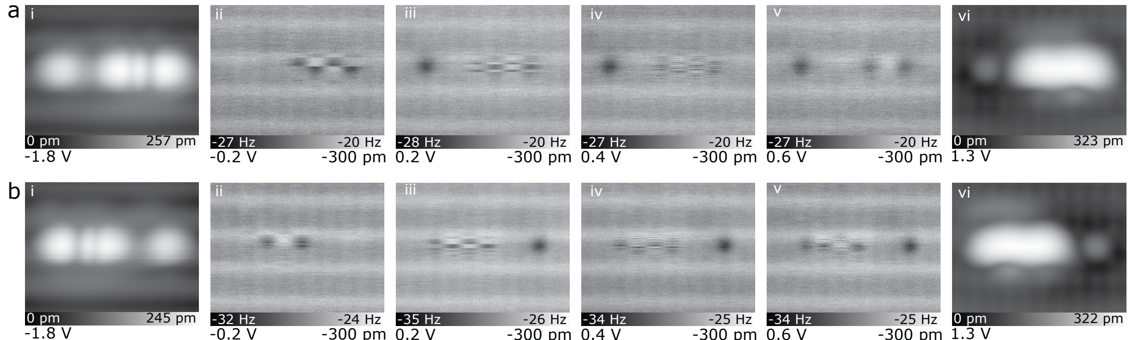

FIGURE 5.27: **Polarization of a 4 DB chain.** (a) and (b) show the right and left polarized chain respectively. (i) shows the filled states STM image, (ii-v) show the Δf maps of the structures, and (vi) shows the empty states STM image. Bias and relative heights are indicated in the lower left and right of each image. Each image is 3 x 4 nm^2.

and DB wire now polarize to the expected state indicated in dark blue. As we move into higher biases, the opposite polarization becomes more visible, making up roughly 30 % of the measured states matching the observations made in Figure 5.27. As can be seen, the total population for a given bias does not always reach 100 %, this was due to a combination of scan noise in the Δf signal (a higher averaging would remove this) as well as mid line scan switching at the higher biases. If the DB wire was observed to switch between states mid scan, this state was just ignored so as to not complicate the plot with more configurations.

The right polarized states shown in Figure 5.28 (c) shows a similar story to 5.28 (a) at voltages lower than 0 V. Interestingly, the (0-+-) state with a neutral perturber in green shows the same configuration in (a) suggesting that preference may be due to a slight variation in the electrostatic potential of the surface. Once both the single DB and the 4 DB wire are negatively charged, they again favour the correct polarization at a lower positive bias with the unfavourable polarization appearing at roughly 40 % with higher biases showing a 50%-50% split at around 0.35 V. The asymmetry in polarization between the left and right polarized case suggests there may be an additional electrostatic perturbation not accounted for.

The unperturbed case shown in Figure 5.28 (e) shows the charging of the 4 DB wire at roughly -0.3 V, slightly lower than the perturbed cases with the charge configuration of the net negative wire evenly switching between the (-+-0) and (0-+-) states. As we increase the bias further we reach the higher charge order (-00-) state in purple. Note that the (-00-) state does not appear in the perturbed case due to the raise in potential from the perturbing DB.

From the results, it appears that a 4 DB wire does not appear to polarize as well as a DB pair outlined in [46]. Using a simple $1/r$ expression to calculate the energy of the system, the difference between the higher energy (- [- 0]) and lower energy (- [0 -]) charge configurations of a 2 DB pair is twice as much as the difference between the higher energy (- [-+-0]) and lower energy (- [0-+-]) charge configuration of a 4 DB wire. This difference could explain why the 4 DB wire is less definitively observed in the lower energy polarization. Alternatively, drawing on the observation that the 4 DB wire appeared to be in the correct polarization at lower biases where there was no measurable current, it suggests that a similar spectroscopic assessment of a DB pair polarization might reveal that it too may more often be found in the higher energy polarization at larger bias values.

5.3.3.1 Si Tip Character and Charged Dangling Bonds

As mentioned above, due to the predicted neutral charge of a Si DB on an AFM tip, the dominant interaction between a tip DB and a surface DB (or H-Si) is covalent in nature with additional ion induced dipole interactions from charged DBs. DB wires imaged with a Si tip will therefore have both covalent and ionic contributions. In addition to these two contributions, measurements over DB wires are further convoluted from the difference in height of the host Si atoms due to lattice distortion. The more negative Δf signal over a negative DB is thus due to the covalent interaction, the induced dipole interaction, and a reduced tip-sample separation between the tip and surface DB. The less negative Δf signal over a positive DB is then due to the covalent, and induced dipole interactions as well as

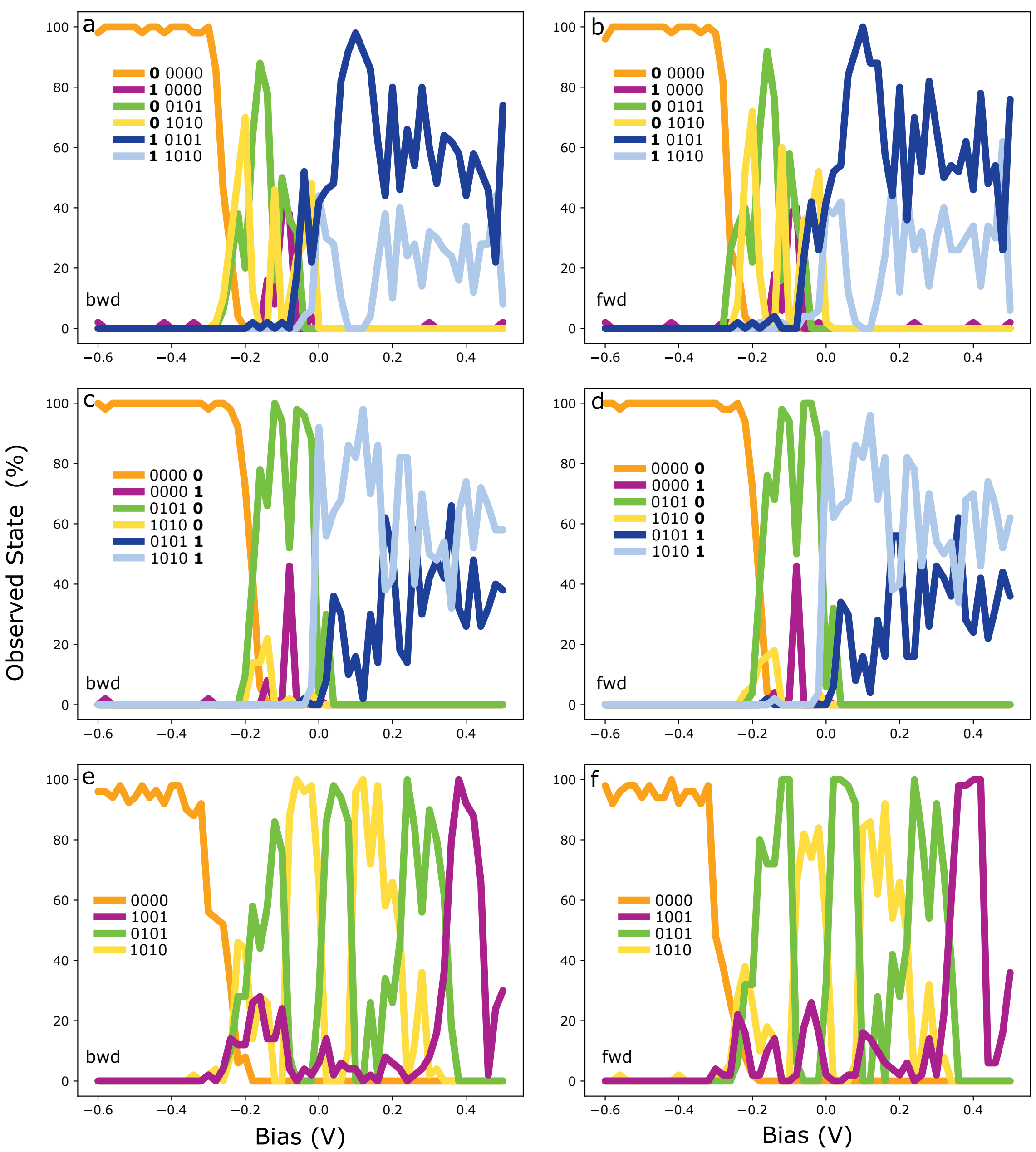

FIGURE 5.28: **Polarization states spectroscopies of 4 DB chain**. Observed polarization state for the left (a,b) and right (c,d) perturbed 4 DB chain (e,f) as well as an unperturbed 4 DB chain for reference. forward and backward scan directions are indicated in lower right of each plot. The polarization states are indicated in each plot with the bold number corresponding to the state of the perturbing DB. 0 corresponds to a neutral/positive DB and 1 corresponds to a negative DB. The population is calculated for each set of 50 line scans at bias increments of 0.02 V. Bias values which do not show a complete 100 % occupation between states had line scans that either switched halfway through the scan or were too noisy to distinguish and were ignored.

an increased tip-sample separation between the tip and surface DB. The height difference between the up and down atoms in a DB wire have been theoretically predicted to be 16 pm, 50 pm, 67 pm, 74 pm, and between 41 pm and 78 pm(length dependent)([356],[269], [357], [359], and [345] respectively) with the difference between the up and down atoms of a bare dimer around 82 pm[6] [359]. Looking at the subtracted $\Delta f(z)$ spectroscopy of Figure 3.24 (a), this height difference alone could corresponded to a difference in Δf of around 6-7 Hz. If the measured difference between the (+) and (-) atoms of a DB wire or bare dimer are indeed a combination of the charge and relative height of the DBs (and not just from the relative height difference), $\Delta f(z)$ spectroscopies should observe an increase in separation in the $\Delta f(z)$ curves between each charged (and uncharged species) with shrinking tip-sample separation.

The results below show an extraction of the $\Delta f(z)$ behaviour from constant height images of a single (+) DB, a 3,4,5, and 6 DB wire, and a bare dimer. Since the constant height images were taken 50 pm apart, all spectroscopies only consist of 3-4 points which have been connected using a spline interpolation. The extracted trends provide enough information to confirm the behaviour of the tip-sample interaction, however, full $\Delta f(z)$ spectroscopies with appropriate background subtractions[155] would be useful to confirm these behaviours.

The single DB was imaged at three different heights at -1.1 V (putting it in the (+) charge state) as shown in Figure 5.29 (a)-(c), with the corresponding spectroscopy in (d). The key take away being that the effective tip height between the H-Si atom and the DB (+) at a constant Δf increases with a reduction in tip height. This supports the claim that the tip-sample interaction is a combination of a covalent and Coulombic interaction as well as an increase in the effective tip-sample separation from lattice distortion. It is worth noting that it is difficult to determine how much of the change in Δf is due to the covalent or Coulombic contributions since the covalent contribution is expected to be dependent on the lattice distortion as well as the DB charge. Separating out each contribution would likely

[6] This calcualtion was done for the unterminated surface. Calculations for a bare dimer on a H-terminated surface would likely lower this number slightly.

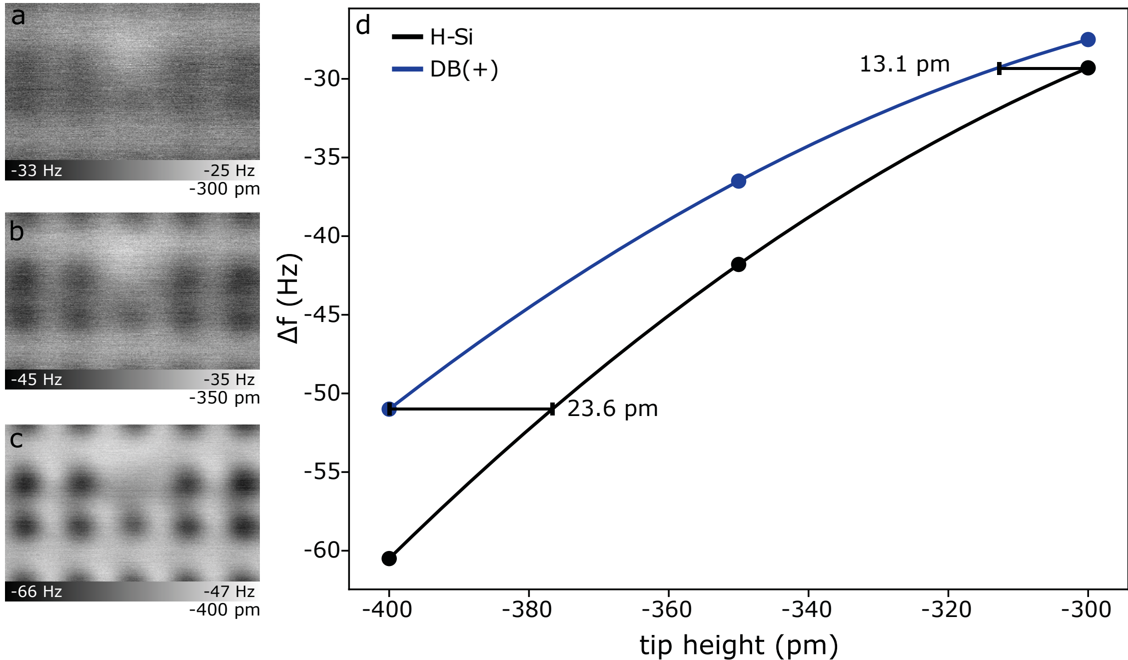

FIGURE 5.29: **Tip height dependence over a single DB.** (a)-(c) Constant height AFM images of a single DB at various heights (as indicated). Imaging bias of -1.1 V, 1.6 x 1.2 nm^2. (d) Extracted Δf above H-Si and the DB at varying heights. Δf values extracted from (a)-(d) with a spline interpolation used to give a line of best fit. Select distances between curves at constant frequency are shown.

require theoretical calculations to model the force of interaction between the tip and (+), (0), and (-) DBs as a function of tip-sample separation.

The three and four DB wires are shown in Figures 5.30 and 5.31 respectively. The constant height images are shown in (a)-(d) and the extracted $\Delta f(z)$ spectroscopies in (e). Similar to the single DB case, the distance between an H-Si atom and a DB(+) increases as the tip height is reduced. The same trend is observed for the H-Si atom relative to the DB(-) as well which shows an even greater increase in effective height as the tip height is reduced. It is difficult to identify if the cause of this difference is a result of the different lattice distortions between (+) and (-) DBs, different induced dipole effects on the tip DB, or different covalent interactions between the DB of the tip and surface. Theoretical simulations which map out

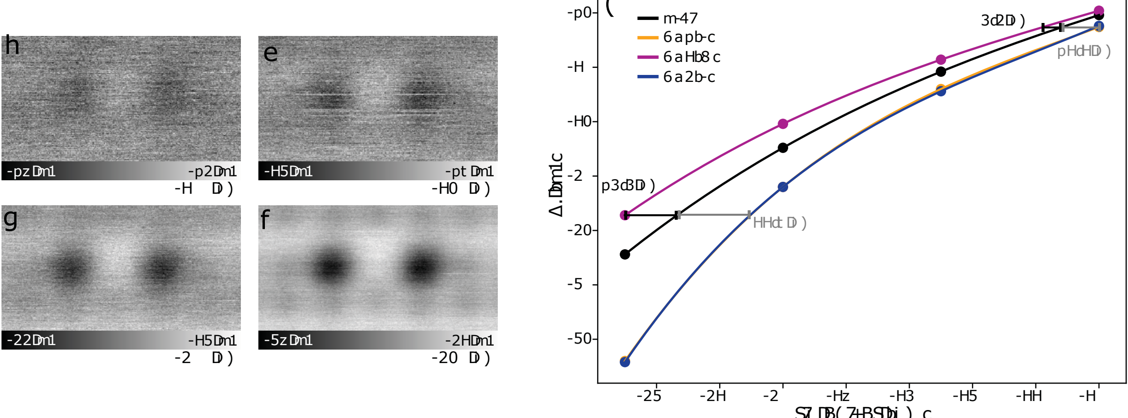

FIGURE 5.30: **Tip height dependence over a 3 DB wire.** (a)-(d) Constant height AFM images of a single DB at various heights (as indicated). Imaging bias of -0.2 V, 2.1 x 1.1 nm^2. (d) Extracted Δf above H-Si and the 3 DB wire at varying heights. Δf values extracted from (a)-(c) with a spline interpolation used to give a line of best fit. Select distances between curves at constant frequency are shown.

the contributions from each interaction are needed. The 4 DB wire case also shows a neutral DB which shows very little difference in Δf between the H-Si atom and a (0) DB.

The five and six DB wire cases shown in Figures 5.32 and 5.33 again show constant height images in (a)-(d) and the extracted $\Delta f(z)$ spectroscopies in (e). At -200 pm and -250 pm, they show similar trends to the three and four DB wire case except that the effective heights of DB (+) is larger than the DB (-). This could be due to many things including a modification in the electrostatic landscape from the additional DBs [6], variations in the lattice distortion as a function of wire length [345], or changes to the tip character from DB creation between measurements. Since each of the DB structures presented here were taken over multiple days and with slightly different tip character, there is likely to be a slight difference in the character of the tip between days. This will have an effect on the measured Δf as well as the initial height setpoint of the tip (compare the Δf scale between Figure 5.32, and 5.30). In order to accommodate for these effects, a more rigorous study should be done which pre screens for any variation in the electrostatic behaviour as well as minimizes

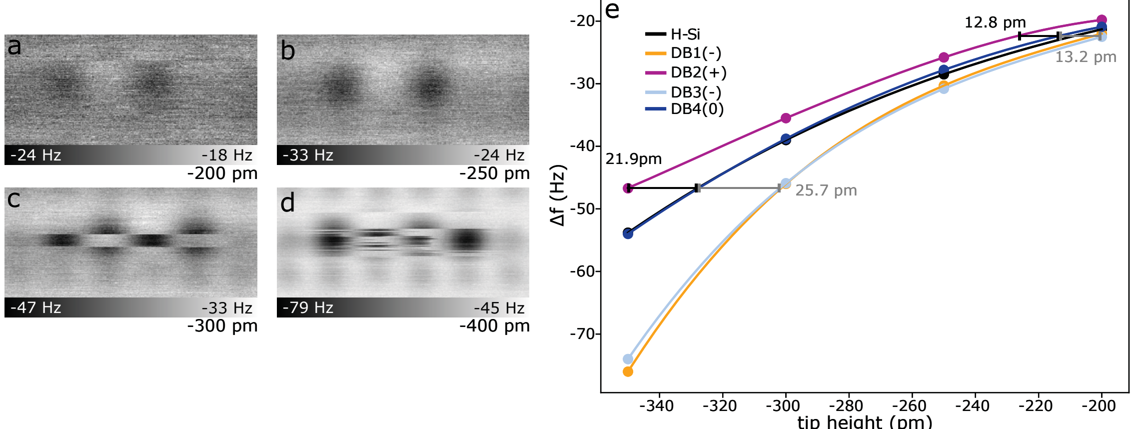

FIGURE 5.31: **Tip height dependence over a 4 DB wire.** (a)-(d) Constant height AFM images of a 4 DB wire at various heights (as indicated). Imaging bias of -0.2 V, 2.3 x 1.0 nm^2. (d) Extracted Δf above H-Si and the 4 DB wire at varying heights. Δf values extracted from (a)-(d) with a spline interpolation used to give a line of best fit. Select distances between curves at constant frequency are shown.

the risk of any tip changes between measurements over DBs of different length (most likely by prepatterning all DB wires of interest.).

With further reduction in tip height, the effects of a tip induced charging can be seen on the DB wires. Due to the attractive nature between the surface and tip DB, the host Si atom of the surface is displaced towards the tip changing its orbital character from sp^2 to sp^3[155, 350]. As mentioned, this change in character lowers the energy of the DB allowing for it to transition between charge states. In the work done by Rashidi *et al.* [155], this transition appeared as a sharp step in the $\Delta f(z)$ spectroscopy. Since the spectroscopies in Figure 5.32 and 5.33 are only made with 4 points, the step feature is absent and the spline interpolation results in a smooth transition between the two charge states warranting the need for more thorough follow up measurements. The 5 DB case also shows that the depth at which this transition can occur can vary for DBs within the wire (looking at the middle left and middle right DB). Since the geometry (and therefor imaging character) between these DBs is calculated to be the same [345], the observed variation in tip induced charging

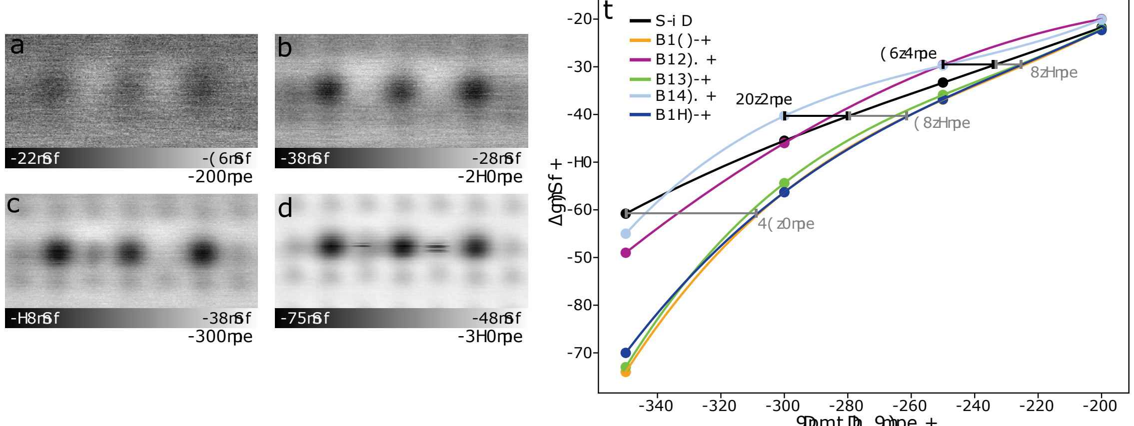

FIGURE 5.32: **Tip height dependence over a 5 DB wire.** (a)-(d) Constant height AFM images of a 5 DB wire at various heights (as indicated). Imaging bias of -0.2 V, 2.75 x 1.24 nm^2. (d) Extracted Δf above H-Si and the 5 DB wire at varying heights. Δf values extracted from (a)-(d) with a spline interpolation used to give a line of best fit. Select distances between curves at constant frequency are shown.

height is likely either from an asymmetric tip, or electrostatic distribution of the surrounding surface.

The last DB structure examined is a single bare dimer in Figure 5.34 with the constant height images in (a)-(d) and the extracted $\Delta f(z)$ spectroscopies in (e). Again, an effective height difference between the H-Si atom, the DB(+) and DB(-) can all be seen with the DB(+) showing a greater difference relative to the H-Si atom than the DB(-) relative to the H-Si atom. When comparing this plot to the 3 DB wire case in Figure 5.30, it confirms the observations made in Figure 5.20 in which the (-) DB of the 3 DB wire had a more negative Δf signal than the (-) DB of the bare dimer. As mentioned previously, assuming that both DBs are in fact negative, this difference in Δf may be due to the different lattice distortions[7] between the species, or a varying covalent interaction. Since the bare dimer is known to form a π bond across the dimer, it could be that this bond formation makes the (-) DB interact

[7] The (-) DB of the DB wire is calculated to be raised by 7 pm [345] while the (-) DB of the bare dimer is expected to be raised by 44 pm [359]. This would result in the opposite trend observed (bare dimer appearing darker) if the measured signal was only due to lattice height.

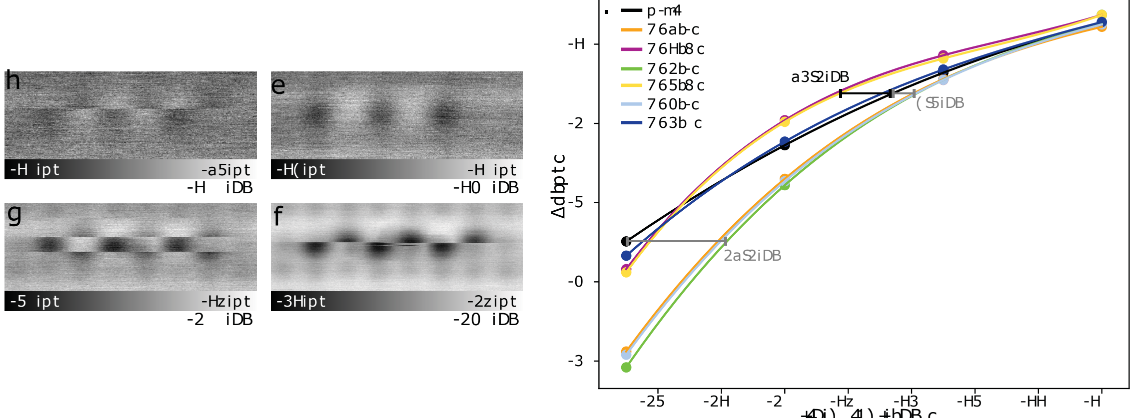

FIGURE 5.33: **Tip height dependence over a 6 DB wire.** (a)-(d) Constant height AFM images of a 6 DB wire at various heights (as indicated). Imaging bias of -0.2 V, 2.75 x 1.24 nm^2. (d) Extracted Δf above H-Si and the 6 DB wire at varying heights. Δf values extracted from (a)-(d) with a spline interpolation used to give a line of best fit. Select distances between curves at constant frequency are shown.

less strongly with the tip DB when compared to the (-) DB of the 3 DB wire. Such claims are only anecdotally founded with the presented data and require more rigorous theoretical and experimental observations.

5.3.3.2 Capping DB Wires

One of the major limitations to using DB wires on the Si surface is that they spontaneously react with H_2 at very low concentrations. As covered in a review by Dürr *et. al.* [363], it was known for some time that certain DB configurations would spontaneously react with H_2 in a vacuum system while others did not. The work later done by Achal *et. al.* [5] used this phenomenon as a benefit in the “make to erase” technique. While useful for advancing the lithographic techniques of DB fabrication, such an effect puts a serious limitation on DB wire design.

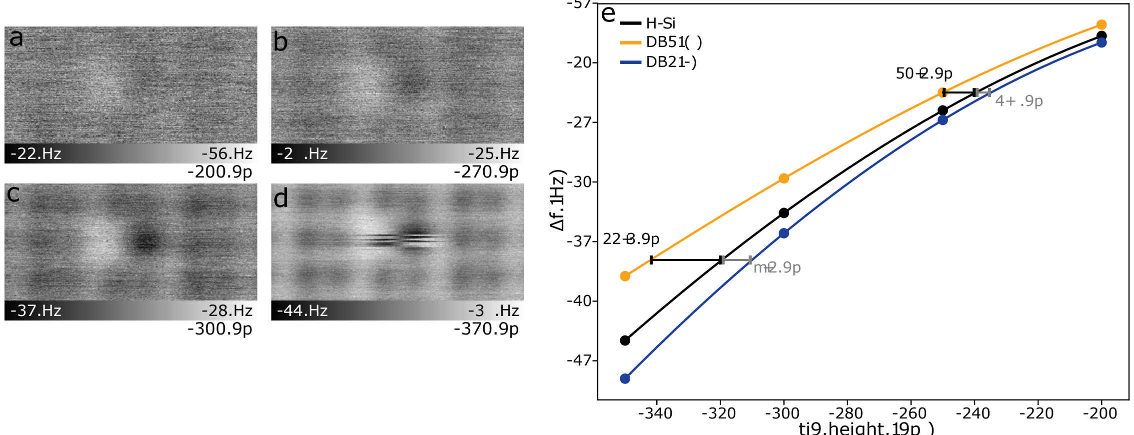

FIGURE 5.34: **Tip height dependence over a bare dimer.** (a)-(d) Constant height AFM images of a bare dimer at various heights (as indicated). Imaging bias of -0.2 V, 2.6 x 1.2 nm^2. (d) Extracted Δf above H-Si and the bare dimer at varying heights. Δf values extracted from (a)-(d) with a spline interpolation used to give a line of best fit. Select distances between curves at constant frequency are shown. Δf extracted from an image where the charge ordering switched mid scan were extrapolated by eye from a line scan.

With the new understanding of the ionic behaviour in DB clusters, it is useful to re-examine several of the DB structures and their interactions with molecular hydrogen as shown in Figure 5.35 exploring new DB cluster configurations. Several DB clusters including DB wires of various length and bare dimer clusters coupled to DB wires were created as shown in Figure 5.35 (a) and (c). Following exposure to molecular hydrogen at a measured pressure of 1×10^{-9} Torr[8], some of the DB clusters were observed to react as shown in Figure 5.35 (b) and (d).

Looking at the bottom left corner of each image before hydrogen exposure, DB wires of length 1-6, and 15 are shown in green, red, dark blue, light blue, yellow, purple, and black respectively. As expected, the 2 and 4 DB wires are completely capped with the 3 and 5 DB wires reduced to 1 DB each. The 6 DB wire has been reduced to two 2 DBs separated by 2 H-Si atoms suggesting that the H_2 molecules do not preferentially attack the ends of

[8]This pressure was chosen because it was the highest pressure achievable without activating the ion pump. The pressure is also predicted [5] to be roughly 2 orders of magnitude lower in the scanning chamber.

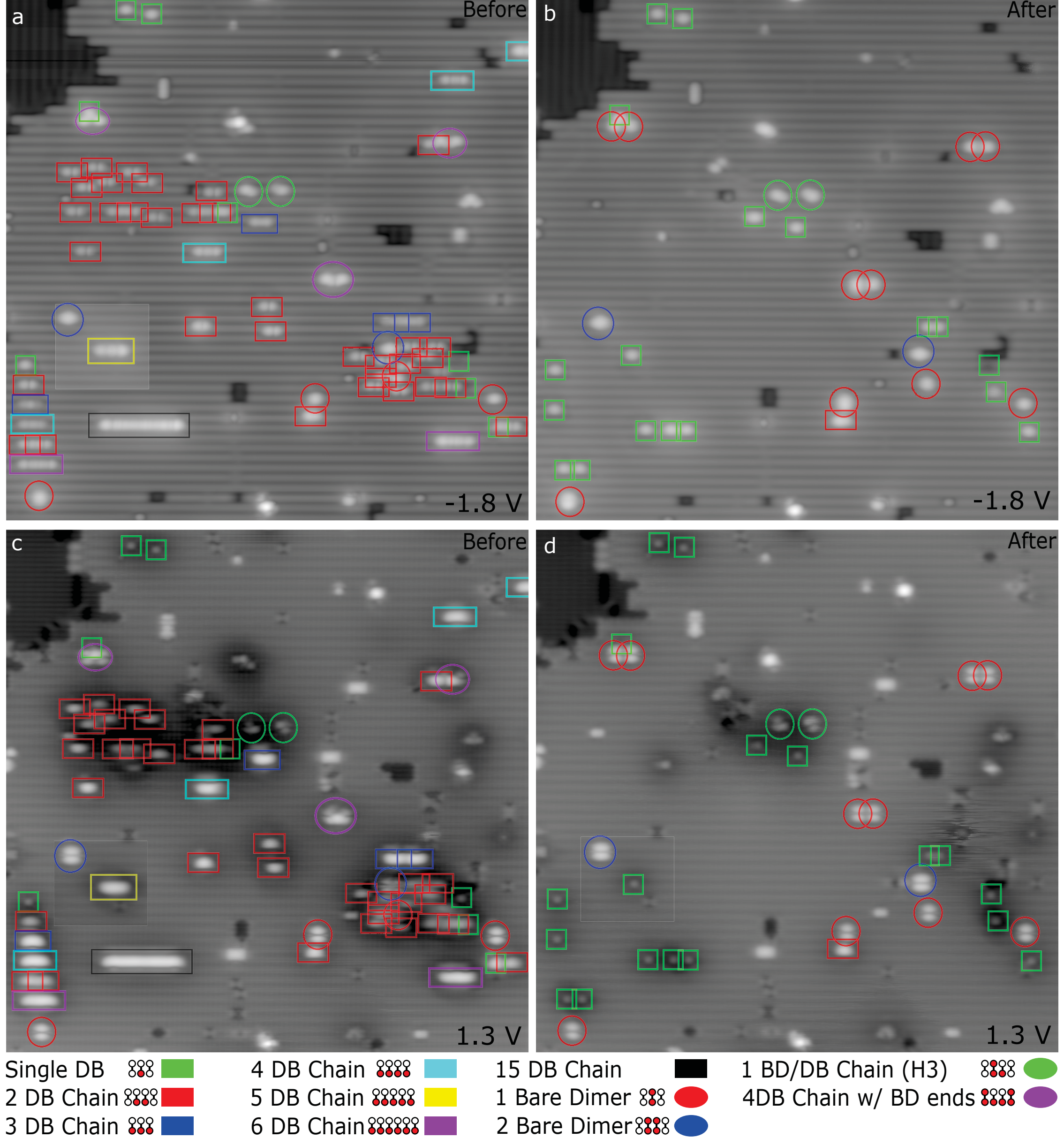

FIGURE 5.35: **H_2 passivation of DB clusters.** (a) Filled states image of several DB clusters before H_2 exposure. (b) Filled states image of same area in (a) after H_2 exposure. (c) Empty states image of the same area in (a) before H_2 exposure. (d) Filled states image of the same area in (a) after H_2 exposure. DB structures are indicated in the key. Bias values are shown in the bottom right of each image. Each scan is 40 x 40 nm^2. The scan area containing the 5 DB wire was after the large scan and overlaid after a mistake in wire structures was realized.

DB wires (note that the 6 DB wire on the bottom right of each image was fully erased). A similar trend is observed on the 15 DB wire which shows 3 DBs remaining, all with at least two H-Si atom separation.

The top left portion of (a) and (c) show a large cluster of 2 DB wires. These, with the 2 DB wires in the bottom right of (a) and (c) were created from clusters of single DBs. The single DBs were created for tip functionalization for DB passivization. They were then turned into 2 DB wires to show that tip induced passivation, when used in parallel with molecular repassivation can allow for the efficient removal of any unwanted DBs.

In addition to 2 DB wires, the top left of the image also features a 4 DB wire with bare dimer ends in the purple circle. After exposure to H_2, the middle 2 DBs were capped leaving two bare dimers. As previously stated in [363], the bare dimer (red circle) or pair of bare dimers (blue circle, same as Figure 5.18) do not spontaneously react with H_2 due to the large energy difference between the two DBs of a bare dimer. A 2 DB wire with a single bare dimer on one end (Shown in Figure 5.17, also referred to as an H3 site) was also patterned shown in green circles and as expected, it was nonreactive to H_2.

More of the same reactions sites can be seen throughout the remainder of the image. With exception to one 2 DB wire in the middle bottom of each image, all DB sites that were patterned along the same side of a dimer row were able to spontaneously react with H_2. Sites which were left unaffected by H_2 all contained bare dimers or single DBs which confirms the limitations of molecular repassivation as an error correction technique.

Since the reaction mechanism of molecular hydrogen involves the transfer of a DB electron to an antibonding state of the H_2 molecule, it would be interesting to repeat these studies on a p-type crystal. A 2 DB wire on the degenerately doped p-type surface may then exist in a (0+/+0) configuration which may prevent the spontaneous reaction of the 2 DB wire with H_2.

Chapter 6

Conclusion

In this thesis, we have looked at advancements made to scanning probe lithography through the incorporation of machine learning leading to autonomous fabrication through surface characterization. In particular, we have shown the successful implementation of an automated fabrication system capable of patterning BASiL devices on a H-Si(100)-2x1 surface. A neural network capable of distinguishing between 7 different surface features has been developed allowing for the distinction between charged defects, uncharged defects, and defect free areas of the surface. This distinction is used to find an optimal location on the surface leading to the automated fabrication of the desired DB devices.

The number of classes and accuracy of the neural network shown in Chapter 4 was improved upon by relabelling the training data, updating it with new defect classes from the defect catalogue in Chapter 3. The defect catalogue utilized a total of 6 different scanning probe imaging modes. These different imaging modes allowed for the probing of various electrical and atomic properties which were supplemented with probe-particle simulations confirming the identity of previously known defects and suggesting classifications of defects which have either not been observed before, or that the identify of has not been confirmed. In particular, the use of a Si-terminated AFM probe allowed for a more detailed interpretation of the surface

than the previously more commonly used H-terminated AFM probe as demonstrated by the enhanced feature contrast.

This Si-apex AFM probe was attributed to a stronger covalent interaction compared to the weaker Van der Waals interaction of a H-apex probe. This covalent character proved useful in distinguishing between the 3 charge states of a surface DB allowing for the charge distribution of DB clusters to be observed for the first time. Both DB wires and bare dimers were created, with the differences in behaviour correlated to the different atomic geometries of the structures. Both the bare dimer and DB wires were revealed to undergo ionic pairing corresponding to the raising and lowering of the host Si atoms with respect to the surface with DB wires only forming this phase with subsequent charging. These observations provide key experimental details needed for additional experimental and theoretical work to demonstrate the viability of using such DB wires as atomic scale device interconnects.

Although significant milestones have been made in this work, it leaves room for many additional experiments and follow up work to further the development of atom scale devices and their fabrication. The defect catalogue of Chapter 3 provides a thorough investigation of many defects of the H-Si(100) surface, however, this list is by no means exhaustive as demonstrated by the diverse number of defects left in the "unknown" class of Chapter 4. By combining the techniques in Chapter 4 with Chapter 3, the defect catalogue can continue to grow through the automation of defect detection. Further insights can be offered by exploring variations of the H-Si surface by applying modifications to the sample preparation procedure or by using various crystal doping types (p-type, arsenic doped n-type, etc.) and concentrations, and crystal faces (Si(111) is of particular interest). In addition, enhancements to the training data can be made in an attempt to further improve the accuracy and range of the neural network used for defect classification. In particular, multiple imaging modes could be used to allow for a more robust neural network.

To improve the automated fabrication, the neural network could be updated to detect the atomic positions of H-Si atoms on the surface, eliminating the need for follow-up scans in

the current fabrication method in Chapter 4. By being able to distinguish each lattice site as capable of hosting a patterned DB or not, BASiL devices could be placed more precisely on the surface reducing the spacial limitations introduced by surface defects. This network could also be trained to detect the atomic position of DBs on the surface in various configurations (single DBs, DB wires, bare dimers, etc) which will prove very useful in the development of automated error correction.

The developments made in identifying charge distributions within DB clusters on the (100) surface highlight the potentially disruptive asymmetry in DB wire behaviour with lattice direction. The (111) surface, which offers a higher symmetry will hopefully remedy this issue and warrants further investigation both in the potential distribution of charges within the structures and their ability to react with H_2. Ultimately, the conductivity of such DB wires will need to be experimentally determined via two or four probe measurements. The results of these experiments will have direct implications on the viability of the needed atomic interconnects for the integration of atom scale devices with semiconductor technologies.

The development of atom-scale devices is an exciting and necessary challenge which needs to be addressed to satisfy the ever increasing need for cheaper, faster, and lower power electronics. While the challenges ahead may appear daunting, key successes continue to be made through the development and application of novel fabrication and characterization techniques. With continued interest, our understanding of and capabilities in fabricating atom scale devices will hopefully lead to their widespread use in future electronic systems.

Bibliography

[1] Mohammad Rashidi, Jeremiah Croshaw, Kieran Mastel, Marcus Tamura, Hedieh Hosseinzadeh, and Robert A Wolkow. Deep learning-guided surface characterization for autonomous hydrogen lithography. *Machine Learning: Science and Technology*, 1(2), 2020. doi:10.1088/2632-2153/ab6d5e.

[2] Jeremiah Croshaw, Thomas Dienel, Taleana Huff, and Robert Wolkow. Atomic defect classification of the H–Si(100) surface through multi-mode scanning probe microscopy. *Beilstein Journal of Nanotechnology*, 11(1):1346–1360, 2020. doi:10.3762/bjnano.11.119.

[3] Jeremiah Croshaw, Taleana Huff, Mohamad Rashidi, John Wood, Erika Lloyd, Jason Pitters, and Robert Wolkow. Ionic Charge Distributions in Silicon Atomic Wires. *arXiv*, nov 2020. URL `http://arxiv.org/abs/2011.08056`.

[4] Roshan Achal, Mohammad Rashidi, Jeremiah Croshaw, David Churchill, Marco Taucer, Taleana Huff, Martin Cloutier, Jason Pitters, and Robert A. Wolkow. Lithography for robust and editable atomic-scale silicon devices and memories. *Nature Communications*, 9(2778), 2018. doi:10.1038/s41467-018-05171-y.

[5] Roshan Achal, Mohammad Rashidi, Jeremiah Croshaw, Taleana R. Huff, and Robert A. Wolkow. Detecting and Directing Single Molecule Binding Events on H-Si(100) with Application to Ultradense Data Storage. *ACS Nano*, 14(3):2947–2955, 2020. doi:10.1021/acsnano.9b07637.

[6] Taleana R. Huff, Thomas Dienel, Mohammad Rashidi, Roshan Achal, Lucian Livadaru, Jeremiah Croshaw, and Robert A. Wolkow. Electrostatic Landscape of a Hydrogen-Terminated Silicon Surface Probed by a Moveable Quantum Dot. *ACS Nano*, 13(9): 10566–10575, 2019. doi:10.1021/acsnano.9b04653.

[7] Mohammad Rashidi, Erika Lloyd, Taleana R. Huff, Roshan Achal, Marco Taucer, Jeremiah J. Croshaw, and Robert A. Wolkow. Resolving and Tuning Carrier Capture Rates at a Single Silicon Atom Gap State. *ACS Nano*, 11(11):11732–11738, 2017. doi:10.1021/acsnano.7b07068.

[8] Jeremiah Croshaw. Github Account. URL `https://github.com/jeremiah-croshaw`.

[9] Michael Riordan and Lillian. Hoddeson. *Crystal fire : the invention of the transistor and the birth of the information age*. Norton, 1998. ISBN 0393318516.

[10] Herman Hollerith. The Electrical Tabulating Machine. *Journal of the Royal Statistical Society*, 57(4):678–698, 1894. doi:10.2307/2979610.

[11] U.S. Census Bureau History: Herman Hollerith and Mechanical Tabulation, 2016. URL `https://www.census.gov/history/www/homepage{_}archive/2016/january{_}2016.html`.

[12] Chronological History of IBM, . URL `https://www.ibm.com/ibm/history/history/history{_}intro.html`.

[13] Cohen Bernard, Gregory Welch, and Robert Campbell. *Makin' numbers : Howard Aiken and the computer*. MIT Press, Cambridge, Mass., 1999. ISBN 0262032635.

[14] Raul Rojas and Ulf. Hashagen. *The first computers : history and architectures*. MIT Press, 2000. ISBN 9780262681377.

[15] A.W. Burks. Electronic Computing Circuits of the ENIAC. *Proceedings of the IRE*, 35(8):756–767, 1947. doi:10.1109/JRPROC.1947.234265.

[16] M. V. Wilkes. *Automatic digital computers.* Methuen, London,, 1956.

[17] IBM Archives: IBM 608 calculator, . URL https://www.ibm.com/ibm/history/exhibits/vintage/vintage{_}4506VV2214.html.

[18] Deloitte. Semiconductors - The Next Wave. 2019. URL https://www2.deloitte.com/content/dam/Deloitte/tw/Documents/technology-media-telecommunications/tw-semiconductor-report-EN.pdf.

[19] Gordon E. Moore. Cramming more components onto integrated circuits. *Electronics*, 38(8), 1965. doi:10.1109/N-SSC.2006.4785860.

[20] Yong-bin Kim. Challenges for Nanoscale MOSFETs and Emerging Nanoelectronics. *Transactions on Electrical and Electronic Materials*, 11(3):93–105, 2010. doi:10.4313/TEEM.2010.11.3.093.

[21] Karl Rupp. 42 Years of Microprocessor Trend Data, 2018. URL https://www.karlrupp.net/2018/02/42-years-of-microprocessor-trend-data/.

[22] Dale R. Patrick and Stephen W. Fardo. *Electricity and electronics fundamentals.* Fairmont Press, Lilburn, GA, 2nd editio edition, 2008. ISBN 9788817360234.

[23] Mark Burrell. *Fundamentals of Computer Architecture.* Macmillan Education UK, London, 2004. doi:10.1007/978-1-137-11313-9.

[24] S. M. Sze and Kwok Kwok Ng. *Physics of semiconductor devices.* Wiley-Interscience, 3rd edition, 2007. doi:10.1002/0470068329.

[25] Chenming. Hu. *Modern semiconductor devices for integrated circuits.* Pearson, 1 edition, 2009. ISBN 0136085253.

[26] Safa Kasap. *Principles of electronic materials and devices.* McGraw-Hill, New York, 4th edition, 2018. ISBN 0078028183.

[27] David Laws. 13 Sextillion & Counting: The Long & Winding Road to the Most Frequently Manufactured Human Artifact in History - CHM, 2018. URL https://computerhistory.org/blogs/.

[28] Victor Zhirnov, Ralph Cavin, and Luca Gammaitoni. Minimum Energy of Computing, Fundamental Considerations. In *ICT - Energy - Concepts Towards Zero - Power Information and Communication Technology*. InTech, feb 2014. doi:10.5772/57346.

[29] Mark Bohr, Robert Chau, Tahir Ghani, and Kaizad Mistry. The High-k Solution. *IEEE Spectrum*, 44(10):29–35, 2007. doi:10.1109/MSPEC.2007.4337663.

[30] Takayasu Sakurai, Akira Matsuzawa, and Takakuni Douseki. *Fully-Depleted SOI CMOS Circuits and Technology*. Springer US, Boston, MA, 2006. doi:10.1007/978-0-387-29218-2.

[31] D Hisamoto, Wen-Chin Lee, J. Kedzierski, H. Takeuchi, K. Asano, C. Kuo, E. Anderson, Tsu-Jae King, J. Bokor, and Chenming Hu. FinFET-a self-aligned double-gate MOSFET scalable to 20 nm. *IEEE Transactions on Electron Devices*, 47(12):2320–2325, 2000. doi:10.1109/16.887014.

[32] Debajit Bhattacharya and Niraj K. Jha. FinFETs: From Devices to Architectures. *Advances in Electronics*, 2014:1–21, 2014. doi:10.1155/2014/365689.

[33] Samuel K. Moore. EUV lithography finally ready for fabs. *IEEE Spectrum*, 55(1): 46–48, jan 2018. doi:10.1109/MSPEC.2018.8241736.

[34] N. Loubet, T. Hook, P. Montanini, C. W. Yeung, S. Kanakasabapathy, M. Guillom, T. Yamashita, J. Zhang, X. Miao, J. Wang, A. Young, R. Chao, M. Kang, Z. Liu, S. Fan, B. Hamieh, S. Sieg, Y. Mignot, W. Xu, S. C. Seo, J. Yoo, S. Mochizuki, M. Sankarapandian, O. Kwon, A. Carr, A. Greene, Y. Park, J. Frougier, R. Galatage, R. Bao, J. Shearer, R. Conti, H. Song, D. Lee, D. Kong, Y. Xu, A. Arceo, Z. Bi, P. Xu, R. Muthinti, J. Li, R. Wong, D. Brown, P. Oldiges, R. Robison, J. Arnold,

N. Felix, S. Skordas, J. Gaudiello, T. Standaert, H. Jagannathan, D. Corliss, M. H. Na, A. Knorr, T. Wu, D. Gupta, S. Lian, R. Divakaruni, T. Gow, C. Labelle, S. Lee, V. Paruchuri, H. Bu, and M. Khare. Stacked nanosheet gate-all-around transistor to enable scaling beyond FinFET. In *Digest of Technical Papers - Symposium on VLSI Technology*, pages T230–T231. Institute of Electrical and Electronics Engineers Inc., jul 2017. ISBN 9784863486058. doi:10.23919/VLSIT.2017.7998183.

[35] Alan C. Seabaugh and Qin Zhang. Low-Voltage Tunnel Transistors for Beyond CMOS Logic. *Proceedings of the IEEE*, 98(12):2095–2110, 2010. doi:10.1109/JPROC.2010.2070470.

[36] Kerry Bernstein, Ralph K. Cavin, Wolfgang Porod, Alan Seabaugh, and Jeff Welser. Device and architecture outlook for beyond CMOS switches. *Proceedings of the IEEE*, 98(12):2169–2184, 2010. doi:10.1109/JPROC.2010.2066530.

[37] C. P. Collier, E. W. Wong, M. Belohradský, F. M. Raymo, J. F. Stoddart, P. J. Kuekes, R. S. Williams, and J. R. Heath. Electronically Configurable Molecular-Based Logic Gates. *Science*, 285(5426):391–394, 1999. doi:10.1126/science.285.5426.391.

[38] Sundus Erbas-Cakmak, Safacan Kolemen, Adam C. Sedgwick, Thorfinnur Gunnlaugsson, Tony D. James, Juyoung Yoon, and Engin U. Akkaya. Molecular logic gates: the past, present and future. *Chemical Society Reviews*, 47(7):2228–2248, 2018. doi:10.1039/C7CS00491E.

[39] A. Prasanna de Silva and Seiichi Uchiyama. Molecular logic and computing. *Nature Nanotechnology*, 2(7):399–410, 2007. doi:10.1038/nnano.2007.188.

[40] C. Joachim, J. K. Gimzewski, and A. Aviram. Electronics using hybrid-molecular and mono-molecular devices. *Nature*, 408(6812):541–548, 2000. doi:10.1038/35046000.

[41] Chandana Karnati and Hai-Feng Ji. Molecular Logic Gates. In *Micromanufacturing and Nanotechnology*, pages 275–297. Springer-Verlag, Berlin/Heidelberg, 2006. doi:10.1007/3-540-29339-6_12.

[42] Alexander Ako Khajetoorians, Jens Wiebe, Bruno Chilian, and Roland Wiesendanger. Realizing All-Spin-Based Logic Operations Atom by Atom. *Science*, 332(6033):1062–1064, 2011. doi:10.1126/science.1201725.

[43] Mayssa Yengui, Eric Duverger, Philippe Sonnet, and Damien Riedel. A two-dimensional ON/OFF switching device based on anisotropic interactions of atomic quantum dots on Si(100):H. *Nature Communications*, 8(2211), 2017. doi:10.1038/s41467-017-02377-4.

[44] Barbara Fresch, Juanita Bocquel, Sven Rogge, R D Levine, and F Remacle. A Probabilistic Finite State Logic Machine Realized Experimentally on a Single Dopant Atom. *Nano Letters*, 17(3):1846–1852, 2017. doi:10.1021/acs.nanolett.6b05149.

[45] Marek Kolmer, Rafal Zuzak, Ghassen Dridi, Szymon Godlewski, Christian Joachim, and Marek Szymonski. Realization of a quantum Hamiltonian Boolean logic gate on the Si(001):H surface. *Nanoscale*, 7(29):12325–12330, 2015. doi:10.1039/C5NR01912E.

[46] Taleana Huff, Hatem Labidi, Mohammad Rashidi, Lucian Livadaru, Thomas Dienel, Roshan Achal, Wyatt Vine, Jason Pitters, and Robert A. Wolkow. Binary atomic silicon logic. *Nature Electronics*, 1:636–643, 2018. doi:10.1038/s41928-018-0180-3.

[47] J. A. Mol, J. Verduijn, R. D. Levine, F. Remacle, and S. Rogge. Integrated logic circuits using single-atom transistors. *Proceedings of the National Academy of Sciences of the United States of America*, 108(34):13969–13972, 2011. doi:10.1073/pnas.1109935108.

[48] Martin Fuechsle, Jill A. Miwa, Suddhasatta Mahapatra, Hoon Ryu, Sunhee Lee, Oliver Warschkow, Lloyd C. L. Hollenberg, Gerhard Klimeck, and Michelle Y. Simmons. A single-atom transistor. *Nature Nanotechnology*, 7(4):242–246, 2012. doi:10.1038/nnano.2012.21.

[49] F. E. Kalff, M. P. Rebergen, E. Fahrenfort, J. Girovsky, R. Toskovic, J. L. Lado, J. Fernández-Rossier, and A. F. Otte. A kilobyte rewritable atomic memory. *Nature Nanotechnology*, 11:926–929, 2016. doi:10.1038/nnano.2016.131.

[50] W. H. Soe, C. Manzano, A. De Sarkar, F. Ample, N. Chandrasekhar, N. Renaud, P. De Mendoza, A. M. Echavarren, M. Hliwa, and C. Joachim. Demonstration of a NOR logic gate using a single molecule and two surface gold atoms to encode the logical input. *Physical Review B*, 83(155443), 2011. doi:10.1103/PhysRevB.83.155443.

[51] Zahid Durrani, Mervyn Jones, Faris Abualnaja, Chen Wang, Marcus Kaestner, Steve Lenk, Claudia Lenk, Ivo W. Rangelow, and Aleksey Andreev. Room-temperature single dopant atom quantum dot transistors in silicon, formed by field-emission scanning probe lithography. *Journal of Applied Physics*, 124(14), 2018. ISSN 10897550. doi:10.1063/1.5050773. URL `http://dx.doi.org/10.1063/1.5050773`.

[52] Xiqiao Wang, Jonathan Wyrick, Ranjit V. Kashid, Pradeep Namboodiri, Scott W. Schmucker, Andrew Murphy, M. D. Stewart, and Richard M. Silver. Atomic-scale control of tunneling in donor-based devices. *Communications Physics*, 3(82), 2020. doi:10.1038/s42005-020-0343-1.

[53] Jonathan Wyrick, Xiqiao Wang, Ranjit V. Kashid, Pradeep Namboodiri, Scott W. Schmucker, Joseph A. Hagmann, Keyi Liu, Michael D. Stewart, Curt A. Richter, Garnett W. Bryant, and Richard M. Silver. Atom-by-Atom Fabrication of Single and Few Dopant Quantum Devices. *Advanced Functional Materials*, 29(52):1903475, 2019. doi:10.1002/adfm.201903475.

[54] Y. He, S. K. Gorman, D. Keith, L. Kranz, J. G. Keizer, and M. Y. Simmons. A two-qubit gate between phosphorus donor electrons in silicon. *Nature*, 571(7765):371–375, jul 2019. doi:10.1038/s41586-019-1381-2.

[55] Samuel Sze Hang Ng, Robert A. Wolkow, Konrad Walus, Jacob Retallick, Hsi Nien Chiu, Robert Lupoiu, Lucian Livadaru, Taleana Huff, Mohammad Rashidi, Wyatt Vine, and Thomas Dienel. SiQAD: A Design and Simulation Tool for Atomic Silicon Quantum Dot Circuits. *IEEE Transactions on Nanotechnology*, 19:137–146, 2020. doi:10.1109/TNANO.2020.2966162.

[56] Marcus McEllistrem, Matthew Allgeier, and John J. Boland. Dangling bond dynamics on the silicon (100)-2 x 1 surface: Dissociation, diffusion, and recombination. *Science*, 279(5350):545–548, 1998. doi:10.1126/science.279.5350.545.

[57] C H Schwalb, M Dürr, and U Höfer. High-temperature investigation of intradimer diffusion of hydrogen on Si(001). *Physical Review B*, 82(193412), 2010. doi:10.1103/PhysRevB.82.193412.

[58] Ricardo Garcia, Armin W. Knoll, and Elisa Riedo. Advanced scanning probe lithography. *Nature Nanotechnology*, 9(8):577–587, 2014. doi:10.1038/nnano.2014.157.

[59] Da-Yin Liao. Automation and Integration in Semiconductor Manufacturing. In *Semiconductor Technologies*, chapter 3. InTech, 2010. doi:10.5772/8569.

[60] Ajit Pal. *Low-Power VLSI Circuits and Systems*. Springer India, New Delhi, 2015. ISBN 978-81-322-1936-1. doi:10.1007/978-81-322-1937-8. URL `http://link.springer.com/10.1007/978-81-322-1937-8`.

[61] David Gohlke, Rohan Mishra, Oscar D. Restrepo, Donghun Lee, Wolfgang Windl, and Jay Gupta. Atomic-Scale Engineering of the Electrostatic Landscape of Semiconductor Surfaces. *Nano Letters*, 13(6):2418–2422, 2013. doi:10.1021/nl400305q.

[62] Julian Stirling, Richard A.J. Woolley, and Philip Moriarty. Scanning probe image wizard: A toolbox for automated scanning probe microscopy data analysis. *Review of Scientific Instruments*, 84(113701), 2013. doi:10.1063/1.4827076.

[63] Richard A.J. Woolley, Julian Stirling, Adrian Radocea, Natalio Krasnogor, and Philip Moriarty. Automated probe microscopy via evolutionary optimization at the atomic scale. *Applied Physics Letters*, 98(25):1–4, 2011. doi:10.1063/1.3600662.

[64] J N Randall, J R Von Ehr, J B Ballard, J H G Owen, and E Fuchs. Automated Scanning Tunneling Microscope image analysis of Si(100):H 2x1 surfaces. *Microelectronic Engineering*, 98:214–217, 2012. doi:10.1016/j.mee.2012.07.021.

[65] J. R. Matey and J. Blanc. Scanning capacitance microscopy. *Journal of Applied Physics*, 57(5):1437–1444, 1985. doi:10.1063/1.334506.

[66] M. E. Suddards, A. Baumgartner, M. Henini, and C. J. Mellor. Scanning capacitance imaging of compressible and incompressible quantum hall effect edge strips. *New Journal of Physics*, 14:083015, 2012. doi:10.1088/1367-2630/14/8/083015.

[67] Guohong Li, Adina Luican, and Eva Y Andrei. Self-navigation of a scanning tunneling microscope tip toward a micron-sized graphene sample. *Review of Scientific Instruments*, 82(7), 2011. doi:10.1063/1.3605664.

[68] K. von Bergmann, M. Bode, A. Kubetzka, M. Heide, S. Blügel, and R. Wiesendanger. Spin-Polarized Electron Scattering at Single Oxygen Adsorbates on a Magnetic Surface. *Physical Review Letters*, 92(046801), 2004. doi:10.1103/PhysRevLett.92.046801.

[69] Uwe Kaiser, Alexander Schwarz, and Roland Wiesendanger. Magnetic exchange force microscopy with atomic resolution. *Nature*, 446(7135):522–525, 2007. doi:10.1038/nature05617.

[70] Nadine Hauptmann, Soumyajyoti Haldar, Tzu Chao Hung, Wouter Jolie, Mara Gutzeit, Daniel Wegner, Stefan Heinze, and Alexander A. Khajetoorians. Quantifying exchange forces of a spin spiral on the atomic scale. *Nature Communications*, 11(1):1–8, dec 2020. ISSN 20411723. doi:10.1038/s41467-020-15024-2. URL `https://doi.org/10.1038/s41467-020-15024-2`.

[71] Sascha Sadewasser and Thilo Glatzel. Kelvin probe force microscopy: MEasureing and Compensating Electrostatic Forces. *Springer Series in Surface Sciences*, 48, 2012. doi:10.1007/978-3-642-22566-6.

[72] H. O. Jacobs, P. Leuchtmann, O. J. Homan, and A. Stemmer. Resolution and contrast in Kelvin probe force microscopy. *Journal of Applied Physics*, 84(3):1168–1173, 1998. doi:10.1063/1.368181.

[73] Roland Wiesendanger. *Scanning Probe Microscopy and Spectroscopy*. Cambridge University Press, 1994. doi:10.1017/CBO9780511524356.

[74] G Binnig and H. Rohrer. Scanning tunnelling microscopy. *Surface Science*, 126(1983): 236–244, 1982. doi:10.1016/0039-6028(83)90716-1.

[75] Mengxi Liu, Shichao Li, Jingyuan Zhou, Zeqi Zha, Jinliang Pan, Xin Li, Jin Zhang, Zhongfan Liu, Yuanchang Li, and Xiaohui Qiu. High-Yield Formation of Graphdiyne Macrocycles through On-Surface Assembling and Coupling Reaction. *ACS Nano*, 12 (12):12612–12618, 2018. doi:10.1021/acsnano.8b07349.

[76] J. Tersoff and D. R. Hamann. Theory of the scanning tunneling microscope. *Physical Review B*, 31(2):805–813, 1985. doi:10.1103/PhysRevB.31.805.

[77] J. Bardeen. Tunneling from a many-particle point of view. *Physical Review Letters*, 6 (2):57–59, 1961. doi:10.1103/PhysRev.131.1083.

[78] R. Smoluchowski. Anisotropy of the electronic work function of metals. *Physical Review*, 60(9):661–674, 1941. ISSN 0031899X. doi:10.1103/PhysRev.60.661.

[79] Joseph E. Griffith. Scanning Tunneling Microscopy. *Annual Review of Material Sciences*, 20:219–244, 1990. doi:10.1146/annurev.ms.20.080190.001251.

[80] N. Egede Christensen and B. Feuerbacher. Volume and surface photoemission from tungsten. I. Calculation of band structure and emission spectra. *Physical Review B*, 10(6):2349–2372, 1974. doi:10.1103/PhysRevB.10.2349.

[81] C. Tserbak, H. M. Polatoglou, and G. Theodorou. Unified approach to the electronic structure of strained Si/Ge superlattices. *Physical Review B*, 47(12):7104–7124, 1993. doi:10.1103/PhysRevB.47.7104.

[82] Germain Salvato-Vallverdu. plotting the density of states and the band diagram using pymatgen and plotly in Python/v3. URL `https://plotly.com/python/v3/ipython-notebooks/density-of-states/`.

[83] D. Kienle, K. H. Bevan, G. C. Liang, L. Siddiqui, J. I. Cerda, and A. W. Ghosh. Extended Hückel theory for band structure, chemistry, and transport. II. Silicon. *Journal of Applied Physics*, 100(4):043715, 2006. doi:10.1063/1.2259820.

[84] Amandine Bellec, Damien Riedel, Gérald Dujardin, Ouarda Boudrioua, Laurent Chaput, Louise Stauffer, and Philippe Sonnet. Electronic properties of the n-doped hydrogenated silicon (100) surface and dehydrogenated structures at 5 K. *Physical Review B*, 80(245434), 2009. doi:10.1103/PhysRevB.80.245434.

[85] Standford Research Systems. About Lock-In Amplifiers: Application Note #3. URL `https://www.thinksrs.com/downloads/pdfs/applicationnotes/AboutLIAs.pdf`.

[86] G Binnig, C. F. Quate, and Ch. Gerber. Atomic Force Microscope. *Physical Review Letters*, 56(930), 1986. doi:10.1103/PhysRevLett.56.930.

[87] M. Lekka and J. Wiltowska-Zuber. Biomedical applications of AFM. *Journal of Physics: Conference Series*, 146, 2009. doi:10.1088/1742-6596/146/1/012023.

[88] Toshio Ando, Takayuki Uchihashi, and Noriyuki Kodera. High-Speed AFM and Applications to Biomolecular Systems. *Annual Review of Biophysics*, 42:393–414, 2013. doi:10.1146/annurev-biophys-083012-130324.

[89] Allard J. Katan and Cees Dekker. High-speed AFM reveals the dynamics of single biomolecules at the nanometer scale. *Cell*, 147(5):979–982, 2011. doi:10.1016/j.cell.2011.11.017.

[90] Franz J Giessibl. The qPlus sensor, a powerful core for the atomic force microscope. *Review of Scientific Instruments*, 90(011101), 2019. doi:10.1063/1.5052264.

[91] Yoshiaki Sugimoto, Pablo Pou, Masayuki Abe, Pavel Jelinek, Rubén Pérez, Seizo Morita, and Óscar Custance. Chemical identification of individual surface atoms by atomic force microscopy. *Nature*, 446:64–67, 2007. doi:10.1038/nature05530.

[92] M. A. Lantz, H. J. Hug, R. Hoffmann, P. J.A. Van Schendel, P. Kappenberger, S. Martin, A. Baratoff, and H. J. Güntherodt. Quantitative measurement of short-range chemical bonding forces. *Science*, 291(5513):2580–2583, 2001. doi:10.1126/science.1057824.

[93] Niko Pavliček and Leo Gross. Generation, manipulation and characterization of molecules by atomic force microscopy. *Nature Reviews Chemistry*, 1(0005), 2017. doi:10.1038/s41570-016-0005.

[94] Bert Voigtländer. *Atomic Force Microscopy*. NanoScience and Technology. Springer International Publishing, 2019. doi:10.1007/978-3-030-13654-3.

[95] Omur E. Dagdeviren and Udo D. Schwarz. Accuracy of tip-sample interaction measurements using dynamic atomic force microscopy techniques: Dependence on oscillation amplitude, interaction strength, and tip-sample distance. *Review of Scientific Instruments*, 90(033707), 2019. doi:10.1063/1.5089634.

[96] Franz J. Giessibl. Principles and Applications of the qPlus Sensor. In S. Morita, F. Giessibl, and R. Wiesendager, editors, *Noncontact Atomic Force Microscopy*, pages 121–142. Springer, Berlin, 2009. doi:10.1007/978-3-642-01495-6_6.

[97] John E. Sader and Suzanne P. Jarvis. Accurate formulas for interaction force and energy in frequency modulation force spectroscopy. *Applied Physics Letters*, 84(1801), 2004. doi:10.1063/1.1667267.

[98] Franz Giessibl. Forces and frequency shifts in atomic-resolution dynamic-force microscopy. *Physical Review B*, 56(24):16010–16015, 1997. doi:10.1103/PhysRevB.56.16010.

[99] Fabio L. Leite, Carolina C. Bueno, Alessandra L. Da Róz, Ervino C. Ziemath, and Osvaldo N. Oliveira. Theoretical models for surface forces and adhesion and their measurement using atomic force microscopy. *International Journal of Molecular Sciences*, 13(10):12773–12856, 2012. doi:10.3390/ijms131012773.

[100] B Y Philip M Morse. Diatomic Molecules According to the Wave Mechanics. II. Vibrational Levels. *Physical Review*, 34(57-64), 1929. doi:10.1103/PhysRev.34.57.

[101] Robert W. Keyes. Bonding and antibonding potentials in group-IV semiconductors. *Physical Review Letters*, 34(21):1334–1337, 1975. doi:10.1103/PhysRevLett.34.1334.

[102] Michel Grandbois, Martin Beyer, Matthias Rief, Hauke Clausen-Schaumann, and Hermann E. Gaub. How strong is a covalent bond. *Science*, 283(5408):1727–1730, 1999. doi:10.1126/science.283.5408.1727.

[103] Christin Yerkes. Average Bond Energies (kJ/mol). URL `http://butane.chem.uiuc.edu/cyerkes/Chem104ACSpring2009/Genchemref/bondenergies.html`.

[104] Wilhelm Melitz, Jian Shen, Andrew C. Kummel, and Sangyeob Lee. Kelvin probe force microscopy and its application. *Surface Science Reports*, 66(1):1–27, 2011. doi:10.1016/j.surfrep.2010.10.001.

[105] S. Hudlet, M. Saint Jean, B. Roulet, J. Berger, and C. Guthmann. Electrostatic forces between metallic tip and semiconductor surfaces. *Journal of Applied Physics*, 77(7): 3308–3314, 1995. doi:10.1063/1.358616.

[106] Leo Polak and Rinke J. Wijngaarden. Quantitative analysis of kelvin probe force microscopy on semiconductors. In *Springer Series in Surface Sciences*, volume 65, pages 227–247. Springer Verlag, 2018. doi:10.1007/978-3-319-75687-5_9.

[107] Wolfram Steurer, Shadi Fatayer, Leo Gross, and Gerhard Meyer. Probe-based measurement of lateral single-electron transfer between individual molecules. *Nature communications*, 6:8353, 2015. doi:10.1038/ncomms9353.

[108] W. Steurer, J. Repp, L. Gross, I. Scivetti, M. Persson, and G. Meyer. Manipulation of the Charge State of Single Au Atoms on Insulating Multilayer Films. *Physical Review Letters*, 114:036801, 2015. doi:10.1103/PhysRevLett.114.036801.

[109] Romain Stomp, Yoichi Miyahara, Sacha Schaer, Qingfeng Sun, Hong Guo, Peter Grutter, Sergei Studenikin, Philip Poole, and Andy Sachrajda. Detection of single-electron charging in an individual InAs quantum dot by noncontact atomic-force microscopy. *Physical Review Letters*, 94(056802), 2005. doi:10.1103/PhysRevLett.94.056802.

[110] T. König, G. H. Simon, H. P. Rust, G. Pacchioni, M. Heyde, and H. J. Freund. Measuring the charge state of point defects on MgO/Ag(001). *Journal of the American Chemical Society*, 131(48):17544–17545, 2009. doi:10.1021/ja908049n.

[111] E. Bussmann and C. C. Williams. Single-electron tunneling force spectroscopy of an individual electronic state in a nonconducting surface. *Applied Physics Letters*, 88 (26):263108, jun 2006. ISSN 00036951. doi:10.1063/1.2209886. URL `http://aip.scitation.org/doi/10.1063/1.2209886`.

[112] Laerte L. Patera, Fabian Queck, Philipp Scheuerer, and Jascha Repp. Mapping orbital changes upon electron transfer with tunnelling microscopy on insulators. *Nature*, 566(7743):245–248, feb 2019. ISSN 14764687. doi:10.1038/s41586-019-0910-3. URL `https://doi.org/10.1038/s41586-019-0910-3`.

[113] Philipp Rahe, Ryan P. Steele, and Clayton C. Williams. Consecutive Charging of a Molecule-on-Insulator Ensemble Using Single Electron Tunnelling Methods. *Nano Letters*, 16(2):911–916, feb 2016. ISSN 15306992. doi:10.1021/acs.nanolett.5b03725. URL `https://pubs.acs.org/sharingguidelines`.

[114] Philipp Scheuerer, Laerte L. Patera, and Jascha Repp. Manipulating and Probing the Distribution of Excess Electrons in an Electrically Isolated Self-Assembled Molecular Structure. *Nano Letters*, 20(3):1839–1845, mar 2020. ISSN 15306992. doi:10.1021/acs.nanolett.9b05063. URL `https://dx.doi.org/10.1021/acs.nanolett.9b05063`.

[115] L Gross, F Mohn, P Liljeroth, J Repp, F Giessibl, and G Meyer. Measuring the charge state of an adatom with noncontact atomic force microscopy. *Science*, 324(5933): 1428–1431, 2009. doi:10.1126/science.1172273.

[116] Ferdinand Huber and Franz J Giessibl. Low noise current preamplifier for qPlus sensor deflection signal detection in atomic force microscopy at room and low temperatures Low noise current preamplifier for qPlus sensor deflection signal detection in atomic force microscopy at room and low temp. 073702, 2017. doi:10.1063/1.4993737.

[117] K. C. Pandey. New π-Bonded Chain Model for Si(111)-(2x1) Surface. *Physical Review Letters*, 47:1913–1917, 1981. doi:10.1103/PhysRevLett.47.1913.

[118] Karl D. Brommer, M. Needels, B. Larson, and J. D. Joannopoulos. Ab initio theory of the Si(111)-(7x7) surface reconstruction: A challenge for massively parallel computation. *Physical Review Letters*, 68:1355–1358, 1992. doi:10.1103/PhysRevLett.68.1355.

[119] Franz J Giessibl. Atomic Resolution of the Si(111)-(7x7) Surface by Atomic Force Microscopy. *Science*, 267(13):68–71, 1995. doi:10.1126/science.267.5194.68.

[120] Masanori Ono, A. Kamoshida, N. Matsuura, E. Ishikawa, T. Eguchi, and Y. Hasegawa. Dimer buckling of the Si(001)2x1 surface below 10 K observed by low-temperature scanning tunneling microscopy. *Physical Review B*, 67(201306(R)), 2003. doi:10.1103/PhysRevB.67.201306.

[121] Robert A. Wolkow. Direct observation of an increase in buckled dimers on Si(001) at low temperature. *Physical Review Letters*, 68(17):2636–2639, 1992. doi:10.1103/PhysRevLett.68.2636.

[122] D H Lee and J D Joannopoulos. Structural Phase Diagrams for the Surface of a Solid :. *Physical Review Letters*, 51(1872), 1983. doi:10.1103/PhysRevLett.51.1872.

[123] A Saxena, E.T. Gawlinski, and J.D. Gunton. Structural Phase Transitions on the Si(100) Surface. *Surface Science*, 160(2):618–640, 1985. doi:10.1016/0039-6028(85)90798-8.

[124] Fredrik Owman. STM study of Si(111)1x1-H surfaces prepared by in situ hydrogen exposure. *Surface Science Letters*, 303(3):L367–L372, 1994. doi:10.1016/0039-6028(94)90772-2.

[125] Wei Ye, Kyoungmin Min, Pamela Peña Martin, Angus A. Rockett, N. R. Aluru, and Joseph W. Lyding. Scanning tunneling spectroscopy and density functional calculation of silicon dangling bonds on the Si(100)-2x1:H surface. *Surface Science*, 609:147–151, 2013. doi:10.1016/j.susc.2012.11.015.

[126] Hiroki Kato, Takumi Taoka, Shozo Suto, Susumu Nishikata, Gen Sazaki, Kazuo Nakajima, Taro Yamada, Ryszard Czajka, Andrzej Wawro, and Atsuo Kasuya. Preparation and Characterization of Ultraclean H:Si(111)-(1x1) Surfaces Studied by HREELS, AFM and STM-STS. *e-Journal of Surface Science and Nanotechnology*, 7:557–562, 2009. doi:10.1380/ejssnt.2009.557.

[127] G S Higashi, Y J Chabal, G W Trucks, and Krishnan Raghavachari. Ideal hydrogen termination of the Si (111) surface. *Applied Physics Letters*, 56(7), 1990. doi:10.1063/1.102728.

[128] Kazutoshi Kaji, Shueh Lin Yau, and Kingo Itaya. Atomic scale etching processes of n-Si(111) in NH4F solutions: In situ scanning tunneling microscopy. *Journal of Applied Physics*, 78(9):5727–5733, 1995. doi:10.1063/1.359633.

[129] Hiroki Kato, Takumi Taoka, Susumu Nishikata, Gen Sazaki, Taro Yamada, Ryszard Czajka, Andrzej Wawro, Kazuo Nakajima, Atsuo Kasuya, and Shozo Suto. Preparation of an Ultraclean and Atomically Controlled Hydrogen-Terminated Si(111)-(1x1) Surface Revealed by High Resolution Electron Energy Loss Spectroscopy, Atomic Force Microscopy, and Scanning Tunneling Microscopy: Aqueous NH 4 F

Etching Process of. *Japanese Journal of Applied Physics*, 46(9A):5701–5705, 2007. doi:10.1143/JJAP.46.5701.

[130] Philippe Allongue, Catherine Henry De Villeneuve, Sylvie Morin, Rabah Boukherroub, and Danial D.M. Wayner. Preparation of flat H-Si(111) surfaces in 40% NH4F revisited. *Electrochimica Acta*, 45(28):4591–4598, 2000. doi:10.1016/S0013-4686(00)00610-1.

[131] R M Feenstra, Y Dong, M P Semtsiv, and W T Masselink. Influence of tip-induced band bending on tunnelling spectra of semiconductor surfaces. *Nanotechnology*, 18(4): 044015, 2007. doi:10.1088/0957-4484/18/4/044015.

[132] R. M. Feenstra. Electrostatic potential for a hyperbolic probe tip near a semiconductor. *Journal of Vacuum Science & Technology B: Microelectronics and Nanometer Structures*, 21(5):2080, sep 2003. ISSN 0734211X. doi:10.1116/1.1606466. URL `http://scitation.aip.org/content/avs/journal/jvstb/21/5/10.1116/1.1606466`.

[133] R. M. Feenstra. SEMITIP, version 6, 2011. URL `http://www.andrew.cmu.edu/user/feenstra/semitip{_}v6/`.

[134] Jing Wang, Lai Jin, Hua Zhou, Huixia Fu, Chuangye Song, Sheng Meng, and Jinxing Zhang. Direct imaging of surface states hidden in the third layer of Si (111)-7x7 surface by p_{z}-wave tip. *Appl. Phys. Lett*, 113(3):31604, 2018. doi:10.1063/1.5038954.

[135] A Sweetman, R Danza, S Gangopadhyay, and P Moriarty. Imaging and manipulation of the Si(100) surface by small-amplitude NC-AFM at zero and very low applied bias. *Journal of Physics: Condensed Matter*, 24(8):084009, 2012. doi:10.1088/0953-8984/24/8/084009.

[136] C. Weiss, C. Wagner, C. Kleimann, M. Rohlfing, F. S. Tautz, and R. Temirov. Imaging Pauli Repulsion in Scanning Tunneling Microscopy. *Physical Review Letters*, 105(8): 086103, 2010. doi:10.1103/PhysRevLett.105.086103.

[137] Christian Weiss, Christian Wagner, Ruslan Temirov, and F. Stefan Tautz. Direct Imaging of Intermolecular Bonds in Scanning Tunneling Microscopy. *Journal of the American Chemical Society*, 132(34):11864–11865, sep 2010. doi:10.1021/ja104332t. URL `https://pubs.acs.org/doi/10.1021/ja104332t`.

[138] J I Martínez, E Abad, C González, F Flores, and J Ortega. Improvement of Scanning Tunneling Microscopy Resolution with H-Sensitized Tips. *Physical Review Letters*, 108 (246102), 2012. doi:10.1103/PhysRevLett.108.246102.

[139] Anna Campbellová, Martin Ondráček, Pablo Pou, Rubén Pérez, Petr Klapetek, and Pavel Jelínek. 'Sub-atomic' resolution of non-contact atomic force microscope images induced by aheterogeneous tip structure: A density functional theory study. *Nanotechnology*, 22(29), 2011. doi:10.1088/0957-4484/22/29/295710.

[140] Hatem Labidi, Mohammad Koleini, Taleana Huff, Mark Salomons, Martin Cloutier, Jason Pitters, and Robert A Wolkow. Indications of chemical bond contrast in AFM images of a hydrogen-terminated silicon surface. *Nature Communications*, 8(14222), 2017. doi:10.1038/ncomms14222.

[141] Jarvis Sp, A M Sweetman, L Kantorovich, E Mcglynn, and P Moriarty. Pauli's Principle in Probe Microscopy. In Christian Joachim, editor, *Advances in Atom and Signle Molecule Machines*, chapter 1. 2014. ISBN 2193-9691.

[142] Ayhan Yurtsever, Yoshiaki Sugimoto, Hideki Tanaka, Masayuki Abe, Seizo Morita, Martin Ondráček, Pablo Pou, Rubén Pérez, and Pavel Jelínek. Force mapping on a partially H-covered Si(111)-(7x7) surface: Influence of tip and surface reactivity. *Physical Review B*, 87(155403), 2013. doi:10.1103/PhysRevB.87.155403.

[143] P. Pou, S. A. Ghasemi, P. Jelinek, T. Lenosky, S. Goedecker, and R. Perez. Structure and stability of semiconductor tip apexes for atomic force microscopy. *Nanotechnology*, 20(26), 2009. doi:10.1088/0957-4484/20/26/264015.

[144] Adam Sweetman, Sam Jarvis, Rosanna Danza, and Philip Moriarty. Effect of the tip state during qPlus noncontact atomic force microscopy of Si(100) at 5 K: Probing the probe. *Beilstein J. Nanotechnol*, 3:25–32, 2012. doi:10.3762/bjnano.3.3.

[145] Morten Møller, Samuel P Jarvis, Laurent Guérinet, Peter Sharp, Richard Woolley, Philipp Rahe, and Philip Moriarty. Automated extraction of single H atoms with STM: tip state dependency. *Nanotechnology*, 28(7), 2017. doi:10.1088/1361-6528/28/7/075302.

[146] Rubén Pérez, Michael C. Payne, Ivan Štich, and Kiyoyuki Terakura. Role of Covalent Tip-Surface Interactions in Noncontact Atomic Force Microscopy on Reactive Surfaces. *Physical Review Letters*, 78:678–681, 1997. doi:10.1103/PhysRevLett.78.678.

[147] Niko Pavliček, Zsolt Majzik, Gerhard Meyer, and Leo Gross. Tip-induced passivation of dangling bonds on hydrogenated Si(100)-2x1. *Applied Physics Letters*, 111(053104), 2017. doi:10.1063/1.4989749.

[148] Joachim Welker, Alfred John Weymouth, and Franz J. Giessibl. The influence of chemical bonding configuration on atomic identification by force spectroscopy. *ACS Nano*, 7(8):7377–7382, 2013. doi:10.1021/nn403106v.

[149] Hongqian Sang, Samuel P. Jarvis, Zhichao Zhou, Peter Sharp, Philip Moriarty, Jianbo Wang, Yu Wang, and Lev Kantorovich. Identifying tips for intramolecular NC-AFM imaging via in situ fingerprinting. *Scientific Reports*, 4(6678), 2014. doi:10.1038/srep06678.

[150] A. S. Foster, A. Y. Gal, J. D. Gale, Y. J. Lee, R. M. Nieminen, and A. L. Shluger. Interaction of Silicon Dangling Bonds with Insulating Surfaces. *Physical Review Letters*, 92(036101), 2004. doi:10.1103/PhysRevLett.92.036101.

[151] A. J. Weymouth, T. Wutscher, J. Welker, T. Hofmann, and F. J. Giessibl. Phantom force induced by tunneling current: A characterization on si(111). *Physical Review Letters*, 106(226801), 2011. doi:10.1103/PhysRevLett.106.226801.

[152] H. Özgür Özer, Simon J. O'Brien, and John B. Pethica. Local force gradients on Si(111) during simultaneous scanning tunneling/atomic force microscopy. *Applied Physics Letters*, 90(133110), 2007. doi:10.1063/1.2717115.

[153] Markus Ternes, César González, Christopher P. Lutz, Prokop Hapala, Franz J. Giessibl, Pavel Jelínek, and Andreas J. Heinrich. Interplay of conductance, force, and structural change in metallic point contacts. *Physical Review Letters*, 106(016802), 2011. doi:10.1103/PhysRevLett.106.016802.

[154] Adam Sweetman and Andrew Stannard. Uncertainties in forces extracted from non-contact atomic force microscopy measurements by fitting of long-range background forces. *Beilstein Journal of Nanotechnology*, 5:386–393, 2014. doi:10.3762/bjnano.5.45.

[155] Mohammad Rashidi, Wyatt Vine, Thomas Dienel, Lucian Livadaru, Jacob Retallick, Taleana Huff, Konrad Walus, and Robert A Wolkow. Initiating and Monitoring the Evolution of Single Electrons Within Atom-Defined Structures. *Physical Review Letters*, 121, 2018. doi:10.1103/PhysRevLett.121.166801.

[156] A Sweetman, S Jarvis, R Danza, J Bamidele, L Kantorovich, and P Moriarty. Manipulating Si(100) at 5 K using qPlus frequency modulated atomic force microscopy: Role of defects and dynamics in the mechanical switching of atoms. *PHYSICAL REVIEW B*, 84:85426, 2011. doi:10.1103/PhysRevB.84.085426. URL `https://journals-aps-org.login.ezproxy.library.ualberta.ca/prb/pdf/10.1103/PhysRevB.84.085426`.

[157] Peter Sharp, Sam Jarvis, Richard Woolley, Adam Sweetman, Lev Kantorovich, Chris Pakes, and Philip Moriarty. Identifying passivated dynamic force microscopy tips on H:Si(100). *Applied Physics Letters*, 100(233120), 2012. doi:10.1063/1.4726086.

[158] Adam Sweetman, Julian Stirling, Samuel Paul Jarvis, Philipp Rahe, and Philip Moriarty. Measuring the reactivity of a silicon-terminated probe. *Physical Review B*, 94:115440, 2016. doi:10.1103/PhysRevB.94.115440.

[159] J. W. Lyding, T-C. Shen, G. C. Abeln, C. Wang, and J. R. Tucker. Nanoscale patterning and selective chemistry of silicon surfaces by ultrahigh-vacuum scanning tunneling microscopy. *Nanotechnology*, 7(2):128–133, 1996. doi:10.1088/0957-4484/7/2/006.

[160] Laetitia Soukiassian, Andrew J. Mayne, Marilena Carbone, and Gérald Dujardin. Atomic-scale desorption of H atoms from the Si(100)-2x1:H surface: Inelastic electron interactions. *Physical Review B*, 68(3):035303, 2003. doi:10.1103/PhysRevB.68.035303.

[161] T. C. Shen, C. Wang, G. C. Abeln, J. R. Tucker, J. W. Lyding, Ph Avouris, and R. E. Walkup. Atomic-scale desorption through electronic and vibrational excitation mechanisms. *Science*, 268(5217):1590–1592, 1995. doi:10.1126/science.268.5217.1590.

[162] E. T. Foley, A. F. Kam, J. W. Lyding, and Ph Avouris. Cryogenic UHV-STM study of hydrogen and deuterium desorption from Si(100). *Physical Review Letters*, 80(6): 1336–1339, 1998. doi:10.1103/PhysRevLett.80.1336.

[163] M. Baseer Haider, Jason L. Pitters, Gino A. Dilabio, Lucian Livadaru, Josh Y. Mutus, and Robert A. Wolkow. Controlled coupling and occupation of silicon atomic quantum dots at room temperature. *Physical Review Letters*, 102(046805), 2009. doi:10.1103/PhysRevLett.102.046805.

[164] T H Nguyen, G Mahieu, M Berthe, B Grandidier, C Delerue, D Stiévenard, and Ph Ebert. Coulomb Energy Determination of a Single Si Dangling Bond. *Physical Review Letters*, 105(226404), 2010. doi:10.1103/PhysRevLett.105.226404.

[165] M. Berthe, A. Urbieta, L. Perdigão, B. Grandidier, D. Deresmes, C. Delerue, D. Stiévenard, R. Rurali, N. Lorente, L. Magaud, and P. Ordejon. Electron transport via local polarons at interface atoms. *Physical Review Letters*, 97(206801), 2006. doi:10.1103/PhysRevLett.97.206801.

[166] Marco Taucer, Lucian Livadaru, Paul G. Piva, Roshan Achal, Hatem Labidi, Jason L. Pitters, and Robert A. Wolkow. Single-electron dynamics of an atomic silicon quantum

dot on the H-Si (100)- (2x1) surface. *Physical Review Letters*, 112(256801), 2014. doi:10.1103/PhysRevLett.112.256801.

[167] Mohammad Rashidi, Marco Taucer, Isil Ozfidan, Erika Lloyd, and Hatem Labidi. Time-Resolved Imaging of Negative Differential Resistance on the Atomic Scale. *Physical Review Letters*, 117(276805), 2016. doi:10.1103/PhysRevLett.117.276805.

[168] Peter Scherpelz and Giulia Galli. Optimizing surface defects for atomic-scale electronics: Si dangling bonds. *Physical Review Materials*, 1(021602(R)), 2017. doi:10.1103/PhysRevMaterials.1.021602.

[169] Erika Lloyd. *Time Resolved Measurments of Dangling Bonds and Surface Structures*. PhD thesis, University of Alberta, 2017.

[170] X. de la Broïse, C. Delerue, M. Lannoo, B. Grandidier, and D. Stiévenard. Theory of scanning tunneling microscopy of defects on semiconductor surfaces. *Physical Review B*, 61(2138), 2000. doi:10.1103/PhysRevB.61.2138.

[171] Walter A. Harrison. Surface reconstruction on semiconductors. *Surface Science*, 55(1): 1–19, 1976. doi:10.1016/0039-6028(76)90372-1.

[172] John E. Northrup. Effective correlation energy of a Si dangling bond calculated with the local-spin-density approximation. *Physical Review B*, 40(5875(R)), 1989. doi:10.1103/PhysRevB.40.5875.

[173] S. R. Schofield, P. Studer, C. F. Hirjibehedin, N. J. Curson, G. Aeppli, and D. R. Bowler. Quantum engineering at the silicon surface using dangling bonds. *Nature Communications*, 4(1649):1–7, 2013. doi:10.1038/ncomms2679.

[174] Hiroyo Kawai, Olga Neucheva, Tiong Leh Yap, Christian Joachim, and Mark Saeys. Electronic characterization of a single dangling bond on n- and p-type Si(001)-(2x1):H. *Surface Science*, 645:88–92, 2016. doi:10.1016/j.susc.2015.11.001.

[175] Taleana Huff. *Atomic Electronics With Silicon Dangling Bonds: Error Correction, Logical Gates, and Electrostatic Environment*. PhD thesis, University of Alberta, 2020.

[176] Marek Kolmer, Szymon Godlewski, Rafal Zuzak, Mateusz Wojtaszek, Caroline Rauer, Aurélie Thuaire, Jean-Michel Hartmann, Hubert Moriceau, Christian Joachim, and Marek Szymonski. Atomic scale fabrication of dangling bond structures on hydrogen passivated Si(001) wafers processed and nanopackaged in a clean room environment. *Applied Surface Science*, 288:83–89, 2014. doi:10.1016/J.APSUSC.2013.09.124.

[177] Taleana R Huff, Hatem Labidi, Mohammad Rashidi, Mohammad Koleini, Roshan Achal, Mark H Salomons, and Robert A Wolkow. Atomic White-Out: Enabling Atomic Circuitry through Mechanically Induced Bonding of Single Hydrogen Atoms to a Silicon Surface. *ACS Nano*, 11(9):8636–8642, 2017. doi:10.1021/acsnano.7b04238.

[178] Moh'd Rezeq, Jason Pitters, and Robert Wolkow. Tungsten nanotip fabrication by spatially controlled field-assisted reaction with nitrogen. *Journal of Chemical Physics*, 124(204716), 2006. doi:10.1063/1.2198536.

[179] M. Dürr and U. Höfer. Hydrogen diffusion on silicon surfaces. *Progress in Surface Science*, 88(1):61–101, 2013. doi:10.1016/J.PROGSURF.2013.01.001.

[180] Mohammad Rashidi and Robert A Wolkow. Autonomous Scanning Probe Microscopy in situ Tip Conditioning through Machine Learning. *ACS Nano*, 12(6):5185–5189, 2018. doi:10.1021/acsnano.8b02208.

[181] Wiener Norbert. *Cybernetics or Control and Communication in the Animal andthe Machine*. MIT press, 2019. ISBN 9780262537841.

[182] Zhilu Chen and Xinming Huang. End-To-end learning for lane keeping of self-driving cars. In *2017 IEEE Intelligent Vehicles Symposium (IV)*, pages 1856–1860. IEEE, 2017. doi:10.1109/IVS.2017.7995975.

[183] German Ros, Sebastian Ramos, Manuel Granados, Amir Bakhtiary, David Vazquez, and Antonio M Lopez. Vision-based Offline-Online Perception Paradigm for Autonomous Driving. In *IEEE Winter Conference on Applications of Computer Vision*, 2015. doi:10.1109/WACV.2015.38.

[184] German Ros, Laura Sellart, Joanna Materzynska, David Vazquez, and Antonio M Lopez. The SYNTHIA Dataset: A Large Collection of Synthetic Images for Semantic Segmentation of Urban Scenes. In *Conference on Computer Vision and Pattern Recognition (CVPR)*, 2016. doi:10.1109/CVPR.2016.352.

[185] Marvin Teichmann, Michael Weber, Marius Zollner, Roberto Cipolla, and Raquel Urtasun. MultiNet: Real-time Joint Semantic Reasoning for Autonomous Driving. In *2018 IEEE Intelligent Vehicles Symposium (IV)*, pages 1013–1020. IEEE, 2018. doi:10.1109/IVS.2018.8500504.

[186] Fausto Milletari, Nassir Navab, and Seyed-Ahmad Ahmadi. V-Net: Fully Convolutional Neural Networks for Volumetric Medical Image Segmentation. In *2016 Fourth International Conference on 3D Vision (3DV)*, pages 565–571. IEEE, 2016. doi:10.1109/3DV.2016.79.

[187] Geert Litjens, Thijs Kooi, Babak Ehteshami Bejnordi, Arnaud Arindra Adiyoso Setio, Francesco Ciompi, Mohsen Ghafoorian, Jeroen A.W.M. van der Laak, Bram van Ginneken, and Clara I. Sánchez. A survey on deep learning in medical image analysis. *Medical Image Analysis*, 42:60–88, 2017. doi:10.1016/J.MEDIA.2017.07.005.

[188] Eli Gibson, Wenqi Li, Carole Sudre, Lucas Fidon, Dzhoshkun I. Shakir, Guotai Wang, Zach Eaton-Rosen, Robert Gray, Tom Doel, Yipeng Hu, Tom Whyntie, Parashkev Nachev, Marc Modat, Dean C. Barratt, Sébastien Ourselin, M. Jorge Cardoso, and Tom Vercauteren. NiftyNet: a deep-learning platform for medical imaging. *Computer Methods and Programs in Biomedicine*, 158:113–122, 2018. doi:10.1016/J.CMPB.2018.01.025.

[189] David Silver, Aja Huang, Chris J. Maddison, Arthur Guez, Laurent Sifre, George van den Driessche, Julian Schrittwieser, Ioannis Antonoglou, Veda Panneershelvam, Marc Lanctot, Sander Dieleman, Dominik Grewe, John Nham, Nal Kalchbrenner, Ilya Sutskever, Timothy Lillicrap, Madeleine Leach, Koray Kavukcuoglu, Thore Graepel, and Demis Hassabis. Mastering the game of Go with deep neural networks and tree search. *Nature*, 529:484–489, 2016. doi:10.1038/nature16961.

[190] Li Deng and Xiao Li. Machine learning paradigms for speech recognition: An overview. *IEEE Transactions on Audio, Speech and Language Processing*, 21(5):1060–1089, 2013. doi:10.1109/TASL.2013.2244083.

[191] Jonathan Schmidt, Mário R. G. Marques, Silvana Botti, and Miguel A. L. Marques. Recent advances and applications of machine learning in solid-state materials science. *npj Computational Materials*, 5(83), 2019. doi:10.1038/s41524-019-0221-0.

[192] Sam Maes, Karl Tuyls, Bram Vanschoenwinkel, and Bernard Manderick. Credit Card Fraud Detection using Fuzzy Logic and Neural Networks. In *CNS '16: Proceedings of the 19th Communications & Networking Symposium*, number 7, pages 1–5, 2016. doi:10.5555/2962686.2962693.

[193] O. Gordon, P. D'Hondt, L. Knijff, S. E. Freeney, F. Junqueira, P. Moriarty, and I. Swart. Scanning tunneling state recognition with multi-class neural network ensembles. *Review of Scientific Instruments*, 90:103704, 2019. doi:10.1063/1.5099590.

[194] A. Krull, P. Hirsch, C. Rother, A. Schiffrin, and C. Krull. Artificial-intelligence-driven scanning probe microscopy. *Communications Physics*, 3(54), 2020. doi:10.1038/s42005-020-0317-3.

[195] Benjamin Alldritt, Prokop Hapala, Niko Oinonen, Fedor Urtev, Ondrej Krejci, Filippo Federici Canova, Juho Kannala, Fabian Schulz, Peter Liljeroth, and Adam S. Foster. Automated structure discovery in atomic force microscopy. *Science Advances*, 6(9), feb 2020. doi:10.1126/sciadv.aay6913.

[196] Muhammad Usman, Yi Zheng Wong, Charles D. Hill, and Lloyd C. L. Hollenberg. Framework for atomic-level characterisation of quantum computer arrays by machine learning. *npj Computational Materials*, 6(19), 2020. doi:10.1038/s41524-020-0282-0.

[197] Giuseppe Bonaccorso. *Machine learning algorithms : popular algorithms for data science and machine learning*. Packt Publishing, Birmingham, UK, 2nd edition, 2018. ISBN 9781789345483.

[198] Abhishek Vijayvargia. *Machine Learning with Python: An Approach to Applied Machine Learning*. Manish Jain for BPB Publications, New Dehli, first edit edition, 2018. ISBN 9789386551931.

[199] Ian Goodfellow, Yoshua Bengio, and Aaron Courville. *Deep Learning*. The MIT Press, Cambridge, 1st edition, 2016. ISBN 9780262035613.

[200] Diederik P. Kingma and Jimmy Ba. Adam: A Method for Stochastic Optimization. *arXiv*, 2014. URL `http://arxiv.org/abs/1412.6980`.

[201] Yann LeCun, Corinna Cortes, and Christopher J. C. Burges. MNIST handwritten digit database. URL `http://yann.lecun.com/exdb/mnist/`.

[202] Alex Krizhevsky, Vinod Nair, and Geoffrey Hinton. CIFAR-10 and CIFAR-100 datasets. URL `https://www.cs.toronto.edu/{~}kriz/cifar.html`.

[203] D. Sculley. Web-scale k-means clustering. *Proceedings of the 19th International Conference on World Wide Web*, pages 1177–1178, 2010. doi:10.1145/1772690.1772862.

[204] Scikit-learn. Clustering, 2019. URL `https://scikit-learn.org/stable/modules/clustering.html`.

[205] David G. Lowe. Distinctive Image Features from Scale-Invariant Keypoints. *International Journal of Computer Vision*, 60(2):91–110, 2004. doi:10.1023/B:VISI.0000029664.99615.94.

[206] Navneet Dalal and Bill Triggs. Histograms of Oriented Gradients for Human Detection. In *International Conference on Computer Vision and Pattern Recognition (CVPR '05)*, pages 886–893, San Diego, United States, 2005. doi:10.1109/CVPR.2005.177.

[207] Cyril Ray and Abedrrahim Sekkaki Othman Benammar. Mean shift: A robust approach toward feature space analysis. *IEEE Transactions on pattern analysis and machine intelligence*, 24(5):603–619, 2002. doi:10.1109/34.1000236.

[208] Richard Sutton and Andrew Barto. *Reinforcement Learning: An Introduction*. MIT Press, 2nd edition, 2018. ISBN 9780262039246.

[209] Mohammad Hadi Modarres, Rossella Aversa, Stefano Cozzini, Regina Ciancio, Angelo Leto, and Giuseppe Piero Brandino. Neural Network for Nanoscience Scanning Electron Microscope Image Recognition. *Scientific Reports*, 7(13282), 2017. doi:10.1038/s41598-017-13565-z.

[210] Maxim Ziatdinov, Artem Maksov, and Sergei V. Kalinin. Learning surface molecular structures via machine vision. *npj Computational Materials*, 3(31), 2017. doi:10.1038/s41524-017-0038-7.

[211] Ross Kindermann, J. Laurie Snell, and American Mathematical Society. *Markov random fields and their applications*. American Mathematical Society, 1980. ISBN 0821850016.

[212] Maxim Ziatdinov, Ondrej Dyck, Artem Maksov, Xufan Li, Xiahan Sang, Kai Xiao, Raymond R. Unocic, Rama Vasudevan, Stephen Jesse, and Sergei V. Kalinin. Deep Learning of Atomically Resolved Scanning Transmission Electron Microscopy Images: Chemical Identification and Tracking Local Transformations. *ACS Nano*, 11(12): 12742–12752, 2017. doi:10.1021/acsnano.7b07504.

[213] Oscar Contreras Carrasco. Gaussian Mixture Models Explained, 2019. URL https://towardsdatascience.com/gaussian-mixture-models-explained-6986aaf5a95.

[214] Oliver M Gordon, Filipe L Q Junqueira, and Philip J Moriarty. Embedding human heuristics in machine-learning-enabled probe microscopy. *Machine Learning: Science and Technology*, 1(1):015001, 2020. doi:10.1088/2632-2153/ab42ec.

[215] Sepp Hochreiter and Jürgen Schmidhuber. Long Short-Term Memory. *Neural Computation*, 9(8):1735–1780, 1997. doi:10.1162/neco.1997.9.8.1735.

[216] Philipp Leinen, Malte Esders, Kristof T. Schütt, Christian Wagner, Klaus-Robert Müller, and F. Stefan Tautz. Autonomous robotic nanofabrication with reinforcement learning. *Science Advances*, 6(36), 2020. doi:10.1126/sciadv.abb6987.

[217] Jessica Thomas. 50 Years of Physical Review B: Solid Hits in Condensed Matter Research. *Physics*, 13:29, 2020. doi:10.1103/Physics.13.29.

[218] G. Binnig, H. Rohrer, Ch. Gerber, and E. Weibel. 7x7 Reconstruction on Si(111) Resolved in Real Space. *Physical Review Letters*, 50:120–123, 1983. doi:10.1103/PhysRevLett.50.120.

[219] R J Hamers, R M Tromp, and J E Demuth. Scanning tunneling microscopy of Si(001). *Physical Review B*, 34(5343), 1986. doi:10.1103/PhysRevB.34.5343.

[220] T. V. Pavlova. Hydrogen inserted into the Si(100)-2x1-H surface: A first-principles study. *arXiv*, 2020. URL `http://arxiv.org/abs/2006.16371`.

[221] Enrico Prati and Takahiro Shinada. Atomic scale devices: Advancements and directions. In *IEEE International Electron Devices Meeting (IEDM)*, pages 1.2.1–1.2.4, San Francisco, 2014. doi:10.1109/IEDM.2014.7046961.

[222] J L O'Brien, S R Schofield, M Y Simmons, R G Clark, A S Dzurak, N J Curson, B E Kane, N S Mcalpine, M E Hawley, and G W Brown. Towards the fabrication of phosphorus qubits for a silicon quantum computer. *Physical Review B*, 64(161401(R)), 2001. doi:10.1103/PhysRevB.64.161401.

[223] Maxim Ziatdinov, Udi Fuchs, James H. G. Owen, John N. Randall, and Sergei V. Kalinin. Robust multi-scale multi-feature deep learning for atomic and defect identification in Scanning Tunneling Microscopy on H-Si(100) 2x1 surface. *arXiv*, 2020. URL http://arxiv.org/abs/2002.04716.

[224] D.J. J. Chadi. Atomic and Electronic Structures of Reconstructed Si(100) Surfaces. *Physical Review Letters*, 43:43–47, 1979. doi:10.1103/PhysRevLett.43.43.

[225] R J Hamers and U K Köhler. Determination of the local electronic structure of atomic-sized defects on Si(001) by tunneling spectroscopy. *Journal of Vacuum Science and Technology*, 7(2854), 1989. doi:10.1116/1.576158.

[226] M. Z. Hossain, Y Yamashita, K Mukai, and J Yoshinobu. Model for C defect on Si(100): The dissociative adsorption of a single water molecule on two adjacent dimers. *Physical Review B*, 67(153307), 2003. doi:10.1103/PhysRevB.67.153307.

[227] Sang-Yong Yu, Hanchul Kim, and Ja-Yong Koo. Extrinsic Nature of Point Defects on the Si(001) Surface: Dissociated Water Molecules. *Physical Review Letters*, 100 (036107), 2008. doi:10.1103/PhysRevLett.100.036107.

[228] Pavel Sobotík and Ivan Ošt'ádal. Transformations of C-type defects on Si(100)-2x1 surface at room temperature-STM/STS study. *Surface Science*, 602(17):2835–2839, 2008. doi:10.1016/j.susc.2008.07.015.

[229] John J.J. Boland. Structure of the H-Saturated Si(100) Surface. *Physical Review Letters*, 65(3325), 1990. doi:10.1103/PhysRevLett.65.3325.

[230] John J. Boland. Scanning tunnelling microscopy of the interaction of hydrogen with silicon surfaces. *Advances in Physics*, 42(2):129–171, 1993. doi:10.1080/00018739300101474.

[231] John J. Boland. Role of bond-strain in the chemistry of hydrogen on the Si(100) surface. *Surface Science*, 261(1-3):17–28, 1992. doi:10.1016/0039-6028(92)90214-Q.

[232] Robert J. Hamers and Yajun Wang. Atomically-Resolved Studies of the Chemistry and Bonding at Silicon Surfaces. *Chemical Reviews*, 96(4):1261–1290, 1996. doi:10.1021/CR950213K.

[233] Prokop Hapala, Georgy Kichin, Christian Wagner, F. Stefan Tautz, Ruslan Temirov, and Pavel Jelinek. Mechanism of high-resolution STM/AFM imaging with functionalized tips. *Physical Review B*, 90(085421), 2014. doi:10.1103/PhysRevB.90.085421.

[234] Prokop Hapala. Probe Particle Model, 2014. URL `https://github.com/ProkopHapala/ProbeParticleModel`.

[235] M Kuzmin, J Mäkelä, J Lehtiö, M Yasir, M Tuominen, Z S Jahanshah Rad, A Lahti, M P J Punkkinen, P Laukkanen, and K Kokko. Imaging empty states on the Ge(100) surface at 12K. *Physical Review B*, 98(155322), 2018. doi:10.1103/PhysRevB.98.155322.

[236] Leo Gross, Fabian Mohn, Nikolaj Moll, Peter Liljeroth, and Gerhard Meyer. The Chemical Structure of a Molecule Resolved by Atomic Force Microscopy. *Science*, 325 (5944):1110–1114, 2009. doi:10.1126/science.1176210.

[237] Harry Mönig, Milica Todorović, Mehmet Z. Baykara, Todd C. Schwendemann, Lucía Rodrigo, Eric I. Altman, Rubén Pérez, and Udo D. Schwarz. Understanding Scanning Tunneling Microscopy Contrast Mechanisms on Metal Oxides: A Case Study. *ACS Nano*, 7(11):10233–10244, 2013. doi:10.1021/nn4045358.

[238] Harry Mönig, Saeed Amirjalayer, Alexander Timmer, Zhixin Hu, Lacheng Liu, Oscar Díaz Arado, Marvin Cnudde, Cristian Alejandro Strassert, Wei Ji, Michael Rohlfing, and Harald Fuchs. Quantitative assessment of intermolecular interactions by atomic force microscopy imaging using copper oxide tips. *Nature Nanotechnology*, 13:371–375, 2018. doi:10.1038/s41565-018-0104-4.

[239] Fabian Mohn, Bruno Schuler, Leo Gross, and Gerhard Meyer. Different tips for high-resolution atomic force microscopy and scanning tunneling microscopy of single molecules. *Applied Physics Letters*, 102(7):1–5, 2013. doi:10.1063/1.4793200.

[240] Georgy Kichin, Christian Weiss, Christian Wagner, F Stefan Tautz, and Ruslan Temirov. Single Molecule and Single Atom Sensors for Atomic Resolution Imaging of Chemically Complex Surfaces. *Journal of the American Chemical Society*, 133(42): 16847–16851, 2011. doi:10.1021/ja204624g.

[241] R Temirov, S Soubatch, O Neucheva, A C Lassise, and F S Tautz. A novel method achieving ultra-high geometrical resolution in scanning tunnelling microscopy. *New Journal of Physics*, 10(053012), 2008. doi:10.1088/1367-2630/10/5/053012.

[242] Violeta Simic-Milosevic, Michael Mehlhorn, and Karina Morgenstern. Imaging the Bonds of Dehalogenated Benzene Radicals on Cu(111) and Au(111). *ChemPhysChem*, 17(17):2679–2685, 2016. doi:10.1002/cphc.201600495.

[243] Yoshiaki Sugimoto and Jo Onoda. Force spectroscopy using a quartz length-extension resonator. *Applied Physics Letters*, 115(173104), 2019. doi:10.1063/1.5112062.

[244] Kenji Hata, Shoji Yoshida, and Hidemi Shigekawa. p(2x2) Phase of Buckled Dimers of Si(100) Observed on n -Type Substrates below 40 K by Scanning Tunneling Microscopy. *Physical Review Letters*, 89(286104), 2002. doi:10.1103/PhysRevLett.89.286104.

[245] Keisuke Sagisaka, Daisuke Fujita, and Giyuu Kido. Phase Manipulation between c(4x2) and p(2x2) on the Si(100) Surface at 4.2 K. *Physical Review Letters*, 91(146103), 2003. doi:10.1103/PhysRevLett.91.146103.

[246] H. Shigekawa, K. Miyake, M. Ishida, S. Ozawa, and K. Hata. Phase Defects on Si(100) Surface, Studied by Scanning Tunnelling Microscopy. *Defect and Diffusion Forum*, 160-161:57–64, may 1998. doi:10.4028/www.scientific.net/DDF.160-161.57.

[247] Mads Engelund, Szymon Godlewski, Marek Kolmer, Rafał Zuzak, Bartosz Such, Thomas Frederiksen, Marek Szymonski, and Daniel Sá Nchez-Portal. The butterfly-a well-defined constant-current topography pattern on Si(001):H and Ge(001):H resulting from current-induced defect fluctuations. *Physical Chemistry Chemical Physics*, 18:19309–19317, 2016. doi:10.1039/c6cp04031d.

[248] Hatem Labidi, Marco Taucer, Mohammad Rashidi, Mohammad Koleini, Lucian Livadaru, Jason Pitters, Martin Cloutier, Mark Salomons, and Robert A. Wolkow. Scanning tunneling spectroscopy reveals a silicon dangling bond charge state transition. *New Journal of Physics*, 17(073023), 2015. doi:10.1088/1367-2630/17/7/073023.

[249] Kitiphat Sinthiptharakoon, Steven R Schofield, Philipp Studer, Veronika BrázdováBr, Cyrus F Hirjibehedin, David R Bowler, and Neil J Curson. Investigating individual arsenic dopant atoms in silicon using low-temperature scanning tunnelling microscopy. *Journal of Physics: Condensed Matter*, 26(1), 2014. doi:10.1088/0953-8984/26/1/012001.

[250] Lequn Liu, Jixin Yu, and J W Lyding. Subsurface dopant-induced features on the Si(100)2x1:H surface: fundamental study and applications. *IEEE Transactions On Nanotechnology*, 1(4):176–183, 2002. doi:10.1109/TNANO.2002.807391.

[251] Lequn Liu, Jixin Yu, and J W Lyding. Atom-resolved three-dimensional mapping of boron dopants in Si(100) by scanning tunneling microscopy. *Applied Physics Letters*, 78:386, 2001. doi:10.1063/1.1339260.

[252] C Domke, Ph Ebert, M Heinrich, and K. Urban. Microscopic identification of the compensation mechanism in Si-doped GaAs. *Physical Review B*, 54(15), 1996. doi:10.1103/PhysRevB.54.10288.

[253] D. H. Lee and J. A. Gupta. Tunable Field Control Over the Binding Energy of Single Dopants by a Charged Vacancy in GaAs. *Science*, 330(6012):1807–1810, 2010. doi:10.1126/science.1197321.

[254] Ph Ebert, M Heinrich, M Simon, C Domke, K Urban, C.K. Shih, M. B. Webb, and M. G. Lagally. Thermal formation of Zn-dopant-vacancy complexes on InP(110) surfaces. *Physical Review B*, 53(4580), 1996. doi:10.1103/PhysRevB.53.4580.

[255] Hiroshi Kajiyama, Y Suwa, S Heike, M Fujimori, J Nara, T Ohno, S Matsuura, T Hitosugi, and T Hashizume. Room-Temperature Adsorption of Si Atoms on H-terminated Si(001)-2 x 1 Surface. *Journal of the Physical Society of Japan*, 74:389–392, 2005. doi:10.1143/JPSJ.74.389.

[256] Michele Ceriotti and Marco Bernasconi. Diffusion and desorption of Si H3 on hydrogenated H:Si (100) - (2x1) from first principles. *Physical Review B - Condensed Matter and Materials Physics*, 76(24):1–12, 2007. ISSN 10980121. doi:10.1103/PhysRevB.76.245309.

[257] Changqing Wang, Yongsheng Zhang, and Yu Jia. A new Si tetramer structure on Si (001). *Solid State Sciences*, 11(9):1661–1665, 2009. doi:10.1016/j.solidstatesciences.2009.06.012.

[258] Amandine Bellec, Damien Riedel, Gérald Dujardin, Nikolaos Rompotis, and Lev N Kantorovich. Dihydride dimer structures on the Si(100):H surface studied by low-temperature scanning tunneling microscopy. *Physical Review B*, 78(165302), 2008. doi:10.1103/PhysRevB.78.165302.

[259] Yuji Suwa, Masaaki Fujimori, Seiji Heike, Yasuhiko Terada, Yoshihide Yoshimoto, Kazuto Akagi, Osamu Sugino, and Tomihiro Hashizume. First Principles Study of Dihydride Chains on H-Terminated Si(100)-2x1 Surface. *Japanese Journal of Applied Physics*, 45(3B):2200–2203, 2006. doi:10.1143/JJAP.45.2200.

[260] Yuji Suwa, Masaaki Fujimori, Seiji Heike, Yasuhiko Terada, Yoshihide Yoshimoto, Kazuto Akagi, Osamu Sugino, and Tomihiro Hashizume. Formation of

dihydride chains on H-terminated Si(100)-2x1 surfaces: Scanning tunneling microscopy and first-principles calculations. *Physical Review B*, 74(205308), 2006. doi:10.1103/PhysRevB.74.205308.

[261] C. C. Cheng and J. T. Yates. H-induced surface restructuring on Si(100): Formation of higher hydrides. *Physical Review B*, 43:4041–4045, feb 1991. doi:10.1103/PhysRevB.43.4041.

[262] Dongxue Chen and John J. Boland. Chemisorption-induced disruption of surface electronic structure: Hydrogen adsorption on the (formula presented) surface. *Physical Review B*, 65(165336), 2002. doi:10.1103/PhysRevB.65.165336.

[263] Paul C. Weakliem, Zhenyu Zhang, and Horia Metiu. Missing dimer vacancies ordering on the Si(100) surface. *Surface Science*, 336(3):303–313, 1995. doi:10.1016/0039-6028(95)00436-X.

[264] J H G Owen, D R Bowler, C M Goringe, K Miki, and G A D Briggs. Identification of the Si(001) missing dimer defect structure by low bias voltage STM and LDA modelling. *Surface Science*, 341(3):L1042–L1047, 1995. doi:10.1016/0039-6028(95)00794-6.

[265] S. Morita, R. Wiesendanger, and E. Meyer, editors. *Noncontact Atomic Force Microscopy*. Springer, Berlin, 1st edition, 2002. doi:10.1007/978-3-642-56019-4.

[266] Y J Chabal and Krishnan Raghavachari. New Ordered Structure for the H-Saturated Si(100) Surface: The (3 x 1) Phase. *Physical Review Letters*, 54:1055–1058, 1985. doi:10.1103/PhysRevLett.54.1055.

[267] Jae Yeol Maeng, Sehun Kim, S K Jo, W P Fitts, and J M White. Absorption of gas-phase atomic hydrogen by Si(100): Effect of surface atomic structures. *Applied Physics Letters*, 79(1):36, 2001. doi:10.1063/1.1379989.

[268] Emily J Buehler and John J Boland. Identification and characterization of a novel silicon hydride species on the Si(100) surface. *Surface Science*, 425(1):L363–L368, 1999. doi:10.1016/S0039-6028(99)00205-8.

[269] Taro Hitosugi, S. Heike, T. Onogi, T. Hashizume, S. Watanabe, Z. Q. Li, K. Ohno, Y. Kawazoe, T. Hasegawa, and K. Kitazawa. Jahn-Teller distortion in dangling-bond linear chains fabricated on a Hydrogen-terminated Si(100)-2x1 surface. *Physical Review Letters*, 82:4034–4037, 1999. doi:10.1103/PhysRevLett.82.4034.

[270] Joshua B. Ballard, James H. G. Owen, Justin D. Alexander, William R. Owen, Ehud Fuchs, John N. Randall, Roberto C. Longo, and Kyeongjae Cho. Spurious dangling bond formation during atomically precise hydrogen depassivation lithography on Si(100): The role of liberated hydrogen. *Journal of Vacuum Science & Technology B*, 32:021805, 2014. doi:10.1116/1.4864302.

[271] B R Trenhaile, Abhishek Agrawal, and J H Weaver. Oxygen atoms on Si(100)-(2x1): Imaging with scanning tunneling microscopy. *Applied Physics Letters*, 89(15):173118, 2006. doi:10.1063/1.2362623.

[272] Ph. Avouris and D. Cahill. STM studies of Si(100)-2x1 oxidation: defect chemistry and Si ejection. *Ultramicroscopy*, 42-44:838–844, 1992. doi:10.1016/0304-3991(92)90366-R.

[273] M A Roberson and S K Estreicher. Vacancy and vacancy-hydrogen complexes in silicon. *Physical Review B*, 49(17040), 1994. doi:10.1103/PhysRevB.49.17040.

[274] Hongqi Xu. Electronic structure of hydrogen-vacancy complexes in crystalline silicon: A theoretical study. *Physical Review B*, 46:1403, 1992. doi:10.1103/PhysRevB.46.1403.

[275] T. Zundel and J. Weber. Trap-limited hydrogen diffusion in boron-doped silicon. *Physical Review B*, 46(4):2071–2077, 1992. doi:10.1103/PhysRevB.46.2071.

[276] C. P. Herrero, M. Stutzmann, and A. Breitschwerdt. Boron-hydrogen complexes in crystalline silicon. *Physical Review B*, 43(2):1555–1575, jan 1991. doi:10.1103/PhysRevB.43.1555.

[277] C K Ong and G S Khoo. The nature of the hydrogen-boron complex of crystalline Si. *Journal of Physics: Condensed Matter*, 3(6):675–680, 1991. doi:10.1088/0953-8984/3/6/005.

[278] R. Rizk, P. de Mierry, C. Song, D. Ballutaud, and B. Pajot. Spectroscopic investigation of hydrogen-dopant complexes in bulk p-type and implanted n-type crystalline silicon. *Journal of Applied Physics*, 70(7):3802–3807, 1991. doi:10.1063/1.349183.

[279] Franz J. Giessibl. High-speed force sensor for force microscopy and profilometry utilizing a quartz tuning fork. *Applied Physics Letters*, 73(26):3956–3958, 1998. doi:10.1063/1.122948.

[280] Hatem Labidi, Martin Kupsta, Taleana Huff, Mark Salomons, Douglas Vick, Marco Taucer, Jason Pitters, and Robert A. Wolkow. New fabrication technique for highly sensitive qPlus sensor with well-defined spring constant. *Ultramicroscopy*, 158:33–37, 2015. doi:10.1016/j.ultramic.2015.06.008.

[281] Jason L Pitters, Paul G Piva, and Robert A Wolkow. Dopant depletion in the near surface region of thermally prepared silicon (100) in UHV. *Journal of Vacuum Science & Technology B*, 30(021806), 2012. doi:10.1116/1.3694010.

[282] Avogadro: an open-source molecular builder and visualization tool. URL `http://avogadro.cc/`.

[283] Marcus D Hanwell, Donald E Curtis, David C Lonie, Tim Vandermeersch, Eva Zurek, and Geoffrey R Hutchison. Avogadro: an advanced semantic chemical editor, visualization, and analysis platform. *Journal of Cheminformatics*, 4(17), 2012. doi:10.1186/1758-2946-4-17.

[284] Thomas A. Halgren. Merck molecular force field. I. Basis, form, scope, parameterization, and performance of MMFF94. *Journal of Computational Chemistry*, 17(5-6):490–519, 1996. doi:10.1002/(SICI)1096-987X(199604)17:5/6<490::AID-JCC1>3.0.CO;2-P.

[285] Clare F. Macrae, Ian J. Bruno, James A. Chisholm, Paul R. Edgington, Patrick McCabe, Elna Pidcock, Lucia Rodriguez-Monge, Robin Taylor, Jacco van de Streek, Peter A. Wood, and IUCr. Mercury CSD 2.0 – new features for the visualization and investigation of crystal structures. *Journal of Applied Crystallography*, 41:466–470, apr 2008. doi:10.1107/S0021889807067908.

[286] Jens Falter, Marvin Stiefermann, Gernot Langewisch, Philipp Schurig, Hendrik Hölscher, Harald Fuchs, and André Schirmeisen. Calibration of quartz tuning fork spring constants for non-contact atomic force microscopy: Direct mechanical measurements and simulations. *Beilstein Journal of Nanotechnology*, 5:507–516, 2014. doi:10.3762/bjnano.5.59.

[287] Yuji Suwa, S Matsuura, M Fujimori, S Heike, T Onogi, H Kajiyama, T Hitosugi, K Kitazawa, T Uda, and T Hashizume. Dopant-Pair Structures Segregated on a Hydrogen-Terminated Si(100) Surface. *Physical Review Letters*, 90(156101), 2003. doi:10.1103/PhysRevLett.90.156101.

[288] Floris A. Zwanenburg, Andrew S. Dzurak, Andrea Morello, Michelle Y. Simmons, Lloyd C L Hollenberg, Gerhard Klimeck, Sven Rogge, Susan N. Coppersmith, and Mark A. Eriksson. Silicon quantum electronics. *Reviews of Modern Physics*, 85(961), 2013. doi:10.1103/RevModPhys.85.961.

[289] Dieter K. Schroder. *Semiconductor Material and Device Characterization*. John Wiley & Sons, Inc., Hoboken, NJ, USA, 3rd edition, 2005. doi:10.1002/0471749095.

[290] A. Imre, G. Csaba, L. Ji, G. Orlov, G. H. Bernstein, and W. Porod. Majority Logic Gate for Magnetic Quantum-Dot Cellular Automata. *Science*, 331(5758):205–208, 2006. doi:10.1126/science.1120506.

[291] Kai Sotthewes, Victor Geskin, René Heimbuch, Avijit Kumar, and Harold J W Zandvliet. Research Update: Molecular electronics: The single-molecule switch and transistor. *APL Materials*, 2(010701), 2014. doi:10.1063/1.4855775.

[292] Stefan Fölsch, Jianshu Yang, Christophe Nacci, and Kiyoshi Kanisawa. Atom-By-Atom Quantum State Control in Adatom Chains on a Semiconductor. *Physical Review Letters*, 103(096104), 2009. doi:10.1103/PhysRevLett.103.096104.

[293] G. P. Lopinski, D. D. M. Wayner, and R. A. Wolkow. Self-directed growth of molecular nanostructures on silicon. *Nature*, 406:48–51, 2000. doi:10.1038/35017519.

[294] Xiao Tong, Gino A Dilabio, and Robert A Wolkow. A Self-Directed Growth Process for Creating Covalently Bonded Molecular Assemblies on the H-Si(100)-3x1 Surface. *Nano Letters*, 4(5):979–983, 2004. doi:10.1021/nl049796g.

[295] Alexander B Sieval, Ricarda Opitz, Huub P A Maas, Michael G Schoeman, Geert Meijer, Frank J Vergeldt, Han Zuilhof, and Ernst J R Sudhölter. Monolayers of 1-Alkynes on the H-Terminated Si(100) Surface. *Langmuir*, 16(26):10359–10368, 2000. doi:10.1021/la001109n.

[296] S. R. Schofield, N. J. Curson, M. Y. Simmons, F. J. Rueß, T. Hallam, L. Oberbeck, and R. G. Clark. Atomically Precise Placement of Single Dopants in Si. *Physical Review Letters*, 91:136104, 2003. doi:10.1103/PhysRevLett.91.136104.

[297] Robert. Wolkow. A Step Toward Making and Wiring Up Molecular-Scale Devices. *Japanese Journal of Applied Physics*, 40(6B):4378–4380, 2001. doi:10.1143/JJAP.40.4378.

[298] J.R Tucker and T-C. Shen. Prospects for Atomically Ordered Device Structures Based on STM Lithography. *Solid State Electronics*, 42(7-8):1061–1067, 1998. doi:10.1016/S0038-1101(97)00302-X.

[299] Ondrej Dyck, Maxim Ziatdinov, David B. Lingerfelt, Raymond R. Unocic, Bethany M. Hudak, Andrew R. Lupini, Stephen Jesse, and Sergei V. Kalinin. Atom-by-atom fabrication with electron beams. *Nature Reviews Materials*, 4(7):497–507, 2019. doi:10.1038/s41578-019-0118-z.

[300] Vijay Badrinarayanan, Alex Kendall, and Roberto Cipolla. SegNet: A Deep Convolutional Encoder-Decoder Architecture for Image Segmentation. *IEEE Transactions on Pattern Analysis and Machine Intelligence*, 39(12):2481–2495, 2017. doi:10.1109/TPAMI.2016.2644615.

[301] Jonathan Long, Evan Shelhamer, and Trevor Darrell. Fully convolutional networks for semantic segmentation. In *2015 IEEE Conference on Computer Vision and Pattern Recognition (CVPR)*, pages 3431–3440, Boston, MA, 2015. IEEE. doi:10.1109/CVPR.2015.7298965.

[302] Hyeonwoo Noh, Seunghoon Hong, and Bohyung Han. Learning Deconvolution Network for Semantic Segmentation. In *2015 IEEE International Conference on Computer Vision (ICCV)*, pages 1520–1528, Santiago, 2015. IEEE. doi:10.1109/ICCV.2015.178.

[303] João Carreira, Rui Caseiro, Jorge Batista, and Cristian Sminchisescu. Semantic Segmentation with Second-Order Pooling. In *Conference on Computer Vision and Pattern Recognition (CVPR)*, pages 430–443, 2012. doi:10.1007/978-3-642-33786-4_32.

[304] Ross Girshick, Jeff Donahue, Trevor Darrell, and Jitendra Malik. Rich Feature Hierarchies for Accurate Object Detection and Semantic Segmentation. In *2014 IEEE Conference on Computer Vision and Pattern Recognition*, pages 580–587, Columbus, OH, 2014. IEEE. doi:10.1109/CVPR.2014.81.

[305] Masaaki Fujimori, Seiji Heike, Yuji Suwa, and Tomihiro Hashizume. Initial-Stage Dihydride Formation on Si(100)-2x1-H Surface. *Japan Journal of Applied Physics*, 42 (11B):1387–1390, 2003. doi:10.1143/JJAP.42.L1387.

[306] Chris Pearson, Brian Borovsky, Michael Krueger, Robert Curtis, and Eric Ganz. Si(001) Step Dynamics. *Physical Review Letters*, 74(14):2710–2713, 1995.

[307] Bryan C. Russel, Antonio Torralba, Kevin P. Murphy, and William T Freeman. LabelMe: a database and web-based tool for image annotation. *International Journal of Computer Vision*, 77(1-3):157–173, 2008. doi:10.1007/s11263-007-0090-8.

[308] Olaf Ronneberger, Philipp Fischer, and Thomas Brox. U-Net: Convolutional Networks for Biomedical Image Segmentation. *arXiv*, 2015. URL http://arxiv.org/abs/1505.04597.

[309] Carole H Sudre, Wenqi Li, Tom Vercauteren, Sébastien Ourselin, and M. Jorge Cardoso. Generalised Dice overlap as a deep learning loss function for highly unbalanced segmentations. In M. Jorge Cardoso, editor, *Deep Learning in Medical Image Analysis and Multimodal Learning for Clinical Decision Support.*, pages 240–248. 2017. doi:10.1007/978-3-319-67558-9_28.

[310] G. Bradski. The OpenCV Library, 2000. URL https://docs.opencv.org/2.4/index.html.

[311] Artem Maksov, Ondrej Dyck, Kai Wang, Kai Xiao, David B. Geohegan, Bobby G. Sumpter, Rama K. Vasudevan, Stephen Jesse, Sergei V. Kalinin, and Maxim Ziatdinov. Deep learning analysis of defect and phase evolution during electron beam-induced transformations in WS2. *npj Computational Materials*, 5(12), 2019. doi:10.1038/s41524-019-0152-9.

[312] Yi-Lung Cheng, Chih-Yen Lee, and Yao-Liang Huang. Copper Metal for Semiconductor Interconnects. In *Noble and Precious Metals - Properties, Nanoscale Effects and Applications*. InTech, 2018. doi:10.5772/intechopen.72396.

[313] Near Uv. Manipulation and Patterning of Surfaces (Nanolithography). In *Fundamentals and Applications of Nano Silicon in Plasmonics and Fullerines*, chapter 5, pages 89–137. Elsevier, 2018. doi:10.1016/b978-0-323-48057-4.00005-0.

[314] Chris A. Mack. *Fundamental principles of optical lithography : the science of microfabrication*. Wiley, 2007. doi:10.1002/9780470723876.

[315] Andrey Sukhorukov. Nonlinear optics: Diffraction cancellation, jan 2011. ISSN 17494885. URL `www.nature.com/naturephotonics`.

[316] N. Nilius, T.M. Wallis, and W. Ho. Development of One-Dimensional Band Structure in Artificial Gold Chains. *Science*, 297(5588):1853–1856, 2002. doi:10.1126/science.1075242.

[317] C. Chen, C. A. Bobisch, and W. Ho. Visualization of Fermi's Golden Rule Through Imaging of Light Emission from Atomic Silver Chains. *Science*, 325(5943):981–985, 2009. doi:10.1126/science.1174592.

[318] S. Fölsch, P. Hyldgaard, R. Koch, and K. H. Ploog. Quantum Confinement in Monatomic Cu Chains on Cu(111). *Physical Review Letters*, 92(5):056803, feb 2004. doi:10.1103/PhysRevLett.92.056803.

[319] Jérôme Lagoute, Xi Liu, and Stefan Fölsch. Electronic properties of straight, kinked, and branched Cu/Cu(111) quantum wires: A low-temperature scanning tunneling microscopy and spectroscopy study. *Physical Review B*, 74:125410, 2006. doi:10.1103/PhysRevB.74.125410.

[320] B Weber, S Mahapatra, H Ryu, S Lee, A Fuhrer, D L Thompson, W C T Lee, G Klimeck, L C L Hollenberg, and M Y Simmons. Ohm's Law Survives to the Atomic Scale. *Science*, 335(2012), 2012. doi:10.1126/science.1214319.

[321] Marek Kolmer, Pedro Brandimarte, Jakub Lis, Rafal Zuzak, Szymon Godlewski, Hiroyo Kawai, Aran Garcia-Lekue, Nicolas Lorente, Thomas Frederiksen, Christian Joachim, Daniel Sanchez-Portal, and Marek Szymonski. Electronic transport in planar atomic-scale structures measured by two-probe scanning tunneling spectroscopy. *Nature Communications*, 10(1573), 2019. doi:10.1038/s41467-019-09315-6.

[322] Stephanie Yong. *Nanofabrication of a CMOS Compatible Device For Macro-to-Atom Interfacing*. PhD thesis, University of Alberta, 2020.

[323] Borislav Naydenov and John J Boland. Engineering the electronic structure of surface dangling bond nanowires of different size and dimensionality. *Nanotechnology*, 24: 275202, 2013. doi:10.1088/0957-4484/24/27/275202.

[324] Hassan Raza. Theoretical study of isolated dangling bonds, dangling bond wires, and dangling bond clusters on a H:Si(001)-2x1 surface. *Physical Review B*, 76(045308), 2007. doi:10.1103/PhysRevB.76.045308.

[325] R Robles, M Kepenekian, S Monturet, C Joachim, and N Lorente. Energetics and stability of dangling-bond silicon wires on H passivated Si(100). *Journal of Physics: Condensed Matter*, 24(44):445004, 2012. doi:10.1088/0953-8984/24/44/445004.

[326] Hiroyo Kawai, Yong Kiat Yeo, Mark Saeys, and Christian Joachim. Conductance decay of a surface hydrogen tunneling junction fabricated along a Si(001)-(2x1)-H atomic wire. *Physical Review B*, 81(195316), 2010. doi:10.1103/PhysRevB.81.195316.

[327] P Domergue, L. Pizzagalli, C. Joachim, A. Altibelli, and A. Baratoff. Conductance of a finite missing hydrogen atomic line on Si(001)-(2x1)-H. *Physical Review B*, 59(24): 15910–15916, 1999. doi:10.1103/PhysRevB.59.15910.

[328] Mikaël Kepenekian, Frederico D Novaes, Roberto Robles, Serge Monturet, Hiroyo Kawai, Christian Joachim, and Nicolás Lorente. Electron transport through dangling-bond silicon wires on H-passivated Si(100). *Journal of Physics: Condensed Matter*, 25 (2):025503, 2013. doi:10.1088/0953-8984/25/2/025503.

[329] Mikaël Kepenekian, Roberto Robles, Christian Joachim, and Nicolás Lorente. Surface-State Engineering for Interconnects on H-Passivated Si(100). *Nano Letters*, 13(3): 1192–1195, 2013. doi:10.1021/NL304611M.

[330] Hassan Raza, Tehseen Z. Raza, and Edwin C. Kan. Electrical transport in a two-dimensional electron and hole gas on a Si(001)-(2x1) surface. *Physical Review B - Condensed Matter and Materials Physics*, 78(19):1–4, 2008. ISSN 10980121. doi:10.1103/PhysRevB.78.193401.

[331] Qi An, Chen Hu, Guanghua Yu, and Hong Guo. Spin-polarized quantum transport in Si dangling bond wires. *Nanoscale*, 12(10):6079–6088, mar 2020. doi:10.1039/D0NR00037J.

[332] H. Büch, S. Mahapatra, R. Rahman, A. Morello, and M. Y. Simmons. Spin readout and addressability of phosphorus-donor clusters in silicon. *Nature Communications*, 4 (2017), 2013. doi:10.1038/ncomms3017.

[333] Felix J Schupp. Single-electron devices in silicon. *Materials Science and Technology*, 33(8):944–962, 2016. doi:10.1080/02670836.2016.1242826.

[334] Matthias Koch, Joris G. Keizer, Prasanna Pakkiam, Daniel Keith, Matthew G. House, Eldad Peretz, and Michelle Y. Simmons. Spin read-out in atomic qubits in an all-epitaxial three-dimensional transistor. *Nature Nanotechnology*, 14(2):137–140, 2019. doi:10.1038/s41565-018-0338-1.

[335] M. A. Broome, S. K. Gorman, M. G. House, S. J. Hile, J. G. Keizer, D. Keith, C. D. Hill, T. F. Watson, W. J. Baker, L. C. L. Hollenberg, and M. Y. Simmons. Two-electron spin correlations in precision placed donors in silicon. *Nature Communications*, 9(980), 2018. doi:10.1038/s41467-018-02982-x.

[336] Fabian Mohn, Leo Gross, Nikolaj Moll, and Gerhard Meyer. Imaging the charge distribution within a single molecule. *Nature Nanotechnology*, 7(4):227–231, 2012. doi:10.1038/nnano.2012.20.

[337] Julia L. Neff and Philipp Rahe. Insights into Kelvin probe force microscopy data of insulator-supported molecules. *Physical Review B*, 91(8), 2015. doi:10.1103/PhysRevB.91.085424.

[338] Clemens Barth and Claude R. Henry. Kelvin Probe Force Microscopy on MgO(001) Surfaces and Supported Pd Nanoclusters. *The Journal of Physical Chemistry C*, 113 (1):247–253, 2009. doi:10.1021/jp807340k.

[339] M. Weinelt, M. Kutschera, R. Schmidt, C. Orth, T. Fauster, and M. Rohlfing. Electronic structure and electron dynamics at Si(100). *Applied Physics A*, 80:995–1003, 2005. doi:10.1007/s00339-004-3127-7.

[340] John J. Boland. Evidence of pairing and its role in the recombinative desorption of hydrogen from the Si(100)-2x1 surface. *Physical Review Letters*, 67(12):1539–1542, 1991. ISSN 00319007. doi:10.1103/PhysRevLett.67.1539.

[341] T. Uda, H. Shigekawa, Y. Sugawara, S. Mizuno, H. Tochihara, Y. Yamashita, J. Yoshinobu, K. Nakatsuji, H. Kawai, and F. Komori. Ground state of the Si(001) surface revisited—is seeing believing? *Progress in Surface Science*, 76(6-8):147–162, 2004. doi:10.1016/J.PROGSURF.2004.05.015.

[342] P. Kruger, A. Mazur, J. Pollmann, and G. Wolfgarten. First-Principles Electronic Structure Theory for Semi-infinite Semiconductors with Applications to Ge(001) (2x1) and Si(001) (2x1). *Physical Review Letters*, 57(12):1468–1471, 1986. ISSN 00319007. doi:10.1103/PhysRevLett.57.1468.

[343] Michael Rohlfing, Peter Krüger, and Johannes Pollmann. Efficient scheme for GW quasiparticle band-structure calculations with applications to bulk Si and to the Si(001)-(2x1) surface. *Physical Review B*, 52(3):1905–1917, 1995. doi:10.1103/PhysRevB.52.1905.

[344] Ji Young Lee, Jin Ho Choi, and Jun Hyung Cho. Antiferromagnetic coupling between two adjacent dangling bonds on Si(001): Total-energy and force calculations. *Physical Review B - Condensed Matter and Materials Physics*, 78(8):1–4, 2008. ISSN 10980121. doi:10.1103/PhysRevB.78.081303.

[345] Ji Young Lee, Jun Hyung Cho, and Zhenyu Zhang. Quantum size effects in competing charge and spin orderings of dangling bond wires on Si(001). *Physical Review B*, 80 (15):3–7, 2009. doi:10.1103/PhysRevB.80.155329.

[346] Shadi Fatayer, Bruno Schuler, Wolfram Steurer, Ivan Scivetti, Jascha Repp, Leo Gross, Mats Persson, and Gerhard Meyer. Reorganization energy upon charging a single molecule on an insulator measured by atomic force microscopy. *Nature Nanotechnology*, 13:376–380, 2018. ISSN 1748-3387. doi:10.1038/s41565-018-0087-1.

[347] Mohammad Rashidi, Jacob A.J. Burgess, Marco Taucer, Roshan Achal, Jason L. Pitters, Sebastian Loth, and Robert A. Wolkow. Time-resolved single dopant charge dynamics in silicon. *Nature Communications*, 7(13258), 2016. doi:10.1038/ncomms13258.

[348] Amandine Bellec, Laurent Chaput, Gérald Dujardin, Damien Riedel, Louise Stauffer, and Philippe Sonnet. Reversible charge storage in a single silicon atom. *Physical Review B - Condensed Matter and Materials Physics*, 88(24):1–5, 2013. ISSN 10980121. doi:10.1103/PhysRevB.88.241406.

[349] Hiromi Okada, Yoshitaka Fujimoto, Katsuyoshi Endo, Kikuji Hirose, and Yuzo Mori. Detailed analysis of scanning tunneling microscopy images of the Si(100) reconstructed surface with buckled dimers. *Physical Review B*, 63(195324):1–7, 2001. doi:10.1103/PhysRevB.63.195324.

[350] Adam Sweetman, Sam Jarvis, Rosanna Danza, Joseph Bamidele, Subhashis Gangopadhyay, Gordon A Shaw, Lev Kantorovich, and Philip Moriarty. Toggling Bistable Atoms via Mechanical Switching of Bond Angle. *Physical Review Letters*, 106(136101), 2011. doi:10.1103/PhysRevLett.106.136101.

[351] Takashi Yokoyama and Kunio Takayanagi. Anomalous flipping motions of buckled dimers on the Si(001) surface at 5 K. *Physical Review B*, 61(8):R5078–R5081, 2000. doi:10.1103/PhysRevB.61.R5078.

[352] Jun Yoshinobu. Physical properties and chemical reactivity of the buckled dimer on Si(100). *Progress in Surface Science*, 77(1-2):37–70, 2004. doi:10.1016/J.PROGSURF.2004.07.001.

[353] A. Sweetman, S. Gangopadhyay, R. Danza, N. Berdunov, and P. Moriarty. QPlus atomic force microscopy of the Si(100) surface: Buckled, split-off, and added dimers. *Applied Physics Letters*, 95(6), 2009. doi:10.1063/1.3197595.

[354] M. Çakmak and G. P. Srivastava. Theoretical study of dangling-bond wires on the H-terminated Si surface. *Surface Science*, 532-535:556–559, 2003. ISSN 00396028. doi:10.1016/S0039-6028(03)00118-3.

[355] Xiao-Yan Ren, Hyun-Jung Kim, Chun-Yao Niu, Yu Jia, and Jun-Hyung Cho. Origin of Symmetric Dimer Images of Si(001) Observed by Low-Temperature Scanning Tunneling Microscopy. *Scientific Reports*, 6:27868, 2016. doi:10.1038/srep27868.

[356] Satoshi Watanabe, Yoshimasa A Ono, Tomihiro Hashizume, and Yasuo Wada. Theoretical study of atomic and electronic structures of atomic wires on an H-terminated Si(100)2x1 surface. *Physical Review B*, 54:R17308–R17311, 1996. doi:10.1103/PhysRevB.54.R17308.

[357] D. R. Bowler and A. J. Fisher. Small polaron formation in dangling-bond wires on the Si(001) surface. *Physical Review B - Condensed Matter and Materials Physics*, 63: 035310, 2000. doi:10.1103/PhysRevB.63.035310.

[358] S. Watanabe, Y. A. Ono, T. Hashizume, and Y. Wada. First-principles study of atomic wires on a H-terminated Si(100)-(2x1) surface. *Surface Science*, 386(1-3):340–342, 1997. ISSN 00396028. doi:10.1016/S0039-6028(97)00338-5.

[359] Jun-Hyung Cho and Leonard Kleinman. Nature of lattice distortion in one-dimensional dangling-bond wires on Si and C. *Physical Review B*, 66(23):235405, 2002. doi:10.1103/PhysRevB.66.235405.

[360] F. Bird, J. Fisher, and R. Bowler. Soliton effects in dangling-bond wires on Si(001). *Physical Review B*, 68(115318), 2003. doi:10.1103/PhysRevB.68.115318.

[361] M. Todorovic, A. J. Fisher, and D. R. Bowler. Diffusion of a polaron in dangling bond wires on Si(001). *Journal of Physics Condensed Matter*, 14(49), 2002. ISSN 09538984. doi:10.1088/0953-8984/14/49/103.

[362] H. Ness and A. J. Fisher. Transmission through Peierls distorted one-dimensional atomic wires: Quantum coherent electron-phonon coupling. *Applied Surface Science*, 162:613–619, 2000. doi:10.1016/S0169-4332(00)00259-2.

[363] M. Dürr and U. Höfer. Dissociative adsorption of molecular hydrogen on silicon surfaces. *Surface Science Reports*, 61(12):465–526, 2006. doi:10.1016/j.surfrep.2006.08.002.

[364] John A Wood, Mohammad Rashidi, Mohammad Koleini, Jason L Pitters, and Robert A Wolkow. Multiple Silicon Atom Artificial Molecules. *arXiv*, 2016. URL `https://arxiv.org/abs/1607.06050`.

[365] John A Wood. *Silicon Dangling Bond Chains - A study of Emergent Electronic Structure and Charging Configurations Formed Through Coupling Between Close-Spaced Dangling Bond Quantum Dots on the Hydrogen Terminated Silicon (100) 2x1 Surface*. PhD thesis, University of Alberta, 2017. URL `https://doi.org/10.7939/R3MW28S56`.

[366] J. Hubbard. Electron correlations in narrow energy bands. *Proceedings of the Royal Society A*, 276(1365), 1963.

[367] Neil W. Ashcroft and N. Mermin, David. *Solid State Physics*. Brooks/Cole Publishing Company, 1976.

[368] Jun Ho Lee and Jun Hyung Cho. Instability of one-dimensional dangling-bond wires on H-passivated C(001), Si(001), and Ge(001) surfaces. *Surface Science*, 605(7-8):L13–L15, 2011. ISSN 00396028. doi:10.1016/j.susc.2011.01.011. URL http://dx.doi.org/10.1016/j.susc.2011.01.011.

[369] E. Pytte. Peierls instability in Heisenberg chains. *Physical Review B*, 10(11):4637–4642, 1974. ISSN 01631829. doi:10.1103/PhysRevB.10.4637.

[370] William Barford and Robert J. Bursill. Peierls transition in the quantum spin-peierls model. *Physical Review Letters*, 95(13):1–4, 2005. ISSN 00319007. doi:10.1103/PhysRevLett.95.137207.

[371] D. K. Campbell, J. Tinka Gammel, and E. Y. Loh. Modeling electron-electron interactions in reduced-dimensional materials: Bond-charge Coulomb repulsion and dimerization in Peierls-Hubbard models. *Physical Review B*, 42(1):475–492, 1990. ISSN 01631829. doi:10.1103/PhysRevB.42.475.